

Electronic Thesis and Dissertation Repository

12-9-2014 12:00 AM

Fragmentation and Wake Formation in Faint Meteors: Implications for the Structure and Ablation of Small Meteoroids

Edward Stokan
The University of Western Ontario

Supervisor
Margaret Campbell-Brown
The University of Western Ontario

Graduate Program in Physics
A thesis submitted in partial fulfillment of the requirements for the degree in Doctor of
Philosophy
© Edward Stokan 2014

Follow this and additional works at: <https://ir.lib.uwo.ca/etd>



Part of the [Other Physics Commons](#)

Recommended Citation

Stokan, Edward, "Fragmentation and Wake Formation in Faint Meteors: Implications for the Structure and Ablation of Small Meteoroids" (2014). *Electronic Thesis and Dissertation Repository*. 2581.
<https://ir.lib.uwo.ca/etd/2581>

This Dissertation/Thesis is brought to you for free and open access by Scholarship@Western. It has been accepted for inclusion in Electronic Thesis and Dissertation Repository by an authorized administrator of Scholarship@Western. For more information, please contact wlsadmin@uwo.ca.

**Fragmentation and wake formation in faint meteors:
implications for the structure and ablation of small meteoroids**

(Thesis format: integrated article)

by

Edward Stokan

Graduate Program in Physics

A thesis submitted in partial fulfillment
of the requirements for the degree of
Doctor of Philosophy

The School of Graduate and Postdoctoral Studies
The University of Western Ontario
London, Ontario, Canada

© Edward Stokan 2014

Abstract

Meteors with peak magnitudes fainter than +2 are typically called faint meteors, resulting from the atmospheric entry and ablation of meteoroids less massive than 10^{-4} kg. The processes of luminous wake formation and fragmentation, which occur during ablation, are poorly understood for faint meteors, and are important constraints for models of meteoroid structure. The goal of this work is to improve understanding of these processes through analysis of high-resolution intensified video observations, and creation of a detailed meteoroid ablation model.

In the first part of this work, thirty faint meteors observed with the Canadian Automated Meteor Observatory (CAMO) are analysed, revealing meteor trails with widths up to 100 m at heights above 110 km. These widths vary with height as the inverse of the atmospheric density, suggesting that formation of the wake is related to collisions between evaporated meteoric atoms and atmospheric molecules.

Next, nine fragmenting faint meteors captured with CAMO are examined. Fragments from eight of the nine meteors are found to have transverse speeds up to 100 m s^{-1} . These speeds are not explained by aerodynamic separation theory typically used for brighter meteors that fragment at lower heights. Instead, fragment separation by rotational breakup of the meteoroid or electrostatic repulsion are considered, giving meteoroid strength estimates up to 1 MPa. These strengths are typical of meteorite-producing meteoroids and are larger than expected for small meteoroids.

Finally, a single-body ablation model, based on modelling collisions between the meteoroid, meteoric atoms, and atmospheric molecules, is devised to explain wake formation. Syn-

thetic meteor trail widths and lengths, as well as light curves and deceleration profiles, are compared to observations of nine meteors from the first part of this thesis. The widths of simulated meteor wakes show good agreement with observations, but simulated wake lengths are too short. This suggests that collisional de-excitation of meteoric particles is a plausible process for wake formation, but also that meteoroid fragmentation likely increases the length of the meteor wake. Compared to observations, simulated light curves are longer, and simulated meteoroids experience less deceleration, suggesting that meteoroid fragmentation should be investigated in the next iteration of the model.

Keywords: meteors, meteoroids, meteor wake, meteor trail, meteoroid fragmentation, meteoroid ablation modelling, direct simulation Monte Carlo, image processing, interplanetary dust

Co-Authorship Statement

Versions of three of the chapters of this thesis have been previously published or submitted for publication:

Chapter 3: Stokan, E., Campbell-Brown, M. D., Brown, P. G., Hawkes, R. L., Doubova, M., Weryk, R. J., (2013). *Optical trail widths of faint meteors observed with the Canadian Automated Meteor Observatory*. Monthly Notices of the Royal Astronomical Society, 433 (2), 962-975.

Chapter 4: Stokan, E., Campbell-Brown, M. D., (2014). *Transverse motion of fragmenting faint meteors observed with the Canadian Automated Meteor Observatory*. Icarus, 232, 1-12.

Chapter 5: Stokan, E., Campbell-Brown, M. D., (2014). *A particle-based model for ablation and wake formation in faint meteors*. Monthly Notices of the Royal Astronomical Society, accepted November 29, 2014.

I (Edward Stokan) wrote each of these manuscripts, performed the measurements and analysis discussed in Chapters 3 and 4, and devised and implemented the model discussed in Chapter 5. The contributions of the co-authors are as follows:

- For Chapter 3, Margaret Campbell-Brown, Peter Brown, Robert Hawkes, and Robert Weryk provided advice, as well as suggestions to improve the manuscript. Maria Doubova assisted in selecting meteors for measurement and helped develop the ImageJ script to measure meteor trail widths.

- For Chapters 4 and 5, Margaret Campbell-Brown provided advice and improvements to the manuscripts.
- All video observations discussed in this thesis were captured with the Canadian Automated Meteor Observatory (CAMO), an automated system developed and maintained by the Meteor Physics Group at the University of Western Ontario. The reduction software METAL, by Robert Weryk, was used to calculate meteoroid trajectories and meteor light curves. CAMO, observations, and reductions are discussed in Chapter 2.

Acknowledgements

I thank my supervisor, Margaret Campbell-Brown, for many years of patient, thoughtful, and generous support during the development of this thesis. I also thank Peter Brown, Bob Hawkes, and Rob Weryk for additional mentoring, and all of the members of the Meteor Physics Group at Western for many interesting and motivating discussions. Financial support from the Natural Sciences and Engineering Research Council of Canada and the University of Western Ontario is gratefully acknowledged. Finally, I thank my parents, Laura and Gene, and my brother, Dave, for all of their encouragement and support.

Contents

Title page	i
Abstract	ii
Co-authorship statement	iv
Acknowledgements	vi
Table of contents	vii
List of figures	xi
List of tables	xiv
1 Introduction	1
1.1 Thesis motivation, and introduction to meteor physics	1
1.2 Observations of faint meteors	13
1.2.1 Photographic	13
1.2.2 Radar	17
1.2.3 Video	25
1.2.4 Other techniques	38
1.2.5 Summary of observations	41
1.3 Models of ablation for faint meteors	43
1.3.1 Single-body fundamentals	43
1.3.2 The dustball model	48
1.3.3 Alternative models for meteoroid fragmentation	52
1.3.4 High-resolution, sputtering, and other models	56

1.3.5	Summary of modelling	58
1.4	Thesis goals	59
2	Observations and reductions	75
2.1	The Canadian Automated Meteor Observatory	75
2.1.1	Hardware	76
2.1.2	Software	79
2.2	Reduction of meteor video	84
2.2.1	Astrometry	84
2.2.2	Photometry	88
3	Measurement of the trail widths of faint meteors	92
3.1	Introduction	92
3.1.1	The importance of meteor trail widths	92
3.1.2	Previous studies of optical and ion trail widths	94
3.1.3	Study goals	99
3.2	Instrumentation	100
3.3	Data reduction	103
3.3.1	Determination of meteor trajectories and orbits using wide-field data	103
3.3.2	Measurement of meteor trail widths using narrow-field data	104
3.3.3	Correction of image bloom in trail widths using a stellar calibration curve	107
3.3.4	Conversion of measurements from pixels to metres, effect of image smear, and final trail width uncertainty	111
3.4	Results and discussion	112
3.4.1	Illustration of measurement procedure: representative event	113
3.4.2	General results from all meteors studied	122
3.5	Conclusions	129
4	Observations of gross fragmentation in faint meteors	135
4.1	Introduction	135
4.2	Instruments and analysis	138

4.2.1	The Canadian Automated Meteor Observatory	138
4.2.2	Wide-field reductions	140
4.2.3	Narrow-field reductions	141
4.3	Observations of fragmentation	144
4.3.1	Single fragmentation	145
4.3.2	Multiple fragmentations	148
4.3.3	Complex fragmentation	151
4.3.4	Summary of observations	153
4.4	Models of fragmentation	155
4.4.1	Aerodynamic loading	158
4.4.2	Rotation	158
4.4.3	Electrostatic repulsion	161
4.4.4	Explosive devolatilization	164
4.5	Conclusions and future studies	166
5	High-resolution ablation modelling for small meteoroids	173
5.1	Introduction	173
5.2	Ablation model	178
5.2.1	Review of faint meteor ablation models	178
5.2.2	Model overview	180
5.2.3	Assumption of negligible shielding and excited particle interactions	182
5.2.4	Collisions with the meteoroid	185
5.2.5	Particle-particle interactions	187
5.2.6	Generating narrow-field images and light curves	189
5.3	Observations	191
5.3.1	The Canadian Automated Meteor Observatory (CAMO)	191
5.3.2	Wide-field reductions	191
5.3.3	Narrow-field reductions	192
5.3.4	Selected meteors	194
5.4	Model results and analysis	196

5.4.1	Sample meteor analysis: 20101103_063032	196
5.4.2	General results from all of the meteors	203
5.5	Discussion of model assumptions and improvements	209
5.6	Conclusions	216
6	Conclusions	223
6.1	Summary of work	223
6.2	Next steps	225
A	Copyright permissions	230
	Curriculum vitae	239

List of Figures

1.1	Illustration of meteor ablation and terms	2
1.2	Sample light curve sketches	6
1.3	Sketch of two meteoroid fragmentation modes	7
1.4	Explanation of orbital parameters	9
1.5	Illustration of sporadic sources	11
1.6	Sketch of radar detection of meteors and effect of trail width	18
1.7	Sketch of an image intensifier	26
1.8	Sample noise histograms for an image intensified frame	28
1.9	A sample frame from an intensified camera	29
1.10	Illustration of interaction between the meteoroid and atmosphere	44
2.1	Locations of the CAMO stations	76
2.2	Snapshots of a meteor from the narrow-field, wide-field, and influx cameras	77
2.3	Spectral response of CAMO Gen III intensifiers	79
2.4	Photographs of the CAMO shed, enclosure, and cameras	80
2.5	Derivation of a meteoroid trajectory by the intersection of planes method	85
2.6	Derivation of the astrometric plate	86
2.7	Derivation of trajectory residuals	87
2.8	An example of flat-fielding	89
2.9	Sample photometric plate for the Elginfield wide-field camera	90
3.1	Schematic of the trail width measurement process	101
3.2	Sample narrow-field images of meteor 20101103_071855	101
3.3	Sample trail width measurement for meteor 20101103_071855	104
3.4	Pixel brightness profile of the trail segment measured in Figure 3.3	105

3.5	Comparison of the trail and tracking angles	106
3.6	Sample stellar width calibration graph for the Tavistock narrow-field camera . .	107
3.7	Illustration of the perspective angle	111
3.8	The light curve for meteor 20101020_095900	113
3.9	Narrow-field images of 20101020_095900	117
3.10	The trail width of 20101020_095900 as a function of distance along the meteor at 108 km	118
3.11	The corrected, peak trail width of 20101020_095900 as a function of height . .	120
3.12	Comparison of trail widths computed from each station for 20101020_095900 .	121
3.13	Variance in computed trail widths between stations for 20101020_095900 . . .	121
3.14	The peak, corrected trail width for all meteors as a function of height	123
3.15	Particle collision cross sections as a function of relative speed	125
3.16	The largest corrected trail width measured for each meteor in this survey, com- pared with results from other surveys	126
4.1	Image filtering for event 20120523_080013	143
4.2	Snapshots of single fragmentation	146
4.3	Transverse displacement of fragments for the meteor in Fig. 4.2	146
4.4	Sample light curves for meteors showing fragmentation	149
4.5	Snapshots of multiple fragmentations	150
4.6	Transverse displacement of fragments for the meteor in Fig. 4.5	150
4.7	Snapshots of complex fragmentation	152
4.8	Transverse displacement of fragments for the meteor in Fig. 4.7	152
5.1	Illustration of the perspective angle	181
5.2	Schematic of a collision between the meteoroid and an atmospheric particle . .	186
5.3	Observed and simulated light and deceleration curves for 20101103_063032 . .	197
5.4	Simulated and observed narrow-field images of 20101103_063032	199
5.5	Simulated and observed trail brightness profiles for 20101103_063032	200
5.6	Observed and simulated trail width of 20101103_063032	201
5.7	Meteor appearance as a function of minimum collision energy	203

5.8	Collision energy, radial, and trail distance as a function of collision number . .	204
5.9	Simulated and observed trail width and length curves for 20101103_063032 . .	205
5.10	Snapshots of meteors showing disagreement between observed and simulated morphology	205
5.11	Snapshots of meteors showing a trail not replicated by the simulation	206
5.12	Snapshots of meteors showing good agreement between observations and the model	206
5.13	Simulated and observed trail widths	210
5.14	Simulated and observed trail lengths	211
5.15	Simulated and observed light curves	212
5.16	Simulated and observed deceleration profiles	213

List of Tables

1.1	Selected meteor showers	10
1.2	Comparison of modelled (dustball) meteoroid bulk densities	53
2.1	Summary of the CAMO system	81
3.1	Meteor trail widths modelled by Jones (1995)	96
3.2	Properties of eight high-altitude Leonids observed by Spurný et al. (2000) . . .	98
3.3	Parameters for the stellar width calibration curves	109
3.4	Heights, speeds, and peak magnitudes of the thirty observed meteors	114
3.5	Maximum trail widths measured for the thirty meteors	115
3.6	The average fractional difference in trail widths computed from each station . .	123
4.1	Fit parameters for transverse displacement of fragments versus time	147
4.2	All fragment transverse speeds measured in this survey	154
4.3	Properties of the meteors observed in this survey	156
4.4	Meteoroid orbits calculated for the meteors observed in this study	157
4.5	Radiant and convergence angle for each meteor	157
4.6	Summary of rotational fragmentation calculations	161
4.7	Summary of calculations for fragmentation due to electrostatic charging	164
5.1	Ratio of densities of evaporated and atmospheric particles at the first collision .	185
5.2	Properties of the nine meteors selected for modelling	195
5.3	Model fit parameters for the nine meteors	209

Chapter 1

Introduction

1.1 Thesis motivation, and introduction to meteor physics

Meteoroids comprise some of the most numerous and pristine bodies in the Solar System. The International Astronomical Union defines a *meteoroid* as, “a small object moving in interplanetary space, of a size considerably smaller than an asteroid, and considerably larger than an atom or molecule.” Nearly seven million small meteoroids, with masses between 10^{-6} and 10^{-4} kg ($r_{\text{met}} \sim 0.04 - 0.2$ cm, assuming spherical meteoroids with a density of 3000 kg m^{-3}), intersect the Earth each day (Brown et al. 2002), providing ample opportunity to study the structure and composition of interplanetary bodies as an alternative to sending spacecraft and sample return missions. Ultimately, determining the structure and orbit of meteoroids provides information about the distribution of material throughout the Solar System, an important constraint for models of Solar System formation and evolution. Similarly, studying the properties of meteoroids aids in mitigating impact hazards to instruments and personnel in low Earth orbit.

Meteoroids travel at geocentric speeds between between 11 and 72 km s^{-1} . As they enter the atmosphere, high-energy (up to 1 keV) collisions with atmospheric molecules and atoms heat the meteoroid and cause it lose mass, or *ablate*, mainly through evaporation (Ceplecha et al. 1998, Rogers et al. 2005). Evaporated, excited meteoric atoms form a luminous region around the meteoroid called the *meteor trail* or *wake*, which results in the shooting star phenomenon

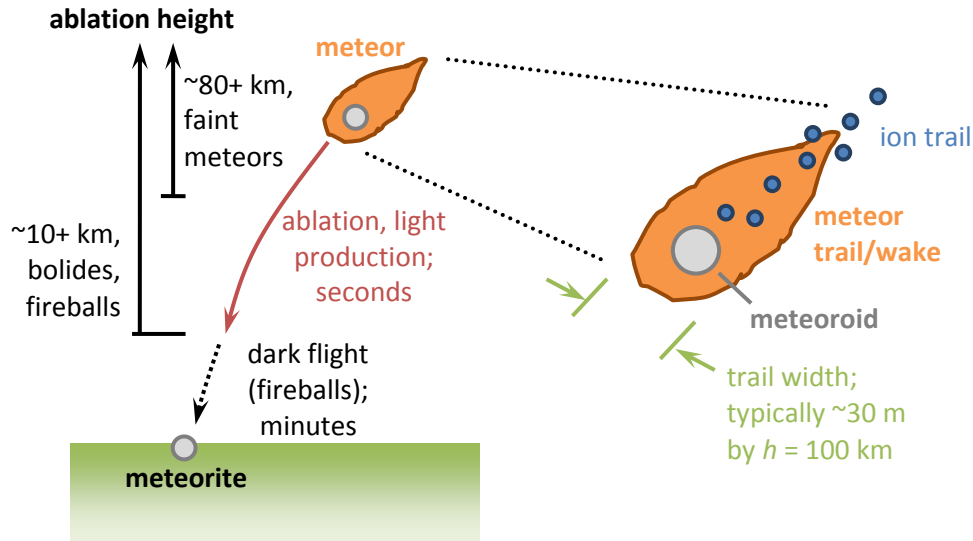


Figure 1.1: Illustration of a meteoroid’s flight and ablation when entering the atmosphere. Faint meteors typically become too dark to observe above heights of 80 km, while bright objects can produce light over longer intervals. The meteor wake, consisting of excited atoms, and ion trail, consisting of ions and electrons, are also illustrated. Meteor wakes have been observed with widths ranging from 1 m to 1 km at heights of 100 km and above, which will be discussed in Section 1.2 in more detail.

called the *meteor*, as illustrated in Figure 1.1. Similarly, meteoric ions form an *ion trail* that can be detected with radar.

Meteors typically last a second or less and can be visually observed from the ground with image-intensified cameras or the naked eye, depending on the brightness of the meteor. The meteor brightness is related to the mass, speed, and composition of the meteoroid, and will be discussed in more detail in the review of meteoroid ablation modelling given in Section 1.3. The variation of meteor brightness as a function of time or meteoroid height, called the *light curve*, is important for determining the initial meteoroid mass and other physical properties. The light curve may also indicate whether the meteoroid fragments during atmospheric entry, which can provide estimates of the strength of the meteoric material. Combining meteoroid properties inferred from the light curve with the trajectory and orbit calculated from observations is ultimately what provides information about the large-scale composition of the Solar System.

For the light curve, meteor brightness is measured in units of photometric magnitude, m_{ph} , where

$$m_{\text{ph}} = -\frac{5}{2} \log_{10} I + C, \quad (1.1)$$

I is the luminous power emitted by the meteoroid, and C is a normalisation constant. Eq. (1.1) gives the *apparent magnitude*, but the *absolute magnitude* M_{ph} , which is the magnitude normalised to an observation distance of 100 km, can be found with

$$M_{\text{ph}} = m_{\text{ph}} + 5 \log_{10} \left(\frac{100 \text{ km}}{r} \right), \quad (1.2)$$

given the range to the meteoroid, r . Magnitude is an inverse logarithmic scale, so values that are more negative represent brighter objects.¹

The shape of the light curve is used to interpret how the meteoroid ablates. Most models (Ceplecha et al. 1998) assume that the meteor's luminous power output is proportional to the rate of kinetic energy loss for the meteoroid,

$$I = -\tau \frac{d}{dt} \left(\frac{1}{2} m v^2 \right) = -\tau \left(\frac{1}{2} \frac{dm}{dt} v^2 + m v \frac{dv}{dt} \right), \quad (1.3)$$

where τ is the *luminous efficiency*, the portion of kinetic energy dissipated as meteor light, while m and v are the mass and speed of the meteoroid, respectively.² For most meteoroids ($v > 16 \text{ km s}^{-1}$, Ceplecha et al. 1998), the dominant term in Eq. (1.3) is the mass loss term as the meteoroid deceleration is negligible, giving

$$I \approx -\frac{\tau}{2} \frac{dm}{dt} v^2. \quad (1.4)$$

The luminous efficiency varies with meteoroid speed, composition (spectral emissions), and the spectral sensitivity of the recording system (Ceplecha et al. 1998, Weryk & Brown 2013).

¹An increase in brightness by a factor of one hundred results in a -5 change in magnitude.

²The discussion of meteoroid ablation models in Section 1.3 will provide the derivation of Eq. (1.3).

Since values for the luminous efficiency are poorly constrained (typically between 0.1 and 10 per cent, Weryk & Brown 2013), it is suitable to assume that τ remains constant during the meteoroid's ablation. Subsequently, the meteor brightness varies with the rate of ablation, dm/dt , and an estimate for the meteoroid mass may be computed by integrating the observed light curve,

$$m_p \approx \frac{2}{\tau v^2} \int I(t) dt, \quad (1.5)$$

where I may be determined from the observed light curve by rearranging Eq. (1.1). Since mass m_p is derived using the light curve, it is called the *photometric mass*.

Increases in meteor brightness indicate more rapid meteoroid ablation. Consideration of the conservation of energy in collisions between the meteoroid and atmospheric molecules and atoms reveals

$$\frac{dm}{dt} \propto S \rho_{\text{atm}}, \quad (1.6)$$

or that the rate of ablation is proportional to the cross-sectional area of the meteoroid, S , as well as the mass density of the atmosphere, ρ_{atm} .³ As a result, meteoroids that do not fragment produce a characteristic *single-body* light curve that slowly increases in brightness and then rapidly decreases, assuming that the meteoroid is homogeneous and ablates self-similarly (like a spherical meteoroid that decreases in radius as the mass decreases).⁴ In contrast, when fragmentation occurs, the effective cross-sectional area of the meteoroid is increased, which increases the rate of ablation, and begins to increase the meteor brightness rapidly. Depending on how the meteoroid fragments, a variety of light curve shapes can result, ranging from fragmentation events at certain heights producing spikes in brightness (flares), or continuous fragmentation causing the peak in brightness to shift closer to the beginning of the light curve. Also, since fragmented meteoroids ablate more rapidly than a single body with the same mass,

³This proportionality will also be derived and explained in more detail in Section 1.3.

⁴The slow initial increase in brightness for a single-body light curve occurs since the atmospheric density increases more rapidly than the meteoroid cross-sectional area decreases due to ablation, in Eqs. (1.3) and (1.6). As the mass of the meteoroid approaches zero, the cross-sectional area decreases very rapidly, overwhelming the increase in atmospheric density, resulting in a rapid decrease in brightness at the end of the light curve.

their light curves are shorter than classical single-body light curves.⁵ Sample light curves, illustrating two cases of meteoroid fragmentation and classical single-body ablation, are given in Figure 1.2.

There are two modes for meteoroid fragmentation, as depicted in Figure 1.3: *gross* or *discrete fragmentation* occurs when a meteoroid splits into several fragments at particular points in the trajectory, while *continuous* or *progressive fragmentation* occurs when a meteoroid continuously sheds fragments that are smaller than the principal body. Gross fragmentation is thought to happen when the strength of the meteoric material is exceeded by the pressure of atmospheric flow at the face of the object (Passey & Melosh 1980), and is more commonly observed for larger objects that penetrate deeper into the atmosphere. Conversely, meteoroids that fragment continuously are assumed to have a *dustball* structure, with grains of various sizes embedded in a volatile matrix (Hawkes & Jones 1975b). The matrix boils off as the meteoroid is heated, gradually releasing the grains as the meteoroid enters the atmosphere. In some cases, gross fragmentation can be observed directly as the fragments become separated and bright enough to appear as distinct objects. Continuous fragmentation is more difficult to observe as the fragments are very small and numerous, and are assumed to contribute to the width and length of the meteoroid wake, instead. Both modes of fragmentation are poorly understood for faint meteors, and influence interpretations of meteoroid properties from light curves.

Small meteoroids with masses less than 10^{-4} kg ($r_{\text{met}} \sim 0.2$ cm with a meteoroid density of 3000 kg m^{-3}) are mostly ablated ($\sim 1/1000$ of the original mass) by a height of 80 km, at which point, the meteor is too dim to be seen even by most image-intensified systems. Larger meteoroids ($r_{\text{met}} \sim 20$ cm, Ceplecha et al. 1998) cease light production at lower heights, where they are decelerated to their terminal velocity. This is called the dark flight phase, and can last several minutes before the meteoroid reaches the ground, where it may be recovered as a *meteorite*. As the brightness of the meteor is related to the rate of mass loss, small meteoroids

⁵Alternately, if the meteoroid is not of homogeneous composition, volatile portions may ablate rapidly, while refractory portions may ablate slowly, producing a light curve that varies from the single-body example but does not involve fragmentation. This phenomenon is called differential ablation, and is discussed in more detail in Sections 1.2.4 and 1.3.4.

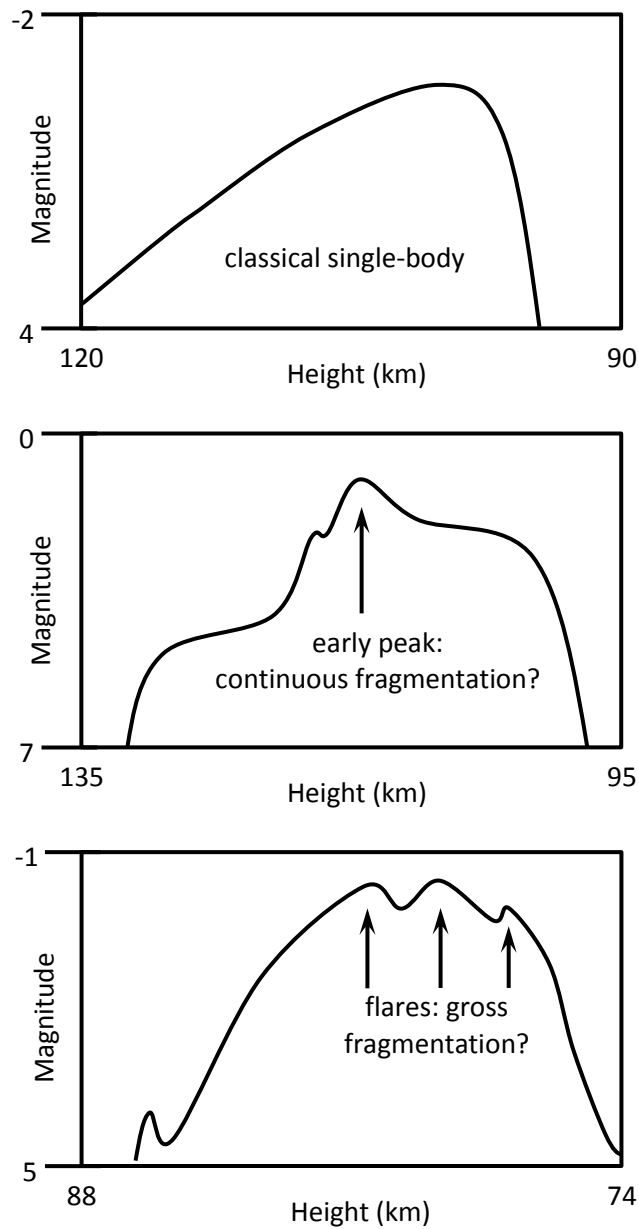


Figure 1.2: Sample light curve sketches, showing a classical light curve from a non-fragmenting meteoroid (top), a light curve for a continuously fragmenting body (middle), and a light curve with weak flares from a gross fragmenting body (bottom). The top and middle light curves are adapted from Campbell-Brown & Koschny (2004), while the bottom curve is adapted from Stokan & Campbell-Brown (2014). Height and magnitude ranges are appropriate for faint meteors studied in this thesis.

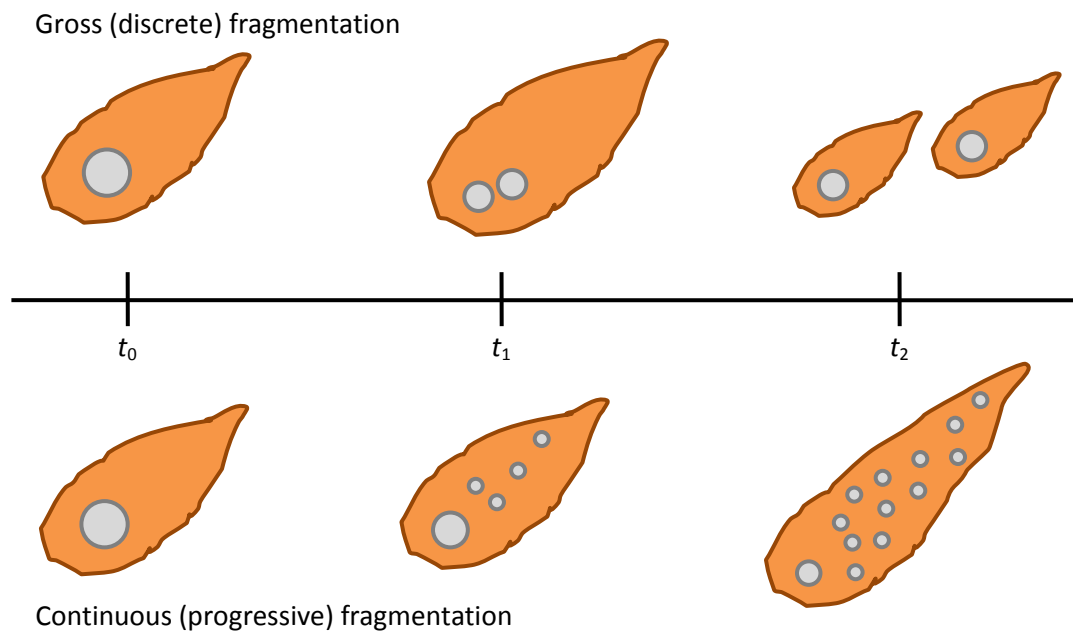


Figure 1.3: Two fragmentation modes for meteoroids: gross fragmentation (upper sketch) occurs when a meteoroid fragments once (or a discrete number of times). When there are few fragments of similar size, they slowly separate and can sometimes be distinguished. Continuous fragmentation (lower sketch) occurs when the meteoroid continuously loses fragments much smaller than the main size of the body. These fragments slowly separate and increase the length of the meteor wake.

produce *faint meteors*, while larger objects produce bright meteors called *bolides* or *fireballs*. The largest fireballs, called *impactors*, are extremely rare events that can produce light until they impact the ground and produce a crater. Faint meteors are typically dimmer than magnitude +2, near the sensitivity limit for unaided visual observations.

The orbit of a meteoroid is described by orbital parameters with respect to the Sun. The semi-major axis, a , gives half of the longest diameter of the elliptical orbit, while the perihelion and aphelion distances, q_{per} and q_{aph} , give the minimum and maximum distance from the Sun. These distances are illustrated in the top sketch of Figure 1.4. The eccentricity, e , describes whether the orbit is circular ($e = 0$), elliptical ($0 < e < 1$), parabolic ($e = 1$), or hyperbolic ($e > 1$), and is calculated using

$$e = \frac{q_{\text{aph}} - q_{\text{per}}}{q_{\text{aph}} + q_{\text{per}}}. \quad (1.7)$$

The inclination the object's orbital plane with respect to the ecliptic, the plane containing the Earth's orbit around the Sun, is given by i . The ascending node is the position where the object crosses the ecliptic (from below to above), and its angular location with respect to the Sun's position at the vernal equinox (a reference direction) is called the longitude of the ascending node, Ω . The argument of perihelion, ω , gives the angular location of perihelion with respect to the ascending node. These are illustrated in the bottom sketch of Figure 1.4. Finally, the *Tisserand parameter* with respect to Jupiter,

$$T_j = \frac{a_j}{a} + 2 \cos i \sqrt{\frac{a(1 - e^2)}{a_j}}, \quad (1.8)$$

is a quantity that is approximately conserved when a meteoroid's orbit is perturbed by Jupiter (with semi-major axis a_j). T_j serves as a rough indicator of the origin of a meteoroid: $T_j \geq 3$ indicates an asteroidal origin, $2 \leq T_j < 3$ indicates that the object may have originated from a Jupiter family comet (with short period, less than 20 years), while $T_j < 2$ suggests association with a long-period comet.

Meteoroids start off as parts of larger bodies that have been disrupted. Typically, comets

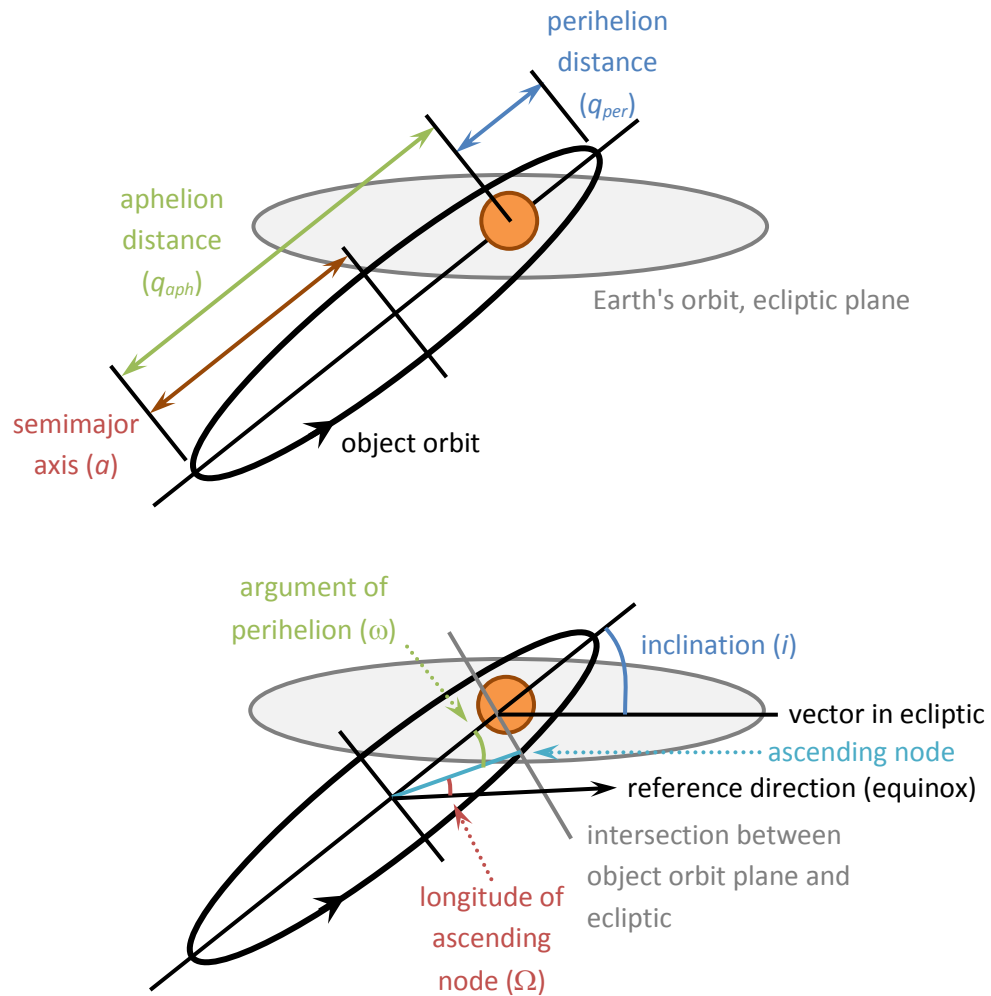


Figure 1.4: An illustration of orbital parameters for a meteoroid. The top sketch shows the semi-major axis, perihelion distance, and aphelion distance, while the bottom one shows the inclination, ascending node, longitude of ascending node, and argument of perihelion.

Table 1.1: Selected meteor showers, with shower name, date of peak in 2014 (from IMO Meteor Shower Calendar 2014), zenithal hourly rate (ZHR, indicator of the number of meteors per hour), average speed at the Earth, suspected parent body (Jenniskens 2004, 2006), and parent body type (SP and LP comets are short-period, or Jupiter-family, and long-period comets, respectively, while HT is Halley-type, or intermediate-period, comets).

Name	Peak date (in 2014)	ZHR	Speed (km s ⁻¹)	Parent	Type
Quadrantids	January 3	120	41	2003 EH ₁	asteroid
Lyrids	April 22	18	49	C/1861 G1 Thatcher	LP comet
Eta Aquariids	May 6	65	66	1P/Halley	HT comet
Perseids	August 13	100	59	109P/Swift-Tuttle	HT comet
Draconids	October 8	var.	20	21P/Giacobini-Zinner	SP comet
Orionids	October 21	25	66	1P/Halley	HT comet
Leonids	November 17	15	71	55P/Tempel-Tuttle	HT comet
Geminids	December 14	120	35	3200 Phaethon	asteroid
Ursids	December 22	10	33	8P/Tuttle	SP comet

begin to sublimate within 5 AU (750 million kilometres) of the Sun (de Pater & Lissauer 2010), releasing meteoroids with a small relative velocity. As a result, these meteoroids initially follow the orbit of the parent body, but slowly disperse due to slight differences in orbital speed. This dispersion produces a continuous distribution of meteoroids along the orbit of the parent body, a *meteoroid stream*, and can take several orbital periods to form. Collisions between asteroids are hypothesised to also produce meteoroid streams. If the Earth intersects these streams, they are observed as *meteor showers*, a local enhancement in meteor activity where all of the shower's meteors appear to originate from the same point in the sky, called the *radiant*. The meteoroids are called *stream meteoroids*, and showers are named after the constellation nearest to the radiant. Some sample meteor showers are given in Table 1.1.

Meteoroids in space are influenced mostly by the Sun's gravity, but are also subject to perturbations from solar radiation pressure, Poynting-Robertson drag (resulting from anisotropic thermal emission by the meteoroid due to its motion), passages near other planets and bodies (typically Jupiter), and other effects. These perturbations alter the orbit of stream meteoroids over time, separating them from the orbit of their parent body. Meteoroids not associated with a stream are called *sporadic meteoroids*, and have an unknown parent body. The majority of

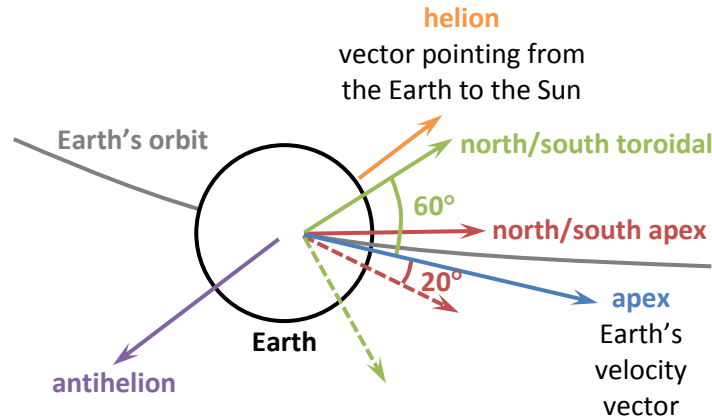


Figure 1.5: An illustration of six apparent sources for sporadics. The helion and antihelion sources point towards and opposite the Sun, respectively. The north and south apex sources point 20° north and south of the apex direction, which is the direction of the Earth’s travel. Similarly, the north and south toroidal sources are 60° north and south of the apex direction.

meteoroids that impact the Earth are sporadics coming from six apparent sources (Campbell-Brown & Jones 2006, Campbell-Brown 2008): the helion and antihelion sources, pointing towards and opposite the Sun, respectively; the north and south apex sources, 20° above and below the ecliptic in the direction of the Earth’s orbit around the Sun; and the north and south toroidal sources, 60° above and below the ecliptic. These are sketched in Figure 1.5. Modelling the behaviour and activity of sporadics is challenging, but important because of the danger they can pose to objects in Earth’s orbit (Drolshagen et al. 2008).⁶ A sporadic flux model by Wiegert et al. (2009) suggests that the majority of sporadic meteoroids encountered by the Earth, with sizes ranging from 10 μm to 0.1 m, originate from a few comets that can efficiently transfer material to the Earth’s orbit, such as 2P/Encke and 55P/Temple-Tuttle. Interestingly, no cometary meteorites have been recovered, which hinders direct study of their properties (Campins & Swindle 1998).

Meteoroids that are bound to the Solar System ($e < 1$) can travel with heliocentric speeds up to 42 km s^{-1} at 1 AU. The Earth has an orbital speed of 30 km s^{-1} , making the maximum

⁶McBride (1997) estimates that meteoroid streams contribute about ten per cent of the annual mean flux of potentially hazardous objects encountered by spacecraft in low Earth orbit. Conversely, McBride & McDonnell (1999) propose that spacecraft could suffer a year’s worth of damage during a strong, “storm-like” enhancement of the Leonids.

meteoroid speed 72 km s^{-1} relative to the Earth, provided the meteoroid is in a retrograde orbit.⁷ Conversely, the meteoroid has a minimum geocentric speed of 11 km s^{-1} , the escape speed from Earth. An object entering the atmosphere at 72 km s^{-1} at a height of 95 km has an approximate Mach number (ratio of body speed to the local speed of sound) of 270, about ten times higher than spacecraft upon controlled re-entry (Boyd 2000). These conditions are termed *hypersonic*, and collisions between atmospheric particles and the meteoroid are extremely energetic.

Meteoroid ablation, fragmentation, and wake formation are poorly understood for faint meteors in hypersonic conditions. This is principally due to a lack of observations to constrain physical models. Similarly, such conditions are hard to replicate in the laboratory. As noted earlier, characterising these processes will lead to a better understanding of meteoroid composition (and ultimately, Solar System composition) as well as damage mitigation for objects in low Earth orbit. This thesis presents analysis of new high-resolution video observations of faint meteor wake and fragmentation to comment on the ablation processes and structure of small meteoroids, respectively. A single-body small meteoroid ablation model is proposed to explain meteor wake formation, constrained by these observations.

Observations of ablation, wake formation, and fragmentation for faint meteors will be discussed in Section 1.2 to provide a context for the contributions of this thesis. Afterwards, an overview of the current state of meteoroid ablation modelling will be presented in Section 1.3. Finally, the goals of the thesis will be outlined in Section 1.4.

⁷Interstellar particles have heliocentric speeds in excess of 42 km s^{-1} and may travel faster than 72 km s^{-1} as observed on the Earth, but are difficult to discern from meteoroids that are bound to the Solar System due to uncertainties in observations. An example of a recent study is the year-long optical survey by Musci et al. (2012) that revealed 22 potential interstellar meteoroids out of a sample size of 1739. The authors concluded that it was unlikely that any of these meteoroids were of interstellar origin.

1.2 Observations of faint meteors

1.2.1 Photographic

Meteor photography is the earliest form of instrument-based observation, with efforts beginning in 1885. The first meteoroid orbits, meteorite discoveries (that were associated with meteors), and models of meteoroid structure were based on photographic observations of meteors. Photography allows for precise measurements of meteoroid trajectory, limited by lens and film quality, but is constrained by low sensitivity (typically ~ 0 limiting magnitude) and the need for mechanical devices, choppers, to periodically block the lens to allow for measurement of meteoroid motion over long exposures.

Some of the first scientific results from meteor photography were produced by Whipple (1938, 1954) using a two-camera setup at Harvard. Use of two cameras allowed for the calculation of meteoroid trajectory by triangulation. Each camera had a wide, 60° field of view and a magnitude sensitivity limit of -1 . The cameras were separated by 38 km, and were pointed to capture meteoroids at a height of 80 km. A mechanical shutter operating at 20 Hz was placed on one camera to allow for the calculation of meteoroid velocity. The principal results (Whipple 1938) were the radiant, heights, decelerations, and orbits for six meteors (a Perseid, a Geminid, and six sporadics). A later study presented the orbits of 144 meteoroids, associating 95 of the meteoroids with 21 possible streams, and suggested that all of the observed streams originated from comets (Whipple 1954).

Efforts to observe fainter meteors resulted in specialised cameras, such as the Baker Super-Schmidt cameras operated by the Harvard Meteor Program in the 1950s (Whipple 1951). These cameras were more sensitive than previous instruments, with limiting meteor magnitude of $+4$, while retaining a wide, 40° field of view. A rotating shutter, operating at 3600 Hz, allowed for precise measurement of meteoroid speeds and deceleration. Observations with these cameras resulted in over four hundred high-precision meteoroid orbits (Jacchia & Whipple 1961). Analysis revealed that the principal source of meteoroids in the observed size range was comets, in

agreement with Whipple (1954).

Analysis of Schmidt camera observations suggested that fragmentation was an important process in faint meteors, and that the small meteoroids might be more fragile, porous, and crumbly compared to objects that produced bright meteors. Jacchia (1955) commented that faint meteors brightened very rapidly after appearing, producing anomalously-shaped light curves that sometimes peaked towards the beginning of the meteor trajectory. This was in contrast to the late-peaked light curves that were expected based on the assumption of non-fragmenting, single-body objects.⁸ Meteoroids with anomalous light curves also tended to decelerate more rapidly than expected. As deceleration and brightness output is proportional to the exposed surface area, these observations suggested that the meteoroids fragmented. Supporting this, Hawkins & Southworth (1958) carefully examined a random sample of three hundred Super-Schmidt meteors and found them to have systematically shorter light curves than expected for non-fragmented bodies. Continuous, progressive fragmentation was proposed to occur for most faint meteors, but flares in a few meteors suggested that large-scale, instantaneous gross fragmentation of the meteoroid was also a possibility.

Moving to higher-resolution observations, Hawkins & Whipple (1958) studied the trail widths of 51 faint meteors (limiting magnitude +4) captured with the 48-inch Schmidt camera and telescope at the Palomar Observatory. Images were recorded at fine spatial resolution (6.6° field of view, allowing objects with a diameter of 4 cm to be resolved clearly) but analysis was complicated by issues with atmospheric seeing, film quality, and meteors being out of focus.⁹ Also, the range to each meteoroid could only be estimated, since there was only one telescope to observe the meteors. Later, Cook et al. (1962) studied 33 Geminid meteors with the same

⁸From the discussion in Section 1.1, it may be recalled that classical models assume that meteor brightness is proportional to the rate of ablation, which is proportional mainly to the meteoroid cross-sectional area and atmospheric density. Comparing meteoroids with identical masses, fragmented objects have a much larger effective cross-sectional area compared to single-body objects, resulting in more rapid ablation, meteors that peak in brightness nearer to the beginning of the light curve, and shorter light curves. Figure 1.2 sketches light curves from single-body and fragmenting meteoroids. Meteoroid ablation models and equations for meteor brightness and meteoroid deceleration will be discussed in Section 1.3.

⁹For example, 1" of seeing at a range of 135 km would correspond to approximately 65 cm, limiting the resolution of small objects.

instrument, which allowed for better estimation of meteoroid range based on the previously observed ablation heights of Geminids. Image focus and broadening was also more carefully considered in this subsequent study. Ultimately, meteor trail widths of the order 1 m (up to 6 m) were obtained, arguably larger than expected if the meteoroid was a single-body object. As a result, fragmentation was again suggested to be an important process for ablation associated with faint meteors. Hawkes & Jones (1978) investigated rotational breakup of meteoroids as a mechanism for creating these meteor trails. This effort, as well as others to quantify meteor trail widths to comment on meteoroid structure and determine their effect on radar observations, and will be discussed in Section 1.2.2.

Later on, efforts became more focused on brighter meteors and possible meteorite recovery. Fireball networks, with dozens of cameras equipped with wide-angle or fish-eye lenses, were set up in the former Czechoslovakia (the Czechoslovak Network, later becoming the European Network, EN), the United States (the Prairie Network, PN), and Canada (the Meteorite Observation and Recovery Project, MORP). Each network aided in the recovery of at least one meteorite (Pribřam in 1959 and Neuschwanstein in 2002 for EN, Lost City for PN in 1970, and Innisfree for MORP in 1977) and provided many observations of bright meteors over large areas of the sky. Summarised details are provided in Halliday (1973) and Ceplecha (1986). McCrosky & Ceplecha (1970) noted that even meteoroids that produced very bright meteors observed with the Prairie Network were sometimes poorly characterised by the assumption of single-body ablation. These meteoroids were found to have very low density and strength compared to meteorites. Subsequently, Ceplecha & McCrosky (1976) refined their previous analysis to account for the Lost City meteorite and divided meteoroids into several discrete strength classes, helping to explain differences in ablation heights and fragmentation among brighter meteors.

Kramer (1968) proposed that meteoroid fragmentation could explain some hyperbolic orbits calculated for bright, photographic meteors. Arguing that measurement uncertainties could not explain the relatively large number of hyperbolic orbits calculated, and that gravitational

perturbation alone could not account for the calculated orbits, Kramer suggested that the ejection of fragments from a parent body with a highly elliptical orbit could result in meteoroids with hyperbolic orbits. To help justify this hypothesis, two meteor observations were presented, one of which exhibited several flares (interpreted to be fragmentation) and seemed to accelerate, while the other was seen to fragment into two distinguishable pieces at a height of 73 km. For the second meteor, the fragments appeared to have speed differences of $+1.37 \pm 0.30$ and $-1.28 \pm 0.30 \text{ km s}^{-1}$ compared to the original body. Interestingly, no follow up study was performed, likely due to the rarity of bright meteors showing fragmentation, as well as difficulty in performing a precise analysis of fragment speeds.

To explain the cause of fragmentation, Beech & Brown (2000) suggested that rapid rotation of meteoroids during ablation could initiate breakup. Eleven bright fireballs out of a sample of 259 captured with MORP revealed flickering, or periodic flares, in light curves. There appeared to be little correlation between flickering frequency, amplitude (typically the magnitude variation for the flares was $\Delta M_{\text{ph}} \sim 0.5$), meteoroid mass, speed, or height, suggesting that the flickering was related to meteoroid rotation present before the beginning of the ablation process. Flickering up to 500 Hz was observed for MORP events. The Peekskill bolide, a bright, estimated -13 peak magnitude meteor, fortuitously recorded on several home video cameras in October 1992 (Brown et al. 1994, Beech et al. 1995), flickered with frequencies ranging from 7 to 20 Hz preceding fragmentation at a height of 41 km.¹⁰ At this height, the pressure from atmospheric flow at the face of the object, assumed to be 80 cm in diameter, was insufficient to crush the object. Similarly, the lateral displacement of the fragments 5 s after fragmentation matched the expected displacement for a rotational frequency of 20 Hz. As a result, rotational bursting was suggested as a fragmentation mechanism, yielding object strengths of the order 1 MPa for the MORP objects, and 10 – 50 MPa for the Peekskill meteoroid. This contrasted with lower strength estimates for objects originating from comets and rubble-pile asteroids.

¹⁰Interestingly, the Peekskill bolide is named after the resulting meteorite that impacted a parked car in Peekskill, NY. The bolide was initially observed on October 9, 1992 in West Virginia, but travelled in a north-easterly direction towards New York.

In modern times, meteor photography has largely been superseded by video observations, but serendipitous observations can still play a role. An example is a spectroscopic observation of a single -8 magnitude meteor with the European Southern Observatory Very Large Telescope (Jenniskens et al. 2004). The width of the meteor wake was found to be on the order of 7 m, but this was thought to be due to the meteor being out of focus. Similarly, spectroscopy revealed nearly constant temperature across the trail, also thought to be due to improper image focus.

1.2.2 Radar

As a meteoroid ablates and travels into the atmosphere, high-speed collisions with atmospheric particles ionise meteoric atoms, forming a plasma that surrounds the meteoroid and a charged trail. A radar beam directed at the meteor can scatter off of the plasma surrounding the meteoroid, resulting in a *head echo*, or the electrons in the trail, resulting in a *trail echo* (McIntosh 1961, Jones & Webster 1991, Mathews 2004). Specular trail echoes are observed when the propagation direction of the radar beam is perpendicular to the meteor trail, resulting in coherent, in-phase reflection from electrons inside the first *Fresnel zone* as depicted in Figure 1.6.¹¹ Head echoes can be detected regardless of the orientation and velocity vector of the meteoroid, but require systems with up to four magnitudes more power compared to specular trail echo radar systems (Pellinen-Wannberg 2005). Radar is typically more sensitive than photographic or intensified video systems, observing meteoroids in the size range of 0.002 – 0.02 cm (Elford 2001), with particular systems having limiting visual magnitudes of +7 (CMOR, specular trail echoes; Jones et al. 2005), +13 (AMOR, specular trail echoes; Baggaley et al. 1994), and +10

¹¹The first Fresnel zone is the segment of the ion trail over which the most significant specular reflection occurs. Reflections from the edges of the Fresnel zone have a phase difference of π compared to reflections from the centre, resulting in destructive interference. This is illustrated in Figure 1.6.

Interestingly, high-power head echo radars are able to detect non-specular trail echoes in certain cases. The direction of the radar beam must be perpendicular to the geomagnetic field lines at the location of the meteor trail. Turbulence in the trail allows for the formation of field aligned irregularities that are detected due to their relatively large radar cross sections. As a result, portions of the meteor trail may be visible, even though the meteoroid descends towards the radar and the trail has no specular point. Additional details of these anomalous range-spread trail echoes are given in Dyrud et al. (2002) and Mathews (2004).

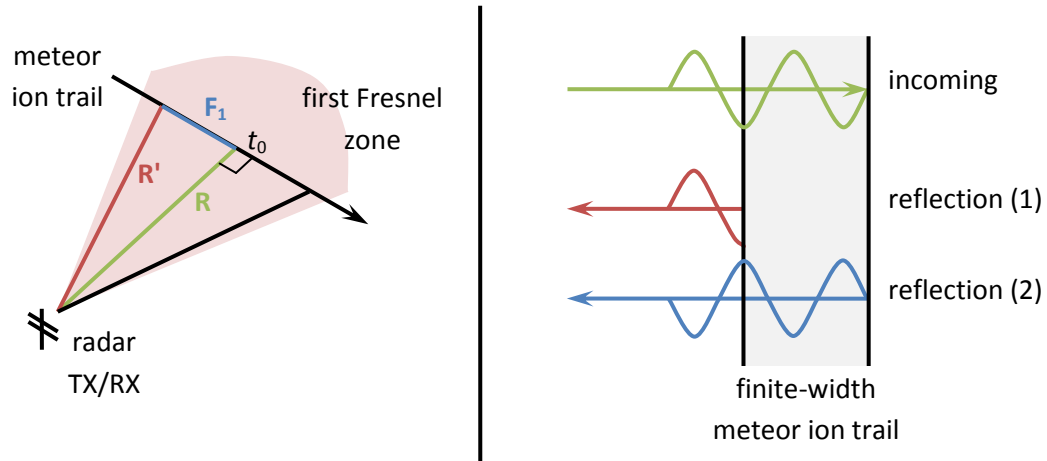


Figure 1.6: A sketch of specular backscatter radar on the left, and destructive interference from a finite-width ion trail on the right. The first Fresnel zone indicates where radar signals are scattered back and interfere constructively. The fringes of the Fresnel zone indicate where the path length difference $2R$ (green path) versus $2R'$ (red path) is half of the radar wavelength, giving destructive interference. On the right, a hypothetical signal is returned from the near (reflection 1) and far (reflection 2) side of a finite width ion trail. In this case, the trail is $5/4$ of the signal wavelength, resulting in completely destructive interference upon reflection. If width of the ion trail is at least of the same order as the signal wavelength, the return signal is significantly attenuated.

(EISCAT, head echoes; Pellinen-Wannberg et al. 1998). Similarly, the Arecibo Observatory 430 MHz radar is able to detect particles down to the size of $0.5 \mu\text{m}$ (Janches et al. 2003).

The interaction between the meteor's ionization and an incident radar beam and are dictated by the density of electrons comprising the head and trail, as well as the radar frequency (Poulter & Baggaley 1977, Mathews 2004, Close et al. 2004). In the case of specular trail echoes at typical VHF radar frequencies around 30 MHz, the radar beam penetrates the trail and scatters from each electron individually when the linear electron density is $< 10^{14}$ electrons per metre (Ceplecha et al. 1998). This is called an *underdense* echo, and is typical of faint meteors. Complications arise when the radius of the meteor's ion trail is similar to (or larger than) the radar wavelength, as destructive interference can result even for parts of the trail in the first Fresnel zone, as depicted on the right of Figure 1.6. At higher densities, $> 10^{14}$ electrons per metre, *overdense* echoes occur when the radar beam does not penetrate the trail, and instead reflects from it as from a conductive surface.

Observing meteors with radar has several benefits compared to photographic and video methods: meteors can be observed regardless of sky conditions (and while the Sun is up), there is a large collecting area for observations, and smaller objects can be observed. This makes radar suitable for studying the flux and mass distributions of shower and sporadic meteoroids (Campbell-Brown & Jones 2006, Blauuw et al. 2011a,b), as well as identifying new showers, and investigating orbits and radiant of shower meteoroids (Brown et al. 2008, 2010). These are examples of studies that were performed relatively recently with the Canadian Meteor Orbit Radar (CMOR), but a review of other specular trail echo studies is presented in Ceplecha et al. (1998) and Elford (2001), while examples of head echo surveys of meteoroid populations include Hunt et al. (2004) and Janches et al. (2014).

The principal disadvantage of radar observations is that they are subject to a number of biases. Perhaps most significant is signal attenuation in specular trail echoes due to a finite ion trail radius. Consider two electrons, on the near and far side of an underdense trail. These electrons equivalently scatter incident radar signals but with a phase difference given by the ratio of their separation (the trail width) to the signal wavelength. If the electrons are separated by half of a radar wavelength, then there is full destructive interference and no signal is reflected. This is the situation depicted on the right of Figure 1.6. If the ion trail has a Gaussian radial distribution, the original amplitude of the signal, A_0 , is attenuated to

$$A(\lambda, r_t) = A_0 \exp \left[- \left(\frac{2\pi r_t}{\lambda} \right)^2 \right], \quad (1.9)$$

where r_t is the trail radius, and λ is the signal wavelength (Manning 1958, Greenhow & Hall 1960). Since the mass of the meteoroid is estimated based on the amplitude of the returned signal, attenuation due to a finite trail radius results in incorrect meteoroid mass and flux estimates. The height distribution of meteors is also affected, since atmospheric density decreases with increasing height, resulting in wider trails. Above a certain height, trails are wide enough that most signals are attenuated and few meteors are detected, called the *height ceiling effect*.

The height at which this occurs is dependent on the radar wavelength.¹² Head echoes are not subject to signal attenuation from finite trail widths, nor the height ceiling effect, but have their own unique set of biases related to uncertainty in the radar scattering cross section (Close et al. 2002, 2007, 2008) that could potentially be improved using constraints from simultaneous optical observations (Jones & Webster 1991).

One of the first theoretical investigations of meteor ion trail widths was by Manning (1958). Trail radii on the order of 14 collisional mean free path lengths were found using a model that treated evaporated meteoric particles as undergoing a random walk in the atmosphere. Meteoroid speed was found to weakly influence the trail radii, ranging from 12.3 to 14.5 mean free path lengths for speeds between 11 and 72 km s⁻¹, respectively. Many simplifying assumptions were made in these calculations, so the main contribution of this work was to bring attention to the effect of finite trail widths on radar signal attenuation.

Greenhow & Hall (1960) observed meteors with a dual-frequency radar system. Many more meteors were observed with a radar wavelength of 17 m compared to 8 m, illustrating the effect of finite ion trail widths (recall Eq. (1.9)). Similarly, meteors were distributed around a mean height of 97 km when observed with a wavelength of 8 m, compared to a mean height of 103 km for the 17 m observations. Taking the ratio of trail echo amplitudes at 8 and 17 m allowed for the calculation of trail radii, which was found to vary between 1 m at a height of 97 km to nearly 3 m at a height of 103 km, in rough agreement with the Super-Schmidt photographic observations by Hawkins & Whipple (1958).

Kascheyev & Lebedinets (1963) developed another model for the formation of the meteor ion trail and found that there was a strong, nearly linear relationship between trail radius and meteoroid speed. At a speed of 10 km s⁻¹, the trail radius was equal to 2.4 atmospheric mean free path lengths, while at 70 km s⁻¹, the radius increased to 13.3 mean free paths. This was in contrast to the earlier findings of Manning (1958), and likely resulted from including a speed-dependent collision free path length for particles, and employing a diffusion cross section

¹²The height ceiling is ~ 110 km for a 30 MHz (10 m wavelength) radar (Weryk, personal communication).

referenced from the quantum mechanical calculations of Massey & Sida (1955).

Subsequent dual-frequency radar observations investigated the velocity dependence of the initial trail radii. Baggaley (1970) used radar with wavelengths of 11 m and 30 m to observe trail radii ranging from 0.48 to 2.90 m at heights between 90 and 115 km, agreeing with previous observations of Greenhow & Hall (1960). The height dependence of the trail radii, r_t , was parametrised as

$$r_t \propto \rho_{\text{atm}}^a, \quad (1.10)$$

where ρ_{atm} is the atmospheric mass density at the height of observation. The exponential factor a was found to be -0.45 ± 0.03 . An additional correction term for the finite speed of the meteoroid was also included to improve trail width estimates, and investigation revealed $b = 0.57 \pm 0.16$, where

$$r_t \propto v^b, \quad (1.11)$$

v being the meteoroid speed.¹³ A later study by Baggaley (1980) provided revised values $a = -0.42 \pm 0.07$ of $b = 1.0 \pm 0.3$, from a study of sporadic and Geminid meteors.

The studies by Baggaley revealed a weaker height dependence than expected by previous modelling efforts. For comparison, Manning (1958) and Kascheyev & Lebedinets (1960) found $a = -1$ effectively. Motivated by this, Hawkes & Jones (1978) proposed that fragments from a rotating dustball meteoroid could possess significant transverse speeds, resulting in wide trails that vary less with height than expected. The authors calculated that a trail radius of 0.8 m at a height of 95 km could be attained by a magnitude +7 meteor that had a rotational speed between 3700 to 5000 rad s^{-1} ($\sim 600 - 800$ Hz). A consideration of collisional spin-up in meteoroids before atmospheric entry yielded expected rotational speeds of the order of 8×10^4 and 2×10^3 rad s^{-1} ($\sim 13\,000$ and 300 Hz) for bodies of mass 10^{-3} and 1 g, respectively, potentially explaining the observed trail radii. The authors cautioned, however, that the pre-atmospheric rotational speed estimates exhibited significant variance based on two empirical

¹³The speed correction term takes into account that the echo amplitude is decreased if the meteoroid does not traverse the entire first Fresnel zone by the time the trail width diffuses to the radar wavelength.

model parameters. Consequently, investigation of brighter objects with narrower trails resulting from fragmentation at lower heights was suggested to decrease uncertainty in the rotational speeds.

Alternately, Jones (1995) proposed that a weak dependence on height for the trail radii may have resulted from inaccurately treating the trail density distribution as Gaussian when interpreting observations. Numerically simulating twenty elastic collisions for each of a sample of 10 000 meteoric particles at various heights in the atmosphere revealed a non-Gaussian radial trail density profile, which was able to explain the difference between previous model predictions and the weak height variation observed for trail widths. Unfortunately, subsequent radar studies continued to assume a Gaussian radial profile, likely due to relative simplicity and the expectation that a non-Gaussian trail would diffuse to a Gaussian profile by the time of observation.

A unique study was performed by Steel & Elford (2001) using very long wavelength radar, 50 and 150 m, in an attempt to determine the actual, unbiased height distribution of meteors independent of the height-ceiling effect. They found that the height of the peak in the number distribution of meteors increased even when moving from a wavelength of 50 to 150 m. This was an unexpected result. As the peak meteor distribution height increased even for these very large wavelengths, the authors suggested that methods other than radar observation may ultimately be needed to accurately quantify the height distribution of meteors.

One of the most recent efforts to quantify meteor trail radii was by Jones & Campbell-Brown (2005), using radar with 7.9 and 10.0 m wavelengths and assuming a Gaussian radial distribution for 10 000 sporadic meteors with mean magnitude of +6.5. Special attention was paid to correct for the rotation of the radar polarisation through the ionosphere (Faraday rotation) as well as attenuation of echo signal between transmitted pulses, effects not considered in previous studies. The study found trail radii between 0.5 m at 80 km and 1.3 m at 100 km, similar to the results of Greenhow & Hall (1960). Conversely, the trail radii were found to have a weak *inverse* dependence on meteoroid speed, with $b = -0.20 \pm 0.01$ in Eq. (1.11), in con-

trast to previous studies and models. As a result, the authors suggested further investigation, including removing the assumption of a Gaussian radial density profile for the trail.

While significant effort was being expended in quantifying the widths of meteor ion trails, other studies began to observe and consider the effects of meteoroid fragmentation on radar observations. Greenhow & Neufeld (1957) discovered that the ionization curve, which is the radar analogue of the light curve, plotting electron line density as a function of height, was shorter and rose more rapidly to the peak line density than expected. This was analogous to the photographic observations by Jacchia (1955) and Hawkins & Southworth (1958), discussed earlier in Section 1.2.1. Similarly, Verniani (1973) analysed nearly 6000 faint meteors and found that, on average, meteors appeared to traverse a mean length of 10.2 km in the atmosphere before being sufficiently ablated to no longer be detected, about half of the theoretical, single-body expectation of 21.9 km. Meteors were also found to be about a magnitude “brighter” (in terms of detected electron line density) than expected. Since the mass loss (and thus, ion production) of a meteor is proportional to the cross-sectional area interacting with the atmosphere, both studies proposed that fragmentation was a significant effect for radar meteors, as was previously suggested for the faint photographic meteors.

Considering gross fragmentation, Elford & Campbell (2001) found that characteristic Fresnel oscillations in the meteor echo could be smoothed out by having the meteoroid fragment into as few as ten pieces. Their model provided an explanation for the absence of Fresnel oscillations in some radar observations. Mathews et al. (2010) observed periodic oscillations in the strength of the head echoes observed by the Arecibo incoherent scatter radar at 46.8 and 430 MHz. A simple model accounted for these oscillations with the superposition of signals returned from two separating fragments. An investigation of two samples of 500 meteors (one population of sequential observations and the other selected randomly) revealed that the majority of head echoes displayed these oscillations, leading the authors to suggest that most meteoroids underwent fragmentation, even at the small sizes detected with this radar.¹⁴

¹⁴Differential ablation provided an alternate explanation for the oscillations and flares observed by Mathews et al. (2010). Janches et al. (2009) suggested that ablation of an inhomogeneous meteoroid could explain the flares

Campbell-Brown & Jones (2003) considered fragmentation on a smaller scale to describe differences in observations of Geminid echo amplitudes at three radar frequencies versus modelled expectations. Up to 2000 fragments were simulated for each meteor, with constant, Gaussian, hollow, or higher order radial distributions. The ion trail was assumed to follow either an exponential or Gaussian radial distribution for each fragment. Fragment masses followed a power-law distribution,

$$\frac{dn}{dm} = km^{-s_f}, \quad (1.12)$$

where k is a normalisation constant, and the mass distribution index, s_f , was inferred from optical observations of the 2000 Leonids to be between 1.6 and 2.0.¹⁵ The initial ion trail radius was assumed to take a value between ten and twenty atmospheric mean collision free path lengths. The height of fragmentation that best fit observations was found to be 240 km, and a fragment transverse speed of 0.24 m s^{-1} was found to correspond to the height distribution of the radial separation of the fragments. Interestingly, this eventually led to a pre-atmospheric rotational speed of approximately $4500 \pm 500 \text{ rad s}^{-1}$ ($\sim 720 \text{ Hz}$) for the Geminid meteoroids, similar to the findings of Hawkes & Jones (1978), and within expectations for a body of cometary strength and 10^{-9} kg mass. Most importantly, fragmentation was able to explain differences between expectations and radar observations.

Direct radar observations of macroscopic fragmentation were presented by Baggaley & Grant (2004), where rapid changes in the phase of radar reflected from a meteor trail were interpreted to represent multiple specular (t_0) points being detected, each belonging to a different fragment. Of 4185 echoes recorded over three days, 34 echoes showed phase changes, and two seemed to show three fragments. The study suggested that important information about meteoroid structure could be inferred by studying fragmentation of shower meteoroids, but there were no subsequent investigations.

observed with the Arecibo radar as different materials ablate at different heights, each corresponding to certain meteoroid temperatures. Possible optical observations of differential ablation will be discussed in Section 1.2.4, while models will be introduced in Section 1.3.4.

¹⁵The mass distribution index is an indicator of the relative abundance of small particles in a mass distribution. Larger values indicate increasing preference for smaller particles in the distribution.

These radar studies have highlighted the importance and difficulty of quantifying meteor trail widths. The attenuation due to a finite trail width can bias meteoroid mass, height distributions, and flux estimates derived using radar. The physical process that forms the trail, as well as meteoroid fragmentation, are poorly understood and observed. Video observations of meteors are an independent method to resolve these uncertainties and will be discussed next.

1.2.3 Video

Some of the most striking observations of meteors have been captured with video. Bright bolides, such as Peekskill (Brown et al. 1994) and Chelyabinsk (Borovička et al. 2013, Brown et al. 2013), were recorded on hand-held, security, and vehicle dashboard cameras, showing fragmentation and allowing for the investigation of the initial masses of the meteoroids.¹⁶ For fainter meteoroids, video is recorded with low-light-level television (LLTV) or image-intensified cameras, which are more sensitive. Intensified video bridges the gap between photographic and radar observations: the high sensitivity of intensified video allows for observations of small meteoroids that are approaching the population visible with radar while not being subject to the same biases.

The principles of a digital, intensified video system are illustrated in Figure 1.7. Light from the meteor is focused onto the image intensifier photocathode, converted to electrons, amplified by the intensifier, and converted back to light by a phosphor screen. A gain factor of 10 was achieved with early devices, but modern, third-generation intensifiers, comprised of one or more microchannel plates (MCPs), amplify incoming light by factors up to 100 000. The light output by the image intensifier is then focused into a digital camera equipped with a charge-coupled device (CCD). A CCD is another array that counts the number of impinging photons and converts it to a voltage. Each element of the CCD array is called a pixel, and

¹⁶The Peekskill bolide, which occurred in October 1992 with a peak magnitude of -13 , was discussed earlier in Section 1.2.1. The Chelyabinsk bolide occurred on February 15, 2013, and had an estimated peak magnitude of nearly -28 , with an initial speed of $\sim 19 \text{ km s}^{-1}$ (Brown et al. 2013, Borovička et al. 2013). Rapid fragmentation resulted in an airburst with an estimated energy of 500-kt TNT equivalent at a height of $\sim 30 \text{ km}$. Over 100 kg of chondritic meteorites were found in areas south and southwest of Chelyabinsk, Russia.

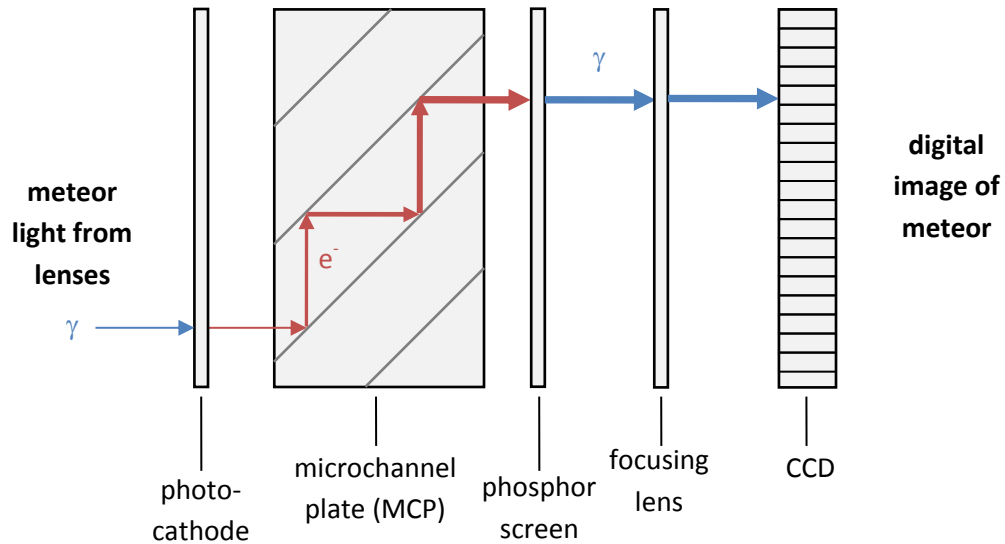


Figure 1.7: A sketch of a third-generation image intensifier with microchannel plates. γ represents photons, while e^- are photoelectrons.

images, each frame of the video, are obtained by converting the charge stored in each pixel to a brightness value.

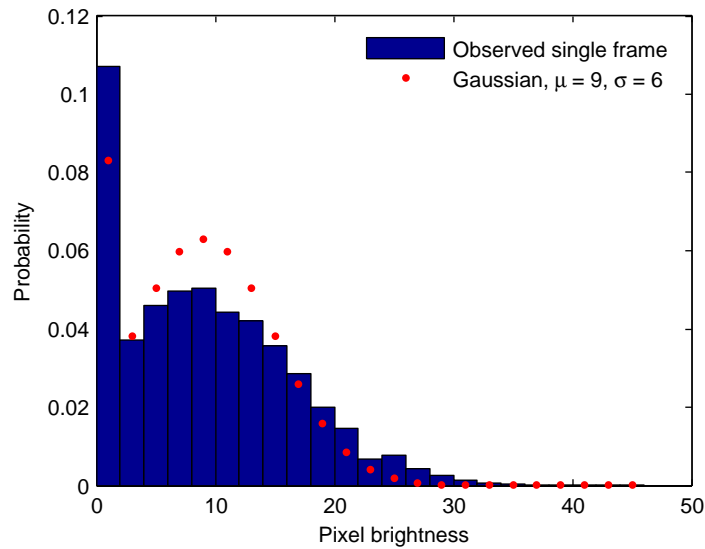
There are some unique disadvantages to intensified digital video observations. The precision of the meteoroid position in each frame is limited by the pixel size. Bright meteors can cause image saturation, where the relationship between meteor and pixel brightness is no longer linear. Image bloom may also occur, artificially brightening the region around some bright meteors. Both of these effects decrease the accuracy of meteoroid photometric masses. Finally, noise can be a significant concern when observing faint meteors. Types of noise include: dark current, where signal is generated by an intensifier or CCD without any incident photons; shot noise, related to statistical variations in the discrete number of photons received by the intensifier and CCD; CCD readout noise, related to the uncertainty in converting a number of electrons in each pixel to a voltage; and noise related to converting the analogue voltage signal of a CCD to a digital image.¹⁷ A profile of the noise recorded by an intensified cam-

¹⁷The dark current is related to thermal excitation of electrons in the intensifier or CCD, which are counted identically to incident photons converted to electrons. As a result, dark current is additive, independent of pixel brightness, and is related to the temperature of the camera. Conversely, shot noise follows a Poisson distribution and is proportional to the pixel brightness.

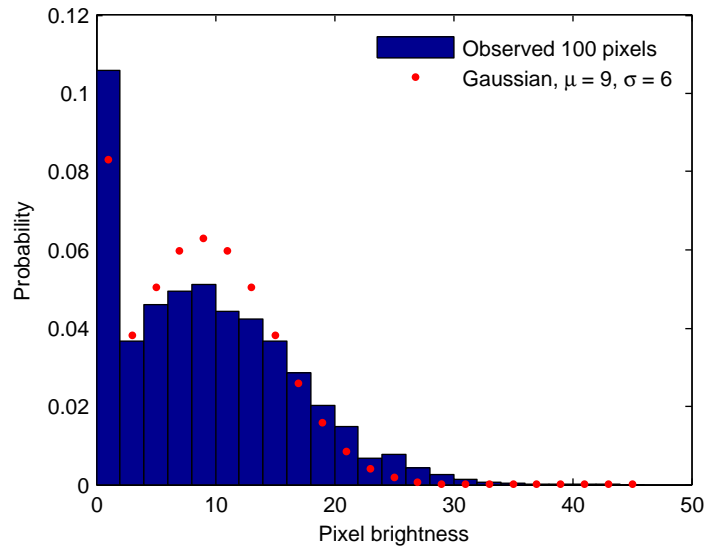
era pointed at a dark scene is given in Figure 1.8. Systematic artefacts, such as diminished sensitivity in regions of the intensifier or CCD, or gradual decrease in the intensifier gain with age, may also affect meteor photometry, and a sample intensified camera image is given in Fig. 1.9. Noise can be decreased by taking median or mean combines of pixel brightness values across several consecutive frames, use of wavelet transforms, and other techniques, while image artefacts can be compensated for by flat-fielding (effectively dividing the brightness across the frame by the brightness observed when looking at a uniformly-lit source) and performing regular brightness calibrations.

As with photography and radar, video has been used to survey the flux and mass-frequency distribution of meteoroids, both from sporadic and shower sources. General introductions to optical and video observations of meteors are given in Hawkes & Jones (1986), Campbell-Brown (2004), and Borovička (2006). This review will focus on the contributions of meteor light curves to the understanding of small meteoroid structure, as well as high-resolution wake and fragmentation observations.

In the 1970s, Jones & Hawkes developed an intensified video system to observe meteors that were fainter than those gathered by the Super-Schmidt photographic cameras (+4 magnitude), but were also independent of the biases of radar observations (Hawkes & Jones 1973). The system was comprised of a 25 mm image intensifier coupled via fibre optics to a vidicon tube, which recorded the meteors on video tape. A 25 mm $f/0.95$ lens was used, giving an approximate $21 \times 26^\circ$ field of view, and meteor sensitivity to magnitude +7, though the limiting magnitude varied in the field of view, particularly along the edges (Hawkes & Jones 1975a). Jones & Hawkes (1975) observed nearly four hundred faint meteors with this system and found that meteors were luminous over an average height interval of 6.7 ± 0.7 km, shorter than expected for single-body meteoroids that did not fragment. These results matched earlier Super-Schmidt results of Hawkins & Southworth (1958) and radio observations of Verniani (1973), and continued to suggest that small meteoroids fragmented and possessed a crumbly, dustball structure.



(a) Noise over all pixels for a single frame



(b) Noise for 100 selected pixels over 100 frames

Figure 1.8: Histograms showing the pixel brightness values for an intensified video frame when the camera is recording a uniform dark source (an example of dark current). In (a), the brightness of all pixels for a single frame is recorded, while in (b), the brightness of 100 pixels over 100 frames is recorded. Brightness profiles are similar for each case and are somewhat matched by a Gaussian distribution with a mean brightness value of 9, and a standard deviation of 6.



Figure 1.9: A sample frame from an image intensified camera. Dark portions related to dirt on the camera enclosure are marked with white arrows, while a meteor is marked with a green arrow. The mean brightness of the frame varies with distance to the edge, an example of vignetting. To compensate for these artefacts, the image is flat-fielded (procedure is discussed in Chapter 2).

Though the dustball structure had been proposed several times to describe observations of faint meteors, there was little quantitative treatment until a model was presented by Hawkes & Jones (1975b). In this model, the meteoroid is comprised of two components: stony, refractory fragments (each of equivalent mass, 10^{-9} kg in this case) held together in a volatile glue. As the meteoroid descends, all of the energy is consumed in heating and then vaporising the glue, releasing the grains. The grains then ablate as single-body objects with no mutual interactions. Physical quantities, such as the heat capacity and thermal conductivity of the meteoroid, were referenced from previous observationally-constrained models, but other important quantities, such as the melting temperature and heat of vaporisation of the glue were estimated based on the beginning heights of meteors.¹⁸

In the end, the dustball model reproduced the mass-independent beginning heights of faint meteors, finding that all of the glue melted before the meteoroid became luminous. As a result, the grains always began ablating at the same height, matching observations of McKinley (1961), Jacchia et al. (1967), and Verniani (1973), discussed earlier in Sections 1.2.1 and 1.2.2. This also explained the short luminous trails and early-peaked light curves of faint meteors observed with photography, radar, and video. Meteors with a peak magnitude of +7 were modelled as an example for the faint meteor case. Simultaneously, the nearly-classical behaviour of the light curves of brighter meteors was explained by more gradual fragmentation and grain loss occurring during the meteoroid's luminous trajectory. Meteors with a peak magnitude of -3 were considered for this case.

The quantitative dustball model by Hawkes & Jones was successful in explaining the shape and length of light curves for both faint and bright meteors, but some of the important physical properties, such as the amount of energy required to vaporise a unit mass of meteoroid material, called the *specific heat of ablation*, Q_{abl} , were estimated. Originally, Q_{abl} was estimated to be on the order of 10^6 J kg⁻¹ based on the heat of vaporisation of stone, but a video study by Hapgood et al. (1982) computed $Q_{\text{abl}} \sim 10^5$ J kg⁻¹ for Perseid meteors. Beech (1984, 1986)

¹⁸The dustball model and its associated equations will be discussed in more detail in Section 1.3.

subsequently found similar values for Perseids, South Taurids, Geminids, and Draconids from Super-Schmidt photographic data. These studies implied that meteoroids from certain showers might be more fragile than expected, but also highlighted the uncertainty in some important parameters for the model.

Additional high-quality observations allowed for refinement of the dustball model. Campbell et al. (1999) modified the model to allow for a power law mass distribution (as in Eq. (1.12)) for the fragments comprising the meteoroid. Grain masses ranging from 10^{-13} to 10^{-6} kg were used to model two hundred observed Perseids and Leonids, and it was found that similar mass indices were appropriate for both showers. Campbell et al. (2000) observed 79 Leonids from the 1998 shower with a mixture of second- and third-generation image-intensified cameras, performed two-station trajectory reductions, and analysed the light curves to determine photometric masses. The beginning and ending height of the observed Leonids, with peak magnitudes between +0.3 and +6.1 were found to show little dependence on meteor magnitude, verifying the predictions of the dustball model and suggesting that there was little variance in the grain sizes between individual Leonid meteoroids. Preliminary modelling suggested that fragments with a dense stony or iron composition became luminous too low in the atmosphere, and it was more likely that the meteoroids contained some porous stone, volatile metal (such as sodium), or organic components.

Koten et al. (2004) observed 496 shower meteors with peak magnitudes ranging from +4.7 to -2.1 and found that beginning heights of fast cometary meteoroids (Perseids, Orionids, Leonids) increased in relation to the photometric mass. This trend was less apparent for slower cometary meteoroids (Taurids) and absent for asteroidal objects (Geminids). A model predicting the minimum brightness at which a meteor was visible with the cameras used in this study was able to account for the proportionality between beginning height and photometric mass. This suggested that Perseids, Orionids, and Leonids were already ablating by the time they were detected, and that the observed beginning heights were due to sensitivity limitations of the camera system as opposed to the onset of intensive ablation. The opposite was suggested

to be true for the Geminids, with light curves that began at nearly the same height, independent of mass. Since the Geminids had a lower height for the onset of intensive ablation, this suggested that objects from asteroidal bodies may have larger heat capacities (and possibly, heats of ablation) than objects from cometary parents. Meteors were observed with a two-station image-intensified video setup with a 25° field of view and a limiting magnitude of +5.5, located in Central Europe (or Spain, for the Leonid observations).

A subsequent study by Koten et al. (2006) examined high-altitude meteors (> 130 km) in more detail. Classical ablation theory, which requires the meteoroid to be heated to a temperature that allows for intensive evaporation through collisions with atmospheric molecules, does not explain the brightness of meteors at these extreme heights. Instead, the authors examined *sputtering*, or pre-thermal ejection of meteoric particles resulting from collisions between atmospheric particles and the meteoroid. Light curves observed above 130 km displayed unusual peaks and dips in brightness not characteristic of the behaviour below 130 km, where traditional ablation was expected occur. This provided evidence of sputtering. Similarly, Leonids accounted for 145 of 164 meteors observed to begin above 130 km. Since sputtering yield, the number of meteoric particles ablated per incoming atmospheric particle, is highly sensitive to meteoroid speed, the authors argued that Leonids, with a speed of 71 km s^{-1} , would be expected to comprise the the majority of meteors beginning above 130 km if sputtering was the dominant source of brightness at these extreme heights.

Koten et al. (2006) also observed that as the initial mass of the meteoroid increased, the peak in the light curve moved closer to the end height, approaching a single-body light curve. This suggested that continuous fragmentation associated with the dustball model had a more significant effect on the light curves of fainter, smaller meteoroids. A few meteors showed a terminal flare and disappeared very rapidly, leading to the suggestion that some meteoroids with steep zenith angles could catastrophically fragment at the end of their trajectory. Finally, fragmentation that occurred before ablation and light production was suggested as an explanation for a few meteors that showed anomalously high (> 160 km) beginning heights. No direct

observations of fragmentation were reported, however.

The 1998 and 1999 Leonid multi-instrument aircraft campaigns (MAC) provided additional high-quality light curve observations (Jenniskens & Butow 1999, Jenniskens et al. 2000). Murray et al. (2000) observed two hundred Leonids, presenting 48 light curves of various shapes. Applying the dustball model with a power law grain mass distribution yielded a slightly smaller mass index $s_f = 1.75$ in 1999 than in 1998, where $s_f = 1.95$. A smaller mass distribution index means a more significant contribution from larger particles, and it was hypothesised that the 1999 Leonids were ejected at a later date than the 1998 counterparts, leading the authors to suggest that meteoroids that spend more time separated from their parent body may become more thoroughly fragmented. Subsequently, Beech & Murray (2003) found a more significant difference in the mass indices between the 1998 and 1999 Leonids (1.6 vs. 1.0, respectively) using an analytical ablation model. Interestingly, studying the sodium emission light curves of several Leonids showed that evaporation of sodium began at the same time as the overall meteor light emission, refuting the earlier suggestion that sodium might be a significant part of the glue in a dustball meteoroid (Murray et al. 2000).

Some unique results from the 1998 Leonid MAC were presented by Murray et al. (1999), showing a single Leonid with an extremely wide meteor wake (450 m radius), and another that appeared to fragment into several pieces during luminous flight. Two image-intensified cameras were used, one with a wide 16.3° field of view and +8.3 limiting stellar magnitude, and the other with a narrower 9.5° field of view and +8.9 limiting magnitude. The meteor with large wake was detected by the narrow-field camera at an estimated height of 138 km, and a magnitude of +1.6. The meteor later reached a peak magnitude of -4 as detected by the wide-field camera. This wake was far larger than expected from previous photographic and radar studies (typically of the order of ~ 1 m), but was also measured relatively high in the atmosphere. As the edge of the wake was well-defined with a sharp drop in brightness not characteristic of image blooming, the authors suggested the measured wake was physical. The fragmenting meteoroid was also observed with the narrow-field camera, at a height of 125 km and a

magnitude of +4.8, showing two bodies separated by about 560 m with the smaller fragment exhibiting an instantaneous wake length of 190 m. Preliminary calculations with the dustball model suggested that grain masses of the order 10^{-16} kg were required to produce the observed wake length, much smaller than expected values of 10^{-13} to 10^{-6} kg.

Though low-resolution video data, such as meteor light curves and beginning heights, provided constraints for the dustball model, particularly the meteoroid heat of vaporisation and glue melting temperature, high-resolution wake length data provided stricter constraints for the mass distribution of meteoroid grains. Early efforts at observing meteor wake were presented by Robertson & Hawkes (1991), who used an 8.1° field of view intensified system with a sensitivity limit of +7.5 to find two meteors exhibiting statistically-significant wake lengths from a sample of 27. The wake was found by plotting a line of best fit to all of the pixels in each digitised frame, with each pixel being weighted by brightness. A statistically significant meteor wake was observed if the linear fit describing the meteor wake for multiple frames matched the direction of travel. For the two meteors, estimated lengths of 160 and 780 m were found, corresponding to 7 and 30 pixels in the digitised video, respectively. Since so few meteors appeared to exhibit wake, the authors suggested that fragmentation may have occurred late in the ablation of the meteoroid, not letting the fragments lag significantly behind the main body. An alternate possibility was that the fragments were all of very similar size, not allowing for significant differences in deceleration between the bodies. Ultimately, the authors cautioned that a small sample size of 27 meteors was not representative and urged further studies.

A later study by Shadbolt & Hawkes (1995) employing a similar system and analysis, finding similar results: one meteor out of 25 exhibited wake, but the shortest wake that could be observed was estimated to be on the order of 200 m. Considering the results of this study and the one by Robertson & Hawkes (1991), Shadbolt & Hawkes suggested that the grains comprising the observed sporadic meteoroids must occupy a limited range of masses, likely from 10^{-10} to 10^{-8} kg. Subsequently, Fisher et al. (2000) found significant wake lengths in four of nine meteors studied with an intensified two-station system. One meteor showed wake lengths

up to 1.9 km over eight frames. The fraction of meteors that showed wake was larger than in previous studies, but this was likely due to more careful examination of videos, rejecting meteors that were too dim to be measured properly, as well as employment of image enhancements such as wavelets.

Fisher et al. (2000) and LeBlanc et al. (2000) both reviewed the wide, fragmenting Leonids originally reported by Murray et al. (1999) from the 1998 MAC campaign. Both authors emphasised that measuring the width of the meteor wake was important in addition to measuring the length, as there was little consensus with previous (photographic and radar) observations, and quantifying trail widths are important to improving the accuracy of radar observations. LeBlanc et al. (2000) also reported on some unusual, jet-like features in ground-based observations of several 1998 Leonid meteors. The jets reached up to 1.9 km in extent, though similar features were sometimes noticed on stationary images of Jupiter, suggesting that they might be instrumental artefacts.

Very wide Leonid meteors were also observed by Spurný et al. (2000). Widths up to nearly 4 km were observed in seven meteors at heights above 135 km. Extreme beginning heights, up to 200 km, were also noted for these bright meteors (one with peak magnitude -12.5 , the rest around -7). The meteors initially exhibited a diffuse, cone-like structure at heights above 160 km, eventually condensing to an elliptical shape that resembled a comet, which finally led to the typical droplet shape, associated with intensive ablation, at heights below 135 km. Each meteor was noted to be quite faint above 135 km, with magnitudes between $+6$ and $+4$. The authors discounted instrumental broadening of the observed wakes by noting that meteors with equivalent brightness at different heights showed different morphologies. Ambiguous, jet-like features were also recorded, as in LeBlanc et al. (2000). These wide and extremely high meteors were unexpected and unexplained by conventional meteoroid ablation models, as discussed earlier in the review of the sputtering study by Koten et al. (2006).¹⁹ Similarly, the authors estimated that ablated meteoric material required a transverse speed (perpendicular to

¹⁹The study by Koten et al. (2006) was partially motivated by attempting to explain the extremely high Leonids observed by Spurný et al. (2000).

the meteoroid's direction of travel) of nearly 100 km s^{-1} to reach the observed wake radius.

Another observation of a wide Leonid meteor wake was presented by Stenbaek-Nielsen & Jenniskens (2004), showing a single, -3 peak magnitude meteor with a $\sim 100 \text{ m}$ wide wake at a relatively low height of 105 km . This meteor exhibited an interesting morphology, with a shock-like structure at the head of the meteor, in contrast to the conical and elliptical shapes noted by Spurný et al. (2000). These observations were not explained by detailed, small-scale, single-body ablation models of Boyd (2000) and Popova et al. (2000), which predicted widths of order 1 m (though at heights around 95 km).²⁰ As a result, Stenbaek-Nielsen & Jenniskens suggested that some sort of radiative process could be contributing to the wake, as the mean free path of ultraviolet photons is on the order of 100 m at a height of 100 km . Spurný et al. (2000) alternately suggested that electrostatic repulsion may disperse the particles comprising the wake.

The most recent and comprehensive intensified video study of meteor trail widths was performed by Kaiser et al. (2004), making use of a two-station telescopic system with an extremely narrow 0.4° field of view, and a limiting magnitude of $+9$. A total of 34 meteors were captured by both cameras, exhibiting a maximum width of $1.4 \pm 0.7 \text{ m}$. One meteor, captured by a single station, showed an estimated width of 10 m , however. The widths observed in this survey were more similar to the photographic observations of Hawkins & Whipple (1954) and Cook et al. (1962), and the ion trail width measurements of Jones & Campbell-Brown (2005), rather than the extreme widths observed with intensified video by Murray et al. (1999), Spurný et al. (2000), and Stenbaek-Nielsen & Jenniskens (2004). This was likely due to careful quantification of trail widths through determination of the full width at half maximum (FWHM) of the observed trail brightness profiles, as well as exclusion of instrumental blooming by subtraction of stellar FWHMs. The previous intensified video studies appeared to measure the width of a meteor to a constant threshold brightness, likely the mean background, and did not

²⁰The high-resolution models by Boyd (2000) and Popova et al. (2000) focus on the properties of the flow around the meteoroid, rather than the meteoroid's ablation. The goal is to comment on the state and dimensions of the meteor wake. These models will be discussed in Section 1.3.

attempt to account for instrumental artefacts. Similarly, the mean meteor height for the survey by Kaiser et al. (2004) was 83 km, perhaps helping to explain the relatively narrow widths compared to the previous Leonid sightings, with beginning heights between 105 and 200 km.

High-resolution observations of faint meteors provide estimates of the length and width of the meteor wake. As mentioned previously, wake lengths are important to quantify the size distribution of grains comprising a dustball meteoroid, while widths can help account for biases in radar observations, as well as describe the behaviour of excited particles that are evaporated from the meteoroid. Unfortunately, the small number of high-resolution observations has led to inconsistencies between surveys, as trails nearly 1 km wide have been observed in some studies, while others have found widths on the order of 1 m. Similarly, very few direct observations of gross fragmentation have been presented for faint meteors.

With regards to fragmentation, Murray et al. (1999), Fisher et al. (2000), and LeBlanc et al. (2000) suggested that some dustball meteoroids might be comprised of smaller grains ($m \sim 10^{-16}$ kg) than previously expected, based on the analysis of a single fragmenting Leonid. Koten et al. (2006) suggested that fragmentation might be responsible for meteors that disappeared rapidly, as well as meteors beginning at extreme heights, above 160 km. Most other studies of fragmentation have involved observations (for example: Halliday et al. 1981, Ceplecha & McCrosky 1992, Brown et al. 1994, Borovička & Kalenda 2003) and modelling (Baldwin & Sheaffer 1971, Chyba et al. 1993, Artemieva & Shuvalov 2001, Ceplecha & Revelle 2005) of bolides. Borovička (2006) summarises these studies, listing bolide meteoroid strengths ranging from 0.025 MPa, for weak cometary material, to 14 MPa, for chondritic material. Watanabe et al. (2003) and Tóth & Klačka (2004) suggested that Leonid shower outbursts could be related to the fragmentation of clusters of meteoroids in space, very difficult to observe since the meteoroids have not become luminous. It is clear that observations and explanations of the gross fragmentation of small meteoroids remain elusive.

To provide more consistent observations of faint meteor wake and fragmentation, automated, high-resolution systems such as AIM-IT (Gural et al. 2004) and the Canadian Auto-

mated Meteor Observatory (CAMO, Weryk et al. 2013) have been developed. CAMO is an automated, two-station, intensified video system with a camera that records meteors across a wide 28° field of view to allow for trajectory calculation and observation of the entire light curve, and a camera that records meteors in high-resolution (three to four metres per pixel for meteoroids at a range of 135 km) for examination of fragmentation and meteor wake. The observations for this thesis were obtained with CAMO, and the system will be discussed in more detail in Chapter 2.

1.2.4 Other techniques

Photographic, radar, and intensified video observations provide the bulk of faint meteor records, but other instruments also provide useful data. Emission spectra from a meteor can be recorded with a camera by placing a prism or diffraction grating between the principal lens and the image intensifier or film, splitting the light into its constituent wavelengths. This allows the composition of the wake and meteoroid to be investigated by examining the atomic, molecular, and ionic emission lines. The temperature of the gas around the meteoroid, as well as other parameters, may also be investigated using models constrained by spectral observations. The first treatment of meteor spectra was presented by Borovička (1993), where it was found that the spectrum of a -9 magnitude fireball at heights below 50 km could be explained by a model of a gas in thermal equilibrium at temperatures between 3500 to 4700 K. A second, faint component at 10 000 K was interpreted to be the meteoroid's shock front, and was found to be brighter for faster meteors (Borovička 1994). The wake was found to not be in thermal equilibrium; instead, the excitation energy of particles comprising the wake was thought to be dissipated through radiative processes.

Perhaps most interestingly, Borovička (1993) found that the chemical abundance of the luminous gases around the meteoroid varied as a function of time. This was the first evidence of a phenomenon called *differential ablation*, where volatile materials, such as sodium, evaporate first from the meteoroid, while refractory materials, such as calcium, evaporate at lower

heights. Differential ablation was first proposed by McNeil et al. (1998) to explain differences in relative abundances between meteorites and the upper atmosphere, expected to be the same since meteoroids were thought to be the primary source of metal in the mesosphere. In particular, while meteorites tend to have equal abundances of sodium and calcium, lidar measurements of the atmosphere showed an overabundance of sodium by two orders of magnitude. The authors argued that calcium, which melts at higher temperatures than sodium, was released lower in the atmosphere, where it was more rapidly consumed in chemical reactions to form complexes. Though this study implicitly assumed that meteorite compositions accurately reflected the composition of an average meteoroid, it was a good first description of differential ablation that would later be investigated in more detail with a model by Vondrak et al. (2008), and arguably observed with high-power large-aperture (HPLA) radar by Janches et al. (2009).

Other spectral studies commented on meteoroid and parent body composition. Borovička et al. (1999) observed differential ablation of sodium in the upper part of the trajectories of the 1998 Leonids, a behaviour not observed in the Perseids and other meteors. This suggested that the Leonids fragmented at relatively high altitudes, revealing sodium for rapid ablation. Relative abundances of magnesium, iron, calcium, and sodium suggested carbonaceous CI-chondritic composition for Leonid meteoroids.

Conversely, a later study (Borovička et al. 2005) revealed that the majority of 97 mostly sporadic meteoroids showed non-chondritic composition, while nearly a third appeared sodium depleted. The sodium depleted meteoroids were split into three categories: objects on asteroidal orbits, possibly related to meteorites, with only iron lines; objects with small perihelion distances, $q < 0.2$ AU, where the sodium was thought to be thermally depleted; and objects on Halley-type comet orbits, where it was hypothesised that cosmic ray exposure in the Oort cloud depleted the sodium. Variance in composition amongst observed Geminids suggested parent body inhomogeneity. This was investigated in more detail for the Draconids by Borovička et al. (2014), where early sodium release was seen to be correlated with early-peaked light curves, large meteoroid decelerations, and large wakes, suggesting fragmentation. Thus, differences in

meteoroid structure were observed even for objects from the same parent body, possibly related to when the meteoroids were released.

Milley et al. (2007) attempted to study light production in meteors through laser ablation of a chondritic (L5) meteorite. An Nd:YAG laser (532 nm wavelength) was applied to the meteorite in 10 ns pulses, delivering 15 mJ per pulse. The light production region extended nearly 2 mm from the meteorite, and atomic Ca, Fe, Na, N, Mg, Si, and O lines were observed to comprise the spectra, along with lines from singly ionised Fe and Mg. Interestingly, the emission lines appeared to be superimposed on a continuum with peak wavelength around 500 nm, corresponding to a temperature of 5800 K, similar to the observations of Borovička (1993, 1994). Multiple laser ablation trials revealed slight variances in the spectra, likely related to the inhomogeneity of the meteorite, which suggested the plausibility of differential ablation (Hawkes et al. 2008). The size of the region of light production was not directly comparable to wake measurements as the meteorite was kept at room temperature and pressure. Future studies planned to experiment in vacuum conditions to provide better comparisons with meteor observations, but were not followed up. A brief investigation of laser ablation literature (see Amoruso et al. 1999 for example) suggests that laser ablation of meteorites in vacuum may be a feasible and unique way of investigating light production and the luminous efficiency, which is poorly defined.

Moving on to other techniques, infrasonic and seismic observation of meteors offer an independent method of meteoroid mass determination, though this is typically restricted to large meteoroids and fireballs. ReVelle (1976) outlined the formation of meteoric infrasound, modelling the meteoroid as a line source that propagates cylindrical waves. Several meteors were analysed in this work, but there were large uncertainties in the initial kinetic energies derived for the meteoroids, due to perturbative factors such as temperature and wind stratification in the atmosphere. Edwards et al. (2008) validated meteor infrasound theory by comparing video and infrasound observations of meteors with peak magnitude brighter than -2 , and the relationship between airburst yield and infrasonic signal period was investigated by Ens et al. (2012). Esti-

mates of the initial kinetic energy for several bolides, such as the Indonesian bolide (Silber et al. 2011), Grimsby (Brown et al. 2011), and Chelyabinsk (Brown et al. 2013), were derived from infrasonic observations.

1.2.5 Summary of observations

Summarising the important points:

1. Faint meteors are most commonly observed with photography, radar, and intensified video. The typical limiting magnitude for each technique is 0 for photo, +7 (CMOR) to +11 (AMOR) for specular trail echo radar, and +6 for intensified video. Physical properties and the structure of small meteoroids may be ascertained using ablation models constrained with meteor observations. Observations also allow for estimates of meteoroid flux, as well as investigation of the properties and parent bodies of meteoroid showers. Photographic observations are no longer common, but some older, high-quality observations, such as photographs taken by the Super-Schmidt cameras, are still used to constrain meteoroid ablation models. New techniques, such as the analysis of meteor emission spectra and infrasound emanations, promise to yield more information on meteoroid composition and the ablation process.
2. Models of single-body ablation and light production show poor agreement with observations of most faint meteors. As a result, the two-component dustball ablation model was formulated, assuming that the meteoroid is composed of grains of refractory material embedded in a volatile matrix. During ablation, the matrix melts first, releasing the grains that ablate independently at lower heights. The dustball model is able to match the observed light curve of many faint meteors, suggesting that fragmentation is common for small meteoroids during ablation. Some of the model's physical parameters, such as the heat of evaporation and boiling temperature of the matrix, are poorly constrained, however.

3. The dimensions of the wake of faint meteors are poorly characterised. Quantifying the width of the meteor wake is essential for correcting biases in radar observations, which can affect estimates of meteoroid mass and flux. Widths of less than 10 m at heights up to 100 km were obtained from photographic and radar surveys, as well as one intensified video study of sporadic meteors. Conversely, intensified video studies of Leonids revealed widths ranging from 100 m to 1 km, though at heights above 110 km. A better consensus between studies is required. Wake lengths are also ambiguous. It is expected, from the dustball model, that grains of different sizes should become separated once they are removed from the main meteoroid, producing an observable meteor trail. Lengths less than 200 m have been observed for meteors where the model predicted lengths on the order of 1 km, suggesting an inconsistency in observations or the dustball model.

4. Gross fragmentation for small meteoroids is poorly understood, mostly due to a lack of observations. At least one faint Leonid meteor was observed to fragment into two pieces with intensified video, while radar observations indicate that around eight per cent of faint meteors fragment into two or three pieces. The cause of this fragmentation is unknown—pulverisation due to pressure from the atmospheric flow at the front of the meteoroid is taken to be the usual cause of gross fragmentation for bright meteors, but this yields unrealistically low strengths at the heights of faint meteors. Rotation and electrostatic charging have also been suggested as fragmentation mechanisms, but have not been investigated quantitatively. Obtaining accurate estimates of the strength of meteoric material is important for determining the composition of small meteoroids.

Next, an introduction to meteoroid ablation models will be presented, starting with a derivation of the basic single-body ablation equations.

1.3 Models of ablation for faint meteors

1.3.1 Single-body fundamentals

The simplest model for meteoroid ablation assumes that the meteoroid does not fragment. As noted in Section 1.2, observations have revealed that this assumption is not valid for most small meteoroids, but an examination of single-body ablation is a good first step in describing the behaviour of a fragmenting object. The basic equations for light production and deceleration of a single-body meteoroid will now be derived from considerations of momentum and energy conservation. The ultimate goal of ablation modelling is to comment on the structure of meteoroids (single-body versus dustball; derivation of meteoroid density, heat of ablation, strength, and other physical quantities) by comparing simulated results with observations.

First, consider a meteoroid travelling with speed v through the atmosphere that has a mass density of ρ_{atm} . In the time interval Δt , the meteoroid travels length $l = v\Delta t$, sweeping out a cylindrical volume given by

$$V = S v \Delta t, \quad (1.13)$$

where S is the cross-sectional area of the meteoroid. This is illustrated in Figure 1.10. Atmospheric particles are dispersed throughout that volume, appearing stationary since their speeds are generally $< 1 \text{ km s}^{-1}$ while the speed of the meteoroid is between 11 and 72 km s^{-1} . The total mass of all atmospheric particles encountered in time step Δt is then

$$m_{\text{atm}} = \rho_{\text{atm}} V = \rho_{\text{atm}} S v \Delta t. \quad (1.14)$$

For convenience, the frame of reference where the meteoroid is moving with speed v and the atmosphere is at rest (illustrated in the top right of Fig. 1.10) may now be considered. Since the atmospheric particles are approximately stationary compared to the meteoroid, their initial speed is $v_{\text{atm},i} = 0$. After they collide with the meteoroid, they have a speed $v_{\text{atm},f}$, which has

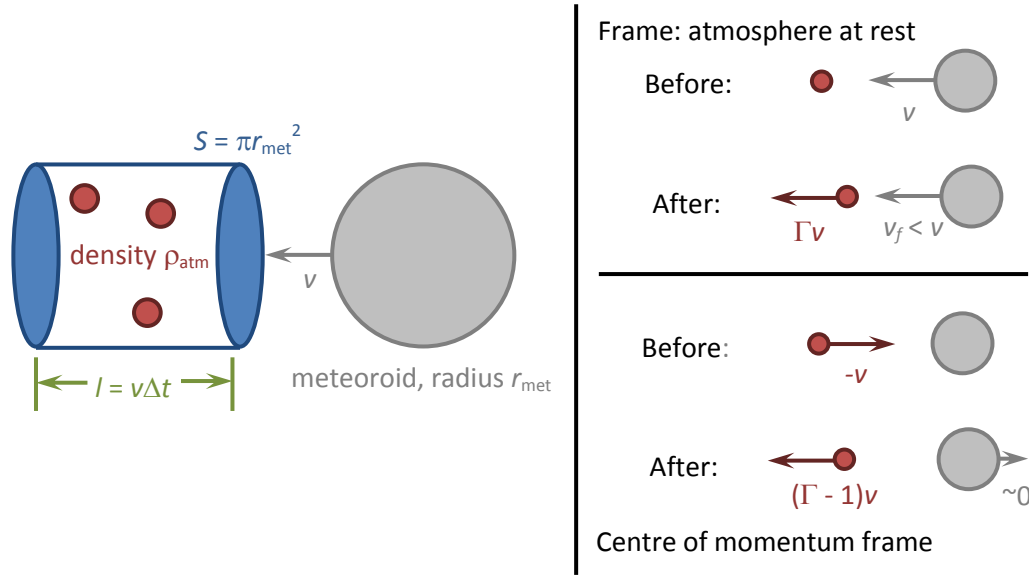


Figure 1.10: Illustration of the column of air that interacts with the meteoroid (shown for the special case of a sphere with radius r_{met} and cross-sectional area πr_{met}^2) during time step Δt . On the right, two illustrations of collisions between air molecules and the meteoroid. The top right panel shows the frame of reference where the atmosphere is at rest, while the bottom right panel shows the frame where the meteoroid is at rest (i.e. the frame where the centre of mass is not moving, or the centre of momentum frame).

the following range

$$v_{\text{atm},f} \approx \begin{cases} v, & \text{(totally inelastic)} \\ 2v, & \text{(totally elastic)} \end{cases} \quad (1.15)$$

depending on the elasticity of the collision, and noting that m , the mass of the meteoroid, is much larger than the mass of the atmospheric column traversed over a small enough time step, m_{atm} , given by Eq. (1.14). To represent the elasticity of the collision, the drag coefficient $\Gamma \in [0, 2]$ is introduced, such that $v_{\text{atm},f} = \Gamma v$, where a value of 1 is a totally inelastic collision, while a value of 2 is a totally elastic collision.²¹ By conservation of momentum, the change in meteoroid momentum over time step Δt is then $\Delta p = -\Delta p_{\text{atm}}$, or

$$\Delta p = -m_{\text{atm}} v_{\text{atm},f} = -\Gamma \rho_{\text{atm}} S v^2 \Delta t. \quad (1.16)$$

²¹ $\Gamma < 1$ represents the special case of particles getting deflected around the meteoroid without transferring momentum. This is a concern for brighter meteors that penetrate to heights below 80 km, where the atmosphere is dense enough that it becomes appropriate to treat both the atmosphere and meteoroid as fluids (Popova 2004).

The force on the meteoroid is

$$F = \lim_{\Delta t \rightarrow 0} \frac{\Delta p}{\Delta t} = -\Gamma \rho_{\text{atm}} S v^2. \quad (1.17)$$

The negative sign indicates that the meteoroid is decelerated through collisions with atmospheric particles.

Next, the energy imparted to the meteoroid through collisions with atmospheric particles may be computed. The centre-of-momentum frame of reference between an atmospheric particle and the meteoroid (depicted in the bottom right of Fig. 1.10) must now be considered. Since the mass of the meteoroid is much larger than the mass of an atmospheric molecule, the meteoroid is approximately stationary in that frame of reference. Similarly, the atmospheric particle has initial speed $-v$, and final speed $(\Gamma - 1)v$, where it may be recalled that totally inelastic and elastic collisions correspond to $\Gamma = 1$ and 2 , respectively. The energy imparted to the meteoroid by collisions with atmospheric molecules during the time interval Δt is $\Delta E = -\Delta E_{\text{atm}}$, or

$$\begin{aligned} \Delta E &= \frac{1}{2} m_{\text{atm}} (-v)^2 - \frac{1}{2} m_{\text{atm}} [(\Gamma - 1)v]^2 \\ &= \frac{1}{2} m_{\text{atm}} \Gamma (2 - \Gamma) v^2 \\ &= \frac{1}{2} \rho_{\text{atm}} \Gamma (2 - \Gamma) S v^3 \Delta t, \end{aligned} \quad (1.18)$$

and the power imparted to the meteoroid is $P = \Delta E / \Delta t$, or

$$P = \frac{1}{2} \rho_{\text{atm}} \Gamma (2 - \Gamma) S v^3. \quad (1.19)$$

This energy is used to increase the temperature of the meteoroid and cause mass loss through evaporation or sublimation. If some fraction of the incoming energy f_{abl} goes into ablating the meteoroid, and the heat of ablation (the amount of energy required to ablate a specific mass of

meteoroid material) is Q_{abl} , then the rate of mass loss is

$$\frac{dm}{dt} = -\frac{f_{\text{abl}}}{Q_{\text{abl}}} \frac{dE}{dt} = -\frac{\rho_{\text{atm}} \Gamma(2 - \Gamma) f_{\text{abl}} S v^3}{2Q_{\text{abl}}}, \quad (1.20)$$

where the negative sign ensures that $dm/dt < 0$. A new parameter called the *heat transfer coefficient*, Λ , which is related to the fraction of energy used to ablate the meteoroid, may be introduced to simplify Eq. (1.20) as

$$\frac{dm}{dt} = -\frac{\Lambda \rho_{\text{atm}} S v^3}{2Q_{\text{abl}}}. \quad (1.21)$$

Equations (1.17) and (1.21) give the deceleration and rate of mass loss for the meteoroid, respectively. The deceleration of the meteoroid may be measured once the meteoroid's trajectory through the atmosphere has been calculated. Mass loss is not directly measurable, but the light output of the meteor serves as an analogue. Traditionally, the power radiated by the meteor, I , has been modelled as a fraction, τ , of the meteoroid's kinetic energy dissipated through interaction with the atmosphere,

$$I = -\tau \frac{d}{dt} \left(\frac{1}{2} m v^2 \right) = -\tau \left(\frac{1}{2} \frac{dm}{dt} v^2 + m v \frac{dv}{dt} \right). \quad (1.22)$$

I is the radiated luminous power of the meteor, while τ is called the luminous efficiency, or the fraction of energy radiated as light.²² The right side of Eq. (1.22) is negative because $dm/dt < 0$ and $dv/dt < 0$. Small meteoroids with $v > 16 \text{ km s}^{-1}$ (Ceplecha et al. 1998) are mostly ablated before they decelerate significantly, allowing Eq. (1.22) to be simplified as

$$I \approx -\frac{\tau}{2} \frac{dm}{dt} v^2, \quad (1.23)$$

since the deceleration term is negligible compared to the mass loss term. Using Eq. (1.23),

²²There is a large amount of uncertainty in the luminous efficiency, related to the spectral emissions of the meteor and the sensitivity of the observation system. Typically, $\tau \sim 0.1 - 10$ per cent (Weryk & Brown 2013).

as well as the conversion between luminous power and magnitude introduced earlier as Eq. (1.1), a simulated meteor light curve may be produced and compared to observations.

To summarise, the classical equations for single-body meteoroid ablation are

$$\frac{dv}{dt} = -\frac{\Gamma S \rho_{\text{atm}} v^2}{m}, \quad (1.24)$$

$$\frac{dm}{dt} = -\frac{\Lambda S \rho_{\text{atm}} v^3}{2Q_{\text{abl}}}, \quad (1.25)$$

and

$$I = -\frac{\tau}{2} \frac{dm}{dt} v^2. \quad (1.26)$$

The meteoroid's deceleration may be simulated with Eq. (1.24) and the light curve with Eqs. (1.25) and (1.26). This allows for an estimate of the initial mass, density, and speed of an observed meteoroid by simulating objects and varying those parameters until the simulated light curve and deceleration match observations.

Some approximations and limitations of the classical ablation equations may now be discussed briefly. In deriving Eqs. (1.24) and (1.25), it was assumed that the change in meteoroid mass over the time step Δt is negligible, as is done by most authors (Bronshten 1983, Ceplecha et al. 1998). In reality, the meteoroid is ablating and the change in mass must be considered, but it is likely that the error introduced by neglecting Δm is smaller the uncertainty in atmospheric density, drag coefficient, and other parameters on the right side of the equations, as well as in the observations of the meteoroid deceleration and light production. Similarly, the recoil from atoms and ions being evaporated from the meteoroid may be considered in more detail, but it is suitable to assume isotropic release of particles (zero net recoil) in absence of a meteoroid shape model or observational constraints.²³

Similarly, there is significant uncertainty in the luminous efficiency, τ , as well as its variance on meteoroid speed, composition, height, and mass. Weryk & Brown (2013) offer a recent

²³Isotropic release of evaporating atoms and ions from the meteoroid approximates the evaporating surface as being spherical, isothermal, and homogeneous, or that the meteoroid is rapidly rotating.

discussion and attempt at deriving τ . Non-classical light curves (the middle and bottom light curves in Fig. 1.2) can result from non-fragmenting meteoroids if they are inhomogeneous and undergo differential ablation since each meteoric material would have its own τ value depending on the spectral lines emitted and the sensitivity of the optical system. As a result, the light emitted by the meteoroid is not strictly indicative of the rate of ablation, dm/dt , and several mechanisms are able to explain non-classical light curves. Nonetheless, integrating the light curve gives a preliminary estimate of the meteoroid mass, and fragmentation is one of the most commonly accepted explanations for non-classical shapes for light curves.

1.3.2 The dustball model

A single-body ablation of a homogeneous meteoroid produces a light curve that slowly increases in brightness and then rapidly decreases, as previously depicted in Fig. 1.2. The peak brightness is near the ending height of the light curve, as a result. The beginning height of a single-body light curve, given a certain limiting magnitude for observations, is proportional to the initial mass of the body, also. Faint meteors tend not to follow these trends, so Hawkes & Jones (1975b) devised the two-component dustball model, in which the meteoroid is comprised of refractory fragments that are released to ablate as independent bodies with the progressive melting of the volatile binding matrix, sometimes called glue.

First, the surface of the meteoroid is heated to the boiling point of the glue. The height at which this occurs was calculated by Ceplecha & Padevet (1961) with a number of assumptions. Since the expression is complicated, it will be omitted from this review. After the meteoroid's surface has been heated, Hawkes & Jones (1975b) stipulate that the power transferred to the meteoroid by atmospheric collisions, Eq. (1.19), is used to simultaneously heat the remainder of the meteoroid to the boiling temperature of the glue, as well as sublimate the glue. Thus,

$$dE = -(c\Delta T + f_g L_g)dm, \quad (1.27)$$

where c is the average specific heat capacity of the meteoroid (the amount of energy per unit mass required to increase the meteoroid temperature by one unit), ΔT is the difference between the pre-atmospheric and boiling temperature of the meteoroid, f_g is the fraction of the meteoroid comprised of glue, and L_g is the heat of vaporisation for the glue. This is in contrast to the single-body case, where energy goes solely into ablating the meteoroid, $f_{\text{abl}} dE = -Q_{\text{abl}} dm$ as seen in Eq. (1.20). Now, since the power input dE/dt is equivalent to the single-body case,

$$\frac{dm}{dt} = -\frac{\Lambda S \rho_{\text{atm}} v^3}{2(c\Delta T + f_g L_g)}, \quad (1.28)$$

which gives the mass of the parent dustball as a function of time. Mass that is lost from the parent dustball is assumed to be in fragments, each of equivalent mass $m_{\text{frag}} = 10^{-9}$ kg in the initial model by Hawkes & Jones (1975b). Each fragment undergoes single-body ablation, as given by Eqs. (1.24) - (1.26), and the light output is summed to give the total meteor light output.

As discussed in Section 1.2, the original model by Hawkes & Jones (1975b) was able to simultaneously explain light curves that peak in brightness near the beginning of the trajectory, as well as beginning heights that are independent of mass, both of which are commonly observed for faint meteors. Subsequently, Campbell-Brown & Koschny (2004) modified the model to explicitly track meteoroid temperature by considering energy input into three sinks,

$$\frac{dE}{dt} = mc \frac{dT_{\text{met}}}{dt} + 4\sigma_{\text{SB}} \epsilon S (T_{\text{met}}^4 - T_{\text{atm}}^4) + Q_{\text{abl}} \frac{dm}{dt}. \quad (1.29)$$

The term on the left of Eq. (1.29) is the energy transferred from the atmosphere to the meteoroid, represented earlier by Eq. (1.19). On the right side, the first term is the energy used to heat the meteoroid, the middle term describes radiative losses, while the third term is the energy consumed in ablating material. T_{met} and T_{atm} are the temperatures of the meteoroid and atmosphere, respectively, σ_{SB} is the Stefan-Boltzmann constant, ϵ is the emissivity of the meteoroid, and it is assumed that the total surface area of the meteoroid is equivalent to $4S$,

where S is the cross-sectional area as before.

Eq. (1.29) is a single differential equation for two quantities that vary with time, m and T_{met} , so a second equation is required to describe the meteoroid mass. Campbell-Brown & Koschny employed the Knudsen-Langmuir equation for mass loss due to evaporation,

$$\frac{dm}{dt} = \psi \left(\frac{\mu}{2\pi k_B T_{\text{met}}} \right)^{1/2} (P_{\text{sat}} - P_{\text{vap}})S, \quad (1.30)$$

where ψ is the condensation coefficient (the probability that an evaporated meteoric particle will condense onto the meteoroid), μ is the average mass of a meteoric particle, k_B is the Boltzmann constant, P_{sat} and P_{vap} are the saturation and current vapour pressures for evaporated meteoric gas. The saturation pressure is given by the Clausius-Clapeyron equation,

$$P_{\text{sat}} = P_b \exp \left[\frac{Q_{\text{abl}}\mu}{k_B} \left(\frac{1}{T_b} - \frac{1}{T_{\text{met}}} \right) \right], \quad (1.31)$$

where P_b is the ambient pressure when meteoric material is boiled at temperature T_b . Eq. (1.31) makes a number of assumptions, the most significant of which is that the heat of ablation (equivalently the heat of sublimation) does not vary from the reference temperature T_b to the meteoroid temperature T_{met} , but these are necessary to derive an independent mass loss equation.²⁴

Combining Eq. (1.30) and (1.31) gives an expression for dm/dt that can be combined with the energy equation, Eq. (1.29) to simultaneously solve for the meteoroid temperature and mass. This combination of equations describes the behaviour of the parent dustball, as well as the fragments once they are detached from the parent. Detachment occurs when the dustball reaches the boiling temperature, as in Hawkes & Jones (1975b), but the calculation is performed a bit differently. Referencing Bronshten's (1983) examination of the temperature of

²⁴Similarly, Eq. (1.30) implicitly assumes that the temperature of the gas surrounding the meteoroid is equivalent to the meteoroid temperature, which may not be the case, especially for faint meteors where the atmosphere is of such low density that it is difficult to quantify a temperature. Borovička (1993) also noted that the wake was not in thermal equilibrium.

a cylinder in an isothermal atmosphere, Campbell-Brown & Koschny determine the depth, x_0 , to which the meteoroid is heated to $1/e$ of the surface temperature (when it reaches the glue boiling temperature). A shell with that thickness,

$$x_0 = \left(\frac{\lambda_c}{\rho_{\text{met}} c} \cdot \frac{H^*}{v_\infty \cos z} \right)^{1/2}, \quad (1.32)$$

melts and releases grains that ablate independently. In Eq. (1.32), λ_c and ρ_{met} are the mass density and thermal conductivity of the meteoroid, respectively, H^* is the scale height of the atmosphere (the height interval over which the density is decreased by $1/e$), v_∞ is the initial speed of the meteoroid, and z is the zenith angle. The part of the parent dustball that is not melted is assumed to be at $1/e$ of the glue boiling temperature. A significant improvement over the model of Hawkes & Jones (1975b) is allowance for a mass distribution for the grains. A Gaussian mass distribution gives a late-peaked light curve that resembles a single-body, but a power-law distribution (Eq. (1.12)) can give a variety of shapes depending on the mass index s_f .

Three Leonids were fit in the paper by Campbell-Brown & Koschny (2004) as a first test of the model. Kikwaya et al. (2011) used the same model to simultaneously fit the light curves and deceleration profiles of 107 shower and sporadic meteoroids to find a distinction in bulk densities between Halley-type comets ($\sim 1000 \text{ kg m}^{-3}$) and Jupiter-family comets and asteroids ($> 3000 \text{ kg m}^{-3}$). This provided quantitative evidence of differences in the structures of meteoroids from asteroidal versus cometary parent bodies.

Borovicka et al. (2007) introduced another variant of the dustball model in which fragments are conceptualised to erode from the parent meteoroid. The traditional mass loss equation is used for the parent meteoroid,

$$\frac{dm}{dt} = -\frac{\Lambda S \rho_{\text{atm}} v^3}{2} \left(\frac{1}{Q_{\text{abl}}} + \frac{1}{Q_{\text{er}}} \right), \quad (1.33)$$

with an additional heat of erosion term Q_{er} to represent the energy consumed in removing

fragments. Once fragments are separated from the main body, they ablate without further erosion, as given by Eq. (1.25). Fitting seven Draconid meteors, Borovicka et al. found that the heat of erosion was about 15–30 times smaller than the heat of ablation, and that power-law mass distributions with masses ranging between 10^{-9} and 10^{-11} kg were appropriate. Draconid bulk densities were found to be extremely small, $< 200 \text{ kg m}^{-3}$, suggesting a porous structure for these meteoroids.

Thus, two models describing the ablation and fragmentation of small meteoroids in the atmosphere were independently developed. Campbell-Brown et al. (2013) compared the two by fitting high-resolution observations of ten faint meteors captured with the Canadian Automated Meteor Observatory (CAMO). It was found that both were able to adequately fit the meteor light curves and deceleration profiles, but failed to match the observed meteor wake lengths. This suggested that new, high-resolution observations could be used to improve both models, but also hinted that the method for selecting model parameters (such as meteoroid density, glue boiling temperature, and heat of erosion) to match observations should be reviewed. Kikwaya et al. (2011) employed a numerical technique to minimise differences (residuals) between observations and simulations to find the ideal model parameters for each of the 107 meteors examined, but it was noted that many of the meteors did not converge to a unique set of parameters. In effect, the numerical technique converged on local minima for residuals in the solution space, as opposed to the global minimum. Perhaps this was also the case for the two models compared in Campbell-Brown et al. (2013), since the grain mass distributions, bulk, and grain densities for each meteor varied between the two models, as seen in Table 1.2. In any case, development of both models continues with the advent of new, high-resolution observations.

1.3.3 Alternative models for meteoroid fragmentation

Quasi-continuous fragmentation (QCF) is an alternative method of modelling faint meteor ablation, described by Novikov et al. (1998) and Babadzhanov (2002). This method is similar to

Table 1.2: A comparison of bulk densities for ten faint meteors computed using the model by Campbell-Brown & Koschny (2004), and Borovička et al. (2007).

Name	Campbell-Brown & Koschny (2004) (kg m^{-3})	Borovička et al. (2007) (kg m^{-3})
20101016_070052	7500	3000
20101016_075031	2500	7500
20101020_094418	800	310
20101020_100214	2000	800
20101103_045928	4500	2900
20101103_053624	1000	950
20101103_061856	1500	1410
20101103_071855	1000	1180
20101103_065820	6500	1000
20101103_015015	6000	2800

the erosion model by Borovička et al. (2007) in that a separate heat of fragmentation triggers the release of grains from the parent dustball. Analytical solutions to the mass loss and deceleration equations are derived using number of approximations, such as an isothermal atmospheric density profile. An advantage of this approach is that closed-form analytical solutions allow for faster fitting of observed data than numerical models. Babadzhanov (2002) was able to fit 111 of 197 bright photographic meteors with the QCF model, suggesting its applicability. Meteoroid bulk densities ranging from 400 (Halley-type cometary parent) to 2900 kg m^{-3} (asteroidal parent) were determined. As with the erosion model, the beginning and ending heights of fragmentation are free parameters to be input to the model. Additionally, the height interval over which the fragments are luminous must be specified.

Bellot Rubio et al. (2002) argued that fragmentation was not an important process for faint photographic meteors by fitting the light curves and deceleration profiles of 370 Super-Schmidt events with magnitudes between +2.5 and -5 . Observations from 270 of the 370 selected meteors were adequately fit by single-body ablation, and densities such as $600 \pm 100 \text{ kg m}^{-3}$ for the Perseids (cometary) and $1900 \pm 700 \text{ kg m}^{-3}$ for the Geminids (asteroidal) were obtained. Unfortunately, the light curves captured by the Super-Schmidt cameras had very few points (generally four or less), making it difficult to compare any model with the selected observa-

tions. Similarly, the authors noted that the modelled beginning heights tended to be too high compared to observations, repeating the initial observations that suggested fragmentation was an important process. Nonetheless, this study was interesting because it yielded density values to compare with fragmentation-based models.

Passey & Melosh (1980) developed a model of gross fragmentation for fireballs, constrained by dimensions of terrestrial crater fields. In this model, fragmentation occurs when pressure exerted on the front of the meteoroid by the atmosphere, $\rho_{\text{atm}}v^2$, exceeds the strength of the meteoroid material. This mechanism was presented by Baldwin & Sheaffer (1971) in an earlier study. Strengths of the order 0.5 – 500 MPa were expected based on studies of meteorites, though Baldwin & Sheaffer noted that strength, σ_{met} , was expected to vary with body mass as

$$\sigma_{\text{met}} = \sigma_0 \left(\frac{m_0}{m_{\text{met}}} \right)^\xi, \quad (1.34)$$

where σ_0 and m_0 are reference fragment strengths and masses (of meteorites) measured in the lab, while ξ took values such as 1/6 or 1/12. As result of Eq. (1.34), smaller meteoroids are expected to be stronger than larger objects, though video observations seem to indicate otherwise (Borovička 2006), as noted earlier in Section 1.2.

In the model by Passey & Melosh (1980), fragments are assumed to ablate independently with behaviour described by the classical single-body equations once separated from the main body. To explain the observed crater fields, Passey & Melosh suggested three mechanisms to create a transverse velocity component (perpendicular to the meteoroid velocity) between fragments: bow shock interaction, centrifugal force from a spinning meteoroid, and crushing of the parent meteoroid. The interaction between bow shocks is quantified as

$$v_t = \left(C \cdot \frac{r_1}{r_2} \cdot \frac{\rho_{\text{atm}}}{\rho_{\text{met}}} \right)^{1/2} v, \quad (1.35)$$

where v_t is the transverse velocity component of fragment 2 due to fragment 1 (with radii r_2 and r_1 , respectively), and C is the minimum separation, in number of meteoroid radii, re-

quired between fragments before interaction is negligible. From crater distributions, Passey & Melosh suggested values for C between 0.02 and 1.52, but a detailed hydrocode simulation by Artemieva & Shuvalov (2001) computed a value of $C = 0.19$. The rotational contribution to transverse fragment speeds was poorly constrained as it depended on the height of fragmentation, but increased in significance with increasing meteoroid size. Finally, crushing was suggested to provide an equal contribution to transverse speeds as bow shock interaction, but no calculations were provided. In the end, the models by Passey & Melosh (1980) and Artemieva & Shuvalov (2001) were able to roughly reproduce the size of selected terrestrial crater fields, but the large number of free parameters made it difficult to comment definitively on impactor sizes, densities, trajectories, or fragmentation heights.

Few models exist to explain gross fragmentation in smaller meteoroids. As discussed in Section 1.2, rotation was suggested as a fragmentation mechanism by Hawkes & Jones (1978) and Campbell-Brown & Jones (2003), who calculated that rotation speeds of the order 5000 rad s^{-1} ($\sim 800 \text{ Hz}$) were appropriate for small meteoroids. Beech & Brown (2000) observed much smaller rotational rates for the Peekskill bolide, around 20 Hz , but estimated strengths from 1 to 50 MPa based on rotational bursting.

Alternately, Spurný & Ceplecha (2008) suggested triboelectric charging as a mechanism for high altitude fragmentation, but did not present any calculations. Sorasio et al. (2001), Mendis et al. (2005), and Mendis & Maravilla (2009) investigated thermionic emission from small meteoroids, concluding that this could be a significant source of electron emission from meteoroids in addition to ablation. The models found that the meteoroid becomes negatively charged by atmospheric electrons at heights above 140 km . Subsequently, between 140 and 100 km , thermionic emission begins to remove electrons from the meteoroid, and below 100 km , ablation rapidly removes electrons and produces an ion trail. The charging behaviour above 140 km suggests the hypothesis by Spurný & Ceplecha (2008) may be valid, but this requires further investigation.

1.3.4 High-resolution, sputtering, and other models

As new constraints from high-resolution intensified video and spectral observations become available, models are beginning to investigate the wake and state of the flow around small meteoroids. Boyd (2000) employed the direct simulation Monte Carlo (DSMC) method to investigate the flow around a 1 g Leonid travelling 72 km s^{-1} at a height of 95 km. In DSMC, interactions between atmospheric particles, meteoric particles, and the meteoroid itself are simulated with collisions. Collisions with the meteoroid impart energy and momentum to evaporate meteoric particles and decelerate the meteoroid, respectively. Collisions between highly-energetic particles around the meteoroid form the luminous wake and the ion trail. The classical ablation equations, Eqs. (1.24), (1.25), and (1.26), are solved by direct evaluation of particle interactions and averaging over large populations or long timescales.²⁵

Boyd's (2000) calculations revealed that a wake of diameter $\sim 6 \text{ m}$ formed around the modelled Leonid, matching intensified video observations of faint meteors at similar heights (Kaiser et al. 2004). The wake appeared to be in thermal equilibrium with temperatures of the order 10^3 K . Spectral observations revealed similar temperatures around the meteor head, but also found that it was difficult to quantify the temperature of the wake, which might not be in thermal equilibrium (Borovička 1993). Simulating the ablation of a cometary meteoroid yielded a larger, higher temperature wake compared to an asteroidal meteoroid, suggesting that differences in meteor wake might indicate different compositions. This model was a promising first attempt to explain new observations, but was never followed up, perhaps due to lack of observational constraints.

Popova et al. (2000) also developed a model to investigate the properties of meteor wake at heights above 80 km. Incoming atmospheric particles are treated as a beam, attenuated by the dense wake immediately around the meteoroid. A number of approximations were made in

²⁵This method is applicable at height ranges for small meteoroids (generally $h > 90 \text{ km}$) where the atmospheric density is small enough such that the macroscopic behaviour is well-described by interactions between pairs of particles. At lower heights typical of brighter objects, a continuum-based fluid mechanics model is more appropriate.

the model (such as assuming spherical or cylindrical symmetry for flow around the meteoroid) making it difficult to evaluate, but preliminary wake temperature values ranging between 5000 and 10 000 K were produced, roughly matching spectral observations. The extent of the wake was found to be much smaller than in Boyd's (2000) investigation, under 20 cm in diameter at a height of 100 km for a 1 cm Leonid at 72 km s^{-1} , which did not agree with intensified video observations.

Vinković (2007) devised a high-resolution model based on particle collisions to investigate sputtering and the appearance of meteors at heights above 130 km. Atmospheric particles colliding with the meteoroid eject meteoric particles before the meteoroid is heated to the evaporation point. A detailed model by Rogers et al. (2005) found sputtering to be a significant source of mass loss for small ($m < 10^{-3} \text{ kg}$), fast meteoroids (typically $v > 60 \text{ km s}^{-1}$). These sputtered particles, all assumed to have a speed of 20 km s^{-1} relative to the meteoroid, then collide with atmospheric particles. The locations of the collisions are tracked with respect to the meteoroid to prepare a synthetic image analogous to an intensified video frame. The modelled shape of the meteor matched earlier high-altitude Leonid observations (Spurný et al. 2000) in a qualitative sense, and general trends, such as the width of the wake decreasing with decreasing height, were also reproduced. Quantitative comparisons with observations were not performed, but it is not likely that this would yield much information about the meteoroid, since there are few free parameters (such as meteoroid density, mean meteoric particle mass) in the model.

Though particle-based Monte Carlo modelling is a novel way to make use of high-resolution video observations to comment on meteoroid structure and ablation, other sophisticated models describe the contribution of meteoric material to the atmosphere (Vondrak et al. 2008) as well as the interaction between radar waves and the head plasma immediately around the meteoroid (Dyrud et al. 2008), for example. The Chemical Ablation Model (CAMOD) by Vondrak et al. (2008) quantitatively describes differential ablation of non-fragmenting meteoroids, which also includes sputtering, diffusion of material in the meteoroid, and meteoroid melting based on the

equation of state for olivine. Height distributions for meteors measured by radar head echoes were reproduced by the model, as well as general relative abundances of meteoric metals and ions (Na, K, Fe, Mg, Si) in the upper atmosphere, but the anomalous sodium to calcium ratio first commented on by McNeil et al. (1998) was not explained.

Dyrud et al. (2008) presented a two-step simulation to investigate how the meteor head echo radar cross section varied with the distribution of ions around the meteoroid and orientation between the meteor and incident radar waves. The first step generated a density distribution for the ions comprising the meteor plasma using a Monte Carlo technique called particle-in-cell (PIC), while the second step took this distribution and evaluated its interaction with incident radar waves. Varying the angle between the meteor and the radar wave did not have a significant effect on the radar cross section. Reflections from an assumed Gaussian ionisation profile varied significantly from the simulated profile, however. This suggested the importance of calculating a realistic ionisation profile when attempting to interpret observations, similar to what was found for meteor trail echoes by Jones (1995).

1.3.5 Summary of modelling

In summary:

1. Single-body theory is the most basic model for meteoroid ablation, but it does not adequately describe the behaviour of most faint meteors. Faint meteors decelerate more rapidly than predicted, are luminous over shorter height intervals than predicted, and emit light at different rates than predicted.
2. Continuous meteoroid fragmentation and dustball theory accounts for these discrepancies. New high-resolution video observations suggest improvements are required for contemporary ablation theory, however.
3. Gross fragmentation is incompletely understood, as mentioned in Section 1.2. Aerodynamic crushing, rotation, and electrostatic charging have been suggested as mechanisms

for meteoroid disruption, but have not been quantitatively evaluated using observations.

4. High-resolution (and spectral) observations have allowed for more detailed modelling of meteor wakes and the flow around faint meteors, but the field is early in its development, partially due to the lack of consistent observations.

1.4 Thesis goals

The general motivation of this thesis is to improve understanding of meteoroid ablation, fragmentation, and composition through analysis of high-resolution video observations and numerical modelling. Better understanding of these processes for faint meteors leads to better knowledge of Solar System composition, as well as the hazards of micrometeoroid impacts for objects in low Earth orbit.

As seen in Sections 1.2 and 1.3 of this review, improved observations lead to more detailed models, which ultimately lead to better understanding. The goal of this thesis is to use new high-resolution observations of faint meteors (which will be introduced in Chapter 2) to comment on the structure of small meteoroids and associated ablation processes. Specifically, the optical trail widths of thirty faint meteors are measured in Chapter 3. Widths up to 100 m at heights above 110 km are observed, and an effort is made to explain them as purely photochemical wake resulting from de-excitation of energetic particles around the meteoroid. Chapter 4 examines nine unique faint meteors that show gross fragmentation as well as significant transverse speeds for the resulting fragments. Several fragmentation mechanisms are evaluated, and meteoroid strengths are derived. Chapter 5 introduces a particle-based Monte Carlo model for single-body meteoroid ablation to explain properties of the wake of nine faint meteors observed in Chapter 3. Finally, Chapter 6 reviews the relevant findings and suggests next steps for the analysis of faint meteors.

Bibliography

Artemieva, N. A., Shuvalov, V. V., (2001). Motion of a fragmented meteoroid through the planetary atmosphere. *Journal of Geophysical Research*, 106 (E2), 3297-3309.

Amoruso, S., Bruzzese, R., Spinelli, N., Velotta, R., (1999). Characterization of laser-ablation plasmas. *Journal of Physics B: Atomic, Molecular, and Optical Physics*, 32, R131-R172.

Babadzhanov, P. B., (2002). Fragmentation and densities of meteoroids. *Astronomy & Astrophysics*, 384, 317-321.

Baggaley, W. J., (1970). The determination of the initial radii of meteor trains. *Monthly Notices of the Royal Astronomical Society*, 147, 231-243.

Baggaley, W. J., (1980). Measurements of the velocity dependence of the initial radii of meteor trails. *Bulletin of the Astronomical Institute of Czechoslovakia*, 31 (5), 308-311.

Baggaley, W. J., Bennett, R. G. T., Steel, D. I., Taylor, A. D., (1994). The Advanced Meteor Orbit Radar Facility: AMOR. *Quarterly Journal of the Royal Astronomical Society*, 35, 293-320.

Baggaley, W. J., Grant, J., (2004). Radar measurements of macro fragmentation in meteoroids. *Earth, Moon, and Planets*, 95, 655-662.

Baldwin, B., Sheaffer, Y., (1971). Ablation and breakup of large meteoroids during atmospheric entry. *Journal of Geophysical Research*, 76 (19), 4653-4668.

Beech, M., (1984). The structure of meteoroids. *Monthly Notices of the Royal Astronomical Society*, 211, 617-620.

Beech, M., (1986). The Draconid meteoroids. *The Astronomical Journal*, 91 (1), 159-162.

Beech, M., Brown, P., (2000). Fireball flickering: the case for indirect measurement of meteoroid rotation rates. *Planetary and Space Science*, 48, 925-932.

Beech, M., Brown, P., Hawkes, R. L., Ceplecha, Z., Mossman, K., Wetherill, G., (1995). The fall of the Peekskill meteorite: video observations, atmospheric path, fragmentation record and orbit. *Earth, Moon, and Planets*, 68, 189-197.

Beech, M., Murray, I. S., (2003). Leonid meteor light-curve synthesis. *Monthly Notices of the Royal Astronomical Society*, 345, 696-704.

Bellot Rubio, L. R., Martínez González, M. J., Ruiz Herrera, L., Licandro, J., Martínez Delgado, D., Rodríguez Gil, P., Serra-Ricart, M., (2002). Modelling the photometric and dynamical behaviour of Super-Schmidt meteors in the Earth's atmosphere. *Astronomy & Astrophysics*, 389, 680-691.

Blaauw, R. C., Campbell-Brown, M. D., Weryk R. J., (2011a). Mass distribution indices of sporadic meteors using radar data. *Monthly Notices of the Royal Astronomical Society*, 412, 2033-2039.

Blaauw, R. C., Campbell-Brown, M. D., Weryk R. J., (2011b). A meteoroid stream survey using the Canadian Meteor Orbit Radar - III. Mass distribution indices of six major meteor showers. *Monthly Notices of the Royal Astronomical Society*, 414, 3322-3329.

Borovička, J., (1993). A fireball spectrum analysis. *Astronomy & Astrophysics*, 279, 627-645.

Borovička, J., (1994). Two components in meteor spectra. *Planetary and Space Science*, 42 (2), 145-150.

- Borovička, J., (2006). Physical and chemical properties of meteoroids as deduced from observations. In: Asteroids, Comets, Meteors, Proceedings of the 229th Symposium of the International Astronomical Union, edited by D. Lazzaro, S. Ferraz-Mello, J. A. Fernández. Cambridge: Cambridge University Press. 249-271.
- Borovička, J., Kalenda, P., (2003). The Morávka meteorite fall: 4. Meteoroid dynamics and fragmentation in the atmosphere. *Meteoritics & Planetary Science*, 38 (7), 1023-1043.
- Borovička, J., Koten, P., Shrbený, L., Štork, R., Hornoch, K., (2014). Spectral, photometric, and dynamic analysis of eight Draconid meteors. *Earth, Moon, and Planets*, August 2014, 17pp.
- Borovička, J., Koten, P., Spurný, P., Boček, J., Štork, R., (2005). A survey of meteor spectra and orbits: evidence for three populations of Na-free meteoroids. *Icarus*, 174, 15-30.
- Borovička, J., Spurný, P., Brown, P., Wiegert, P., Kalenda, P., Clark, D., Shrbený, L., (2013). The trajectory, structure and origin of the Chelyabinsk asteroidal impactor. *Nature*, 503, 235-237.
- Borovička, J., Spurný, P., Koten, P., (2007). Atmospheric deceleration and light curves of Draconid meteors and implications for the structure of cometary dust. *Astronomy & Astrophysics*, 473, 661-672.
- Borovička, J., Štork, R., Boček, J., (1999). First results from video spectroscopy of 1998 Leonid meteors. *Meteoritics & Planetary Science*, 34, 987-994.
- Boyd, I. D., (2000). Computation of atmospheric entry flow about a Leonid meteoroid. *Earth, Moon, and Planets*, 82-83, 93-108.
- Brown, P. G., Assink, J. D., Astiz, L., Blaauw, R., Boslough, M. B., Borovička, J., Brachet, N., Brown, D., Campbell-Brown, M., Ceranna, L., Cooke, W., de Groot-Hedlin, C., Drob, D. P., Edwards, W., Evers, L. G., Garces, M., Gill, J., Hedlin, M., Kingery, A., Laske, G.,

- Le Pichon, A., Mialle, P., Moser, D. E., Saffer, A., Sliber, E., Smets, P., Spalding, R. E., Spurný, P., Tagliaferri, E., Uren, D., Weryk, R., Whitaker, R., Krzeminski, Z., (2013). A 500-kiloton airburst over Chelyabinsk and an enhanced hazard from small impactors. *Nature*, 503, 238-241.
- Brown, P., Ceplecha, Z., Hawkes, R. L., Wetherill, G., Beech, M., Mossman, K., (1994). The orbit and atmospheric trajectory of the Peekskill meteorite from video records. *Nature*, 367, 624-626.
- Brown, P., McCausland, P. J. A., Fries, M., Silber, E., Edwards, W. N., Wong, D. K., Weryk, R. J., Fries, J., Krzeminski, Z., (2011). The fall of the Grimsby meteorite–I: Fireball dynamics and orbit from radar, video, and infrasound records. *Meteoritics & Planetary Science*, 46 (3), 339-363.
- Brown, P., Spalding, R. E., ReVelle, D. O., Tagliaferri, E., Worden, S. P., (2002). The flux of small near-Earth objects colliding with the Earth. *Nature*, 420, 294-296.
- Brown, P., Weryk, R. J., Wong, D. K., Jones, J., (2008). A meteoroid stream survey using the Canadian Meteor Orbit Radar, I. Methodology and radiant catalogue. *Icarus*, 195, 317-339.
- Campbell, M. D., Brown, P. G., LeBlanc, A. G., Hawkes, R. L., Jones, J., Worden, S. P., Correll, R. R., (2000). Image-intensified video results from the 1998 Leonid shower: I. Atmospheric trajectories and physical structure. *Meteoritics & Planetary Science*, 35, 1259-1267.
- Campbell, M., Hawkes, R., Babcock, D., (1999). Light curves of shower meteors: implications for physical structure. In: *Meteoroids 1998*, edited by W. J. Baggaley, V. Porubčan. Bratislava: Astronomical Institute of the Slovak Academy of Sciences. 363-366.
- Campbell-Brown, M. D., (2004). Optical observations of meteors. *Earth, Moon, and Planets*, 95, 521-531.

- Campbell-Brown, M. D., (2008). High resolution radiant distribution and orbits of sporadic radar meteoroids. *Icarus*, 196, 144-163.
- Campbell-Brown, M. D., Borovička, J., Brown, P. G., Stokan, E., (2013). High-resolution modelling of meteoroid ablation. *Astronomy & Astrophysics*, 557, A41, 13pp.
- Campbell-Brown, M., Jones, J., (2003). Determining the initial radius of meteor trains: fragmentation. *Monthly Notices of the Royal Astronomical Society*, 343, 775-780.
- Campbell-Brown, M. D., Jones, J., (2006). Annual variation of sporadic radar meteor rates. *Monthly Notices of the Royal Astronomical Society*, 367, 709-716.
- Campbell-Brown, M. D., Koschny, D., (2004). Model of the ablation of faint meteors. *Astronomy & Astrophysics*, 418, 751-758.
- Campins, H., Swindle, T. D., (1998). Expected characteristics of cometary meteorites. *Meteoritics & Planetary Science*, 33, 1201-1211.
- Ceplecha, Z., (1986). Photographic fireball networks. In: *Asteroids, Comets, Meteors II*, edited by C. I. Lagerqvist, B. A. Lindblad, H. Lundsted, H. Rickman. Reprocentralen HSC, Uppsala University, Sweden. 575-582.
- Ceplecha, Z., Borovička, J., Elford, W. G., ReVelle D. O., Hawkes, R. L., Porubčan, V., Šimek, M., (1998). Meteor phenomena and bodies. *Space Science Reviews*, 84, 327-471.
- Ceplecha, Z., McCrosky, R. E., (1976). Fireball end heights: a diagnostic for the structure of meteoric material. *Journal of Geophysical Research*, 81 (35), 6257-6275.
- Ceplecha, Z., McCrosky, R. E., (1991). Gross-fragmentation of meteoroids and bulk density of Geminids from photographic fireball records. In: *Asteroids, Comets, Meteors 1991*, edited by A. W. Harris, E. Bowell. Houston: Lunar and Planetary Institute. 109-112.
- Ceplecha, Z., Padevět, V., (1961). The beginning of rapid evaporation of meteors of different dimensions. *Bulletin of the Astronomical Institute of Czechoslovakia*, 12 (5), 191-195.

- Ceplecha, Z., ReVelle, D. O., (2005). Fragmentation model of meteoroid motion, mass loss, and radiation in the atmosphere. *Meteoritics & Planetary Science*, 40 (1), 35-54.
- Chyba, C. F., Thomas, P. J., Zahnle, K. J., (1993). The 1908 Tunguska explosion: atmospheric disruption of a stony meteoroid. *Nature*, 361, 40-44.
- Close, S., Oppenheim, M., Hunt, S., Dyrud, L., (2002). Scattering characteristics of high-resolution meteor head echoes detected at multiple frequencies. *Journal of Geophysical Research*, 107 (A10), SIA 9, 12pp.
- Close, S., Oppenheim, M., Hunt, S., Coster, A., (2004). A technique for calculating meteor plasma density and meteoroid mass from radar head echo scattering. *Icarus*, 168, 43-52.
- Close, S., Brown, P., Campbell-Brown, M., Oppenheim, M., Colestock, P., (2007). Meteor head echo radar data: Mass-velocity selection effects. *Icarus*, 186, 547-556.
- Close, S., Hamlin, T., Oppenheim, M., Cox, L., Colestock, P., (2008). Dependence of radar signal strength on frequency and aspect angle of nonspecular meteor trails. *Journal of Geophysical Research*, 113, A06203, 8pp.
- Cook, A. F., Hawkins, G. S., Stienon, F. M., (1962). Meteor trail widths. *The Astronomical Journal*, 67 (3), 158-162.
- de Pater, I., Lissauer, J. J., *Planetary sciences*. Cambridge University Press, 2010.
- Drolshagen, G., Dikarev, V., Landgraf, M., Krag, H., Kuiper, W., (2008). Comparison of meteoroid flux models for near Earth space. *Earth, Moon, and Planets*, 102, 191-197.
- Dyrud, L. P., Oppenheim, M. M., Close, S., Hunt, S., (2002). Interpretation of non-specular radar meteor trails. *Geophysical Research Letters*, 29 (21), 8, 4pp.
- Dyrud, L., Wilson, D., Boerve, S., Trulsen, J., Pecseli, H., Close, S., Chen, C., Lee, Y., (2008). Plasma and electromagnetic wave simulations of meteors. *Advances in Space Research*, 42, 136-142.

Edwards, W. N., Brown, P. G., Weryk, R. J., ReVelle, D. O., (2008). Infrasonic observations of meteoroids: preliminary results from a coordinated optical-radar-infrasound observing campaign. *Earth, Moon, and Planets*, 102, 221-229.

Elford, W. G., (2001). Novel applications of MST radars in meteor studies. *Journal of Atmospheric and Solar-Terrestrial Physics*, 63, 143-153.

Elford, W. G., Campbell, L., (2001). Effect of meteoroid fragmentation on radar observations of meteor trails. In: *Proceedings of the Meteoroids 2001 Conference*, edited by B. Warmbein. ESA SP-495, Noordwijk: ESA Publications Division. 419-423.

Ens, T. A., Brown, P. G., Edwards, W. N., Silber, E. A., (2012). Infrasound production by bolides: a global statistical study. *Journal of Atmospheric and Solar-Terrestrial Physics*, 80, 208-229.

Fisher, A. A., Hawkes, R. L., Murray, I. S., Campbell, M. D., LeBlanc, A. G., (2000). Are meteoroids really dustballs? *Planetary and Space Science*, 48, 911-920.

Greenhow, J. S, Hall, J. E., (1960). The importance of initial trail radius on the apparent height and number distributions of meteor echoes. *Monthly Notices of the Royal Astronomical Society*, 121 (2), 183-197.

Greenhow, J. S, Neufeld, E. L., (1957). The variation of ionization along a meteor trail. *Monthly Notices of the Royal Astronomical Society*, 117 (4), 359-369.

Gural, P. S., Jenniskens, P. M., Varros, G., (2004). Results from the AIM-IT meteor tracking system. *Earth, Moon, and Planets*, 95, 541-552.

Halliday, I., (1973). Photographic fireball networks. In: *Evolutionary and Physical Properties of Meteoroids*, edited by C. L. Hemenway, P. M. Millman, A. F. Cook. National Aeronautics and Space Administration SP 319, 1-8.

Halliday, I., Griffin, A. A., Blackwell, A. T., (1981). The Innisfree meteorite fall: a photographic analysis of fragmentation, dynamics and luminosity. *Meteoritics*, 16 (2), 153-170.

Hapgood, M., Rothwell, P., Royrvik, O., (1982). Two-station television observations of Perseid meteors. *Monthly Notices of the Royal Astronomical Society*, 201, 569-577.

Hawkes, R., Jones, J., (1973). An inexpensive meteor observing system. *The Observatory*, 93, 233-235.

Hawkes, R. L., Jones, J., (1975a). Television observations of faint meteors—I. Mass distribution and diurnal rate variation. *Monthly Notices of the Royal Astronomical Society*, 170, 363-377.

Hawkes, R. L., Jones, J., (1975b). A quantitative model for the ablation of dustball meteors. *Monthly Notices of the Royal Astronomical Society*, 173, 339-356.

Hawkes, R. L., Jones, J., (1978). The effect of rotation on the initial radius of meteor trains. *Monthly Notices of the Royal Astronomical Society*, 185, 727-734.

Hawkes, R. L., Jones, J., (1986). Electro-optical meteor observation techniques and results. *Quarterly Journal of the Royal Astronomical Society*, 27, 569-589.

Hawkes, R. L., Milley, E. P., Ehrman, J. M., Woods, R. M., Hoyland, J. D., Pettipas, C. L., Tokaryk, D. W., (2008). What can we learn about atmospheric meteor ablation and light production from laser ablation? *Earth, Moon, and Planets*, 102, 331-336.

Hawkins G. S., Southworth, R. B., (1958). The statistics of meteors in the Earth's atmosphere. *Smithsonian Contribution to Astrophysics*, 2 (11), 349-364.

Hawkins, G. S., Whipple, F. L., (1958). The width of meteor trails. *The Astronomical Journal*, 63 (1261), 283-291.

Hunt, S. M., Oppenheim, M., Close, S., Brown, P. G., McKeen, F., Minardi, M., (2004). Determination of the meteoroid velocity distribution at the Earth using high-gain radar. *Icarus*, 168, 34-42.

Jacchia, L. G., (1955). The physical theory of meteors. VIII. Fragmentation as a cause of the faint-meteor anomaly. *The Astrophysical Journal*, 121, 521-527.

Jacchia, L. G., Whipple, F. L., (1961). Precision Orbits of 413 Photographic Meteors. *Smithsonian Contributions to Astrophysics*, 4, 97-129.

Janches, D., Dyrud, L. P., Broadley, S. L., Plane, J. M. C., (2009). First observation of micrometeoroid differential ablation in the atmosphere. *Geophysical Research Letters*, 36, L06101, 5pp.

Janches, D., Nolan, M. C., Meisel, D. D., Mathews, J. D., Zhou, Q. H., Moser, D. E., (2003). On the geocentric micrometeor velocity distribution. *Journal of Geophysical Research*, 108 (A6), SIA 1, 14pp.

Janches, D., Plane, J. M. C., Nesvorný, D., Feng, W., Vokrouhlický, D., Nicolls, M. J., (2014). Radar detectability studies of slow and small zodiacal dust cloud particles. I. The case of Arecibo 430 MHz meteor head echo observations. *The Astrophysical Journal*, 796:41, 20pp.

Jenniskens, P., (2004). 2003 EH₁ is the Quadrantid shower parent comet. *The Astronomical Journal*, 127, 3018-3022.

Jenniskens, P., *Meteor showers and their parent comets*. Cambridge University Press, 2006.

Jenniskens, P., Butow, S. J., (1999). The 1998 Leonid multi-instrument aircraft campaign—an early review. *Meteoritics & Planetary Science*, 34, 933-943.

Jenniskens, P., Butow, S. J., Fonda, M., (2000). The 1999 Leonid multi-instrument aircraft campaign—an early review. *Earth, Moon, and Planets*, 82-83, 1-26.

Jenniskens, P., Jehin, E., Cabanac, R. A., Laux, C. O., Boyd, I. D., (2004). Spectroscopic anatomy of a meteor trail cross section with the European Southern Observatory Very Large Telescope. *Meteoritics & Planetary Science*, 39 (4), 609-616.

Jones, J., Brown, P., Ellis, K. J., Webster, A. R., Campbell-Brown, M., Krzeminski, Z., Weryk, R. J., (2005). The Canadian Meteor Orbit Radar: system overview and preliminary results. *Planetary and Space Science*, 53, 413-421.

Jones, J., Campbell-Brown, M., (2005). The initial train radius of sporadic meteors. *Monthly Notices of the Royal Astronomical Society*, 359, 1131-1136.

Jones, J., Hawkes, R. L., (1975). Television observations of faint meteors—II. Light curves. *Monthly Notices of the Royal Astronomical Society*, 171, 159-169.

Jones, J., Webster, A. R., (1991). Visual and radar studies of meteor head echoes. *Planetary and Space Science*, 39, 873-878.

Jones, W., (1995). Theory of the initial radius of meteor trains. *Monthly Notices of the Royal Astronomical Society*, 275, 812-818.

Kaiser, N., Brown, P., Hawkes, R. L., (2004). Optical trail width measurements of faint meteors. *Earth, Moon, and Planets*, 95, 579-586.

Kascheyev, B. L., Lebedinets, V. N., (1963). The initial radius of ionized meteor trails. *Smithsonian Contribution to Astrophysics*, 7, 19-22.

Kikwaya, J.-B., Campbell-Brown, M. D., Brown, P. G., (2011). Bulk density of small meteoroids. *Astronomy & Astrophysics*, 530, A113, 17pp.

Koten, P., Borovička, J., Spurný, P., Betlem, H., Evans, S., (2004). Atmospheric trajectories and light curves of shower meteors. *Astronomy & Astrophysics*, 428, 683-690.

Koten, P., Spurný, P., Borovička, J., Evans, S., Elliott, A., Betlem, H., Štork, R., Jobse, K., (2006). The beginning heights and light curves of high-altitude meteors. *Meteoritics & Planetary Science*, 41 (9), 1305-1320.

Kramer, E. N., (1968). On the structure and chemical composition of meteor bodies of cometary origin. In: *Physics and Dynamics of Meteors*, edited by L. Kresak, P. M. Millman. Dordrecht, D. Reidel, 236-238.

LeBlanc, A. G., Murray, I. S., Hawkes, R. L., Worden, P., Campbell, M. D., Brown, P., Jenniskens, P., Correll, R. R., Montague, T., Babcock, D. D., (2000). Evidence for transverse spread in Leonid meteors. *Monthly Notices of the Royal Astronomical Society*, 313, L9-L13.

Manning, L. A., (1958). The initial radius of meteoric ionization trails. *Journal of Geophysical Research*, 63 (1), 181-196.

Massey, H. S. W., Sida, D. W., (1955). XXIII. Collision processes in meteor trails. *Philosophical Magazine*, 46 (373), 190-198.

Mathews, J. D., (2004). Radio science issues surrounding HF/VHF/UHF radar meteor studies. *Journal of Atmospheric and Solar-Terrestrial Physics*, 66, 285-299.

Mathews, J. D., Briczinski, S. J., Malhotra, A., Cross, J., (2010). Extensive meteoroid fragmentation in V/UHF radar meteor observations at Arecibo Observatory. *Geophysical Research Letters*, 37, L04103, 5pp.

McBride, N., (1997). The importance of the annual meteoroid streams to spacecraft and their detectors. *Advances in Space Research*, 20 (8), 1513-1516.

McBride, N., McDonnell, J. A. M., (1999). Meteoroid impacts on spacecraft: sporadics, streams, and the 1999 Leonids. *Planetary and Space Science*, 47, 1005-1013.

McCrosky, R. E., Ceplecha, Z., (1970). Fireballs and the physical theory of meteors. *Bulletin of the Astronomical Institute of Czechoslovakia*, 21 (5), 271-296.

McIntosh, B. A., (1962). The meteoric head echo. *Journal of Atmospheric and Terrestrial Physics*, 24, 311-315.

McNeil, W. J., Lai, S. T., Murad, E., (1998). Differential ablation of cosmic dust and implications for the relative abundances of atmospheric metals. *Journal of Geophysical Research*, 103 (D9), 10,899-10,911.

Mendis, D. A., Maravilla, D. (2009). A note on the altitude profiles of the electron production in the atmosphere by micrometeoroids entering it at different speeds. *Geophysical Research Letters*, 36, L22804, 6pp.

Mendis, D. A., Wong, W.-H., Rosenberg, M., Sorasio, G., (2005). Micrometeoroid flight in the upper atmosphere: electron emission and charging. *Journal of Atmospheric and Solar-Terrestrial Physics*, 67, 1178-1189.

Milley, E. P., Hawkes, R. L., Ehrman, J. M., (2007). Meteor luminosity simulation through laser ablation of meteorites. *Monthly Notices of the Royal Astronomical Society*, 382, L67-L71.

Murray, I. S., Beech, M., Taylor, M. J., Jenniskens, P., Hawkes, R. L., (2000). Comparison of 1998 and 1998 Leonid light curve morphology and meteoroid structure. *Earth, Moon, and Planets*, 82-83, 351-367.

Murray, I. S., Hawkes, R. L., Jenniskens, P., (1999). Airborne intensified charge-coupled device observations of the 1998 Leonid shower. *Meteoritics & Planetary Science*, 34, 949-958.

Musci, R., Weryk, R. J., Brown, P., Campbell-Brown, M. D., Wiegert, P. A., (2012). An optical survey for millimeter-sized interstellar meteoroids. *The Astrophysical Journal*, 745:161, 6pp.

- Novikov, G. G., Lebedinets, V. N., Blokhin, A. V., (1984). The fragmentation of meteoroids. I. Quasicontinuous fragmentation. *Soviet Astronomy Letters*, 10, 27-29.
- Passey, Q. R., Melosh, H. J., (1980). Effects of atmospheric breakup on crater field formation. *Icarus*, 42, 211-233.
- Pellinen-Wannberg, A., (2005). Meteor head echoes – observations and models. *Annales Geophysicae*, 23, 201-205.
- Pellinen-Wannberg, A., Westman, A., Wannberg, G., Kaila, K., (1998). Meteor fluxes and visual magnitudes from EISCAT radar event rates: a comparison with cross-section based magnitude estimates and optical data. *Annales Geophysicae*, 116, 1475-1485.
- Popova, O., (2005). Meteoroid ablation models. *Earth, Moon, and Planets*, 95, 303-319.
- Popova, O. P., Sidneva, S. N., Shuvalov, V. V., Strelkov, A. S., (2000). Screening of meteoroids by ablation vapor in high-velocity meteors. *Earth, Moon, and Planets*, 82-83, 109-128.
- Poulter, E. M., Baggaley, W. J., (1977). Radiowave scattering from meteoric ionization. *Journal of Atmospheric and Terrestrial Physics*, 39, 757-768.
- ReVelle, D. O., (1976). On meteor-generated infrasound. *Journal of Geophysical Research*, 81 (7), 1217-1230.
- Robertson, M. C., Hawkes, R. L., (1991). Wake in faint television meteors. In: *Asteroids, Comets, Meteors 1991*, edited by A. W. Harris, E. Bowell. Houston: Lunar and Planetary Institute. 517-520.
- Rogers, L. A., Hill, K. A., Hawkes, R. L., (2005). Mass loss due to sputtering and thermal processes in meteoroid ablation. *Planetary and Space Science*, 53, 1341-1354.
- Shadbolt, L., Hawkes, R. L., (1995). Absence of wake in faint television meteors. *Earth, Moon, and Planets*, 68, 493-502.

Silber, E. A., Le Pichon, A., Brown, P. G., (2011). Infrasonic detection of a new-Earth object impact over Indonesia on 8 October 2009. *Geophysical Research Letters*, 38, L11201, 5pp.

Sorasio, G., Mendis, D. A., Rosenberg, M., (2001). The role of thermionic emission in meteor physics. *Planetary and Space Science*, 49, 1257-1264.

Spurný, P., Betlem, H., Jobse, K., Koten, P., van't Leven, J., (2000). New type of radiation of bright Leonid meteors above 130 km. *Meteoritics & Planetary Science*, 35, 1109-1115.

Spurný, P., Ceplecha, Z., (2008). Is electric charge separation the main process for kinetic energy transformation into the meteor phenomenon? *Astronomy & Astrophysics*, 489, 449-454.

Steel, D. I., Elford, W. G., (1991). The height distribution of radio meteors: comparison of observations at different frequencies on the basis of standard echo theory. *Journal of Atmospheric and Terrestrial Physics*, 53 (5), 409-417.

Stenbaek-Nielsen, H. C., Jenniskens, P., (2004). A “shocking” Leonid meteor at 1000 fps. *Advances in Space Research*, 33, 1459-1465.

Tóth, J., Klačka, J., (2004). Fragmentation of Leonids in space and a model of spatial distribution of meteoroids within the Leonid stream. *Earth, Moon, and Planets*, 95, 181-186.

Verniani, F., (1973). An analysis of the physical parameters of 5759 faint radio meteors. *Journal of Geophysical Research*, 78 (35), 8429-8462.

Vinković, D., (2007). Thermalization of sputtered particles as the source of diffuse radiation from high altitude meteors. *Advances in Space Research*, 39, 574-582.

Vondrak, T., Plane, J. M. C., Broadley, S., Janches, D., (2008). A chemical model of meteoric ablation. *Atmospheric Chemistry and Physics*, 8, 7015-7031.

Watanabe, J., Tabe, I., Hasegawa, H., Hashimoto, T., Fuse, T., Yoshikawa, M., Abe, S., Suzuki, B., (2003). Meteoroid clusters in Leonids: evidence of fragmentation in space. *Publications of the Astronomical Society of Japan*, 55 (3), L23-L26.

Weryk, R. J., Brown, P. G., (2013). Simultaneous radar and video meteors—II: Photometry and ionisation. *Planetary and Space Science*, 81, 32-47.

Weryk, R. J., Campbell-Brown, M. D., Wiegert, P. A., Brown, P. G., Krzeminski, Z., Musci, R., (2013). The Canadian Automated Meteor Observatory (CAMO): System overview. *Icarus*, 225, 614-622.

Whipple, F. L., (1938). Photographic meteor studies. *Proceedings of the American Philosophical Society*, 79 (4), 499-548.

Whipple, F. L., (1951). The Baker super-Schmidt meteor cameras. *The Astronomical Journal*, 56 (1193), 144-145.

Whipple, F. L., (1954). Photographic meteor orbits and their distribution in space. *The Astronomical Journal*, 59 (6), 201-217.

Wiegert, P., Vaubaillon, J., Campbell-Brown, M., (2009). A dynamical model of the sporadic meteoroid complex. *Icarus*, 201, 295-310.

Chapter 2

Observations and reductions

2.1 The Canadian Automated Meteor Observatory

The Canadian Automated Meteor Observatory (CAMO) is a two-station, automated, intensified-video system for the observation of faint meteors. One goal of CAMO is to provide simultaneous observations of meteors captured with the Canadian Meteor Orbit Radar (CMOR). This allows for investigation of radar biases, such as attenuation of trail echoes resulting from trail widths that are at least as large as the radar wavelength, as well as better understanding of the formation and diffusion of the ion trail (Weryk & Brown 2012). CAMO also observes meteors at resolutions up to 3 m per pixel, allowing for analysis of the length and width of the wake of meteors, and providing new constraints for models of meteoroid ablation. Meteoroid fragmentation may be observed directly, and the strength of the meteoroid may be subsequently calculated with models. Since the system has two stations, trajectory solutions and orbits are computed for each meteor.

All of the meteors that were analysed in this work were observed using CAMO. Details of the system and the reduction procedure for observations will now be discussed. A complete overview of the system is available in Weryk et al. (2013).



Figure 2.1: A map of southern Ontario, Canada, showing the locations of the two CAMO stations. Tavistock is marked as 1, while Elginfield is 2. Map provided by Google.

2.1.1 Hardware

One of the CAMO stations is co-located with CMOR at Tavistock, Ontario (43.265°N , 80.772°W), while the other is housed at Elginfield Observatory in Middlesex Centre, Ontario (43.193°N , 81.316°W) Canada. The locations of both stations, separated by a baseline of 45 km, are illustrated in Figure 2.1. Each station contains three cameras, which form the *guided* (or *tracking*) and *influx* systems.

The guided system is comprised of one wide-field (28° field of view) and one narrow-field (1.5° FOV) camera. The large field of view for the wide-field camera allows most meteor light curves to be observed completely, and meteoroid trajectories to be computed. Metre-scale observations of meteor morphology and fragmentation are recorded by the narrow-field camera, which smoothly tracks the meteor in real time. For the influx system, a single wide-field camera (20° FOV) provides observations for calculation of high-precision light curves, trajectories, and orbits. A comparison of the video recorded by each camera is given in Figure 2.2. The majority of meteors analysed in this project were observed with the guided system.

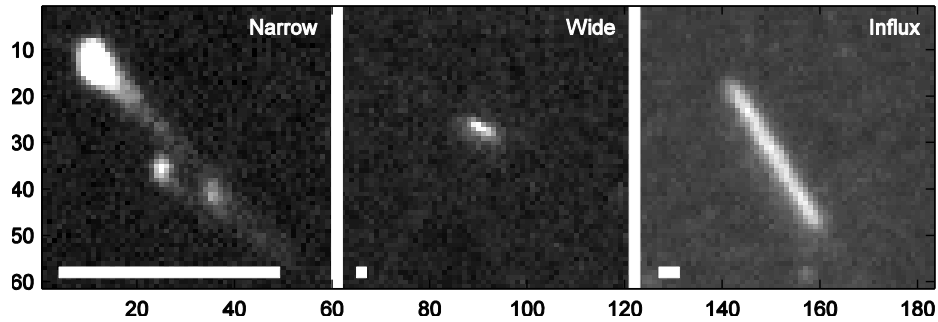


Figure 2.2: The same meteor (20101010_023500) observed by the narrow-field, wide-field, and influx cameras. In each frame, the meteor is travelling towards the top left. Gross fragmentation is uniquely visible in the narrow-field frame. The long trail in the influx frame is due to the relatively long exposure time (~ 0.05 s) compared to the other cameras (~ 0.01 s). A scale bar indicating approximately 180 m is placed at the bottom of each frame.

For the guided system, Imperx IPX-VGA120L cameras are used for the narrow- and wide-field applications, lens-coupled to 18 mm ITT NiteCam 380i third-generation image intensifiers. The cameras have a resolution of 640×480 pixels with an image depth of 12-bits per pixel to limit saturation from brighter events. A 25 mm $f/0.85$ lens is used for the wide-field camera, while the narrow-field camera is attached to a 545 mm $f/11$ (effective) refracting telescope. To track the meteor in flight, galvanometers rotate two mirrors on orthogonal axes, which continuously directs meteor light into the fixed telescope. The galvanometers are programmed to track the meteor using a polynomial fit to the meteoroid trajectory observed with the wide-field system, which will be discussed in Section 2.1.2. The wide-field camera captures between 60 and 80 frames per second, while the narrow-field captures 110 frames per second to show instantaneous meteor morphology. The angle subtended by a pixel is approximately $6.6''$ and $140''$ for the narrow- and wide-field cameras, producing an image scale of 4.3 and 92 m per pixel at a range of 135 km.

The influx system uses a Cooke PCO.1600 camera coupled to a third-generation ITT intensifier. Initially, an 18 mm diameter intensifier, the same as used for the cameras of the guided system, was used for the influx system, but this was upgraded to a 25 mm device in November 2011. This upgrade increased the recorded video frame size to 1600×1200 from 1024×1024 .

A 50 mm $f/0.95$ lens gives a pixel scale of $71''$, or 46 m per pixel at 135 km. The influx cameras record at 20 frames per second, with an image depth of 14-bits.

Since pixels of the influx system subtend about half of the angle of pixels in the guided system's wide-field camera, the influx system produces higher precision meteoroid trajectories, speeds, and orbits. Similarly, greater dynamic range resulting from the 14-bit image depth allows for the computation of light curves with greater precision than the tracked system. The main disadvantage is the influx system's low frame rate compared to the guided system; consequently, since trajectories and light curves are calculated based on user picks for the meteoroid position and meteor brightness in each frame, respectively (discussed in Section 2.2), uncertainty in the reductions from influx system observations is increased. Ultimately, the majority of the trajectories and light curves computed for the meteors analysed in this thesis were based on observations from the guided system's wide-field cameras, rather than the cameras of the influx system. This is because the influx system did not capture all of the meteors recorded with the guided system, as the collecting volumes for both systems do not completely overlap.¹

The limiting stellar magnitude for the wide-field, narrow-field, and influx cameras are +7.5, +7, and +8.5, respectively. The faintest meteors that can be observed with each camera are approximately two magnitudes brighter than the limiting stellar magnitude, since meteors spread their light over several pixels as they move across the field of view. The spectral response of the system corresponds best to the Johnson-Cousins R-band, as seen in Figure 2.3. As a result, all photometric calibrations (which will be discussed in Section 2.2) are done with respect to the R-band.

All three of the cameras are enclosed inside a small shed with an automated roof. The roof retracts, revealing the cameras, if ambient temperature, wind, and visibility conditions are met. A small external camera gives an indication of sky conditions by monitoring the relative magnitude of Polaris, while a weather station provides information on wind speed, outside temperature, and humidity. For additional protection, the guided cameras and telescope are

¹The collecting volume is the volume in the sky where cameras from both stations have overlapping fields of view. Meteors inside the collecting volume are observed with both stations, a requirement for a trajectory solution.

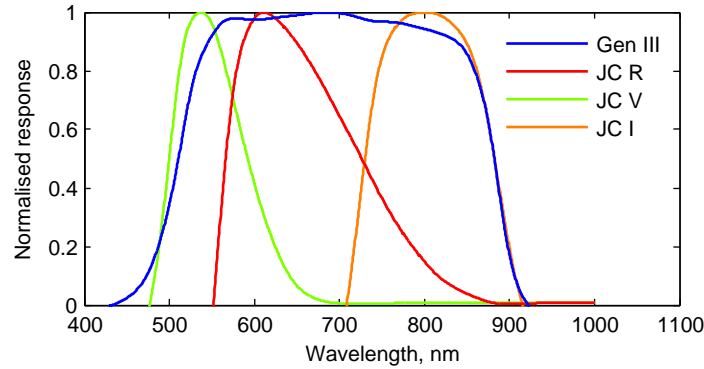


Figure 2.3: Spectral response of CAMO Gen III intensifiers, as well as Johnson-Cousins R, V, I bands.

located in a small, temperature-controlled enclosure. The CAMO shed, enclosure, and cameras are shown in Figure 2.4.

Camera video is streamed to hard disk using digital video frame-grabbers, and stored in uncompressed form. Time information for each frame is provided by GPS receivers, ensuring that video from each camera from both stations is synchronised. In practise, there is a small amount of delay between timestamps from the influx and tracking systems, likely related to different amounts of video data streamed per frame (the influx system records at 1600×1200 , while the tracking system records at 640×480) since there is negligible delay between the cameras of the tracking system. The delay is typically about one frame in the influx system (~ 0.05 s) and is quantified by comparing solutions of the same meteor from both systems.

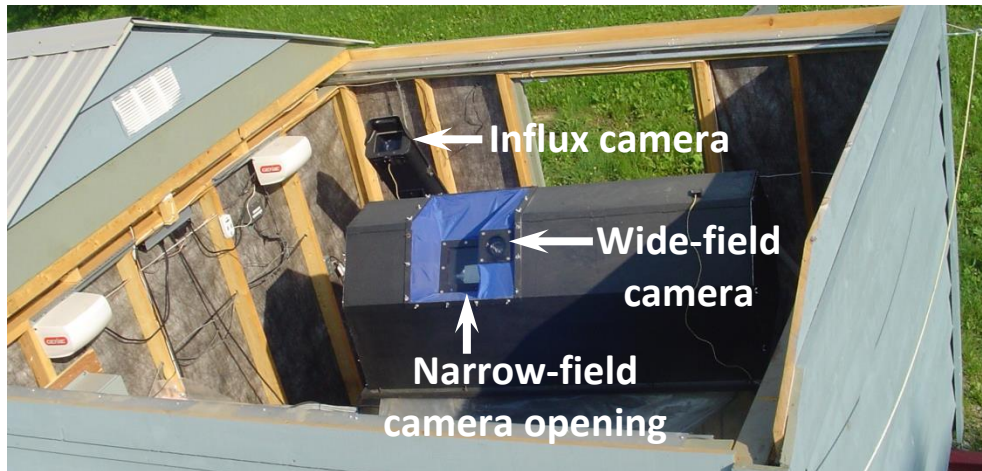
Specifications for the CAMO system are summarised in Table 2.1.

2.1.2 Software

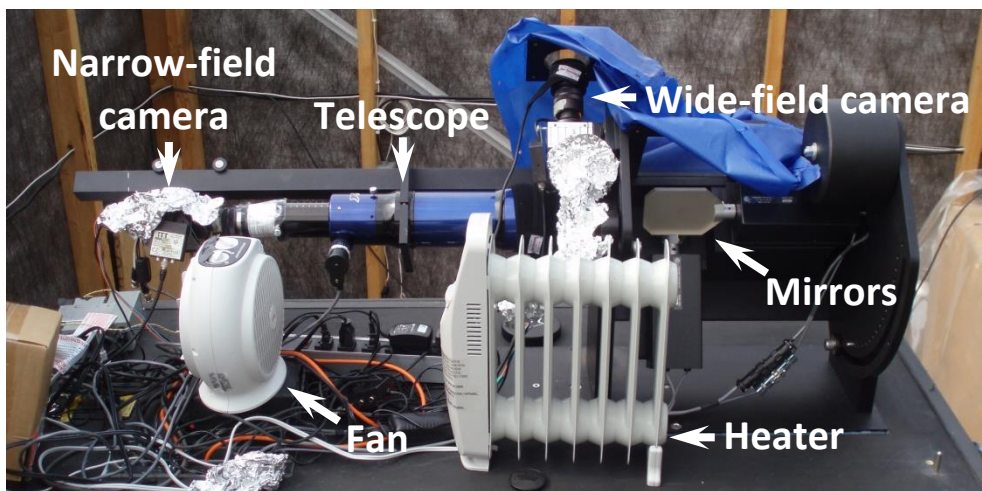
The software package ASGARD (Weryk et al. 2008) detects meteors recorded by the guided system’s wide-field camera in real time. The goal of real-time automated meteor detection is to cut the video recorded over the entire night into segments that show individual meteors, and also to allow the guided narrow-field cameras to track the meteor. Automated reductions, giving a rough trajectory and light curve of each observed meteor, are also prepared. Meteors are



(a) Shed



(b) Shed with roof open, showing cameras and enclosure



(c) Wide- and narrow-field cameras with enclosure removed

Figure 2.4: Photographs of the CAMO shed (a), enclosure (b), and cameras (c).

Table 2.1: Summary for each of the cameras in the CAMO system. The narrow-field camera's fine spatial resolution (4.4 m per pixel at a range of 135 km), high frame rate, and automatic tracking of the meteor allow for detailed study of meteor morphology, while the wide-field and influx cameras are used to capture meteor light curves and calculate meteoroid trajectories and orbits.

	Narrow-field	Wide-field	Influx
Pixel scale	6.7''	146''	71''
Pixel scale at 135 km	4.4 m	96 m	46 m
Video resolution	640 × 480	640 × 480	1600 × 1200
Field of view	1.5°	28°	21°
Frame rate	80 – 110 s ⁻¹	60 – 110 s ⁻¹	20 s ⁻¹
Image depth	12-bit	12-bit	14-bit
Limiting mag. (meteor)	+5	+5	+7.5

detected by examining each recorded wide-field frame for groups of pixels that are persistently brighter than the background brightness. The meteor detection and tracking process will now be discussed, and additional details are given in Weryk et al. (2008, 2013).

First, the background brightness in the wide-field video is quantified by computing each pixel's mean and standard deviation in brightness over several frames. A low pass filter is applied for each pixel to reduce the effect of noise, particularly instantaneous bright spots that occur in a single frame due to thermal oscillations in the image intensifier. The low pass filtered value of a pixel in frame n is

$$y_n = x_n + (y_{n-1} - x_n) \exp\left(-\frac{2\pi f_c}{f_s}\right), \quad (2.1)$$

where x_n is the unfiltered pixel brightness in frame n , f_c is the smoothing frequency, and f_s is the camera frame rate.² Alternately, Eq. (2.1) can be understood as a weighted mean of all of the previous pixel values x_n since recording was started (K frames back),

$$y_n = \frac{\sum_{k=0}^K w_k x_{n-k}}{\sum_{k=0}^K w_k}, \quad (2.2)$$

²The smoothing frequency is a time-based weighting for pixel values: pixel values from a time interval at least $1/2\pi f_c$ before the current frame have their weighting reduced by more than $\exp(-1)$.

with weighting factor

$$w_k = \exp\left(-\frac{2\pi k f_c}{f_s}\right). \quad (2.3)$$

This filter reduces the effect of noise in causing spurious meteor detections.

To detect meteors, the locations of any pixels that are above a brightness threshold (set at five standard deviations above the mean background) are logged. The frame is broken into 8×8 pixel tiles, and any tiles that show at least six pixels with brightness above the threshold are considered as a possible meteor detection. If four consecutive frames show detections within a 16-pixel radius, the detections are counted as a meteor. Alternately, if a new detection is within a 16-pixel radius of a detection in a previous meteor detection (having detections in at least four consecutive previous frames) in a non-consecutive frame, then the new detection is counted as part of the previous meteor. This allows a meteor to still be tracked even if noise causes a single spurious detection elsewhere in the frame.

In practise, these parameters allow the software to automatically detect approximately two thirds of meteors over the course of an evening. This fraction may be increased by lowering the meteor detection threshold (from five standard deviations above the mean background brightness), but these fainter events tend to be tracked poorly with the narrow-field camera. When a meteor is detected, video from the narrow- and wide-field cameras is cut into a short segment (typically 2 - 5 s) around the meteor detection to allow for convenient data analysis.

To track meteors with the narrow-field camera, a linear fit is prepared for the position of the meteor as a function of time, using data from the first seven frames captured with the wide-field camera. The *guide plate*, a relationship between the pixel location of a portion of the sky captured in the wide-field camera and the mirror orientation required to point the narrow-field camera at the same portion of the sky, is used to continuously aim the mirrors at the meteor, directing light into the narrow-field camera. Since the galvanometers are updated at a rate of 2000 Hz, and have a slew rate of 2000° per second, most meteors are tracked smoothly and appear stationary in the narrow-field video. Unfortunately, as the first seven frames are used to compute a fit to track the meteor, the onset of intensive ablation is not recorded in narrow-field

videos. Also, if the fit to the meteor motion is inaccurate, which can result from spurious picks in the meteor location due to noise, the meteor may appear to move around in the narrow-field video, which causes image smearing. Improper tracking may also result if the guide plate is inaccurate, which can occur if the cameras are moved slightly during system maintenance.

To generate a guide plate, a mosaic image of the wide-field camera's field of view is constructed using the narrow-field camera. The mirrors are scanned across their entire range of motion in 1° increments. At each increment, 24 frames are recorded by the narrow-field camera and averaged. These images are then stitched together to create the mosaic image. Stars in the mosaic image are cross-referenced with those in wide-field image by the user. These star pairs are then used to generate the guide plate (an affine mapping, allowing translation, scaling, and rotation) linking mirror pointing and pixel location in the wide-field camera.

ASGARD also reduces CAMO events automatically without user intervention, computing meteoroid trajectory, orbit, and the meteor light curve. The pixel location of the meteor in the video from each station's wide field camera is converted to local zenith and azimuth coordinates using an *astrometric plate*, which is manually created and will be discussed in Section 2.2. The meteoroid trajectory is then determined using MILIG (Borovička 1990), which computes a line of best fit to the meteoroid positions observed from both stations using iterative non-linear least squares fitting. The orbit is calculated using the methods of Ceplecha (1987), and the light curve is derived from the sum of the brightness for the pixels comprising the meteor. These procedures will be discussed in more detail in the next section. The automated reductions provide a good first look into a meteoroid's trajectory, but have large uncertainties related to spurious picks for the meteoroid position due to noise, so all reductions for meteors analysed in this thesis were performed manually.

2.2 Reduction of meteor video

The software package METAL (Weryk & Brown 2012, 2013) provides a convenient user interface to analyse recorded meteors and was used to calculate the trajectory and light curve for all of the meteors observed in this thesis. The reduction procedure performed for each event will now be described.

2.2.1 Astrometry

As noted earlier, the iterative solver MILIG (Borovička 1990) is used to compute the meteoroid trajectory. The first approximation of the trajectory is calculated as the line of intersection between two planes, each containing one of the stations, and defined by vectors leading from the station to the meteor starting and ending points. This situation is sketched in Figure 2.5. This solution is later refined by considering the position of the meteor in each of the frames of the video from each station, rather than just the beginning and end points. First, however, the pixel position of the meteor the video from each wide-field camera must be converted to local horizontal coordinates (zenith and azimuth angle) for each station. This is done by creating an astrometric plate for each station in METAL, with the following procedure:

1. Stars in the narrow-field video are selected by the user, giving their pixel location (x, y) .
2. The celestial coordinates of each star are then referenced from the SKY2000 Master Catalogue, Version 4 (Myers et al. 2002) and converted to local zenith and azimuth coordinates (θ, ϕ) for the selected station.
3. The zenith and azimuth coordinates are projected onto a flat plane representing the camera's field of view, giving coordinates (p, q) for comparison with the pixel location, as illustrated in Figure 2.6.

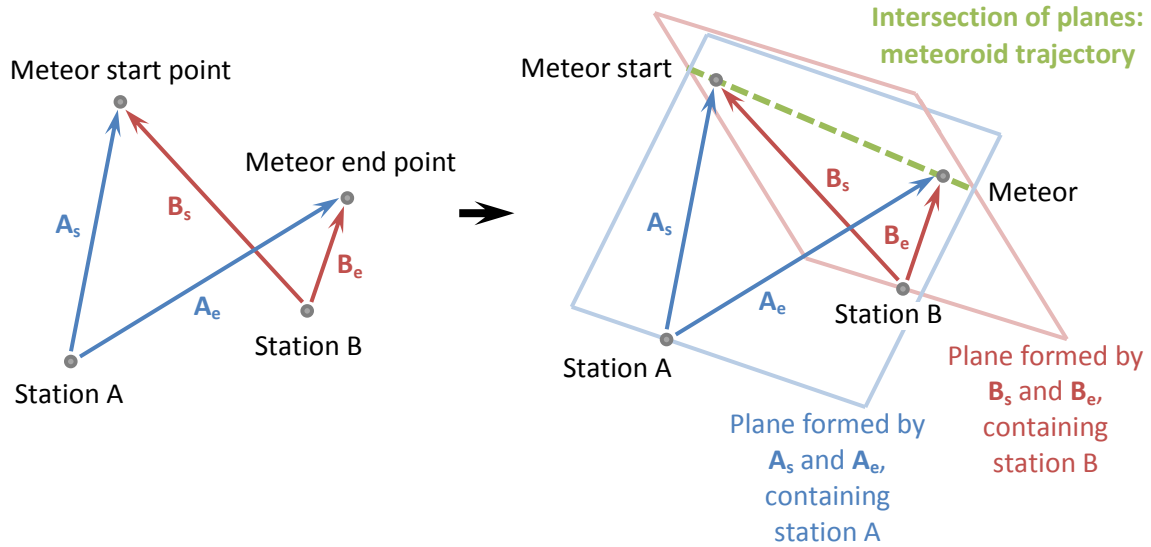


Figure 2.5: Two station observations of a meteor's start and end point, used to derive the meteoroid trajectory. Vectors A_s and A_e lead from station A to the starting and ending point of the meteor, respectively, while B_s and B_e are the corresponding vectors for station B. Vectors A_s and A_e and the location of station A define a plane, while B_s , B_e , and the location of station B define another. The intersection of these two planes gives a first approximation for the meteoroid trajectory.

4. A third order fit relating projection coordinates (p, q) to pixel coordinates (x, y) ,

$$p(x, y) = p_0 + p_1x + p_2y + p_3x^2 + p_4xy + p_5y^2 + p_6x^3 + p_7x^2y + p_8xy^2 + p_9y^3, \quad (2.4)$$

(and similarly for $q(x, y)$) is then calculated. This is the astrometric plate, which allows the pixel position of the meteor to be converted to local zenith and azimuth for each station, necessary for a trajectory solution with MILIG. As there are ten coefficients in the expressions for $p(x, y)$ and $q(x, y)$, at least ten stars must be selected, though in practise at least twenty stars were selected to create the plates for analysis of data in this thesis.

To refine the initial trajectory solution calculated by the intersection of planes, the distance between the observed position of the meteoroid and the corresponding meteoroid position given by the trajectory solution is calculated for each frame, called the *residual*. This is illustrated in

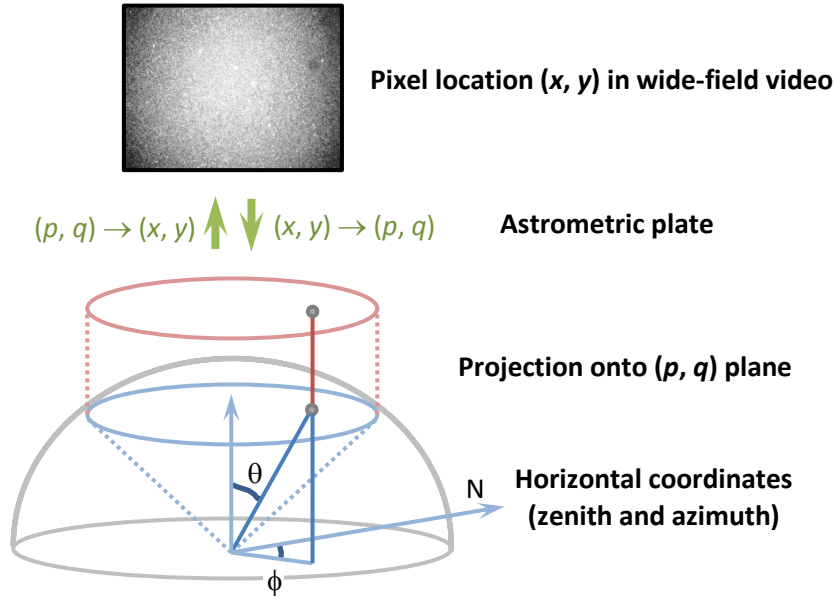


Figure 2.6: Diagram showing the process of deriving the astrometric plate. The zenith and azimuth coordinates (θ, ϕ) of a star observed at pixel (x, y) in the wide-field video are projected onto a flat plane, giving (p, q) coordinates. The astrometric plate is a relationship between (x, y) and (p, q) (and thus, θ and ϕ), required to specify the location of the meteoroid in the sky for computation of the trajectory.

Figure 2.7. The goal is to fit all of the observed positions best by minimising the sum of the squared residuals. Station A is located at $\mathbf{R}_A = [X_A, Y_A, Z_A]$, while the meteoroid's position at time t_i given by trajectory fit is $\mathbf{R}_m = [X_m, Y_m, Z_m]$. The vector leading to the meteoroid's actual observed position at time t_i from station A is called $\mathbf{V}_i = \mu[\xi_i, \eta_i, \zeta_i]$, while the vector leading to the meteoroid's position given by the trajectory fit at the same time is $\mathbf{V}_m = \mathbf{R}_m - \mathbf{R}_A$. Finally, the vector leading from the starting point of the meteor along the trajectory fit is called the radiant vector, $\mathbf{U}_R = [\xi_R, \eta_R, \zeta_R]$.

If the position of the meteor is perfectly represented by the trajectory fit, then $\mathbf{V}_m = \mathbf{V}_i$, and the meteor appears to overlap (or lie on) the calculated trajectory from the perspective of the narrow-field camera. The cross product $\mathbf{U}_R \times \mathbf{V}_i$ gives a vector that is perpendicular to the motion of the meteor in the plane of the frame, while $\mathbf{V}_i \times (\mathbf{U}_R \times \mathbf{V}_i)$ gives a vector along the motion of the meteor in the frame. If the computed trajectory does not pass through the observed meteor position, the residual in both of these components, $D_{i,\text{perp}}$ and $D_{i,\text{para}}$, may be

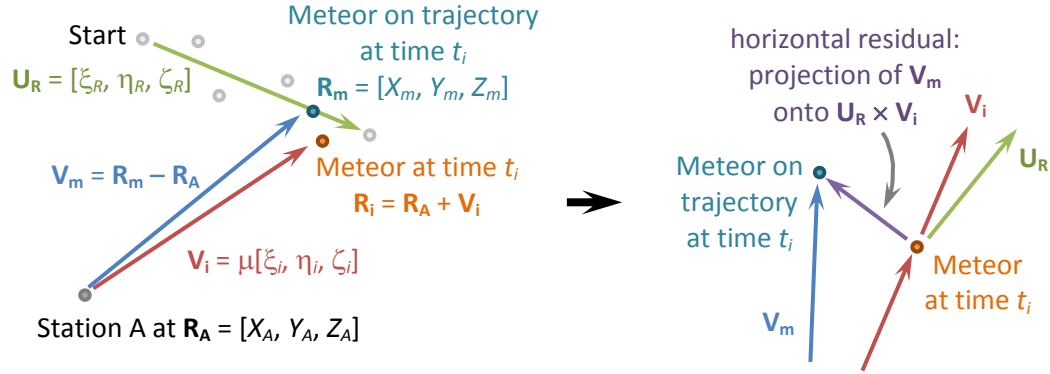


Figure 2.7: Diagram showing the vectors required to calculate the residual between the observed and fit position of the meteor.

calculated by taking the projection of \mathbf{V}_m onto these two vectors,

$$D_{i,\text{perp}} = \frac{\mathbf{V}_m \cdot (\mathbf{U}_R \times \mathbf{V}_i)}{|\mathbf{U}_R \times \mathbf{V}_i|}, \quad (2.5)$$

and

$$D_{i,\text{para}} = \frac{\mathbf{V}_m \cdot (\mathbf{V}_i \times \mathbf{U}_R \times \mathbf{V}_i)}{|\mathbf{V}_i \times \mathbf{U}_R \times \mathbf{V}_i|}. \quad (2.6)$$

The sum of the squared residuals for each frame is found, $D^2 = \sum (D_{i,\text{perp}}^2 + D_{i,\text{para}}^2)$, and minimised using the gradient method, which varies the free parameters X_m, Y_m, Z_m and ξ_R, η_R, ζ_R describing the position and velocity of the meteoroid, respectively. Additional information regarding calculation of the trajectory with MILIG is available in Ceplecha (1987) and Borovička (1990).

There are two main contributions to the uncertainty in the calculated meteoroid trajectory: the uncertainty in the astrometric plate, and more significantly, the uncertainty in the position picks for the meteor in each frame of the video. To quantify the uncertainty related to the position picks, a Monte Carlo approach is used, adding a random, Gaussian-distributed variation to the pixel position of the meteor in each video frame. A systematic deviation in the pixel position is also applied over all frames. The random and systematic offset in position models the subjectivity in having users select the position of the meteor, which is spread out over several

pixels (see Figure 2.2), in all frames of the wide-field video. One thousand sets of meteor position picks with simulated offsets are processed with MILIG, each giving a separate trajectory solution. The position and height of the meteoroid for each frame, as well as the range between the stations and the meteoroid, are then computed as mean values across the thousand trials, while the associated standard deviations give the uncertainties.

Meteoroid orbits are then calculated using the method of Ceplecha (1987). The meteoroid velocity computed with MILIG is corrected for the rotation of the Earth (diurnal aberration) as well as the gravitational attraction of the Earth (zenithal attraction). The heliocentric velocity of the meteoroid is calculated by subtracting the Earth's orbital velocity from the corrected geocentric velocity of the meteoroid. Orbital parameters, such as the semi-major axis, eccentricity, and inclination are then calculated. These describe the current, or osculating, orbit of the meteoroid and are used to indicate (via the Tisserand parameter, an orbital invariant introduced in Chapter 1) whether the meteoroid is associated with an asteroidal or cometary parent body.

2.2.2 Photometry

Quantifying the brightness, or absolute magnitude, of the meteor in each frame of the recorded wide-field video is done through comparison of the brightness of the meteor and stars in the field of view. First, a flat is applied to each frame of the video to correct for differences in the relative sensitivity of each pixel. This is shown in Figure 2.8. Traditionally, a flat is prepared by subjecting the camera to a source of uniform brightness and recording the output. As it is difficult to disassemble the guided system to apply a uniform source in the laboratory, a flat is prepared in-situ each night by taking a stack of frames recorded over the entire night and calculating the median value for each pixel. Since stars and other bright objects move across the field of view, this median combined image approximates the response when viewing a uniformly dark source. This flat is then applied for photometric analysis of all meteors recorded over that night.

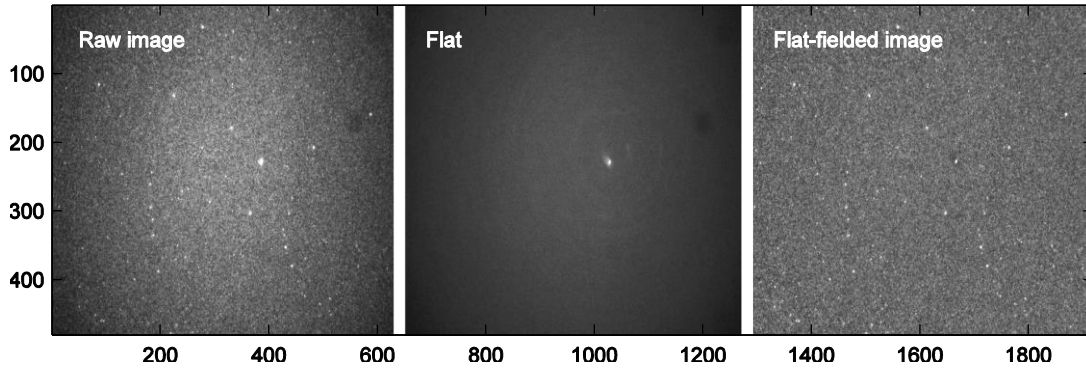


Figure 2.8: An example of a wide-field frame being flat-fielded. On the left is a frame captured by the wide-field camera, while the centre shows the median combine of all frames captured over that night. The right shows the flat-fielded frame, with more uniform brightness across the field of view. The group of bright pixels near the centre of the flat is due to Polaris, which is nearly stationary in this camera’s field of view over the night. Also, a dark spot on the right side of the raw image is corrected in the flat-fielded image.

Once the flat has been applied to the video, a *photometric plate* is prepared by comparing the observed pixel brightness of stars to their catalogue (SKY2000 Version 4, Myers et al. 2002) R-band magnitudes. An instrumental magnitude is calculated for each star in the wide-field video by taking the logarithm of the brightness sum of the pixels comprising the star,

$$M_{\text{ins}} = -\frac{5}{2} \log_{10} \sum_{x,y} p(x,y), \quad (2.7)$$

where the brightness of the pixel at (x,y) is given by $p(x,y)$. The instrumental magnitude for each star is then plotted versus the catalogue magnitude, and a linear regression is performed. The slope of the line of best fit is unity, since magnitudes are being plotted on both axes, but the vertical intercept of the line of best fit, or the *photometric offset*, is recorded, and is used to convert instrumental magnitude of a meteor to its R-band magnitude. A sample photometric plate is illustrated in Figure 2.9.

Apparent meteor magnitudes are determined by selecting all of the pixels containing the meteor in each frame of the video, computing instrumental magnitudes with Eq. (2.7), and converting the resulting instrumental magnitudes to R-band apparent magnitudes, m_R , using

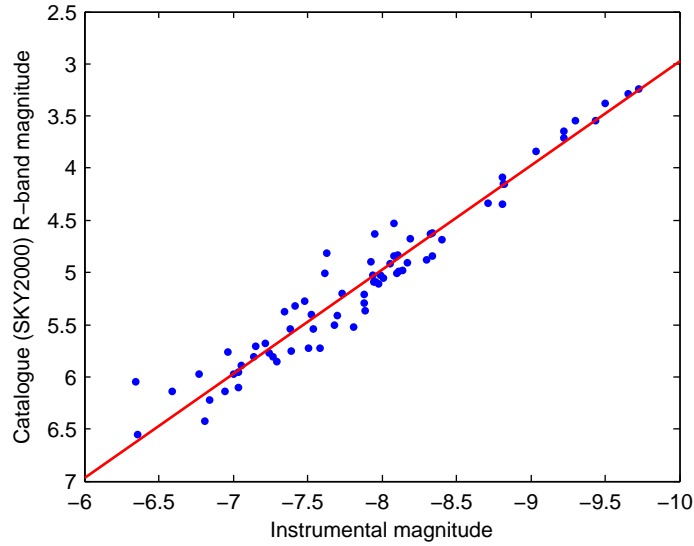


Figure 2.9: Sample photometric plate for the Elginfield wide-field camera on October 20, 2010. The catalogue (SKY2000) R-band magnitudes of a number of stars visible with the wide-field camera have been plotted as a function of their instrumental magnitudes, given by Eq. (2.7). The photometric offset is 12.97 ± 0.09 for this date, given by the vertical intercept of the line of best fit.

the photometric offset, β ,

$$m_R = M_{\text{ins}} + \beta. \quad (2.8)$$

Absolute magnitudes, M_R , are later obtained by correcting the observed magnitude to a range of 100 km using instantaneous range to the meteoroid, r , in each frame from the MILIG trajectory solution.

$$M_R = m_R + 5 \log_{10} \left(\frac{100 \text{ km}}{r} \right). \quad (2.9)$$

Bibliography

Borovička, J., (1990). The comparison of two methods of determining meteor trajectories from photographs. *Bulletin of the Astronomical Institutes of Czechoslovakia*, 41, 391-396.

Ceplecha, Z., (1987). Geometric, dynamic, orbital, and photometric data on meteoroids from photographic fireball networks. *Bulletin of the Astronomical Institutes of Czechoslovakia*, 38, 222-234.

Myers, J. R., Sande, C. B., Miller, A. C., Warren, W. H., Jr., Tracewell, D. A., (2002). SKY2000 Master Catalog, Version 4. Goddard Space Flight Center, Flight Dynamics Division, V/109.

Weryk, R. J., Brown, P. G., (2012). Simultaneous radar and video meteors-I: Metric comparisons. *Planetary and Space Science*, 62, 132-152.

Weryk, R. J., Brown, P. G., (2013). Simultaneous radar and video meteors-II: Photometry and ionisation. *Planetary and Space Science*, 81, 32-47.

Weryk, R. J., Brown, P. G., Domokos, A., Edwards, W. N., Krzeminski, Z., Nudds, S. H., Welch, D. L., (2008). The Southern Ontario All-sky Meteor Camera Network. *Earth, Moon and Planets*, 102, 241-246.

Weryk, R. J., Campbell-Brown, M. D., Wiegert, P. A., Brown, P. G., Krzeminski, Z., Musci, R., (2013). The Canadian Automated Meteor Observatory (CAMO): System overview. *Icarus*, 225, 614-622.

Chapter 3

Measurement of the trail widths of faint meteors

A version of this chapter has been published as:

- Stokan, E., Campbell-Brown, M. D., Brown, P. G., Hawkes, R. L., Doubova, M., Weryk, R. J., (2013). *Optical trail widths of faint meteors observed with the Canadian Automated Meteor Observatory*. Monthly Notices of the Royal Astronomical Society, 433 (2), 962-975.

3.1 Introduction

3.1.1 The importance of meteor trail widths

When a meteoroid enters the atmosphere, it begins to rapidly ablate. Atoms are ejected from the meteoroid and collide with ambient atmospheric atoms at large relative speeds. A region of excited atoms and ions is thus formed almost instantaneously around the meteoroid, producing a visible meteor and leaving a trail of charged particles that can be observed with radar systems. Radar observations of meteors quantify the meteoroid flux to the Earth (Campbell-Brown &

Jones 2006) as a function of meteoroid mass (Close et al. 2007), as well as the relationship between meteoroid velocity, ion trail radius, and meteor beginning and ending heights (Greenhow & Hall 1960). As the amplitude of the returned radar signal from a meteor echo depends on the width and distribution of the ions and electrons in the trail, it is essential to quantify the initial trail radius of a meteor to calculate correct meteoroid masses and determine observation biases. Assuming a Gaussian radial distribution for ions in the meteor trail, the amplitude of the returned signal, A_0 , is attenuated to A_i as a function of the initial ion trail radius, r_i , and the signal wavelength, λ for underdense echoes

$$A_i(\lambda, r_i) = A_0 \exp \left[- \left(\frac{2\pi r_i}{\lambda} \right)^2 \right]. \quad (3.1)$$

For example, the reflected signal from a 29 MHz radar, with a wavelength of approximately 10 m, is attenuated by a factor of ten for an initial ion trail radius of 2.5 m. Fast and faint meteors occurring high in the atmosphere, where the trail radius is expected to be largest, are thus not detected as effectively as other meteors. An optical survey of trail widths can help to quantify the finite initial ion trail radii, although the ion trail is expected to be narrower than the visible trail by virtue of larger collisional cross sections for ions versus atoms (Phelps 1991), as well as lower energy requirement to excite versus ionize an atom.

Studying the optical trail widths and morphology of meteors is also important in understanding the meteoroid ablation process for small meteoroids, $m \leq 10^{-3}$ kg, in the rarefied atmosphere above 100 km. A trail width on the order of the atmospheric mean free path may be explained by collisions of excited particles, which emit light, while a wider trail may have resulted from other processes, such as fragmentation (Hawkes & Jones 1978, Campbell-Brown & Jones 2003), or radiative transfer (Jenniskens 2004, Stenbaek-Nielsen & Jenniskens 2004). The ablation of faint meteoroids high in the atmosphere is poorly understood due to the high velocity of the meteoroid, typically around 70 km s^{-1} , and the low density of the atmosphere above 100 km. Knowledge of trail widths serve as the foundation for high-resolution models

of ablation, such as direct simulation Monte Carlo (Boyd 2000), and plasma-based simulations (Oppenheim et al. 2008, Dyrud et al. 2008). Despite its importance, few measurements of meteor trail widths have been made.

3.1.2 Previous studies of optical and ion trail widths

Previous optical studies of meteor trails have been limited by the simultaneous requirements of high spatial resolution, sensitivity to faint (magnitude $\sim +5$) meteors, and large collecting area. Most studies have been able to achieve only two of the three requirements at once. Multiple-wavelength radar studies of the trails of faint meteors have produced estimates of the ion trail width, but are not directly comparable to the optical trail width. A review of optical and ion trail studies in chronological order is now presented to provide a context for this current study.

The earliest optical survey of meteor trail widths, by Hawkins & Whipple (1958), made use of the 48-inch Schmidt camera at Mount Palomar observatory. This was a single-station, large-aperture, photographic system that captured meteor trails as streaks of light comparable in width to stars. The width was measured in six spots along the trail, and was quantified as the full width at half maximum (FWHM) of the Gaussian light profiles. Atmospheric seeing, chromatic aberration, and other effects were corrected by finding a nearby star in the same exposure as the meteor trail, and subtracting the FWHM of the star from the trail width. An estimated correction factor for the meteor being out of focus was also applied. Fifty-one trails were measured, giving widths up to 3 m and a mean survey width of 1.3 ± 0.5 m. Meteors as faint as magnitude +4 were studied. As this was a single station study, the range to the meteor had to be estimated, which was done by assuming a uniform beginning height of 100 km for all meteors. This made the image scale and focus correction questionable, as both are dependent on the range.

A subsequent study with the same telescope was performed by Cook, Hawkins & Stienon (1962). In this case, thirty-three Geminid meteors with magnitudes up to +9.1 were observed, but measurements were performed on nine that were the brightest, yielding widths up to $9.3 \pm$

1.5 m in parts of the trail, and overall widths up to 5.75 m. The issue of range determination in the previous study was somewhat addressed by selecting Geminids for observation, with an assumed beginning height of 93 km and a known radiant. Issues of focus correction were addressed by studying how the width of stars varied when moved out of focus.

In addition to refining the trail measurements by Hawkins & Whipple (1958), the study by Cook et al. (1962) was also motivated by triple-wavelength radar observations of meteors by Greenhow & Hall (1960). Measurements of meteor ion trails at simultaneous wavelengths of 4.3 m, 8.3 m and 17 m revealed that each time the radar wavelength was increased, a larger number of faint (mag. > +6), meteors were detected. Two effects were considered in producing destructive interference in the backscattered signal: finite meteoroid velocity, and finite initial ion trail radius. By taking a ratio of Eq. (3.1) for $\lambda = 8.3$ m and 17 m, initial ion trail radii were found to vary almost linearly with height, between 1 m at 90 km to nearly 3 m at 115 km.

Efforts to model the meteor trail width were presented by Manning (1958), and Kascheyev & Lebedinets (1963). Manning (1958) determined that the initial ion trail radius would be between $12.3\lambda_{\text{mfp}}$ and $14.5\lambda_{\text{mfp}}$ for meteor velocities between 11–72 km s⁻¹, where λ_{mfp} was the ambient atmospheric mean free path. In contrast, Kascheyev & Lebedinets (1963) found that the trail should have a stronger velocity dependence, between $2.4\lambda_{\text{mfp}}$ at 10 km/s and $13.3\lambda_{\text{mfp}}$ at 70 km s⁻¹. Manning (1958) calculated his values by assuming a large, velocity-independent atmospheric mean free path for the energetic ions released from the meteoroid, as well as an amount of energy lost per collision, and then using these to determine the ion trail formation radius as a function of time. Kascheyev & Lebedinets (1963) assumed a more realistic expression for the mean free path of energetic ions, determined the number of collisions before the ions were thermalised, and found the displacement of the ions at thermalisation. The results of both models suggested that large wavelength radar was most appropriate to study meteors at the highest velocities and altitudes, where the initial ion trail radii were expected to be largest. Also, both models implicitly stated that trail radius should increase with altitude in the same fashion as atmospheric mean free path, a stronger dependence on height than was observed by

Table 3.1: Exact Gaussian (r_{exact}) and numerical simulation ion trail radii (r_{sim}) by trail model by Jones (1995), and dual-frequency radar observations (r_{obs}) by Baggaley (1980). The top set are Geminids, while the bottom set are sporadics.

Height (km)	r_{obs} (m)	r_{exact} (m)	r_{sim} (m)
92	0.64	0.83	0.82
97	0.76	1.78	1.57
102	1.05	3.80	2.34
107	1.75	8.11	2.59
112	≥ 2.0	17.31	2.44
92	0.44	0.952	0.96
97	1.32	2.031	1.70
102	1.96	4.372	2.45
107	2.40	9.241	2.79
112	≥ 2.50	19.71	3.44

the optical and radar surveys.

Additional dual-wavelength studies were made by Baggaley (1970, 1980), who found initial ion trail radii varied between 0.5 m at 90 km and nearly 3 m at 110 km. Jones (1995) used these results and performed a detailed simulation to determine whether the observed initial ion trail radii could be reproduced. The model assumed that ions were evaporated from the meteoroid with an initial velocity given by the meteoroid velocity. A realistic, velocity-dependent expression for the collision cross section was employed, and the ion position was calculated in three dimensions for up to twenty collisions using the associated mean free path. Two methods were used to determine the modeled ion trail radius: an exact expression for the root mean square (RMS) model radius was derived assuming a Gaussian profile, and a particle simulation using 10^4 particles was employed to determine the actual model profile, in addition to an effective trail radius. The results showed that, for heights under 97 km, the Gaussian RMS trail radius matched the observations by Baggaley (1980) to within an order of magnitude. Conversely, at larger heights, only the detailed simulation results matched the observations. The results are summarised in Table 3.1. This was the first model to suggest a non-Gaussian density profile for the initial ion trail, and that future models should simulate the movement of individual particles.

Boyd (2000) took a novel approach to simulating meteoroid ablation through use of the direct simulation Monte Carlo (DSMC) method, typically used to simulate the flow field around re-entering spacecraft. This study was motivated by previous spectral observations and provided a detailed model of the environment around an ablating meteoroid. A single Leonid meteoroid of radius 1 cm at a height of 95 km and a velocity of 72 km s^{-1} was studied, and it was found that the density distribution of ablated particles was nearly Gaussian as a function of distance perpendicular to the trail, with a diameter of nearly 6 m. This was not directly comparable to radar observations, as no provision for particle ionization was included in the simulation, but the trail radius appeared to be the same order of magnitude as previous radar and optical observations.

Observations during the 1998 Leonid multi-instrument aircraft campaign (MAC) (Jenniskens & Butow 1999) provided several new optical trail width measurements of Leonid meteors. Though our current survey focuses on fainter meteors, observations of these bright Leonids are included in this review as important contributions to the limited studies of the optical widths of meteors. Spurný et al. (2000) observed eight Leonids with large beginning heights, above 150 km, using two image-intensified video cameras. The system had a field of view of 25° , with a limiting meteor magnitude of +1. Spectral sensitivity was from 330–880 nm. Extremely large widths, of the order of kilometres, were observed and are summarised in Table 3.2. Instrumental corrections were not considered as meteors at lower altitudes displayed morphology consistent with classical ablation, as well as smaller widths.

Additional Leonid measurements were taken by LeBlanc et al. (2000), using an image intensified camera on the Leonid MAC aircraft. The instrument had an 85 mm, $f/2.0$ lens, giving a $9.5^\circ \times 7.3^\circ$ field of view, with an angular resolution of 0.9' per pixel, at 30 frames per second. A Leonid with a *nebulous* appearance was observed at a beginning height of 138 km, displaying a width of nearly 600 m. The peak observed magnitude of the meteor was +2.3, while the peak magnitude outside of the field of view was -4. Instrumental corrections to the width were not considered, outside of comparing the transverse meteor brightness profile to a

Table 3.2: Eight high-altitude Leonids observed with two-station LLTV video, by Spurný et al. (2000). H_B and H_E are the beginning and ending heights, respectively, while M_{\max} was the peak absolute magnitude of the meteor, and H_{\max} is the height at which the maximum width, W_{\max} , was observed. Magnitudes in brackets were estimated.

H_B (km)	H_E (km)	H_{\max} (km)	W_{\max} (km)	M_{\max}
148.8	141.6	142	1.2	-7.6
183.6	151.4	160	1.8	-7.5
154.9	113.4	135	1.6	-7.1
195.0	130.5	148	3.8	-12.5
156.7	112.3	138	1.9	(-6.5)
160.1	110.1	136	1.1	(-6.5)
161.5	131.5	137	1.0	(-6.5)
178.2	140.3	145	1.6	-6.8

meteor with negligible width. Vibration of the aircraft was discounted as artificially widening the trail by examining the widths of stars imaged with the system. Earlier observations on the ground with a single, image-intensified camera with a spatial resolution of 3.15' per pixel, revealed jet-like features in Leonids, producing widths up to 1.9 km at a height of 122 km.

An isolated and fortunate observation of a bright, -3 magnitude Leonid meteor was presented by Stenbaek-Nielsen & Jenniskens (2004). The Leonid, at an estimated height of 110 km and speed of 71.6 km s^{-1} , was observed using an image-intensified, 1000 frame per second system with a resolution of approximately 1.5' per pixel. This yielded a spatial resolution of 59 m per pixel at an estimated range of 135 km. An unexpected apparent spherical shock formed around the meteor head, with a diameter of nearly 200 m, while the optical trail width was at least an order of magnitude smaller. The authors suggested that instrumental bloom from the saturation of the CCD may have contributed to the size of the meteor, and that the large size of the shock was difficult to account for, outside of inefficient UV photochemical processes. Jenniskens et al. (2004) observed another bright -8 magnitude meteor with the European Southern Observatory Very Large Telescope FORS1 spectroscop and determined a trail width (FWHM) of $7.0 \pm 0.4 \text{ m} \cdot \sin \alpha \cdot (H/90 \text{ km})$, where α is the angle between the meteor trail and the instrument slit, and H is the height of observation.

The most recent optical survey of meteor trail widths was performed by Kaiser, Brown &

Hawkes (2004). A two-station, image-intensified, large-aperture (0.40 m) telescope system was used. One station was equipped with a camera operating at 30 frames per second, and the other was equipped with a intensifier-gated (375 Hz) camera. The limiting stellar magnitudes of the stations were +12 and +13, respectively, while the spatial resolutions were 2.2" per pixel and 2.4" per pixel. Eighty-seven meteors were analysed by examining the pixel brightness profile perpendicular to the meteor trail and determining the full width at half maximum. Instrumental bloom and seeing were corrected by subtracting the FWHM of a star of comparable brightness. This method is similar to that used for the earlier optical studies by Hawkins & Whipple (1958), and Cook et al. (1962). Nearly all of the meteors displayed statistically insignificant trail widths after bloom correction, the largest two-station meteor having a width of 1.37 ± 0.71 m. The meteors examined were observed at heights ranging from 60 km to 110 km and at magnitudes between +6.5 and +10.

Jones & Campbell-Brown (2005) provided additional radar observations of initial trail radii for meteors with magnitudes ranging from +5 to +8. The Canadian Meteor Orbit Radar (CMOR) was used to make dual-wavelength (7.8 and 10.0 m) observations of ion trails. Using the same method as Greenhow & Hall (1960), the ratio of the returned amplitudes gave an estimate of the trail radius, assuming a Gaussian profile. Radii ranged from 0.5 m at a height of 80 km, to 1.5 m at 100 km. This height dependence was weaker than expected by the previous models of Manning (1958) and Kascheyev & Lebedinets (1963), but was explained by possible fragmentation of the observed meteoroids, as discussed by Hawkes & Jones (1978).

3.1.3 Study goals

Earlier studies have consistently yielded ion and optical trail widths in the order of ~ 1 – 10 m at heights between 90 km and 110 km. At heights above 130 km, widths of the order ~ 1 km have been observed with image-intensified video systems. The relationship between height, velocity, and trail width is unclear, as is the dominant mechanism behind the creation of the initial trail. The goal of this study is to select a small number (30) of meteors with high

quality observations, and to measure the optical trail widths as a function of meteor height and distance along the meteor trail. The development of a consistent measurement method, as well as derivation of initial results from a small number of high-quality observations from two independent stations, will allow for more comprehensive surveys and modelling in the future.

3.2 Instrumentation

Observations of meteor optical trail widths for this survey were performed with the Canadian Automated Meteor Observatory (CAMO) in Ontario, Canada. CAMO is novel in addressing the simultaneous requirements of fine spatial resolution, faint meteor sensitivity, and large collecting area for a study of optical trail widths.

The Canadian Automated Meteor Observatory is a two-station, image-intensified system that automatically captures meteor events each clear night (Weryk et al. 2013). The two stations are located near Elginfield, Ontario, Canada (43.193° N, 81.316° W) and Tavistock, Ontario, Canada (43.265° N, 80.772° W) with a baseline of approximately 45 km. Each station features a fixed wide-field camera, with an approximate $25^\circ \times 19^\circ$ field of view, and a tracking narrow-field camera, with a $1.2^\circ \times 0.9^\circ$ field of view. Data from the wide-field cameras are used to calculate the trajectory of the meteor as a function of time, while data from the narrow-field cameras are used to measure the trail widths and meteor morphology, as illustrated in Figure 3.1.

Imperx IPX-VGA120 fully digital cameras are used for both the narrow- and wide-field systems, operating at 110 frames per second for the narrow-field camera, and 60–80 frames per second for the wide-field camera. The resolution of both cameras is 640×480 progressive scan, while their image depth is 12-bit, to minimise saturation from bright meteors. The narrow-field camera is attached to a ZenithStar 80 mm aperture, $f/6.8$ telescope for fine spatial resolution. Sample images of a meteor from both narrow-field stations are given in Fig. 3.2.

The telescope has a limited field of view, so the system is designed to automatically track

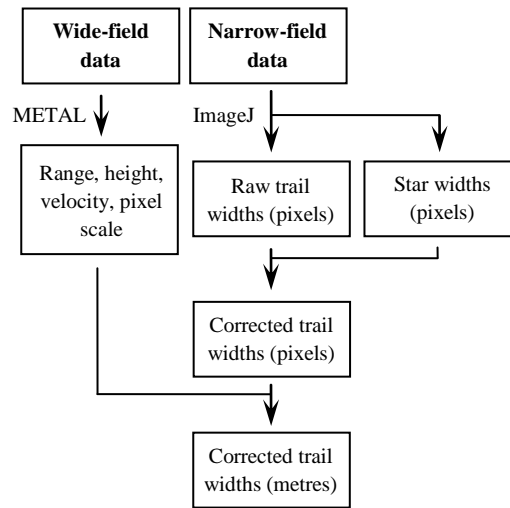


Figure 3.1: A schematic of the trail width measurement process, using narrow- and wide-field data.

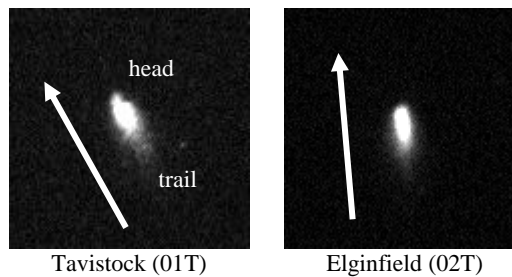


Figure 3.2: Sample images of meteor 20101103.071855, simultaneously observed by the narrow-field system at both CAMO stations. At the time of the image, the meteor was at a height of 110 km, with a speed of 68 km s^{-1} , and an instantaneous absolute magnitude of $+0.7 \pm 0.1$. Each arrow points in direction of travel and is 100 pixels long, corresponding to 433 metres at the observed range of 135 km. Brightness bounds were set to $[0, 250]$ for these images.

meteors in real-time by using two independent mirrors mounted on galvanometers to direct light into the telescope from anywhere in the wide-field system's field of view. The narrow-field tracking system is similar to the AIM-IT system by Gural, Jenniskens & Varros (2004). First, a meteor is detected by All-Sky and Guided Automatic Real-time Detection (ASGARD) software (Weryk et al. 2008) of the CAMO system. Specifically, pixel brightness values in the wide-field system are monitored and a low-pass filter is applied, per-pixel, to reduce impulsive shot noise contributed from the image intensifier. If any 8×8 region of pixels in the wide-field system has at least six pixels above the set detection threshold, typically 5σ above the mean background brightness value, then it is counted as a meteor, provided that the region is detected in at least three consecutive frames. These conservative requirements result in about 67 percent of all meteors visible in the wide-field system being tracked.

To track the meteor in flight, a linear fit is computed to describe the meteor's pixel position in the wide-field system as a function of time. The position of the meteor in seven frames after initial automatic detection are used to generate a first-order polynomial that best describes the motion of the meteor. These pixel positions are converted to galvanometer coordinates using a previously-derived affine transform. The galvanometers are then programmed to smoothly track through the fit polynomial, which keeps the meteor inside the narrow-field system's field of view. The galvanometers can track at an angular velocity up to 2000° per second and update their position at a rate of 2000 Hz to ensure smooth tracking of the meteor.

Each camera is lens coupled to a third-generation, 18 mm ITT NiteCam 380 intensifier. The spectral response of these intensifiers is nominally between 500 nm and 850 nm, represented best by the Johnson-Cousins R-band. Magnitudes are calibrated to correspond to R-band magnitudes (Weryk & Brown 2013). The limiting magnitude of the wide-field system for meteors is +5, giving a mass sensitivity limit near 10^{-5} kg.

It was expected that the meteor trail would be wider than one pixel in the narrow-field system, as the expected trail widths was of the order 1–10 m excluding image blooming, while the pixel scale is 3.2 m per pixel at a range of 100 km. Previous studies described the width

as the full width at half maximum. Meteors captured with the narrow-field system typically displayed maximum pixel brightness above 500 digital units, with a background mean of 20 and a standard deviation of 10, leaving much of the brightness curve well above the background for analysis.

3.3 Data reduction

3.3.1 Determination of meteor trajectories and orbits using wide-field data

Two station data from the wide-field cameras were analysed with the software package METAL (Weryk & Brown 2012). METAL allows a user to select the meteor head in each frame of an event video. An astrometric plate and instrumental-R catalogue magnitude conversion is generated by identifying stars in the field of view. The trajectory solver MILIG (Borovička 1990) is employed to determine the meteoroid's trajectory as a function of time. METAL also computes a light curve for the meteor by allowing users to mask the meteor light in each frame. The brightness of the meteor is compared to the brightness of stars in the field of view for each frame and converted to an apparent magnitude. A flat-field image, previously prepared for each camera, for each night of operation, is employed to improve the accuracy of the photometry. Of particular interest to trail width measurements were the meteor's mean velocity, absolute magnitude, and instantaneous range, height, zenith, and azimuth angle, describing the meteor position as a function of time.

Orbital parameters for each meteor were calculated using methods from Ceplecha (1987). Uncertainties in trajectory and orbital parameters were estimated by simulating 1000 trajectory solutions based on the actual trajectory solution, adding a random displacement for the meteor position in each frame by up to a single pixel. This simulates the uncertainty in consistently picking the meteor's head. The standard deviation in the parameters of the simulated solutions were taken to be the uncertainties for the actual solution. Additional details regarding METAL

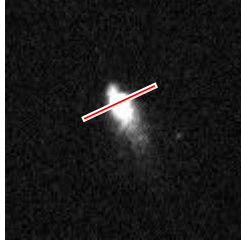


Figure 3.3: A sample width measurement slice for meteor 20101103_071855, as seen by Tavistock. The slice is 40 pixels long (173 m at the meteor’s range), and is located approximately 12 pixels (nearly 50 m) back from the head. The brightness values measured are shown in Figure 3.4. The meteor was travelling at a speed of 68 km s^{-1} , at a height of 110 km, and range of 135 km.

photometry and error estimation is available in Weryk & Brown (2012, 2013).

3.3.2 Measurement of meteor trail widths using narrow-field data

Narrow-field data were processed using the open-source image analysis software ImageJ (Rasband 2012). The raw trail width was measured by creating a measurement line, called a *slice*, perpendicular to the meteor. To reduce uncertainty in measured widths, the angle of the meteor trail in all frames was determined using a linear Hough transform (Duda & Hart 1972). A curve of pixel brightness versus distance perpendicular to the meteor trail was produced for each slice. A sample measurement is shown in Figures 3.3 and 3.4. The slice was moved along the meteor trail in one pixel increments, starting just before the head of the meteor, and moving until the peak brightness of the trail slice was no longer 2σ above the background mean. This procedure was repeated for each frame of each meteor.

As mentioned in Section 3.2, the narrow-field system tracked meteors based on a linear fit computed in real-time from wide-field data. Though the meteor was kept in the field of view, it tended to drift due to changing view geometry, producing an apparent change in position from one frame to another. To simplify measurements, a template matching algorithm (Tseng 2011) was employed to locate the meteor in each frame of an event video. Briefly, this was accomplished by taking a Fourier transform of a selected frame and the initial frame. A convolution

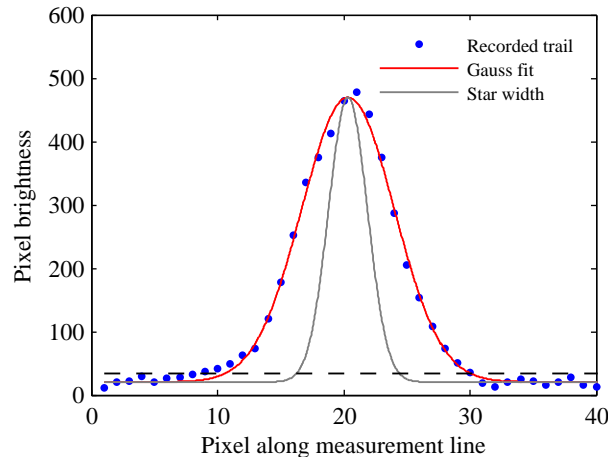


Figure 3.4: The pixel brightness values measured from the slice in Figure 3.3 are shown as blue points, the Gaussian fit to the profile is the red line, and the profile of an equivalent brightness star is the gray line. In this case, $w_{\text{obs}} = 21$ pixels derived from the observed points, $w_{\text{fit}} = 19.4$ pixels from the Gaussian fit, and $w_{\text{FWHM}} = 8.6$ pixels, while $w_{\text{star}} = 8.1$ pixels. As noted in Figure 3.3, this 68 km s^{-1} meteor was captured at a height of 110 km and a range of 135 km for this measurement.

was then performed on the transforms and inverse transformed to yield an image with intensity proportional to the required translation to move the meteor from its position in the selected frame to its position in the initial frame. The translations were recorded for each frame to quantify the frame-to-frame meteor drift and determine a *tracking* angle. The tracking and trail angle are demonstrated in Figure 3.5. If the drift of the meteor was not along the direction of the trail, smearing produced an artificially larger width. The calculation to account for this is introduced in Section 3.3.4.

Each trail measurement slice produced a raw observed width, w_{obs} , calculated as the width of the portion of the transverse trail brightness profile at least two standard deviations above the background brightness. The threshold was set at that level to ensure that noise did not erroneously contribute to the trail width. All of the slices for a single frame were combined to produce a curve of raw trail width as a function of distance along the meteor. Previous studies obtained the full width at half maximum to describe the trail width, so a Gaussian curve was also fit to the transverse brightness profile of each slice. Although Jones (1995) demonstrated that the ion density in the trail might not have a Gaussian profile, in this case it was expected

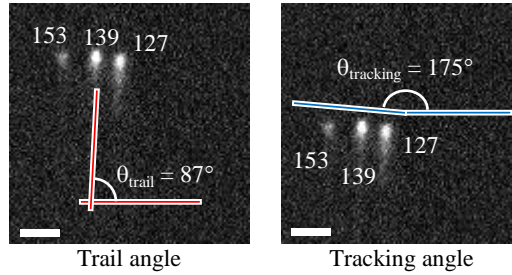


Figure 3.5: Stack of three narrow-field frames for meteor 20101103_033400, as captured by the Elginfield station. The trail angle is shown in the left figure while the tracking angle is shown in the right figure. In this case, there is significant drift of the meteor in a direction not along the trail, resulting in additional instrumental width spread. Frame numbers for each stacked image are indicated, and a scale bar indicates approximately 100 m. Brightness bounds were set to $[0, 150]$. The meteor travelled at a speed of 57 km s^{-1} and was captured at heights between 108 km and 104 km, at an approximate range of 160 km. The peak absolute magnitude for this event was $+2.5 \pm 0.2$.

that the Gaussian point spread function (PSF) exhibited by the narrow-field system when stars were examined would make the profile Gaussian in character, as argued by Hawkins & Whipple (1958). Also, Boyd’s (2000) model of ablated particle density produced a profile similar to a Gaussian. The width of the Gaussian curve to the set threshold of the mean plus 2σ was termed the raw fit width w_{fit} , and the associated Gaussian FWHM was called w_{FWHM} .

Uncertainties for the raw widths were derived by shifting the measurement slice by a random subpixel displacement perpendicular to the meteor trail. As ImageJ used bilinear interpolation brightness values along the angled measurement line, this made a small difference in the raw widths. The standard deviation of eighty random shifts was recorded as the associated uncertainty in width for each slice.

The result of these measurements was a raw observed width, Gaussian fit width, and Gaussian FWHM, curve as a function of distance along the meteor, all measured in pixels, for each frame of a meteor. The peak of each slice’s brightness curve was recorded, for use in image bloom correction. A trail angle, and a tracking angle as a function of time were also recorded.

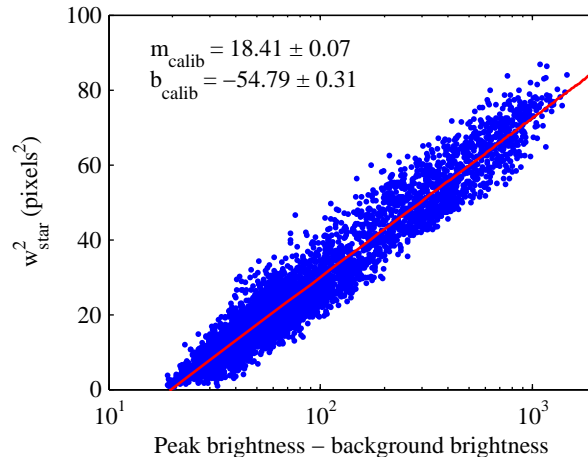


Figure 3.6: Sample stellar calibration graph for Tavistock narrow-field station, 20101103. The calibration graph plots observed squared star width versus the natural logarithm of the peak brightness of the star, minus the background brightness.

3.3.3 Correction of image bloom in trail widths using a stellar calibration curve

To correct image bloom from the system, a two-dimensional isotropic Gaussian was fit to stars that were stationary in the narrow-field system. Stars characterised the image bloom of the system as they are point sources broadened by the system PSF. These stellar Gaussian fits were then used to produce a calibration graph, like Figure 3.6, plotting star width versus peak brightness. Measured meteor trail widths for each slice were corrected by subtracting the width of an equivalent peak brightness star, determined from the calibration graph, from the raw meteor trail width.

The hyperfocal distance of the narrow-field cameras, or the distance past which all objects are in focus, provided the system is focused at infinity, was calculated to ensure that meteors were equivalently in focus as stars, and that bloom corrections derived from observations of stars could be applied to meteors. For the narrow-field camera, with aperture size $D = 80$ mm (effective 50 mm), $f/6.8$ ($N = f/D = 6.8$), and pixel size $7.8 \mu\text{m}$ setting an upper bound to the

blur radius c , the hyperfocal distance,

$$H = ND \left(\frac{D}{c} + 1 \right), \quad (3.2)$$

is 5.9 km. Thus, objects at a range beyond 5.9 km, including all meteors studied, where the average range was over 100 km, were equally in focus as stars observed with the narrow-field camera.

A Gaussian is expected to represent the PSF of the system provided that the most significant effects were contributed by the telescope (diffraction and chromatic aberration, as in Hawkins & Whipple (1958)), as well the CCD (charge leakage between neighbouring pixels, as in Groom et al. (1999)). The Gaussian PSF is isotropic as the pixels of the CCD are square, and contributions to the PSF from diffraction are expected to be a function of radial distance only. Later, in Section 3.4.1, it will be demonstrated that most of the observed Gaussian PSF appears to originate from the CCD or intensifier: a transient, shot noise artefact produced by the intensifier is observed to have a Gaussian brightness profile that is completely removed by bloom correction.

The form of the fit is given by

$$B(x, y) = a + (b - a) \exp \left[-\frac{(x - c_x)^2 + (y - c_y)^2}{2d^2} \right], \quad (3.3)$$

with $B(x, y)$ representing the brightness of pixel (x, y) , a being the background mean level, b being the peak brightness, (c_x, c_y) representing the centre x - and y -pixel of the star, and d being the spread or variance. The width of the Gaussian to threshold brightness B_t may be found by inverting Eq. (3.3). A quick way to get the star width from Eq. (3.3) is to solve for the two roots x_+ and x_- along the line $y = 0$ for the brightness equivalent to the threshold brightness, B_t . As the profile is isotropic, the width of the Gaussian star profile is simply $x_+ - x_-$, giving

$$w_{\text{star}}^2 = 8d^2 \ln(b - a) - 8d^2 \ln(B_t - a). \quad (3.4)$$

Table 3.3: Parameters for stellar width calibration curves for each night of observation. $m_{\text{calib},01}$ and $b_{\text{calib},01}$ are the calibration slope and intercept for Tavistock, while $m_{\text{calib},02}$ and $b_{\text{calib},02}$ are for Elginfield.

Date	$m_{\text{calib},01}$	$m_{\text{calib},02}$	$b_{\text{calib},01}$	$b_{\text{calib},02}$
20101020	17.5 ± 0.2	20.4 ± 0.4	-52.0 ± 0.8	-53 ± 2
20101103	18.41 ± 0.07	21.1 ± 0.2	-54.8 ± 0.3	-59 ± 1
20101106	21.9 ± 0.3	20.9 ± 0.3	-71 ± 1	-56 ± 2

The calibration graph, Figure 3.6, plots the squared star width to the threshold brightness of the mean background plus two standard deviations, versus the natural logarithm of the star's peak brightness minus the background brightness. The result is a linear fit,

$$w_{\text{star}}^2 = m_{\text{calib}} \ln(b - a) + b_{\text{calib}}, \quad (3.5)$$

with a slope, m_{calib} , equivalent to $8d^2$, and an intercept, b_{calib} , of $-8d^2 \ln(B_t - a)$. In the special case of the star FWHM, $B_t = (b + a)/2$ and Eq. (3.5) becomes

$$w_{\text{star,FWHM}}^2 = m_{\text{calib}} \ln 2. \quad (3.6)$$

Stellar calibration graphs were produced for each night of observation, for each station. This was necessary due to changes in the slope and intercept of the curves over each night, as shown in Table 3.3. This was likely due to changes in temperature, humidity, and other conditions in the system or outside.

Raw trail widths were corrected by substituting the peak brightness of the measured meteor profile, as well as the background mean brightness, to the stellar calibration curve to get the width of a star with an equivalent peak brightness, w_{star} . This star width was subtracted from the raw trail width to give a corrected trail width. A similar method was employed by previous optical studies (Hawkins & Whipple 1958, Cook et al. 1962, Kaiser et al. 2004) to correct for

image bloom. The corrected measurements are given by

$$W_{\text{obs,corrected}} = W_{\text{obs}} - W_{\text{star}}, \quad (3.7)$$

$$W_{\text{fit,corrected}} = W_{\text{fit}} - W_{\text{star}}, \quad (3.8)$$

$$W_{\text{FWHM,corrected}} = W_{\text{FWHM}} - W_{\text{star,FWHM}}, \quad (3.9)$$

where w_{obs} is the width of the observed brightness profile 2σ above the background brightness, w_{fit} is the equivalent width for the Gaussian fit to the observed brightness profile, and w_{FWHM} is the FWHM of the Gaussian fit.

Uncertainties in the slope and intercept of the fit were found by using the bootstrap method described by Press et al. (2007). This method produces simulated data sets of equivalent size to a measured data set by randomly selecting points from the measured data set, allowing duplication. By producing fits to the simulated data sets, a distribution of fit values emerge. This allows for determination of the mean fit values, as well as associated uncertainties derived from the standard deviation of the simulated fit values. This method was particularly appropriate here, as the distribution of star brightness (and width) from frame to frame was not explicitly known, but could be implicitly estimated with this method, and converted to a distribution for m_{calib} and b_{calib} .

The uncertainty in the fit slope and intercept were used to calculate the uncertainty in the star width,

$$\Delta w_{\text{star}} = \frac{\Delta(w_{\text{star}}^2)}{2w_{\text{star}}}, \quad (3.10)$$

where w_{star} is given by Eq. (3.5), and

$$\Delta(w_{\text{star}}^2) = \sqrt{\Delta m_{\text{calib}}^2 \ln^2(b - a) + \Delta b_{\text{calib}}^2}. \quad (3.11)$$

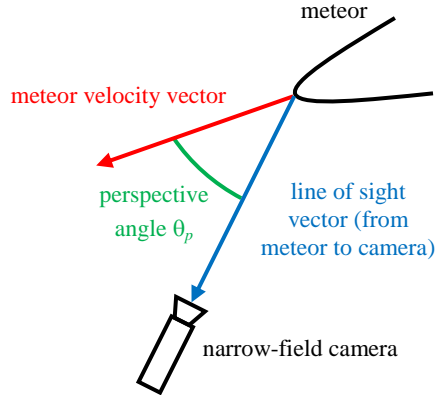


Figure 3.7: Illustration of the perspective angle.

3.3.4 Conversion of measurements from pixels to metres, effect of image smear, and final trail width uncertainty

The corrected trail widths, $w_{\text{corrected}}$, measured in pixels, were converted to final trail widths, w_{final} , in metres, by making use of the range, R , from the narrow-field station to the meteor from the trajectory solution,

$$w_{\text{final}} = w_{\text{corrected}} \cdot p_{\text{scale}} \cdot R. \quad (3.12)$$

The angular scale per pixel for the narrow-field system, p_{scale} , was also used. Similarly, the pixel distance along the meteor trail for each width measurement, d , was converted to metres,

$$d_{\text{final}} = d \cdot \frac{1}{\sin \theta_p} \cdot p_{\text{scale}} \cdot R. \quad (3.13)$$

An additional corrective factor, $1/\sin \theta_p$, was employed to compensate for the perspective of the narrow-field station when viewing the meteor. Figure 3.7 illustrates the angle, θ_p , between the meteor velocity vector and the line of sight vector.

Trail smearing occurs if the meteor drifts, frame-to-frame, in a direction that is not the trail direction, due to imperfect tracking with the narrow-field system. In that case, $\theta_{\text{trail}} \neq \theta_{\text{tracking}}$, where the tracking angle is a function of frame, since it varies as the meteor is tracked. Smearing is also dependent on the apparent distance that the meteor moves in each frame. The

frame-to-frame tracking length, l_{tracking} , measures the difference in the meteor's position in the frame from one frame to the next. l_{tracking} was calculated using a second-order polynomial fit to the stored positions $x(f)$ and $y(f)$ of the meteor, found using the pattern recognition algorithm described in Section 3.3.2,

$$l_{\text{tracking}}(f) = \sqrt{[x(f+1) - x(f)]^2 + [y(f+1) - y(f)]^2}. \quad (3.14)$$

The derivatives of $x(f)$ and $y(f)$ were also calculated, analytically, with respect to frame and used to determine θ_{tracking} ,

$$\theta_{\text{tracking}}(f) = \tan^{-1} \left. \frac{dy}{dx} \right|_f = \tan^{-1} \left. \frac{dy/df'}{dx/df'} \right|_{f'=f}. \quad (3.15)$$

The resulting uncertainty due to trail smearing was

$$\Delta w_{\text{smear}} = l_{\text{tracking}} \sin |\theta_{\text{trail}} - \theta_{\text{tracking}}|. \quad (3.16)$$

The two other sources of trail width uncertainty are variation in the raw width due to pixel interpolation in the original event video, and uncertainty in the width of stars used to correct the raw widths. The total uncertainty in the final, corrected width (in metres) was thus found to be

$$\Delta w_{\text{final}} = p_{\text{scale}} \cdot R \cdot \sqrt{\Delta w_{\text{raw}}^2 + \Delta w_{\text{star}}^2 + \Delta w_{\text{smear}}^2}. \quad (3.17)$$

3.4 Results and discussion

Thirty meteors were observed over three nights (20 October, 3 November, and 6 November 2010) for this study. Those three nights were selected due to the large number of meteors observed each night, and to simplify preparation of stellar calibration curves. Fourteen of the thirty meteors were captured by both narrow-field stations, allowing the agreement between

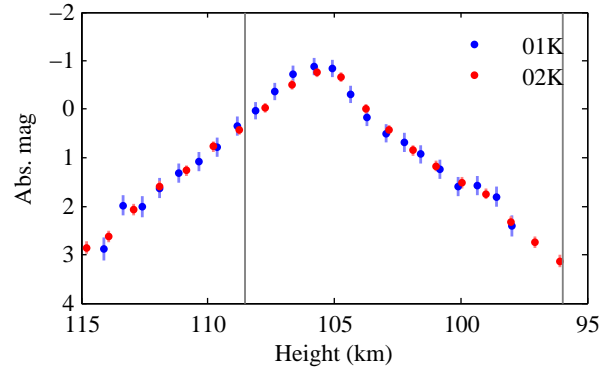


Figure 3.8: The light curve for 20101020_095900 captured with the wide-field system. Blue points represent Tavistock (01K) measurements while red points represent Elginfield (02K) measurements. The grey vertical lines indicate the heights over which the narrow-field system tracked the meteor.

independent width measurements from each station to be tested. The beginning and ending height, geocentric speed, peak absolute magnitude, and maximum observed corrected widths for each meteor are summarised in Tables 3.4 and 3.5.

In the Section 3.4.1, we examine a specific meteor in detail to illustrate the steps in determining final, corrected trail widths from narrow-field images of the meteor. Subsequently, the overall study results for all thirty meteors will be presented in Section 3.4.2.

3.4.1 Illustration of measurement procedure: representative event

A meteor was observed with both CAMO stations on 20 October 2010, at 09:59:00 UTC. The wide-field system detected the meteor from a beginning height of 114.8 km to an ending height of 96.1 km. The meteor’s average speed was observed to be approximately 66.0 km s^{-1} , while the meteor’s peak absolute magnitude was -0.8 ± 0.2 , occurring at a height of 105.8 km. The light curve from both wide-field stations is given in Figure 3.8, showing good agreement between stations.

Both narrow-field cameras began tracking the meteor from a height of 108.5 km down to the terminal height of 96.1 km. This provided a total of 47 frames over both stations for measurement. Figure 3.9 shows four frames from each narrow-field station. Initially, the

Table 3.4: Beginning and ending height (wide-field), speed at infinity, and the peak absolute magnitude for all meteors in this study. A starred event indicates two-station narrow-field coverage. Table 3.5 gives the maximum corrected widths (observed, fit, and FWHM) for each meteor.

Event	h_{beg} (km)	h_{end} (km)	v_{inf} (km s ⁻¹)	M_{peak}
20101020_085550	112.4 ± 0.2	99.0 ± 0.2	63.3 ± 0.5	0.5 ± 0.2
20101020_091633	121.4 ± 0.4	91.8 ± 0.3	68.1 ± 0.3	-2.0 ± 0.2
20101020_094418*	109.5 ± 0.7	98.6 ± 0.3	44.1 ± 1.6	0.9 ± 0.1
20101020_095835	115.9 ± 0.3	96.2 ± 0.3	67.3 ± 0.6	0.4 ± 0.2
20101020_095900*	114.8 ± 0.3	96.1 ± 0.3	66.9 ± 0.5	-0.9 ± 0.2
20101020_100214	106.5 ± 1.3	95.3 ± 1.0	39.6 ± 2.4	1.6 ± 0.2
20101020_101727*	115.2 ± 0.3	94.4 ± 0.2	68.8 ± 0.5	-0.9 ± 0.2
20101020_102134	112.8 ± 0.3	99.9 ± 0.3	68.2 ± 0.9	1.7 ± 0.2
20101020_102311	112.3 ± 0.4	99.7 ± 0.3	68.7 ± 1.0	0.5 ± 0.2
20101020_102652	112.8 ± 0.2	98.1 ± 0.1	66.5 ± 0.5	-0.1 ± 0.1
20101020_102938	115.4 ± 0.2	101.1 ± 0.2	66.2 ± 0.7	0.6 ± 0.2
20101102_233359	88.8 ± 4.0	77.8 ± 3.5	18.5 ± 0.8	1.6 ± 0.2
20101103_031542*	111.7 ± 3.7	95.3 ± 3.1	60.0 ± 2.1	-1.2 ± 0.2
20101103_033400*	111.9 ± 3.7	104.7 ± 3.4	58.4 ± 1.9	2.5 ± 0.2
20101103_045928*	91.3 ± 0.2	84.3 ± 0.2	35.8 ± 0.4	3.4 ± 0.2
20101103_053624*	116.6 ± 0.6	98.2 ± 0.5	65.9 ± 0.3	0.3 ± 0.2
20101103_054049	119.0 ± 2.0	103.9 ± 1.7	70.5 ± 1.7	0.6 ± 0.2
20101103_061127*	98.2 ± 0.2	85.2 ± 0.2	29.7 ± 0.2	2.3 ± 0.2
20101103_061856*	101.9 ± 0.3	85.5 ± 0.2	30.9 ± 0.2	1.6 ± 0.1
20101103_062801*	116.0 ± 0.6	103.9 ± 0.6	66.9 ± 0.5	0.2 ± 0.2
20101103_063032	113.8 ± 1.0	105.8 ± 0.8	71.2 ± 1.5	2.2 ± 0.1
20101103_064336	99.4 ± 0.3	81.5 ± 0.3	35.4 ± 0.3	1.0 ± 0.1
20101103_071855*	116.7 ± 0.7	101.1 ± 0.7	68.8 ± 1.3	0.6 ± 0.1
20101103_072624*	114.4 ± 0.4	104.8 ± 0.4	68.0 ± 0.7	2.0 ± 0.1
20101103_072638	117.1 ± 0.7	88.3 ± 0.4	62.9 ± 0.7	-1.2 ± 0.2
20101103_072700	116.5 ± 0.4	97.4 ± 0.3	66.0 ± 0.3	-0.2 ± 0.2
20101103_073415	97.4 ± 0.2	87.1 ± 0.2	28.3 ± 0.3	3.3 ± 0.2
20101103_073846*	107.6 ± 0.7	93.7 ± 0.4	72.6 ± 1.1	0.8 ± 0.1
20101103_090709	112.2 ± 0.3	93.0 ± 0.3	66.2 ± 0.5	-1.4 ± 0.1
20101106_055725*	112.9 ± 0.9	100.2 ± 0.7	62.9 ± 0.6	-0.1 ± 0.2

Table 3.5: The maximum corrected widths (observed, fit, and FWHM) for all meteors in this study. A starred event indicates two-station narrow-field coverage. A graph of the maximum corrected, observed width for each frame of each meteor video is given in Figure 3.14.

Event	w_{obs} (m)	w_{fit} (m)	w_{FWHM} (m)
20101020_085550	23.5 ± 2.5	28.8 ± 2.3	19.6 ± 3.0
20101020_091633	62.8 ± 8.4	41.2 ± 6.6	18.6 ± 6.3
20101020_094418*	25.8 ± 2.5	13.7 ± 0.7	11.8 ± 3.5
20101020_095835	71.3 ± 3.2	58.9 ± 2.5	35.5 ± 2.4
20101020_095900*	96 ± 12	76.8 ± 7.9	35.9 ± 7.8
20101020_100214	22 ± 16	26 ± 16	19 ± 16
20101020_101727*	86 ± 10	71 ± 10	38 ± 10
20101020_102134	14.0 ± 3.6	19.6 ± 3.1	17.3 ± 3.7
20101020_102311	30.4 ± 3.9	27.9 ± 2.6	25.9 ± 3.2
20101020_102652	78.0 ± 8.4	62.0 ± 7.5	31.8 ± 7.5
20101020_102938	41.4 ± 2.0	35.5 ± 1.0	26.2 ± 1.6
20101102_233359	22 ± 17	32 ± 17	28 ± 16
20101103_031542*	64 ± 15	45 ± 15	33 ± 15
20101103_033400*	27 ± 13	22 ± 12	34 ± 12
20101103_045928*	20 ± 29	18 ± 29	14 ± 30
20101103_053624*	89 ± 31	70 ± 30	37 ± 29
20101103_054049	110.7 ± 4.2	76.3 ± 3.2	40.3 ± 3.1
20101103_061127*	9.5 ± 1.6	10.2 ± 5.5	11.8 ± 2.3
20101103_061856*	15 ± 28	27 ± 29	23 ± 27
20101103_062801*	86 ± 22	79 ± 22	47 ± 17
20101103_063032	40.0 ± 3.2	36.6 ± 1.4	34.3 ± 1.7
20101103_064336	28.4 ± 6.7	19.0 ± 6.7	25.6 ± 6.7
20101103_071855*	80 ± 17	66 ± 14	34 ± 13
20101103_072624*	42.4 ± 2.4	43.5 ± 1.2	33.8 ± 1.1
20101103_072638	174 ± 13	113.8 ± 4.3	36.8 ± 4.2
20101103_072700	89.6 ± 3.6	76.0 ± 1.0	40.8 ± 0.9
20101103_073415	9.4 ± 9.5	12.0 ± 9.2	15.3 ± 9.2
20101103_073846*	30.5 ± 8.0	25.0 ± 6.9	41.8 ± 9.3
20101103_090709	125.6 ± 3.3	89.5 ± 1.6	38.5 ± 1.3
20101106_055725*	70.2 ± 8.4	50.7 ± 7.5	34.7 ± 7.6

meteor appears very wide with a conical shape in Figure 3.9 (a). As the meteor descends in height, it becomes elliptical and begins to narrow, as illustrated in Figures 3.9 (b) and 3.9 (c), finally becoming faint and filament-like in Figure 3.9 (d) near a height of 103 km.

This meteor, 20101020_095900, was chosen as a representative event because it was recorded with both narrow-field stations, allowing for measurement comparisons. It was also observed from a large initial height, and exhibited significant trail width.

Figure 3.10 gives the trail brightness, raw observed trail width, corrected observed trail width, and all three types of corrected trail width for the meteor in the frame depicted in Figure 3.9 (a). In general, it is not expected that the raw widths should agree between stations (they do not, here), as the pixel scale varies with each station's range to the meteor, but both stations have an almost equivalent range (140 km) to this meteor. In this case, the discrepancy in raw widths is due to different amounts of instrumental bloom for each camera, which is apparent in the offset trail brightness curves from each station shown in Figure 3.10 (a), as well as the displaced bloom width correction curves for each station in Figure 3.10 (b). Similarly, different amounts of trail smear occur for both stations, averaging 1.4 pixels perpendicular to the trail for 01T vs. 2.1 pixels for 02T, not reflected in the raw width measurements.

Image bloom is corrected in the final observed trail widths, in Fig. 3.10 (c), and the sizes of the uncertainty bounds are increased due to smearing of the trail. As a result, the final observed widths show better agreement between stations than the raw widths. There remains a small disagreement around 150 m from the meteor's head, but the majority of other corrected trail width points agree between stations within uncertainty. It may also be noted that the peak width of the trail occurs nearly 150 m from the head of the meteor. This is in contrast to the flat shape of the raw trail width curve, and the peak of the meteor trail's brightness curve, which occurs at about 100 m back from the head. The agreement of final, corrected widths between stations, as well as the difference in shape between the brightness and the final width curve together suggest that the trail widths obtained are measurements of the actual meteor trail, and not instrumental bloom artefacts. More generally, the bloom corrections appear reasonable,

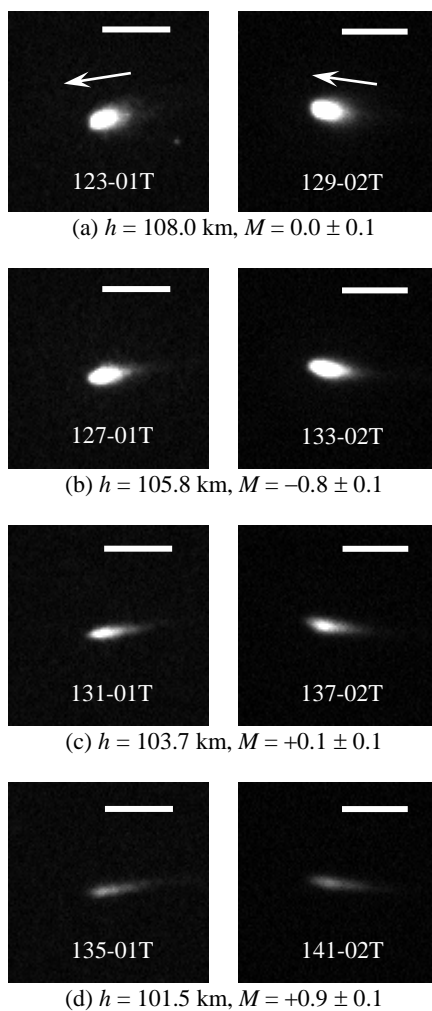


Figure 3.9: Four frames for event 20101020_095900 from Tavistock (01T) and Elginfield (02T) narrow-field cameras. Arrows on the first frames indicate direction of travel. Scale bars on each figure represent approximately 150 m. Frame numbers are indicated on each frame. Pixel brightness bounds are $[0, 500]$ for each frame, where maximum pixel brightness observed for the event is nearly 2000.

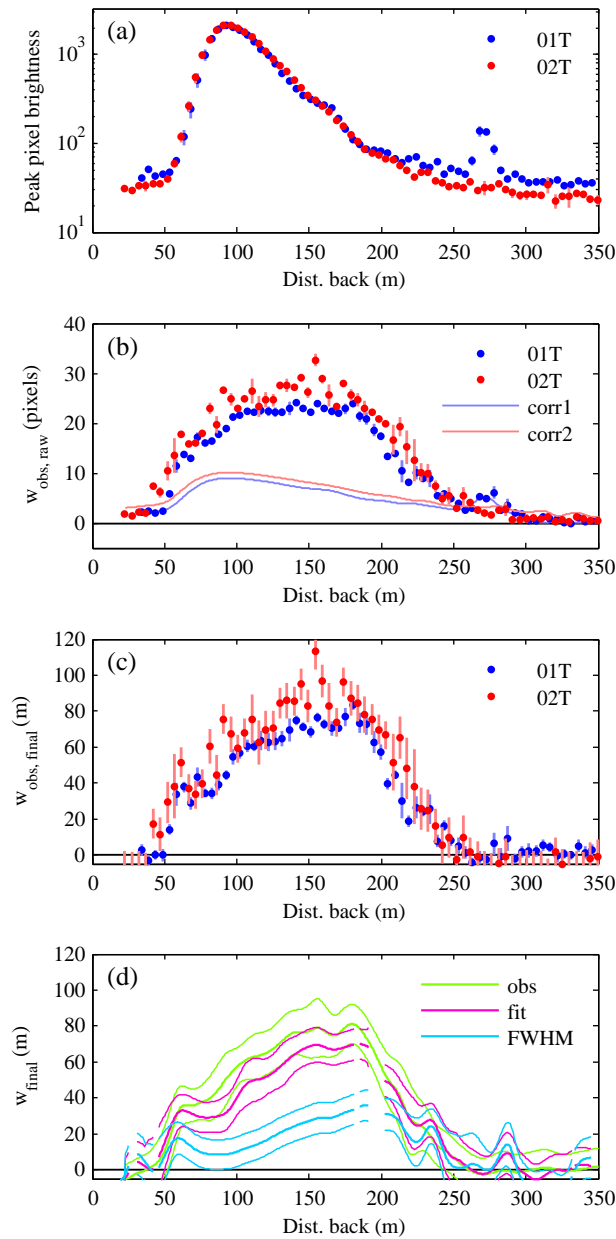


Figure 3.10: Peak trail pixel brightness; raw observed width (and equivalent stellar width used for bloom correction); corrected observed width; and corrected observed, fit, and FWHM widths for the snapshot of 20101020_095900 depicted in Fig. 3.9 (a). The raw width is given in pixels, while the corrected width is given in metres. For Figure 3.10 (d), curves that interpolate data across both stations are plotted. Gaps in the curves are due to non-convergent fits to the slice brightness profile, producing no width values.

with overcorrection rarely occurring, as negative trail widths are rarely produced.

As described earlier, in Section 3.3.3, much of the narrow-field system PSF appears to occur between the image intensifier and CCD array. An example of this is in the correction of the anomalous raw width observed by Tavistock (01T) around 275 m from the meteor's head, visible in Figure 3.10 (b). Looking at Figure 3.9 (a) for Tavistock, there is a small, one frame duration bright spot in the image just below the meteor trail. Although this spot is larger than a pixel, it is not observed from Elginfield. Taken together, this suggests that the spot is a transient bright spot (impulsive shot noise) originating from the image intensifier. Spots like this are common in all of the meteor videos. The detection of the spot is confirmed in the peak in brightness profile at around 275 m distance from the meteor head for Tavistock in Figure 3.10 (a). Although the spot is detected as raw trail width, it is removed in the final, corrected width through the image bloom correction. This suggests that the intensifier and the CCD array contribute most significantly to the observed system PSF, and also, that the bloom correction is effective in removing instrumental width.

Comparing the types of corrected trail widths in Figure 3.10 (d), it appears that the observed, $w_{\text{obs,final}}$, and Gaussian fit, $w_{\text{fit,final}}$, widths, combining data from both stations, agree within uncertainty for this frame of the event. This implies that the Gaussian is a good fit for the transverse trail brightness profile in this case, as shown the sample measurement in Figure 3.4. The trail full-widths at half-maximum are, as expected, significantly narrower than $w_{\text{obs,final}}$ or $w_{\text{fit,final}}$, but more comparable with previous studies. This suggests that the absolute brightness threshold for width measurements, as well as the increased sensitivity of the CAMO system, contributes to the large widths observed in this study relative to previous works.

Figure 3.11 shows the peak observed, fit, and FWHM trail widths for each frame of the meteor capture as a function of height. Looking at the observed and fit widths, the trail starts off very wide, around 80 m, between heights of 110 km and 105 km, then rapidly begins to narrow, becoming negligible within uncertainty around 101 km. The trail FWHM varies less with height, starting at nearly 35 m above 106 km, and then decreasing to become negligible around

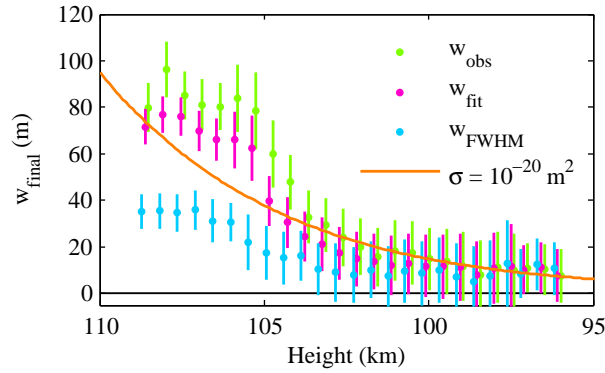


Figure 3.11: The peak, final, corrected widths ($w_{\text{obs,final}}$ in green, $w_{\text{fit,final}}$ in red, $w_{\text{FWHM,final}}$ in blue) for each frame of 20101020_095900 as a function of height. Data from both stations are combined. Points for w_{fit} and w_{FWHM} have been shifted slightly to the left to make the points more visible. The atmospheric mean free path of an atom with collision cross section $\sigma = 10^{-20} \text{ m}^2$, is plotted. The ambient atmospheric mean free path is too small to be seen well in this plot (for reference, $\lambda_{\text{mfp}} \approx 0.4 \text{ m}$ at a height of 105 km). Atmospheric density for λ_{mfp} is from MSIS-E-90 (Hedin 1991).

103.5 km. Below a height of 105 km, the three types of width measurements agree within uncertainty, likely due to the brightness of the trail decreasing such that the half-maximum threshold (for w_{FWHM}) becomes equal to the 2σ above the background threshold (for w_{obs} and w_{fit}). As in the single frame comparison, the trail FWHM values show better agreement with previous optical studies, such as Kaiser et al. (2004), Cook et al. (1962), and Hawkins & Whipple (1958), than the threshold-based trail widths.

The peak, corrected observed trail width measurement, for each individual narrow-field station, for each frame of 20101020_095900 is given in Figure 3.12. Twenty-two frames were observed with both narrow-field stations, showing good agreement between stations for all but two frames. This may be quantified by looking at a fractional difference in peak widths,

$$\Delta w_f = \frac{|w_{\text{final},01} - w_{\text{final},02}|}{\sqrt{\Delta w_{\text{final},01}^2 + \Delta w_{\text{final},02}^2}}, \quad (3.18)$$

between stations, where $w_{\text{final},01}$ and $w_{\text{final},02}$ are the peak, corrected widths for Tavistock and Elginfield, respectively, and $\Delta w_{\text{final},01}$ and $\Delta w_{\text{final},02}$ are the associated uncertainties. There is agreement between stations when $\Delta w_f < 1$, when the difference in peak widths between sta-

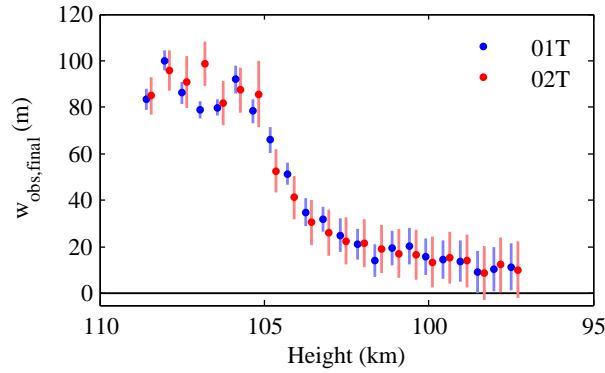


Figure 3.12: The peak corrected observed widths, $w_{\text{obs,final}}$, for each station for each frame of 20101020_095900. Tavistock is 01T, while Elginfield is 02T, marked in blue and red, respectively. For 20 of the 22 frames, there is good agreement of peak corrected trail width measurements between stations, quantified in Figure 3.13.

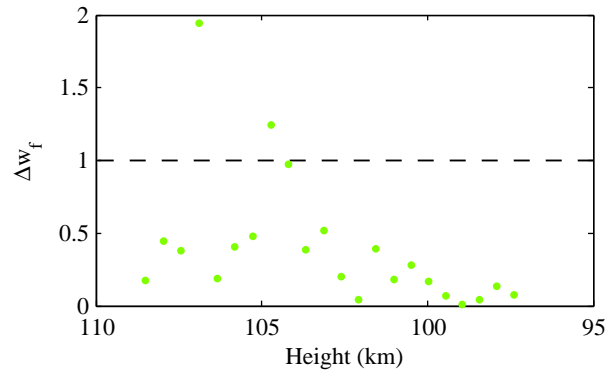


Figure 3.13: The fractional difference, Δw_f , in peak corrected observed widths, $w_{\text{obs,final}}$, between stations for each frame of 20101020_095900. The mean fractional difference over all frames is 0.40, implying good agreement in width measurements between stations.

tions is less than the total uncertainty. Values for all frames of 20101020_095900 are shown in Figure 3.13. It can be seen that $\Delta w_f < 1$ for 20 of the 22 frames, with a mean fractional difference of 0.40, implying good agreement between stations for this event.

Returning to Figure 3.11, the trail width coarsely matches the functional form of the mean free path of a particle in the atmosphere with interaction cross section $\sigma = 10^{-20} \text{ m}^2$. It may be recalled that the mean free path, λ_{mfp} of a well-mixed, Boltzmann-distributed gas of one species with cross section σ and number density ρ is given by

$$\lambda_{\text{mfp}} = \frac{1}{\sqrt{2}} \frac{1}{\sigma \rho}. \quad (3.19)$$

The ambient atmospheric mean free path is too small to be shown in Figure 3.11, about an order of magnitude smaller than the observed trail width. The height dependence of the trail width suggests that it is constrained by the atmospheric density, though the interaction cross section of particles from the energetic meteor are an order of magnitude smaller than the collisional cross section of ambient atmospheric particles.

3.4.2 General results from all meteors studied

The peak observed, corrected trail width for each frame of each meteor capture of this survey is plotted versus height in Figure 3.14. Above a height of 105 km, corrected trail widths up to 180 m, but more commonly between 40–100 m, are observed. At heights below 105 km, the trail widths tend to become negligible within uncertainty. The atmospheric mean free path length of particles with cross sections between 10^{-21} and 10^{-19} m² is also plotted, as well as the ambient atmospheric mean free path, with a cross section of the order 4×10^{-19} m² (Schlatter 2009).

The comparison of width measurement between stations for events recorded with two narrow-field stations is shown in Table 3.6. For each two-station event, the fractional difference in peak corrected observed width values between stations, as given by Eq. 3.18, is determined for each frame and then averaged over all frames. Each event, except 20101106_055725, shows an average fractional difference close to or below 1, implying that the width measurements from the stations agree, and that difference in peak widths between stations is accounted for by the associated uncertainty.

As in the case of the representative event, it is clear that the measured trail widths are at least an order of magnitude larger than the mean free path of ambient atmospheric particles, implying that the trail light production cross section with the atmosphere is an order of magnitude smaller than the atmosphere's ambient collisional cross section. An average, constant cross section may be fit to the trail widths, assuming that it takes a single collision with an atmospheric atom to produce light from excited atoms. Plotting the trail radius (half trail width)

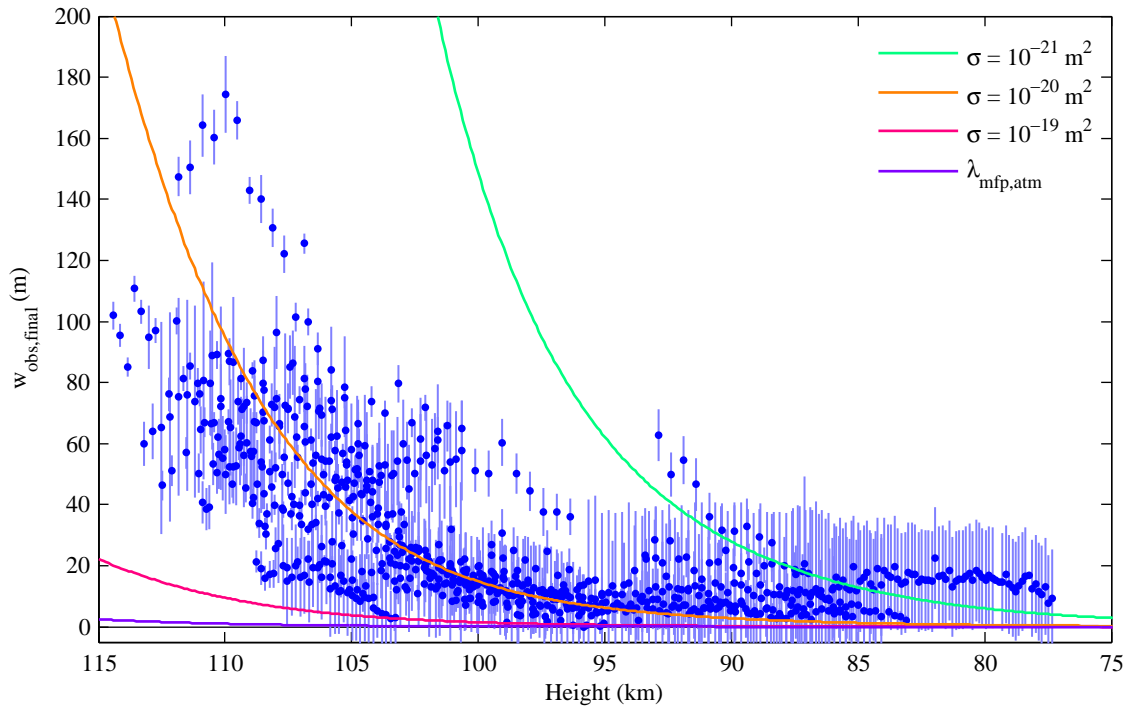


Figure 3.14: Peak corrected, observed trail width for each frame of each meteor video as a function of height. Curves for the mean free path of particles with cross sections between 10^{-21} and 10^{-19} m^2 , and the mean free path of ambient atmospheric particles, are also plotted. Mean free path values are calculated using the MSIS-E-90 density profile (Hedin 1991).

Table 3.6: The average fractional difference, $\Delta\bar{w}_f$, of peak width measurements over all frames between stations for each two-station event. Δw_f is defined by Eq. (3.18).

Event	Frames	$\Delta\bar{w}_f$
20101020_094418	8	0.96
20101020_095900	22	0.40
20101020_101727	8	0.41
20101103_031542	3	0.52
20101103_033400	27	0.45
20101103_045928	16	0.31
20101103_053624	8	0.11
20101103_061127	20	0.32
20101103_061856	37	0.63
20101103_062801	23	0.34
20101103_071855	8	1.05
20101103_072624	10	1.05
20101103_073846	1	0.68
20101106_055725	13	1.41

versus the inverse of the atmospheric density at the height corresponding to the trail radius observations, yields a linear graph with slope equal to the inverse of the average cross section, as in Eq. (3.19). The resulting fit cross section is $1.33 \pm 0.03 \times 10^{-20} \text{ m}^2$ for the observed widths, $1.66 \pm 0.05 \times 10^{-20} \text{ m}^2$ for the fit widths, and $3.2 \pm 0.2 \times 10^{-20} \text{ m}^2$ for the full widths at half maximum. Though the average values vary based on type of trail width measurement, it is important to note that they are all of the order 10^{-20} m^2 .

Collision cross sections of the order 10^{-20} m^2 have been observed for atoms with relative velocities above 20 km s^{-1} by Sida (1969) and Vinković (2007). The variable hard shell model for particle collisions (Bird 1994, Shen 2005) references similar cross sections for atoms at high velocities. Johnson, Liu & Tully (2002) state that the momentum transfer cross section for a particle varies between 10^{-19} m^2 and 10^{-21} m^2 for particles with kinetic energy between 10 eV and 1 keV. This range of energy is appropriate to describe atoms released from a meteor travelling between 18–72 km s^{-1} . For reference, a sodium particle at 18 km/s has a kinetic energy of 39 eV, while an iron particle at 72 km s^{-1} has an energy of 1.5 keV. The dependence of cross section on relative velocity is given in Figure 3.15 according to several references.

A plausible procedure for light emission in the trail are the collisions between ambient atmospheric atoms or molecules and excited atoms from the co-moving high density pocket of gas immediately surrounding the meteoroid. As the meteoroid is travelling at a high velocity in the order of km s^{-1} , the ambient atmospheric particles are stationary in comparison, and a collision cross section of the order 10^{-20} m^2 is appropriate. If the excited atom is not de-excited after the first collision, its speed is decreased as a result of the collision, and subsequent collisions occur at larger cross sections producing shorter mean free path lengths. During some (or all) of these collisions, a photon is released, contributing to the optical meteor trail. As noted previously, detailed simulations by Jones (1995) suggested particle thermalisation after about five collisions, giving an upper bound to the number of collisions before the mean free path length is insignificant compared to the expected trail width. Within uncertainty, this mechanism is consistent with our trail width observations, provided the initial cross section is

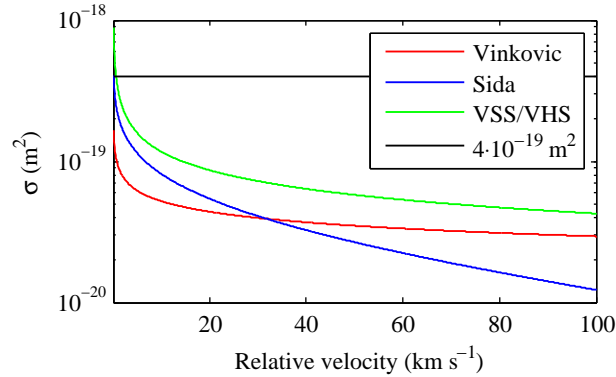


Figure 3.15: Example particle collision cross sections as a function of relative particle velocity, by Vinković (2007), Sida (1969), and Bird (1994) variable soft/hard shell (VSS/VHS) models. The mean ambient atmospheric collisional cross section of $\sim 4 \times 10^{-19} \text{ m}^2$ is also plotted for comparison.

$\sim 10^{-16}$.

At least one alternate possibility for the formation of wide meteor trails is a photochemical process in which energetic collisions between fast meteoroid atoms and atmospheric particles produce ultraviolet photons with extremely small absorption cross sections. These UV photons are absorbed and produce excitation or ionization in ambient atmospheric atoms far from the meteoroid, which then contribute to trail brightness by later, visible wavelength de-excitation or recombination. As noted in the Introduction, this process was suggested by Stenbaek-Nielsen & Jenniskens (2004), but not modeled. Another plausible process worth further investigation is triboelectric charging of meteoroids, which produces anomalous fragmentation and transverse spreading at high altitudes, as discussed by Spurný & Ceplecha (2008).

Further measurements of collision cross sections will have to be done for energetic neutral particles, particularly N, N₂, O, O₂ from the atmosphere, and Na, Mg, Fe, Si, and other metallic elements from the meteoroid to better model the process of optical trail formation. A more detailed simulation of particle collisions, similar to those by Jones (1995) or Boyd (2000), with appropriate cross sections, would help to clarify the process. An additional benefit of a detailed simulation would be to provide comparison with meteor morphology captured with the CAMO's narrow-field cameras. This would help to understand whether alternative processes,

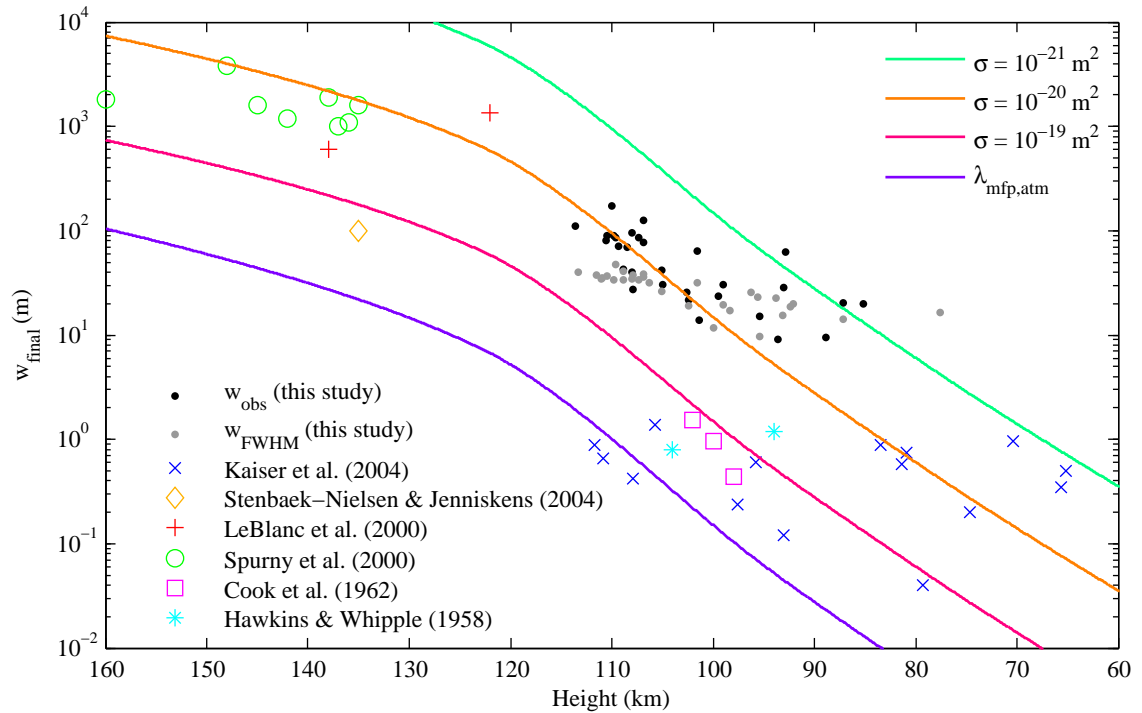


Figure 3.16: Peak width results for each meteor from this survey of optical trail widths, as well as previous surveys. The observed width is given to be consistent with the Leonid measurements (LeBlanc et al. 2000, Spurný et al. 2000, Stenbaek-Nielsen & Jenniskens 2004), and the FWHM is given to be consistent with photographic measurements (Hawkins & Whipple 1958, Cook et al. 1962, Hawkins 1963) and the survey by Kaiser et al. (2004). Uncertainty bars have been omitted for clarity.

such as meteoroid fragmentation or the progressive release of grains, contribute to the trail width in addition to the release of excited atoms and ions from the meteoroid.

Previous photographic studies (Hawkins & Whipple 1958, Cook et al. 1962) measured optical trail widths up to 9.3 m at heights above 100 km, while multi-wavelength radar studies revealed initial ion trail widths up to nearly 6 m at 110 km. Image-intensified, digital camera studies of meteor trails revealed average widths up to 1.37 ± 0.71 m (Kaiser et al. 2004), while measurements of bright Leonids at altitudes above 120 km revealed widths of the order of kilometres (Spurný et al. 2000, LeBlanc et al. 2000), jets (LeBlanc et al. 2000), and spherical structures up to 200 m in diameter around the head of the meteor (Stenbaek-Nielsen & Jenniskens 2004). The results of the current survey, in addition to other optical surveys,

are presented in Figure 3.16. Photographic studies, as well as the video study by Kaiser et al. (2004) have produced smaller widths at equivalent heights compared to the results of this survey, while the intensified video Leonid studies have produced widths roughly consistent with collisional de-excitation of atoms with $\sigma \sim 10^{-20} \text{ m}^2$, as seen here. Differences in study instrumentation and methodology, as well as sampled meteor population, will now be considered to explain the different results from each trail width survey.

For radar-based observations, a discrepancy in trail widths may be explained by noting that fundamentally different trails are being examined: radar measures the ion trails, while the CAMO system studies trails comprised of excited atoms. Assuming that both trails are constrained by collisions with atmospheric particles, the ratio of the ionic collisional cross section versus the atomic collisional cross section would yield a ratio of the widths of the initial ion trail and the optical trail, assuming negligible ion trail diffusion, recombination, or attachment. Phelps (1991) observes that the momentum transfer cross section for N_2^+ with N_2 is 1–2 orders of magnitude larger than the corresponding cross section for N_2 with N_2 for energies between 1– 10^3 eV. A similar relationship exists between the ionic and atomic collision cross sections for Ar. If this ratio of ionic to atomic collision cross section holds for meteoric species, it is reasonable that the initial ion trail be 1–2 orders of magnitude narrower than the visible trail, similar to what is observed when comparing previous radar trail measurements to the results of this study.

Previous photographic studies and the video-based study of Kaiser et al., (2004) quantified trail widths as the full widths at half maximum of the transverse trail brightness profile. For this study, $w_{\text{obs}} > w_{\text{FWHM}}$ typically by a factor of 2–3, as shown in Table 3.5. Also, this study measured the maximum widths observed for multiple short exposures (1/110 s) of the meteor, while the photographic studies measured the widths of the trail integrated over a long exposure. An analogue of this with the current study results would be to average all of the width values observed over a single frame, and subsequently average all of the resulting widths for a single meteor. These average widths would be significantly narrower than the peak widths reported

for this study. This also helps to explain why the Leonid measurements appear to agree better with the measurements of this survey, as instantaneous measurements of the meteor width were taken on high frame rate systems. The width measurements also appeared to be taken to a threshold brightness value, as opposed to the full width at half maximum.

A difference in spectral response may also have contributed to the difference in trail widths observed by the photographic studies and the CAMO system. The majority of meteors observed in the photographic studies of Hawkins & Whipple (1958) and Cook et al. (1962) were captured on Eastman 103a-O blue-sensitive or 103a-E red-sensitive plates, with nominal sensitivity at 410 and 650 nm (and bandpasses of 110 and 50 nm, Reid et al. 1991), respectively, while the intensifiers on the CAMO system have nominal response between 500–850 nm. Having a broader, as well as redder spectral response on the CAMO system may have allowed more of the excitation states of the meteor trail to be observed, resulting in a wider trail. The intensified video systems employed by LeBlanc et al. (2000), Spurný et al. (2000), and Stenbaek-Nielsen & Jenniskens (2004) also had wide sensitivity, from ~350–850 nm, helping to explain the larger widths seen by these surveys.

A final difference may be in the meteor populations studied. Twenty of the thirty meteors observed in this survey had speeds over 60 km s^{-1} . Geminids, with speeds of 35 km s^{-1} , were studied by Cook et al. (1962). The beginning heights of the meteors studied by Kaiser et al. (2005) were distributed evenly from 65–110 km, while the majority (21) of meteors in this study had beginning heights over 110 km. The meteors with the largest beginning heights and velocities tended to display the largest width for this study, not only due to the more rarefied atmosphere at larger heights resulting in larger mean free path lengths, but also likely due to different origins and compositions than the slower objects. Again, this is expressed in the larger trail widths observed for the high-altitude Leonids of Spurný et al. (2000), LeBlanc et al. (2000), and Stenbaek-Nielsen & Jenniskens (2004).

3.5 Conclusions

The goal of this study was to quantify meteor optical trail width as a function of height. Thirty meteors were observed with the CAMO system, and widths up to 100 m were observed at heights above 110 km. The widths correspond to (and vary with height as) the mean free path length travelled by excited atoms emitted from the meteoroid through the atmosphere, with collision cross sections of the order 10^{-20} m². Though these widths are larger than those observed in previous radar and optical studies at equivalent heights, they do not conflict with them due to differences in instrument sensitivity, measurement technique, and sampled meteor populations.

Future work should focus two principal areas. First, detailed, particle-based modelling will help reveal how optical meteor trails are formed, and how their size relates to the meteor's ion trail. Second, additional observations with the CAMO system will better reveal how initial trail widths vary with initial height, velocity, and meteoroid mass. Comparative studies of different meteor showers would also show the correlation of meteoroid composition and parent body with meteor trail width.

Bibliography

Baggaley, W. J., (1970). The determination of the initial radii of meteor trains. *Monthly Notices of the Royal Astronomical Society*, 147, 231-243.

Baggaley, W. J., (1980). Measurements of the velocity dependence of the initial radii of meteor trails. *Bulletin of the Astronomical Institute of Czechoslovakia*, 31 (5), 308-311.

Bird, G. A., *Molecular gas dynamics and the direct simulation of gas flows*. Oxford University Press, 1994.

Borovička, J., (1990). The comparison of two methods of determining meteor trajectories from photographs. *Bulletin of the Astronomical Institutes of Czechoslovakia*, 41, 391-396.

Boyd, I. D., (2000). Computation of atmospheric entry flow about a Leonid meteoroid. *Earth, Moon, and Planets*, 82-83, 93-108.

Campbell-Brown, M., Jones, J., (2003). Determining the initial radius of meteor trains: fragmentation. *Monthly Notices of the Royal Astronomical Society*, 343, 775-780.

Campbell-Brown, M. D., Jones, J., (2006). Annual variation of sporadic radar meteor rates. *Monthly Notices of the Royal Astronomical Society*, 367, 709-716.

Ceplecha, Z., (1987). Geometric, dynamic, orbital, and photometric data on meteoroids from photographic fireball networks. *Bulletin of the Astronomical Institutes of Czechoslovakia*, 38, 222-234.

Close, S., Brown, P., Campbell-Brown, M., Oppenheim, M., Colestock, P., (2007). Meteor head echo radar data: mass-velocity selection effects. *Icarus*, 186, 547-556.

Cook, A. F., Hawkins, G. S., Stienon, F. M., (1962). Meteor trail widths. *The Astronomical Journal*, 67 (3), 158-162.

Duda, R. O., Hart, P. E., (1972). Use of the Hough transformation to detect lines and curves in pictures. *Communications of the ACM*, 15 (1), 11-15.

Dyrud, K., Wilson, D., Boerve, S., Trulsen, J., Pecseli, H., Close, S., Chen, C., Yoonjae, L., (2008). Plasma and electromagnetic wave simulations of meteors. *Advances in Space Research*, 42, 136-142.

Greenhow, J. S, Hall, J. E., (1960). The importance of initial trail radius on the apparent height and number distributions of meteor echoes. *Monthly Notices of the Royal Astronomical Society*, 121 (2), 183-197.

Groom, D. E., Eberhard, P. H., Holland, S. E., Levi, M. E., Palaio, N. P., Perlmutter, S., Stover, R. J., Wei, M., (1999). Point spread function in depleted and partially depleted CCDs. Technical Report DE2001-788013, LBNL-45276, Lawrence Berkeley National Laboratory, 8pp.

Gural, P. S., Jenniskens, P. M., Varros, G., (2004). Results from the AIM-IT meteor tracking system. *Earth, Moon, and Planets* 95, 541-552.

Hawkes, R. L., Jones, J., (1978). The effect of rotation on the initial radius of meteor trains. *Monthly Notices of the Royal Astronomical Society*, 185, 727-734.

Hawkins, G. S., (1963). The initial diameter of meteor trails. *Smithsonian Contributions to Astrophysics*, 7, 23-26.

Hawkins, G. S., Whipple, F. L., (1958). The width of meteor trails. *The Astronomical Journal*, 63 (1261), 283-291.

Hedin, A. E., (1991). Extension of the MSIS thermospheric model into the middle and lower atmosphere. *Journal of Geophysical Research*, 96, 1159-1172.

Jenniskens, P., (2004). Meteor induced chemistry, ablation products, and dust in the middle and upper atmosphere from optical spectroscopy of meteors. *Advances Space Research*, 33, 1444-1454.

Jenniskens, P., Butow, S. J., (1999). The 1998 Leonid multi-instrument aircraft campaign—an early review. *Meteoritics & Planetary Science*, 34, 933-943.

Jenniskens, P., Jehin, E., Cabanac, R. A., Laux, C. O., Boyd, I. D., (2004). Spectroscopic anatomy of a meteor trail cross section with the European Southern Observatory Very Large Telescope. *Meteoritics & Planetary Science*, 39 (4), 609-616.

Johnson, R. E., Liu, M. Tully, C., (2002). Collisional dissociation cross sections for O + O₂, CO and N₂, O₂ + O₂, N + N₂, and N₂ + N₂. *Planetary and Space Science*, 50, 123-128.

Jones, J., Campbell-Brown, M., (2005). The initial train radius of sporadic meteors. *Monthly Notices of the Royal Astronomical Society*, 359, 1131-1136.

Jones, W., (1995). Theory of the initial radius of meteor trains. *Monthly Notices of the Royal Astronomical Society*, 275, 812-818.

Kaiser, N., Brown, P., Hawkes, R. L., (2004). Optical trail width measurements of faint meteors. *Earth, Moon, and Planets*, 95, 579-586.

Kascheyev, B. L., Lebedinets, V. N., (1963). The initial radius of ionized meteor trails. *Smithsonian Contribution to Astrophysics*, 7, 19-22.

LeBlanc, A. G., Murray, I. S., Hawkes, R. L., Worden, P., Campbell, M. D., Brown, P., Jenniskens, P., Correll, R. R., Montague, T., Babcock, D. D., (2000). Evidence for transverse spread in Leonid meteors. *Monthly Notices of the Royal Astronomical Society*, 313, L9-L13.

Manning, L. A., (1958). The initial radius of meteoric ionization trails. *Journal of Geophysical Research*, 63 (1), 181-196.

Oppenheim, M. M., Sugar, G., Bass, E., Dimant, Y. S., Chau, J., (2008). Day to night variation in meteor trail measurements: evidence for a new theory of plasma trail evolution. *Geophysical Research Letters*, 35, L03102, 5pp.

Phelps, A. V., (1991). Cross sections and swarm coefficients for nitrogen ions and neutrals in N₂ and argon ions and neutrals in Ar for energies from 0.1 eV to 10 keV. *Journal of Physical and Chemical Reference Data*, 20 (3), 557-573.

Press, W. H., Teukolsky, S. A., Vetterling, W. T., Flannery, B. P., *Numerical recipes: the art of scientific computing*, third edition. Cambridge University Press, 2007.

Rasband, W. S., ImageJ, U. S. National Institutes of Health, Bethesda, Maryland, USA, <http://imagej.nih.gov/ij/>, 1997-2012.

Reid, I. N, Brewer, C., Brucato, R. J., McKinley, W. R., Maury, A., Mendenhall, D., Mould, J. R., Mueller, J., Neugebauer, G., Phinney, J., Sargent, L. W., Schombert, J., Thicksten, R., (1991). The second Palomar Sky Survey. *Publications of the Astronomical Society of the Pacific*, 103, 661-674.

Shen, C., *Rarefied gas dynamics: fundamentals, simulations and micro flows*. Springer, 2005.

Sida, D. W., (1969). The production of ions and electrons by meteoritic processes. *Monthly Notices of the Royal Astronomical Society*, 143, 37-47.

Schlatter, T. W., (2009). *Atmospheric composition and vertical structure*. National Oceanic and Atmospheric Administration, 54pp.

Spurný, P., Betlem, H., Jobse, K., Kotten, P., van't Leven, J., (2000). New type of radiation of bright Leonid meteors above 130 km. *Meteoritics & Planetary Science*, 35, 1109-1115.

Spurný, P., Ceplecha, Z., (2008). Is electric charge separation the main process for kinetic energy transformation into the meteor phenomenon? *Astronomy & Astrophysics*, 489, 449-454.

Stenbaek-Nielsen, H. C., Jenniskens, P., (2004). A “shocking” Leonid meteor at 1000 fps. *Advances in Space Research*, 33, 1459-1465.

Tseng, Q., (2011). Study of multicellular architecture with controlled microenvironment. Ph. D. thesis, Université de Grenoble.

Vinković, D., (2007). Thermalization of sputtered particles as the source of diffuse radiation from high altitude meteors. *Advances in Space Research*, 39, 574-582.

Weryk, R. J., Brown, P. G., (2012). Simultaneous radar and video meteors—I: Metric comparisons. *Planetary and Space Science*, 62, 132-152.

Weryk, R. J., Brown, P. G., (2013). Simultaneous radar and video meteors—II: Photometry and ionisation. *Planetary and Space Science*, 81, 32-47.

Weryk, R. J., Brown, P. G., Domokos, A., Edwards, W. N., Krzeminski, Z., Nudds, S. H., Welch, D. L., (2008). The Southern Ontario All-sky Meteor Camera Network. *Earth, Moon and Planets*, 102, 241-246.

Weryk, R. J., Campbell-Brown, M. D., Wiegert, P. A., Brown, P. G., Krzeminski, Z., Musci, R., (2013). The Canadian Automated Meteor Observatory (CAMO): System overview. *Icarus*, 225, 614-622.

Chapter 4

Observations of gross fragmentation in faint meteors

A version of this chapter has been published as:

- Stokan, E., Campbell-Brown, M. D., (2014). *Transverse motion of fragmenting faint meteors observed with the Canadian Automated Meteor Observatory*. *Icarus*, 232, 1-12.

4.1 Introduction

As meteoroids enter the atmosphere, they begin to ablate and emit light. The resulting light curve, plotting intensity as a function of height, serves as an important constraint for meteoroid ablation models. These models provide information about ablation processes, meteoroid composition, and atmospheric chemistry (Hawkes & Jones 1975, Boyd 2000, Campbell-Brown & Koschny 2004). Meteoroid fragmentation is also an important process to characterise, as it biases radar observations (Campbell-Brown & Jones 2003, Baggaley & Grant 2004), and can provide insight into meteoroid strength and composition (Ceplecha et al. 1998, Borovička & Kalenda 2003).

Fragmentation can occur on a scale ranging from gross (or macroscopic) fragmentation, where the meteoroid splits into a small number of discernible pieces that separate, to continuous (or microscopic) fragmentation, where the fragments are small and numerous enough to not be distinguishable. Gross fragmentation typically occurs for bright meteors such as Peekskill (Brown et al. 1994), or more recently, Chelyabinsk (Borovička et al. 2013), and is observed directly in video and photographic records, or indirectly as sharp spikes or flares in the meteor light curve. Conversely, continuous fragmentation is expected to be more common for fainter, less massive objects, and has been modelled as an explanation for the size and height-dependence of the faint meteor initial ion trail (Hawkes & Jones 1978, Campbell-Brown & Jones 2003).

Observing gross fragmentation in faint meteors with video is challenging due to the requirements of high brightness sensitivity and fine spatial resolution, both needed to discern the individual, faint fragments. Faint meteors are often observed with backscatter radar rather than video, which is more sensitive to continuous fragmentation (and the associated widening of the ion trail detected by the radar) than gross fragmentation. This may explain why gross fragmentation is observed more commonly in brighter meteors. Possible faint meteor gross fragmentation was observed with radar by Elford & Campbell (2001) as oscillations in the meteor head echo amplitude.

Alternately, fragmentation in faint and bright meteors may be the same physical process, but at different size scales. Jacchia (1955) notes that ablation continuously detaches the grains that comprise a meteoroid. For a small meteoroid producing a faint meteor, these grains are of comparable size to the meteoroid. This is not the case for a brighter, more massive body, which is expected to be much larger than the size of its constituent grains. As a result, smaller meteoroids will appear to continuously fragment, while the continuous fragmentation of larger bodies will not be perceptible. Instead, macroscopic fragmentation related to the inhomogeneity of a larger body would be observed at later stages of the meteoroid ablation.

The principal mechanism for the gross fragmentation of large objects is usually taken to be

aerodynamic loading (Passey & Melosh 1980, Artemieva & Shuvalov 2001). Determining the atmospheric density at the height of fragmentation and calculating a cross-sectional area for the meteoroid (given a shape, mass and assumed density) gives the aerodynamic pressure on the body at the point of fragmentation, which is taken to be equal to the strength of the meteoroid. Strength values of 10^6 and 10^7 Pa have been measured for the Benešov and Sikhote-Alin meteorites, respectively (Artemieva & Shuvalov 2001). Borovička & Kalenda (2003) calculated a strength of 5×10^6 Pa based on the height of fragmentation for the Morávka meteoroid. Passey & Melosh (1980) suggested strengths between $10^5 - 10^8$ Pa for bright meteors that yielded meteorites. Similarly, Popova et al. (2011) determined strengths between $10^5 - 10^7$ Pa in a review of 13 fragmenting meteoroids that produced meteorites.

For fainter objects, macroscopic fragmentation is less understood as the process occurs at relatively large heights ($h \geq 80$ km) where the atmosphere is rarefied. Trigo-Rodríguez & Llorca (2006, 2007) obtained strengths of the order 10^4 Pa for a number of shower meteors with cometary parent bodies. These were determined by assuming that flares in the light curve represented fragmentation and obtaining the corresponding aerodynamic pressure at those heights. Similarly, Borovička, Spurný & Koten (2007) obtained a strength of 5×10^3 Pa for a Draconid meteor, but suggested that meteoroid heating may have been more significant in causing fragmentation than aerodynamic pressure at a height of 100 km. In any case, bright meteors appear stronger than faint meteors, though it should be noted that many of the faint, high-altitude meteors studied were from cometary parent bodies.

Several alternate mechanisms have been proposed for fragmentation associated with faint meteors, such as rotation (Hawkes & Jones 1978), catastrophic charging (Spurný & Ceplecha 2008), or explosive devolatilization (Kramer 1968, Stoch 1991). Evaluation and refinement of these models has been hindered by few direct, high-resolution observations of gross fragmentation in faint meteors. Similarly, the transverse spreading of the fragments from faint meteors is poorly understood. As aerodynamic drag is proportional to the cross-section area of the object, fragments with different masses are expected to drift apart in the direction of travel, forming a

meteor trail. At lower heights, around 50 km, flowfield interaction accounts for dispersion of fragments perpendicular to the meteor trail (Artemieva & Shuvalov 2001). This provides an explanation for deeply-penetrating meteoroids. Conversely, for faint meteors at higher altitudes characterised by free molecular flow, there is negligible flowfield interaction as atmospheric particles collide directly with the meteoroid, with ablated meteor vapour providing negligible shielding (Campbell-Brown & Koschny 2004).

The Canadian Automated Meteor Observatory (CAMO) is a two-station, high-resolution, image-intensified video system that has captured approximately 3000 meteors operating from August 2010 and 2013. Examining the events for fragmentation is an ongoing process, but 1800 have been inspected so far, and 311 were observed to have gross fragmented, showing at least two distinct fragments. Of those meteors, 32 were observed to show possible transverse (perpendicular to meteor trail) motion for the fragments. CAMO is able to provide high-resolution data to constrain models of gross fragmentation in faint meteors, and has already been used to provide new observations of faint meteor trails (Stokan et al. 2013) and test current dustball ablation models (Campbell-Brown et al. 2013). The goals of this study are: to select a small number (9) of the highest-quality observations of faint meteor gross fragmentation, with fragments showing transverse motion; to characterise the fragment transverse motion (determine the speed of the motion and whether the fragments are accelerating, extrapolate a height of fragmentation); and, to apply basic iterations of fragmentation models to suggest what caused the fragmentation and transverse spreading.

4.2 Instruments and analysis

4.2.1 The Canadian Automated Meteor Observatory

CAMO is an image-intensified, automated video system, comprised of two stations located in southern Ontario, Canada. The stations are separated by a baseline of 45 km. At each station, a camera with a wide, 28° field of view (25 mm $f/0.85$ lens) automatically detects meteors

and provides tracking information for a complementary, narrow-field camera that follows the meteor in flight. The narrow-field system uses two mirror-mounted galvanometers to guide light from the meteor into a ZenithStar 80 mm $f/6.8$ telescope. This gives a 1.5° field of view for high spatial resolution observations of the meteor.

The wide- and narrow-field systems both use Imperx IPX-VGA120L cameras with 640×480 pixel resolution at 12-bits per pixel to minimise image saturation. Both systems are lens-coupled to third-generation ITT NiteCam 380i image intensifiers with nominal sensitivity between 500 and 800 nm. The limiting detection magnitude for meteors observed with CAMO is approximately +5, giving an approximate mass sensitivity limit of 10^{-6} kg. The wide-field system operates at 80 frames per second, while the narrow-field system operates at 110 frames per second. The galvanometers tracking the meteor for the narrow-field system update positions at 2000 Hz to ensure smooth tracking based on a linear fit prepared in real-time using wide-field data. This is an evolution of the AIM-IT system developed by Gural, Jenniskens & Varros (2004). All narrow- and wide-field cameras are synchronised by GPS clock to allow for direct comparison of observations from all cameras. In practise, the lag between systems is less than one narrow-field frame.

The detection, tracking, and capture of the meteors with both cameras is completely automated, allowing for a large number of observations per night. Additional details regarding the system are available in Weryk et al. (2013).

For one of the nine meteors studied, wide-field observations were obtained with the CAMO influx system. The influx system is comprised of two high-resolution wide-field cameras (Cooke PCO.1600 with a 50 mm $f/0.95$ lens; one camera at each station) and is used to measure meteoroid orbits with high precision (Musci et al. 2012). The influx cameras also use ITT NiteCam intensifiers and have a similar spectral response as the narrow- and wide-field systems, though with a limiting meteor magnitude of +6.5. The system has a 20° field of view, capturing videos at 1600×1200 resolution, 20 frames per second, with 14-bits per pixel. A delay of 0.06 ms was measured between the influx system and the narrow- and wide-field systems

and compensated for in all calculations.

4.2.2 Wide-field reductions

Data from the double-station wide-field cameras were used to determine the trajectory and light curve for each meteor. The software package METAL (Weryk & Brown 2012) allows the position of the meteor to be selected in each frame of the wide-field video. An astrometric and photometric plate is created for each station by selecting stars in the field of view, calibrating their pixel position and instrumental magnitude (logarithm of the summed brightness of the star) with catalogue position and magnitude, respectively. The trajectory solver MILIG (Borovička 1990), integrated into METAL, calculates the trajectory of the meteor using the position of the meteor in each frame of the videos from both stations. The instrumental, apparent magnitude of the meteor in each frame is converted to an R -band magnitude with the photometric plate, and then converted to an absolute magnitude using the computed range to the meteor at each frame time. Astrometry and photometry using METAL are discussed in more detail in Weryk & Brown (2012, 2013).

The photometric mass, m_p , was computed by integrating the measured light curve,

$$m_p = \int \frac{2}{\tau v^2} I(t) dt, \quad (4.1)$$

where τ is the dimensionless luminous efficiency, v is the average speed of the meteoroid, and $I(t)$ is the intensity or radiant power, converted from the observed absolute magnitude, $M(t)$, knowing that the intensity of a zero-magnitude meteor in the CAMO system's spectral bandpass, I_0 , is 820 W (Weryk & Brown 2013),

$$I(t) = I_0 10^{-0.4M(t)}. \quad (4.2)$$

Weryk & Brown (2013) give new expressions for the luminous efficiency, τ , as related to the

ionization coefficient, β . Simplifying these,

$$\log_{10} \tau = -0.09v^{1/2} - 3.00 \log_{10} v - \frac{9.56}{\log_{10} v} + 10.11, \quad (4.3)$$

where the velocity, v , is given in km s^{-1} . This value of τ is larger than other commonly published values by a factor of 10, consequently making the meteoroid masses smaller by a factor of 10. The photometric mass is then determined by integrating the light curve with Eqs. (4.1) and (4.2), applying τ given by Eq. (4.3), using the average speed measured for the meteoroid.

The orbital parameters of each meteor were calculated using methods from Ceplecha (1987). Uncertainties in the trajectory and orbital parameters were obtained by a Monte-Carlo simulation, computing 1000 trajectory solutions with one pixel of random error in the meteor position for each frame, as well as one pixel of systematic error in a random direction applied to each solution. The standard deviation in the parameters resulting from the 1000 solutions were taken to represent the uncertainty in each parameter.

4.2.3 Narrow-field reductions

Determining the transverse motion of fragments was done by selecting the pixel position of each fragment in each frame of the narrow-field video for each meteor. A fiducial fragment was selected for each video, typically the fragment that was successfully identified in the largest number of frames for the video. The distance, in pixels, of each fragment with respect to the fiducial fragment was then calculated for each frame. To determine the transverse (perpendicular to meteor trail) position of each fragment, the trail angle of the meteor, θ_t , was measured in several frames of the event video. In general, the orientation of the meteor does not change as it's tracked by the narrow-field system, so the trail angle and uncertainty were taken from the mean and standard deviation, respectively, of the trail angle values measured over multiple frames.

The transverse displacement of each fragment **a** with respect to fiducial fragment **b** is then

given by

$$dx'_{a,b} = dx_{a,b} \sin \theta_t + dy_{a,b} \cos \theta_t, \quad (4.4)$$

where $dx_{a,b} = x_a - x_b$, x_a and y_a are the x - and y -pixel coordinates for fragment **a**, and θ_t is measured counterclockwise from the horizontal axis. Finally, the transverse position is converted from pixels to metres,

$$dX'_{a,b} = pRdx'_{a,b}, \quad (4.5)$$

using the pixel scale, p , in radians per pixel, of the narrow-field system and the range from the camera to the meteoroid, R , computed from the wide-field data. The result of this procedure is transverse distance of each fragment with respect to a selected fiducial fragment as a function of time. The along-trail separation was also recorded.

It should be noted that the transverse distance just calculated is the projection of the actual transverse distance between fragments on the image plane of the camera recording the fragmentation. As a result, the actual distance between fragments is larger than, or at least equal to the recorded values. Three of the nine events were captured with both narrow-field stations allowing for possible determination of the true transverse distance between fragments, but the meteors were hazy and showed a large number of fragments that were difficult to mutually identify in both stations. This may be improved in future studies, and the agreement of transverse speeds measured between stations will be discussed in Section 4.3.

To improve the precision of fragment position picks, up to three image improvement filters were applied: background subtraction, wavelet filtering, and median filtering. Background subtraction improves image contrast by taking the mean pixel brightness value across the entire frame and subtracting it from each pixel value. The minimum corrected pixel brightness value is zero. The second filter employed a difference of Gaussians wavelet kernel,

$$g(r; \sigma_1, \sigma_2) = \frac{1}{\sqrt{2\pi\sigma_2^2}} \exp\left(-\frac{r^2}{2\sigma_2^2}\right) - \frac{1}{\sqrt{2\pi\sigma_1^2}} \exp\left(-\frac{r^2}{2\sigma_1^2}\right), \quad (4.6)$$

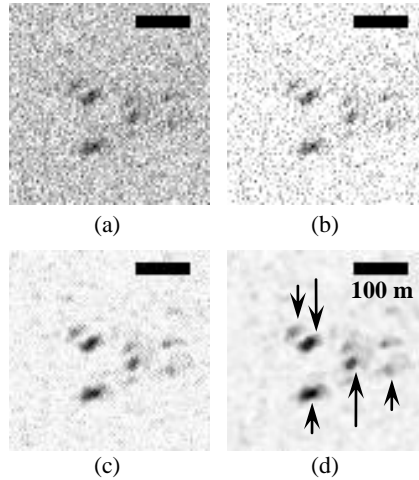


Figure 4.1: An example of image improvement filtering for event 20120523_080013, as observed from the Tavistock (01T) narrow-field station. (a) is the original frame, (b) shows the effect of background subtraction, (c) additionally shows the effect of wavelet filtering, and (d) additionally shows the effect of 3×3 median filtering. Five fragments are marked in the final frame. Scale bars indicate a length of 100 m at the range of the meteor. The image is inverted to show features better.

to remove speckle noise from the frame. This is an approximation of the Mexican hat wavelet. In Eq. (4.6), r is the radial distance from the centre pixel on which the filter is applied, and σ_1 and σ_2 describe the width of the central peak and outer rim. To apply the wavelet filter, the frame was Fourier transformed. The frame transform was multiplied with Eq. (4.6), a bandpass filter in Fourier space used to remove features of high and low spatial frequency, typically speckle and smearing noise, respectively. Equivalently, in image space, any objects with a radius differing from the wavelet radius will be filtered out. The radius of the wavelet was adjustable, and set to the approximate size of fragments present in the image. In general, good results were achieved with $\sigma_1 = 0.60$ and $\sigma_2 = 0.58$ pixels, respectively. The final step was application of a median filter, set to filter each pixel in the frame to the median of the 3×3 grid surrounding the pixel. The effect of the filters are illustrated in Figure 4.1.

A polynomial was then fit by linear least-squares to the perpendicular displacement of each fragment with respect to the fiducial fragment as a function of time. The majority of fragments were fit equally well with first-order and second-order polynomials, comparing fit residuals and observed transverse speed ranges. This indicated negligible transverse acceleration for the

fragments. This will be demonstrated for a few sample events in Section 4.3. The transverse speed of each fragment was determined by these polynomials.

The along-trail displacement was also fit by a first-order polynomial to allow an estimation of the fragmentation height. The total squared distance, both perpendicular and parallel to trail, between each fragment was given by

$$p = \frac{1}{W} \sum_{i=1}^{N_{\text{frag}}} \sum_{j>i}^{N_{\text{frag}}} w_{i,j} (p_i - p_j)^2 \quad (4.7)$$

where p is the polynomial describing the total squared distance between all fragments as a function of time, p_i and p_j are the polynomial fits to the perpendicular (and parallel) displacements of fragments \mathbf{i} and \mathbf{j} as a function of time, $w_{i,j}$ is a weighting factor proportional to the number of points, n_i and n_j for each fragment,

$$w_{i,j} = n_i n_j, \quad (4.8)$$

and W is the sum of the weighting factors. After the polynomial describing the total distance between fragments was computed, the minimum distance was found by finding the time, t_0 , at which the derivative of p is zero,

$$\left. \frac{dp}{dt} \right|_{t=t_0} = 0. \quad (4.9)$$

This time of minimum distance was then converted to a height using the wide-field trajectory solution.

4.3 Observations of fragmentation

For the nine meteors analysed in this study, three fragmentation modes were observed: single (gross) fragmentation, where the meteoroid appeared to fragment once; multiple (gross) fragmentations, where the meteoroid fragmented several times; and complex fragmentation, where

the meteoroid produced a large number of fragments that were not distinct enough to follow (hazy appearance), continuously fragmented, or fragmented several times off-screen, making it difficult to determine the fragmentation hierarchy. A sample event from each fragmentation mode will be reviewed, and general observations about the nine meteors presented after.

4.3.1 Single fragmentation

Two of the nine meteors selected showed single fragmentation. Six narrow-field frames from a sample event, 20101016_070052, are given in Figure 4.2. This meteor was observed on 2010 October 16 at 07:00:52 UTC (the event designation has the form YYYYMMDD_HHMMSS, with the time in UTC). Fragmentation appears to have occurred just before the first frame, which captured the meteor at a height of 83.6 km, producing bright and easily-distinguishable fragments with long trails. Five fragments were identified and tracked, with perpendicular displacements given in Figure 4.3. Computing linear fits to the perpendicular displacement of each fragment as a function of time gives a wide range of speeds, from -78 m s^{-1} to 83 m s^{-1} . A fragmentation height of 83.0 km is extrapolated from the smallest displacement between all fragments (when perpendicular and along-trail distances are considered). This is just after the first frame of the narrow-field video, where separate fragments were already observed, suggesting uncertainty in the fragment positions may have pushed the extrapolated height of fragmentation lower than the actual height.

A second-order fit was also considered for the perpendicular displacement of each fragment. This allows for constant, non-zero transverse acceleration for the fragments. Four of the five fragments showed negligible transverse-component acceleration within uncertainty. The transverse speed of each fragment was also determined to be equivalent within uncertainty for first- and second-order fits, considering the range of speeds for the second-order fits. Finally, the height of fragmentation and the residual of the fit for each fragment did not change significantly between fit orders. Values for the transverse acceleration and speed for each fit order are given in Table 4.1. Taken together, this implies that acceleration in the transverse-trail

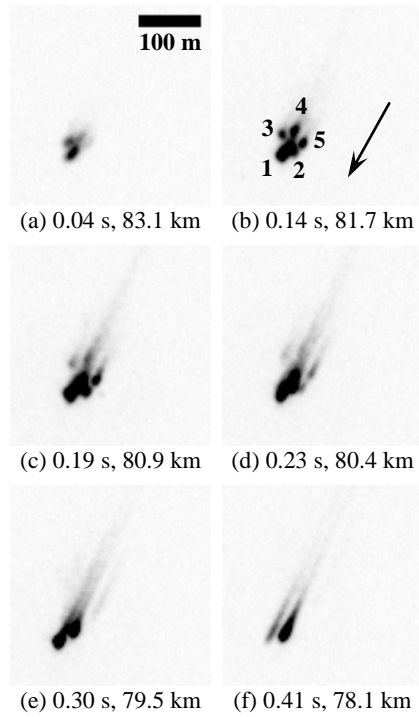


Figure 4.2: Snapshots of single fragmentation event 20101016_070052. A scale bar indicating 100 m is given in the first frame, and the direction of travel as well as fragment numbers are given in the next frame. Times given are the interval after the first frame recorded.

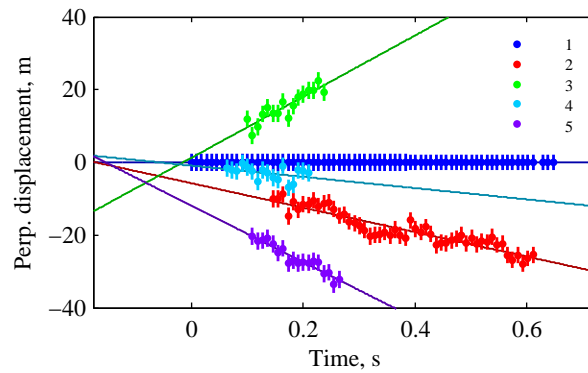


Figure 4.3: Transverse displacement of fragments for meteor 20101016_070052. Fragment numbers correspond to Figure 4.2 and Table 4.1. As in Fig. 4.2, times are given with respect to the first recorded frame. The extrapolated time of fragmentation is 0.03 s, corresponding to a height of 83.0 km. In this case, the fragmentation appears to occur slightly after the convergence of fragments 1, 2, 4, and 5. This is an effect of including the along-trail displacements in Eq. (4.7), as the fragments separated more rapidly in the along-trail than the transverse direction.

Table 4.1: Second- and first-order fit parameters for the fragments of 20101016_070052. Transverse acceleration for all of the fragments is (or is nearly) insignificant. The average transverse speed for the second-order fit for each fragment matches the speed obtained with the first-order fit. Together, this suggests that a first-order fit is adequate to describe the observations, and that transverse acceleration appears negligible.

Frag.	2nd order accel. (m s^{-2})	2nd order speed (m s^{-1})	Linear speed (m s^{-1})
1	0 ± 8	0	0 ± 1.4
2	26 ± 19	-33.6 ± 12.0	-33.6 ± 2.3
3	53 ± 368	84.5 ± 7.3	83.9 ± 14.1
4	258 ± 319	-15.4 ± 37.8	-16.2 ± 12.4
5	9 ± 274	-77.9 ± 1.4	-78.1 ± 11.6

component for each fragment is negligible for this meteor.

The light curve for this meteor (as well as the other sample meteors) is given in Figure 4.4. The curve has a symmetric shape that is not atypical of meteors observed with CAMO’s intensified cameras. Of interest for this particular event is the presence of two apparent peaks, at heights of 80.9 and 79.5 km, as well as a possible flare at 77.9 km. This is unexpected, as peaks and flares are generally associated with fragmentation, yet the narrow-field system showed only one fragmentation at 83.0 km, far above these features. In this case, the peaks may be related to microscopic-scale fragmentation not resolvable with the narrow-field system. This is evident in comparing Fig. 4.2 (b) to (c), and Fig. 4.2 (d) to (e), where the trails behind each fragment become longer and brighter. Another possibility is that volatile material in the meteoroid may have been exposed suddenly and allowed to ablate, causing an unexpected increase in brightness. Alternately, the dip in light curve between the peaks may have been an artefact due to local transient sky conditions. Unfortunately, that part of the meteor trajectory was only observed with the Tavistock (01K) station, making verification with the Elginfield (02K) station impossible. Similarly, it is difficult to state whether or not the flare at 77.9 km is an artefact since it occurred only over a single frame.

The peak absolute magnitude observed for this meteor was -0.7 ± 0.1 , while the photometric mass was 1×10^{-4} kg. This was one of the brightest and most massive meteoroids observed in this study, where photometric masses were typically observed to be $10^{-6} - 10^{-5}$ kg. Similarly,

the speed of this meteoroid was $19.1 \pm 1.0 \text{ km s}^{-1}$, one of the slowest. As a result, the meteor height interval of $86.0 - 75.2 (\pm 0.9) \text{ km}$ is relatively low. Interestingly, the orbital parameters ($a = 2.53 \pm 0.53 \text{ AU}$, $i = 14.5^\circ \pm 1.6$, $T_j = 3.07 \pm 0.50$) indicate that the meteoroid may be of asteroidal origin.

4.3.2 Multiple fragmentations

The majority of meteors in this study (four out of name) showed multiple discrete fragmentations. Meteor 20101010.023500 was first detected at $100.3 \pm 0.4 \text{ km}$ and ended at 87.1 km , with a speed of $31.1 \pm 0.1 \text{ km s}^{-1}$. The light curve is given in Figure 4.4 (b). Unlike the previous meteor, the peak of this light curve occurs towards the end height. The peak absolute magnitude was $+1.5 \pm 0.1$, and $m_p = 6 \times 10^{-5} \text{ kg}$. Orbital elements suggest that this meteoroid is also asteroidal ($a = 1.90 \pm 0.07 \text{ AU}$, $i = 5.8^\circ \pm 0.7$, $T_j = 3.40 \pm 0.08$).

Six narrow-field frames are given in Figure 4.5. The first two frames show fragments from the principal fragmentation, extrapolated to occur at a height of 96.9 km , just before the narrow-field camera began tracking the object. The fragments drift apart at a speed of $59.3 \pm 4.3 \text{ m s}^{-1}$ perpendicular to the meteor trail. The trailing fragment then breaks into two objects, as shown in the next frame. This occurs at a height of 93.3 km . These two fragments spread rapidly with a transverse speed component of $119 \pm 14 \text{ m s}^{-1}$. The trailing fragments then dissipate, and the leading fragment splits into three pieces at a height of 91.7 km . One of the fragments shows a transverse speed of $7 \pm 17 \text{ m s}^{-1}$ relative to the fiducial fragment, which is insignificant within uncertainty. The other fragment shows a much larger separation speed of $118 \pm 10 \text{ m s}^{-1}$. The transverse displacement of each fragment with respect to fragment 1 is shown in Figure 4.6.

As with the previous meteor, first- and second-order fits were applied to the fragment displacement data. For all fragmentations, the transverse acceleration term was negligible within a large uncertainty value. This is likely due to the small number of points for each fit. Similarly, the height of fragmentation did not change, and the residuals to the fit for each fragment's data were not reduced in moving from a linear to a quadratic fit, so a first-order fit was selected as

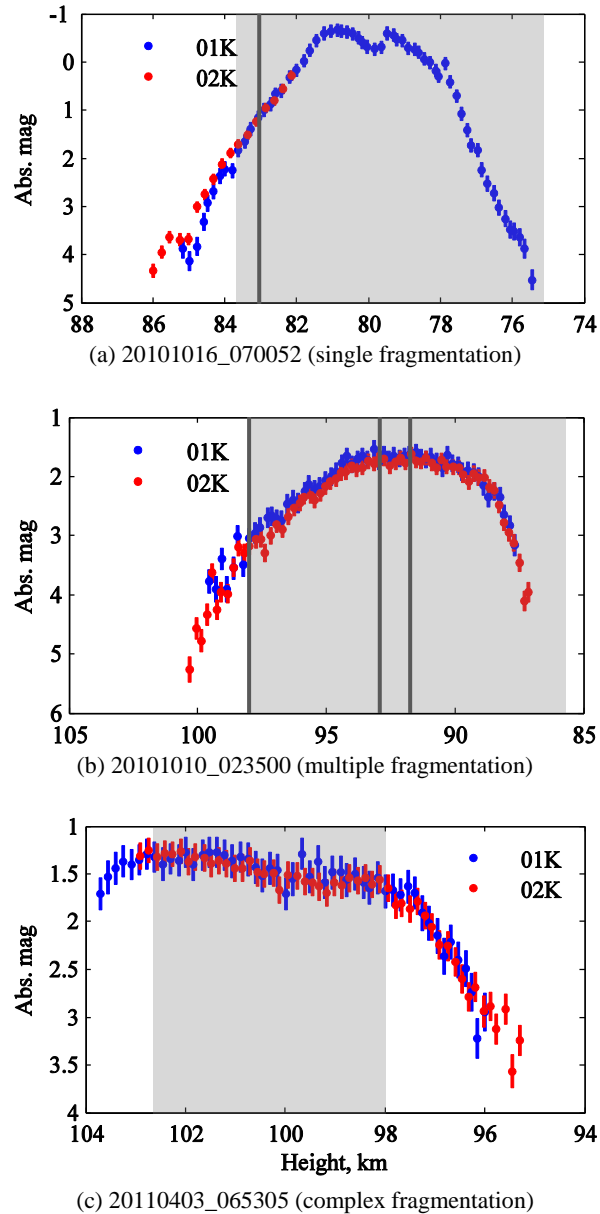


Figure 4.4: Light curves for the three selected sample meteors, observed with both CAMO stations: Tavistock (01K) and Elginfield (02K). The shaded area indicates the height interval over which the meteor was tracked with the narrow-field camera. Vertical lines indicate extrapolated heights of fragmentation.

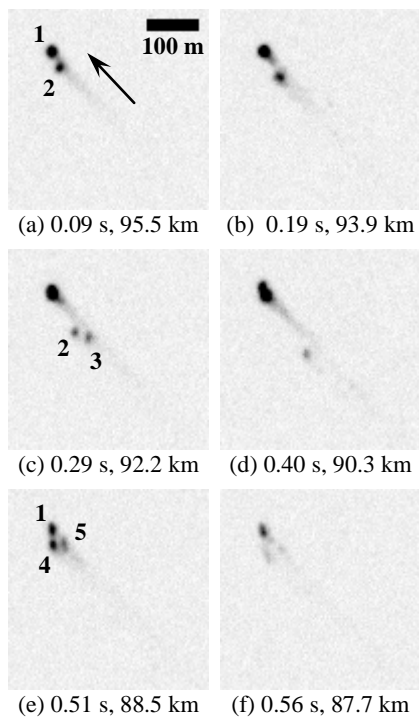


Figure 4.5: Multiple fragmentation event 20101010.023500. A scale bar indicating 100 m is given in the first frame, as well as the direction of travel. The initial fragments are 1 and 2. Fragment 2 splits into 2 and 3. Subsequently, fragment 1 splits into 1, 4 and 5.

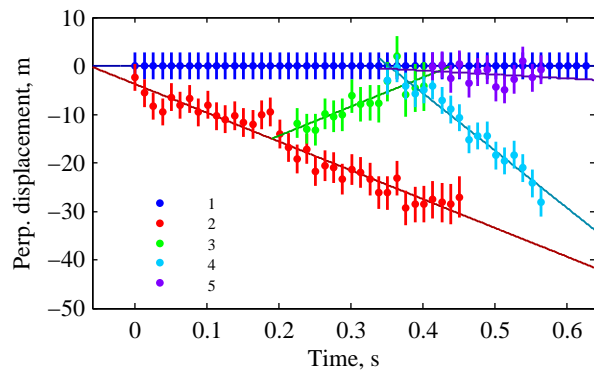


Figure 4.6: Transverse displacement of all fragments for event 20101010.023500. Fragmentations occur at -0.01 , 0.22 , and 0.32 s, at heights of 96.9 , 93.3 , and 91.7 km, respectively.

with the first meteor reviewed.

4.3.3 Complex fragmentation

Three of the nine meteors either continuously fragmented, were very dim and showed a large number of indistinguishable fragments, or fragmented possibly multiple times before the narrow-field video began. These meteors were classified as having undergone *complex* fragmentation. An example event is 20110403_065305, presenting an unexpected arrangement of fragments that appear almost like a stream of small meteoroids rather than the result of the fragmentation of a single body, as seen in the narrow-field frames of Figure 4.7. Seven fragments were identified and tracked from frame to frame, though more are present in the video. The two larger fragments at the front of the meteor appear to converge at a different height (114.7 km) than the group of smaller fragments trailing behind (103.9 km). Both fragmentation heights are above the first frame captured with the narrow-field system, while the height of the first fragmentation is also above the wide-field coverage, indicated by the 104 km first height in the light curve. Unfortunately, as the meteor appeared from the edge of both wide-field cameras' fields of view, the beginning of the light curve, Figure 4.4 (c) was truncated.

Transverse speeds for the fragments ranged from 22 ± 11 to 79 ± 16 m s⁻¹ with respect to the chosen fiducial fragment. A graph of the fragment spread is given in Figure 4.8. The two large fragments at the front of the stream moved apart at a speed of 54.0 ± 4.7 m s⁻¹, while the fragments behind displayed a range of transverse speeds, from -14.1 ± 8.4 to 44 ± 11 m s⁻¹. The peak absolute magnitude recorded was $+1.2 \pm 0.1$, with $m_p = 1 \times 10^{-6}$ kg. This was one of the least massive meteors observed for this study, though it must be recalled that the beginning of the meteor was not recorded, which may artificially decrease the photometric mass. Unlike the previous two sample meteors, it is likely that this meteoroid has a cometary origin based on the high speed, 68.9 ± 0.3 km s⁻¹, and associated orbital parameters ($a = 3.79 \pm 0.40$ AU, $i = 157.7^\circ \pm 0.7$, $T_j = 0.31 \pm 0.41$).

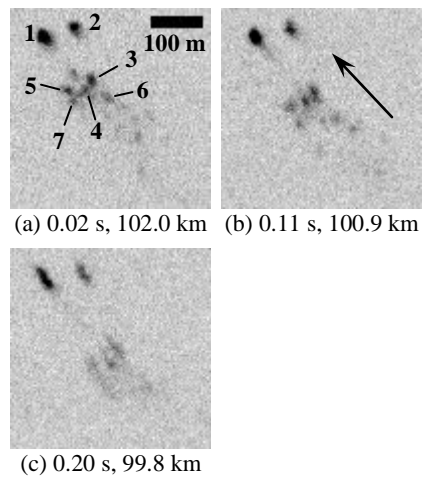


Figure 4.7: Three snapshots of the complex fragmentation event 20110403.065306. The appearance of the swarm is distinct, with two large fragments in front, and a stream of smaller, dimmer fragments that are poorly-differentiated in the back. Seven selected fragments are numbered in the first frame, and a scale bar indicating 100 m is given. The direction of travel is given in the second frame.

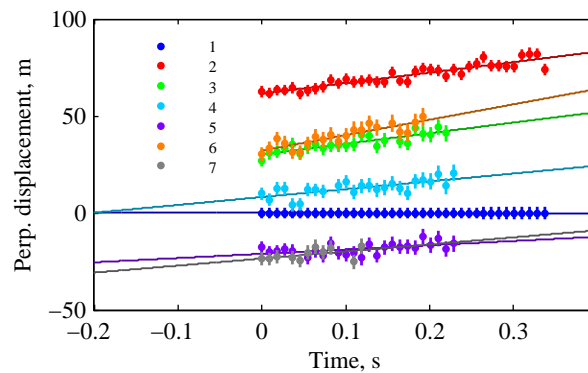


Figure 4.8: Transverse displacement of all fragments of 20110403.065305. Many of the fragments appear to be travelling at nearly the same transverse speed with respect to fragment 1.

4.3.4 Summary of observations

The transverse speeds observed for all fragments of all meteors in this survey are summarised in Table 4.2. Examining the range in transverse speeds across all fragments belonging to a single meteor, values up to $163 \pm 12 \text{ m s}^{-1}$ were obtained. To put these values into context, the aerodynamic loading fragmentation model presented by Artemieva & Shuvalov (2001) gives a fragment separation speed of

$$U = v \sqrt{C \frac{\rho_{\text{atm}}}{\rho_{\text{met}}}}, \quad (4.10)$$

where v is the meteoroid speed, C is a constant related to the number of fragments being produced (ranging from 0.2 for two fragments to 1 for many fragments), and ρ_{atm} and ρ_{met} are the atmospheric and meteoroid densities respectively. Considering meteor 20100914_054515, with $v = 30.2 \text{ km s}^{-1}$, $C = 1$, $\rho_{\text{atm}} = 7.3 \times 10^{-7} \text{ kg m}^{-3}$ at 99.3 km (MSIS-E-90, Hedin 1991), and $\rho_{\text{met}} = 3300 \text{ kg m}^{-3}$ gives $U = 0.45 \text{ m s}^{-1}$, far smaller than the 77.0 m s^{-1} observed. It should be noted that the Artemieva & Shuvalov (2001) model is more appropriate to larger meteoroids (fireballs that produce meteorites) at lower heights where there is denser, continuum flow about the meteoroid, but is the only quantitative model for comparison. Some preliminary modelling will be introduced in the next section to propose methods for meteoroid fragmentation other than aerodynamic loading.

Three meteors, 20100914_054515, 20120322_072602, and 20120523_080013, were recorded with two narrow-field stations allowing for a comparison of transverse speeds obtained from each station. Both stations of 20100914_054515 and 20120322_072602 agreed within uncertainty; conversely, the range in transverse speeds for fragments of 20120523_080013 did not agree between stations. Agreement is influenced by how similar the viewing perspective is between stations: since the transverse speed is defined as occurring in the image plane, different definitions of the plane for each camera can result in different transverse speeds being measured. Similarly, a large number of fragments, as in the case of 20120523_080013, can make it difficult to measure the range in transverse speed between the same fragments as observed

Table 4.2: All observed fragment transverse speeds, as well as the number of fragments, N_{frag} , and the range in transverse speed $v_{t,\text{range}}$. Some events have multiple entries, corresponding to different stations (Tavistock, 01T vs. Elginfield, 02T), or different fragmentation events for multiple fragmentations (I, II, III).

	$v_{t,\text{range}}$ (m s^{-1})	N_{frag}	v_t (m s^{-1})						
20100914	77.0	3	-76.9	-73.9	0.1				
_054515 (01T)	± 8.7		± 7.3	± 17.7	± 4.8				
20100914	85.1	2	0.0	85.1					
_054515 (02T)	± 7.0		± 4.5	± 5.4					
20101010	59.2	2	-59.2	0.0					
_023500 (I)	± 4.7		± 4.2	± 2.1					
20101010	119.0	2	-0.1	118.9					
_023500 (II)	± 15.0		± 3.5	± 14.6					
20101010	118.0	3	-118.0	-7.7	0.0				
_023500 (III)	± 10.5		± 10.3	± 17.1	± 2.1				
20101013	151.1	7	-95.1	-48.5	-30.1	0.0	5.7	49.6	56.0
_064003	± 8.4		± 8.2	± 1.4	± 1.8	± 1.4	± 5.4	± 3.3	± 1.7
20101016	161.3	5	-78.1	-33.6	-16.2	0.0	83.9		
_070052	± 18.3		± 11.6	± 2.3	± 12.4	± 1.4	± 14.1		
20110204	21.2	2	-21.3	-0.1					
_023725	± 4.2		± 3.0	± 3.0					
20110330	46.2	3	-0.1	30.5	46.1				
_061029 (I)	± 3.0		± 2.0	± 4.7	± 2.2				
20110330	23.0	2	-0.1	22.9					
_061029 (II)	± 20.5		± 2.0	± 20.4					
20110403	53.9	2	0.1	54.0					
_065305 (I)	± 6.7		± 4.8	± 4.7					
20110403	58.3	5	-14.1	-6.6	0.0	17.6	44.2		
_065305 (II)	± 14.0		± 8.4	± 24.3	± 8.2	± 8.9	± 11.2		
20120322	1.2	2	0.4	1.6					
_072602 (01T)	± 16.2		± 9.6	± 13.0					
20120322	12.2	2	-0.2	12.0					
_072602 (02T)	± 14.5		± 9.7	± 10.8					
20120523	83.9	7	0.0	11.7	12.4	37.2	41.3	59.6	83.9
_080013 (01T)	± 3.9		± 1.5	± 9.1	± 4.5	± 2.4	± 6.1	± 1.6	± 3.6
20120523	163.2	5	-63.3	-5.1	0.0	46.9	99.9		
_080013 (02T)	± 12.3		± 9.1	± 11.5	± 3.6	± 7.1	± 8.3		

with each camera. Additional complications in the case of 20120523_080013 were different tracking heights for the 01T (94.9 – 84.9 km) and 02T (91.1 – 86.0 km) stations, as the meteor entered the 02T field of view late, and the hazy, ill-resolved appearance of fragments for that meteor.

Table 4.3 presents the observed meteoroid velocity and meteor height interval, as well as the height of peak magnitude, the extrapolated fragmentation height, the peak observed absolute magnitude, the photometric mass, and the fragmentation mode. Orbital parameters for each meteoroid, including the Tisserand parameter with respect to Jupiter, T_j , are given in Table 4.4. The radiant, uncertainty, and convergence angle (angle between the two stations and the meteor) are given in Table 4.5. Four of the objects have $T_j \geq 3$, indicating possible asteroidal origin, while three have $2 \leq T_j \leq 3$, characteristic of Jupiter-family comets. The other two meteoroids may be related to isotropic comets, having smaller Tisserand parameters and high inclinations. Briefly comparing height of fragmentation, range in fragment transverse speeds, and Tisserand parameters, there do not appear to be any correlations. It may have been expected that objects with smaller Tisserand parameters (cometary meteoroids of lower strength and density) fragment higher in the atmosphere, and consequently display a larger range in transverse speeds, due to lower strengths, but this is not the case. It may be recalled that the Tisserand parameter is not a definitive indicator of parent body for a meteoroid, as non-conservative (radiative) forces can change the meteoroid orbit, and thus, its original T_j . Similarly, it is difficult to draw any broad conclusions from a small number of meteors, particularly since they were selected to have a particular characteristic (distinct fragments with significant transverse spread), and may not be representative of their orbital group.

4.4 Models of fragmentation

In the previous section, it was noted that the observed transverse speed of fragments for all meteors was about two orders of magnitude larger than expected from the aerodynamic loading

Table 4.3: Summary table, giving average observed meteor speed, v_{obs} , the beginning and ending height from the wide-field cameras, h_{B} and h_{E} , height at which the peak magnitude occurred, h_{max} , extrapolated height of fragmentation, h_{frag} , peak absolute magnitude, M_{abs} , photometric mass, m_{p} , and fragmentation mode (S - single, M - multiple, C - complex). Some events had more than one height of fragmentation, either based on multiple sites (01T) and (02T), or due to multiple fragmentations (I, II, III, ...).

	v_{obs} (km s^{-1})	h_{B} (km)	h_{E} (km)	h_{max} (km)	h_{frag} (km)	M_{abs}	m_{p} (10^{-6} kg)	Frag. mode
20100914	30.2	98.0	84.4	93.4	104.3 (01T)	1.6	2	C
_054515	± 0.1	± 0.2	± 0.2	± 1.4	99.3 (02T)	± 0.1		
20101010	31.1	100.3	87.1	92.4	96.9 (I)	1.5	60	M (3)
_023500	± 0.1	± 0.4	± 0.4	± 1.1	93.3 (II) 91.7 (III)	± 0.1		
20101013	27.5	97.9	77.5	92.3	100.8	2.5	3	M (2+)
_064003	± 0.1	± 0.2	± 0.2	± 0.2	<91?	± 0.1		
20101016	19.1	86.0	75.2	81.5	83.0	-0.7	100	S
_070052	± 1.0	± 0.9	± 0.9	± 1.3		± 0.1		
20110204	16.0	95.3	78.8	83.2	93.6	1.0	100	S
_023725	± 0.2	± 1.0	± 1.0	± 1.0		± 0.1		
20110330	25.5	95.7	81.2	86.7	94.5 (I)	0.4	10	M (2)
_061029	± 0.1	± 0.2	± 0.2	± 0.4	90.0 (II)	± 0.1		
20110403	68.9	103.7	95.3	102.1	114.7?	1.2	1	C
_065305	± 0.3	± 0.4	± 0.4	± 0.9	103.9?	± 0.1		
20120322	43.8	101.0	85.9	96.3	95.0 (01T)	1.4	0.7	M (2)
_072602	± 0.3	± 0.2	± 0.2	± 0.3	95.4 (02T)	± 0.1		
20120523	29.1	96.0	83.6	92.9	97.2? (01T)	1.7	5	C
_080013	± 0.1	± 0.4	± 0.4	± 1.2	97.0? (02T)	± 0.2		

Table 4.4: Orbital elements for each of the nine meteoroids, including geocentric speed corrected for zenithal attraction and diurnal aberration, v_g , semimajor axis, a , eccentricity, e , inclination, i , argument of perihelion, ω , perihelion distance q_{per} , and Tisserand parameter with respect to Jupiter, T_j .

	v_g (km s^{-1})	a (AU)	e	i ($^\circ$)	ω ($^\circ$)	q_{per} (AU)	T_j
20100914_054515	28.0 ± 0.1	1.78 ± 0.08	0.821 ± 0.003	5.2 ± 0.9	301.0 ± 1.5	0.319 ± 0.009	3.59 ± 0.10
20101010_023500	28.7 ± 0.1	1.90 ± 0.07	0.834 ± 0.003	5.8 ± 0.7	120.4 ± 1.2	0.315 ± 0.007	3.40 ± 0.08
20101013_064003	25.2 ± 0.1	3.41 ± 0.10	0.712 ± 0.008	40.1 ± 0.2	195.8 ± 0.2	0.982 ± 0.001	2.40 ± 0.13
20101016_070052	15.9 ± 1.2	2.53 ± 0.53	0.663 ± 0.069	14.5 ± 1.6	230.5 ± 4.8	0.853 ± 0.023	3.07 ± 0.50
20110204_023725	11.5 ± 0.2	2.50 ± 0.12	0.614 ± 0.019	12.1 ± 0.3	19.2 ± 0.8	0.965 ± 0.002	3.15 ± 0.09
20110330_061029	23.0 ± 0.1	2.85 ± 0.12	0.785 ± 0.007	6.6 ± 0.4	263.1 ± 1.0	0.612 ± 0.006	2.74 ± 0.05
20110403_065305	67.7 ± 0.3	3.79 ± 0.40	0.740 ± 0.028	157.7 ± 0.7	195.5 ± 1.7	0.984 ± 0.003	0.31 ± 0.41
20120322_072602	42.3 ± 0.3	3.73 ± 0.49	0.898 ± 0.012	63.3 ± 0.9	287.9 ± 2.0	0.380 ± 0.013	1.73 ± 0.63
20120523_080013	27.1 ± 0.1	2.51 ± 0.15	0.825 ± 0.007	3.6 ± 0.7	284.5 ± 1.5	0.440 ± 0.010	2.85 ± 0.06

Table 4.5: Geocentric right ascension and declination, α_g and δ_g , respectively, radiant uncertainty, Δ , and convergence angle, Q , for each of the nine meteors observed.

	α_g ($^\circ$)	δ_g ($^\circ$)	Δ ($^\circ$)	Q ($^\circ$)
20100914_054515	3.8	6.4	0.7	19.4
20101010_023500	30.6	7.8	0.5	14.2
20101013_064003	294.1	68.8	0.1	52.3
20101016_070052	348.2	32.7	3.1	12.5
20110204_023725	84.4	-16.3	0.8	21.2
20110330_061029	189.3	6.1	0.5	21.1
20110403_065305	278.6	-10.5	0.4	11.9
20120322_072602	222.1	18.0	0.6	23.4
20120523_080013	248.1	-18.0	0.7	13.1

model of Artemieva & Shuvalov (2001). Other fragmentation mechanisms, including rotational breakup, and electrostatic charging and repulsion, will now be considered.

4.4.1 Aerodynamic loading

In addition to estimating the transverse speed of fragments with Eq. (4.10), the aerodynamic pressure applied to the front of the meteoroid is computed by

$$P_d \approx \Gamma \rho_{\text{atm}} v^2, \quad (4.11)$$

where Γ , the drag coefficient, is assumed to be unity. Using the values for meteoroid velocity and extrapolated fragmentation height given in Table 4.3, the fragmentation pressures varied between 200 – 4000 Pa. Meteoroid strengths are reported to be of the order 10^3 Pa for fragile material to 10^8 Pa for stony material by Hawkes & Jones (1978). It is unlikely that all of the meteoroids studied in this survey are exceptionally fragile, especially if some (those with $T_j \geq 3$) may have originated from asteroidal parent bodies. Instead, this comparison reiterates that aerodynamic loading is inadequate to explain the fragmentation of these faint, high-altitude objects.

4.4.2 Rotation

Rotation as a mechanism of meteoroid fragmentation was first investigated by Hawkes & Jones (1978) and more recently reviewed by Fisher et al. (2000). For this study, we perform some basic calculations assuming that the meteoroid is a rigid body comprised of spherical fragments on a two-dimensional plane. It is assumed that each of the fragments is of equivalent mass and located an equal distance, r , from the centre of mass of the rigid body, given by

$$r \approx \sqrt[3]{\frac{3m_p}{4\pi\rho_{\text{met}}}}, \quad (4.12)$$

where m_p is the photometric mass, and ρ_{met} is the meteoroid density, assumed to take a moderate value of 3300 kg m^{-3} . This value of r is similar to the one obtained if it is assumed that each of the fragments is spherical, of equivalent mass, and densely-packed such that they just touch.

Next, the transverse motion of the meteoroid's centre of mass is determined,

$$v_{\text{cm}} = \frac{1}{m_p} \sum_i m_i v_i, \quad (4.13)$$

where $m_i = m_p/N_{\text{frag}}$ is the mass and v_i is the observed transverse speed of each fragment. Eq. (4.13) simplifies to $v_{\text{cm}} = \bar{v}_i$ as each fragment is assumed to be of equal mass. The transverse motion of each fragment is then determined in the centre of mass frame,

$$v_{\text{cm},i} = v_i - v_{\text{cm}}. \quad (4.14)$$

The maximum observed transverse speed, $v_{\text{cm},\text{max}} = \max(|v_{\text{cm},i}|)$, is then used to compute the centrifugal force for each fragment of the meteoroid,

$$F_{\text{rot}} = \frac{m_p v_{\text{cm},\text{max}}^2}{r}. \quad (4.15)$$

Eq. (4.15) implicitly assumes that all rotation is in the image plane, that all of the speed for the fragment with the largest transverse speed is in the transverse direction, and that the body is rigid (all fragments have the same tangential speed).

The meteoroid's associated rotational frequency is

$$f_{\text{rot}} = \frac{v_{\text{cm},\text{max}}}{2\pi r}. \quad (4.16)$$

If the meteoroid is assumed to approximate a sphere with radius r given by Eq. (4.12), the pressure applied over the entire surface area is given by

$$P_{\text{rot}} = \frac{F_{\text{rot}}}{4\pi r^2}. \quad (4.17)$$

This can be used to estimate a strength value for the meteoroid, based on the observed fragment transverse speeds.

For single and complex fragmentation events, Eqs. (4.12) - (4.17) are applied once. For multiple fragmentation events, the first fragmentation makes use of the entire photometric mass. Subsequent fragmentations set m_p equivalent to the fractional mass of the parent fragment, which also enables r to change for each fragmentation. Similarly, as different fragments are being considered, v_{cm} differs for each fragmentation. The most reliable results are obtained for single fragmentation events, as there are fewer assumptions, but it is expected that applying the method to multiple and complex fragmentations will also yield order of magnitude estimates of meteoroid strength and rotational rates.

The results of rotational modeling are presented in Table 4.6. In contrast to aerodynamic loading, strengths of the order 10^6 Pa are obtained, which fall within the expected range given by Hawkes & Jones (1978), and agree with the strength estimates of larger, meteorite-dropping objects as reviewed in Section 4.1. Rotational speeds of the order 100 – 10 000 Hz are obtained. These are larger than values observed for brighter, more massive objects such as Peekskill, which exhibited a 500 Hz flicker assumed to be rotation (Beech & Brown 2000). Hawkes & Jones (1978) estimated rotation rates of the order 500 Hz for a faint, +7 magnitude meteor, based on the observed trail width, while their model of random collisional erosion outside of the atmosphere predicted rotation rates of 1.3×10^4 Hz for a 10^{-6} kg particle.

The YORP effect (Rubincam 2000, Bottke et al. 2006) should also be considered as a mechanism for increasing the rotation rate of a meteoroid in interplanetary space through asymmetric re-emission of incident sunlight. Bottke et al. (2006) notes that the 6-km asteroid (951) Gaspra at $a = 2.21$ AU would evolve from a rotational period of 12 to 6 h in 2.4×10^8 years, but that the YORP timescale is proportional to the square of the radius of the body, such that a 0.5-km asteroid at the orbit of Gaspra would undergo the same doubling in rotational frequency in a just a few million years. For smaller objects, a model by Breiter, Vokrouhlický & Nesvorný (2010) found that objects down to a size of 10^{-5} m were spun up by the YORP effect. The

Table 4.6: Rotational modeling results for the observed fragmenting meteoroids. The number of fragments, N_{frag} , the total mass considered for the fragmentation, m_{total} , estimated radius of the meteoroid, r , rotational rate, f_{rot} , and pressure applied by centrifugal forces, P_{rot} , are given.

	N_{frag}	m_{total} (10^{-6} kg)	r (10^{-3} m)	f_{rot} (10^3 Hz)	P_{rot} (10^6 Pa)
20100914_054515 (01T)	3	2	0.6	10	2
20100914_054515 (02T)	2	2	0.6	10	2
20101010_023500 (I)	2	60	2	3	0.9
20101010_023500 (II)	2	30	1	7	4
20101010_023500 (III)	3	30	1	9	6
20101013_064003	7	3	0.6	20	8
20101016_070052	5	100	2	7	9
20110204_023725	2	100	2	0.8	0.1
20110330_061029 (I)	3	10	1	4	0.7
20110330_061029 (II)	2	5	0.7	2	0.1
20110403_065305 (I)	2	0.3	0.3	10	0.8
20110403_065305 (II)	5	0.9	0.4	10	1
20120322_072602 (01T)	2	0.7	0.4	0.6	<0.03
20120322_072602 (02T)	2	0.7	0.4	3	<0.1
20120523_080013 (01T)	7	5	0.7	10	2
20120523_080013 (02T)	5	5	0.7	20	7

model considered nonspherical objects of finite thermal conductivity. In the limit of very small or isothermal objects, the *windmill effect* of Paddack & Rhee (1975), where radiation pressure exerts a torque on an asymmetric object, may become more significant. It should be noted that a requirement for the rotational fragmentation of meteoroids in this study must be heating or some other process while entering the atmosphere, otherwise objects that were spun up outside of the atmosphere would simply fragment upon reaching the critical rotation speed.

4.4.3 Electrostatic repulsion

The triboelectric charging and subsequent fragmentation of a meteoroid as it enters the atmosphere has been proposed by Spurný & Ceplecha (2008). The authors suggested that meteoroids gain a positive surface charge as electrons are removed during meteoroid ablation. A significant surface charge would be acquired very rapidly, on the order of 1 s, resulting in large differences in potential throughout the meteoroid. The outcome would be catastrophic

discharge, evaporating parts of the meteoroid, and providing a fragmentation mechanism independent of aerodynamic pressure. Residual charges in the fragments would cause significant transverse motion beyond what is expected aerodynamically. The authors did not attempt to model the process quantitatively.

Sorasio, Mendis & Rosenberg (2001) modeled how a meteoroid ablating in the free molecular flow regime ($r \leq 10^{-3}$ m, $h \geq 80$ km) acquires a charge by thermionic emission. The meteoroid was assumed not to fragment. They found that a $40\ \mu\text{m}$ meteoroid at a speed of $30\ \text{km s}^{-1}$ could obtain a peak charge of nearly 10^5 e, equivalent to a surface potential of 4 V, at a height of 100 km. Later efforts by Mendis et al. (2005) and Mendis & Maravilla (2009) included the effects of ablative charge loss and sputtering, but they were found to have negligible effects on the meteoroid charge and potential for the speed and size range of meteoroids considered in this study.

Another possibility is that the meteoroid acquires a charge before entering the atmosphere and beginning the ablation process. For spacecraft in the Earth's magnetosphere, DeForest (1972) observed potentials of up to 200 V and 100 – 10 000 V in the sunlit and night sides, respectively. Hill & Mendis (1979) noted that a similar procedure could apply to interplanetary dust grains, but that the charging time, inversely proportional to the dimensions of the body, would be much larger.

As an alternative to rotational fragmentation, we may also look at basic electrostatic repulsion as a mechanism of fragmentation. In this case, we are not concerned with how the meteoroid acquires the charge, but what charge is required to produce the observed fragment transverse speeds. Plasma effects are neglected to simplify calculations while providing order of magnitude estimates of meteoroid strength and charge to evaluate this mode of fragmentation.

As with the rotational model, the meteoroid is assumed to be a rigid body of spherical fragments, and Eqs. (4.12) - (4.14) apply. Each fragment is assumed to hold an equal charge.

The electrostatic force of fragment **a** on fragment **b**,

$$\mathbf{F}_{\text{es};a,b} = \frac{1}{4\pi\epsilon_0} \frac{q_a q_b}{r_{a,b}^2} \hat{\mathbf{r}}_{a,b}, \quad (4.18)$$

is evaluated for all fragments, where q_a and q_b are the (equivalent) charges on fragments **a** and **b**, respectively, and $\mathbf{r}_{a,b} = \mathbf{r}_b - \mathbf{r}_a$ is the vector leading from fragment **a** to **b**. Eq. (4.18) is the equation of motion for each fragment, and is evaluated numerically. To constrain the single free parameter, the charge on the fragments, the speeds of the fragments at a large separation (~ 10 cm) is set equal to the maximum observed fragment transverse speed in the centre of mass frame. In practise, the forces between fragments are negligible after the first 5×10^{-4} s, so the particles will have constant velocity.

The meteoroid potential is determined by calculating the potential of the charge configuration comprising the meteoroid. The potential at fragment **a** due to all other fragments **b** is given by

$$V_a = \frac{1}{4\pi\epsilon_0} \sum_b \frac{q_b}{r_{a,b}}. \quad (4.19)$$

The total meteoroid potential is then the sum of the potentials at all fragments, divided by two to prevent double-counting,

$$V_{\text{total}} = \frac{1}{2} \sum_a V_a. \quad (4.20)$$

The results of the electrostatic repulsion modeling are given in Table 4.7. Meteoroid strengths are of the order of 10^6 Pa and are comparable to results obtained with the rotational fragmentation model. More specifically, the strengths derived with the electrostatic model for most meteoroids are nearly half the values obtained with the rotational model. This is likely due to the nature of the force: for rotational fragmentation, a single impulse is applied to the fragments, as the centrifugal force vanishes when the rigid body approximating the meteoroid is broken. Conversely, for electrostatic fragmentation, the force continuously acts on the particles, though it becomes negligible a short time ($\sim 10^{-4}$ s) after fragmentation.

The total meteoroid charges required to produce the observed transverse speeds are of the

Table 4.7: Electrostatic repulsion model results. The charge applied to each fragment, q , the observed pressure due to electrostatic forces at the time of breakup, P_{es} , and the potential of the meteoroid, V_{total} , are given.

	q (10^{11} e)	q_{total} (10^{11} e)	P_{es} (10^6 Pa)	V_{total} (10^5 V)
20100914_054515 (01T)	1	2	0.8	1
20100914_054515 (02T)	1	2	1	1
20101010_023500 (I)	6	10	0.5	3
20101010_023500 (II)	8	20	2	4
20101010_023500 (III)	5	20	3	10
20101013_064003	0.4	3	4	20
20101016_070052	9	40	5	40
20110204_023725	5	9	0.08	2
20110330_061029 (I)	1	3	0.4	3
20110330_061029 (II)	0.5	0.9	0.08	0.5
20110403_065305 (I)	0.2	0.4	0.4	0.5
20110403_065305 (II)	0.1	0.6	0.7	3
20120322_072602 (01T)	0.01	0.03	0.001	0.03
20120322_072602 (02T)	0.07	0.1	0.02	0.1
20120523_080013 (01T)	0.3	3	1	10
20120523_080013 (02T)	0.9	5	4	10

order of 10^{11} e, giving potentials of the order 10^5 V. This is five orders of magnitude larger than what is expected by the models for charging during ablation, but is closer to the potentials ($\geq -10\,000$ V) observed for spacecraft in the night side magnetosphere of Earth. As the meteoroid ablates, electrons are lost, so a large negative potential like -10^4 V would not be expected. It is therefore likely that charge repulsion made only a minor contribution to the fragmentation of the meteoroids in this study (or was one of many effects).

4.4.4 Explosive devolatilization

Another fragmentation mechanism to consider briefly is explosive devolatilization or dehydration during atmospheric entry. As mentioned in the Introduction section, Kramer (1968) observed a meteoroid that fragmented at a height of 72 km, and subsequently suggested that heating of volatiles may instigated the fragmentation.

Stoch (1991) heated samples of hydrated calcium borates and layered silicates and observed

rapid disintegration and sputtering. This disintegration occurred as hydroxide groups in the mineral formed water molecules (which complemented the hydrate water molecules already present). Next, the hydrogen bonds attaching the water to the borate were broken. At 360°, water began to escape the sample, but at 375° the remaining water produced a violent outburst, resulting in fragmentation of the sample. Water bubbles were present in the sample fragments, suggesting that fragmentation occurred when the pressure of the water vapour exceeded the strength of the mineral grains. Heating of layered silicates produced considerable bloating and decrease in density, but no explosions. It is not known how these processes would change at the extremely depleted pressures of the upper atmosphere compared to the laboratory. In any case, the heating of a hydrated mineral is a possible fragmentation mechanism.

Trigo-Rodríguez & Blum (2009) have argued that porous, fragile meteoroids from the outer solar system may contain significant amounts of water due to less impact and radiation processing compared to objects in the inner solar system. Even the stronger, compacted objects in the inner solar system may contain water in their interiors if they are a few millimetres or larger.

Alternately, fragmentation may be associated with differential ablation. Sodium is observed to ablate first in the spectra of Leonids (Borovička, Štork & Boček 1999) and Draconids (Borovička, Spurný & Koten 2007). Madiedo et al. (2013) observed the early appearance and depletion of sodium in the spectra of a magnitude -10.5 fireball and suggested that compaction of the meteoroid in the atmosphere resulted in the early outgassing of sodium. The early ablation of sodium may result in the meteoroid splitting into domains of less volatile material, effectively fragmenting. Sodium outgassing may also be associated with the observed transverse velocities for fragments. Evaluation of these phenomena are beyond the scope of this paper and will require subsequent quantitative investigation, with constraints being provided by spectral observations.

4.5 Conclusions and future studies

We have presented high resolution observations of nine faint meteors showing gross fragmentation. These are some of the first direct observations of this phenomenon. Eight of the nine meteors showed significant and anomalous transverse speeds among the fragments. Acceleration in the transverse direction was negligible. Transverse speeds of the order 100 m s^{-1} were observed, while values of the order 1 m s^{-1} were expected from aerodynamic loading models.

Using the observed transverse fragment speeds as a constraint, we modelled rotational- and charge-based fragmentation. Several simplifications were made to obtain meteoroid strengths of the order 10^6 Pa . This value is unexpected - as discussed in Section 4.1, larger meteoroids that drop meteorites typically have strengths around 10^6 Pa , while faint meteors are inferred to have lower strengths, 10^4 Pa . Rotational speeds between $100 - 10\,000 \text{ Hz}$ were required to produce the observed fragment transverse speeds. These values are larger than expected from previous observations and models (Beech & Brown 2000, Hawkes & Jones 1978). Similarly, meteoroid charges of the order 10^{11} e (producing potentials of 10^5 V) were obtained, up to several orders of magnitude larger than what was predicted by previous models (Mendis et al. 2005, DeForest 1972). These disagreements suggest that additional investigation into the fragmentation of faint meteoroids is needed, making use of the new, high-resolution observations presented here as constraints.

Since a small number of meteors show gross fragmentation with significant transverse spread (32 of nearly 3000 observed with CAMO), the mechanism responsible must be rare and unique. Future studies should work to characterise the fragmentation mechanism, constrained by high-resolution observations. Some questions to answer include:

- How does the meteoroid spin up—what are the relative importances of preatmospheric processes, like the YORP and Paddack effects, compared to in-atmosphere processes, such as flowfield interaction with the meteoroid shape? Investigating how the meteoroid acquires its spin will allow for the determination of the maximum rotation frequency for

comparison with values derived using fragment transverse speeds.

- How does the meteoroid acquire a charge? In orbit, the solar wind deposits a significant charge (electrons) onto the meteoroid's surface, but as the meteoroid ablates, electrons are carried off by evaporation of material and thermionic emission. Fragmentation may be instigated by arcing between charged domains in the meteoroid, and a detailed model of meteoroid charging would be able to evaluate this hypothesis.
- Could other effects, such as explosive devolatilization, cause fragmentation? It is evident that the heating of the meteoroid during ablation is important in triggering fragmentation, otherwise the preatmospheric spin or charge would fragment the meteoroid before it was visible. In addition to affecting meteoroid strength, heating could possibly cause catastrophic devolatilization or dehydration as observed in laboratory samples (Stoch 1991).

Additionally, observations of these faint fragmenting objects may be improved. Combining two-station narrow-field results for a single meteor should ideally produce a three-dimensional description of fragment dispersion. Tracking the fragments in three dimensions would help distinguish between fragmentation mechanisms: rotational breakup would spread the fragments in a plane, while charge breakup or devolatilization would produce radial dispersion of fragments.

Ultimately, the goal of improved observation and understanding of meteoroid fragmentation is to serve as an additional constraint in determining object structure and composition, complementing light curves and spectra.

Bibliography

Artemieva, N. A., Shuvalov, V. V., (2001). Motion of a fragmented meteoroid through the planetary atmosphere. *Journal of Geophysical Research*, 106 (E2), 3297-3309.

Baggaley, W. J., Grant, J., (2004). Radar measurements of macro fragmentation in meteoroids. *Earth, Moon, and Planets*, 95, 655-662.

Beech, M., Brown, P., (2000). Fireball flickering: the case for indirect measurement of meteoroid rotation rates. *Planetary and Space Science*, 48, 925-932.

Borovička, J., (1990). The comparison of two methods of determining meteor trajectories from photographs. *Bulletin of the Astronomical Institutes of Czechoslovakia*, 41, 391-396.

Borovička, J., Kalenda, P., (2003). The Morávka meteorite fall: 4. Meteoroid dynamics and fragmentation in the atmosphere. *Meteoritics & Planetary Science*, 38 (7), 1023-1043.

Borovička, J., Spurný, P., Brown, P., Wiegert, P., Kalenda, P., Clark, D., Shrubený, L., (2013). The trajectory, structure and origin of the Chelyabinsk asteroidal impactor. *Nature*, 503, 235-237.

Borovička, J., Spurný, P., Koten, P., (2007). Atmospheric deceleration and light curves of Draconid meteors and implications for the structure of cometary dust. *Astronomy & Astrophysics*, 473, 661-672.

Borovička, J., Štork, R., Boček, J., (1999). First results from video spectroscopy of 1998 Leonid meteors. *Meteoritics & Planetary Science*, 34, 987-994.

Bottke, W. F., Vokrouhlický, D., Rubincam, D. P., Nesvorný, D., (2006). The Yarkovsky and YORP effects: implications for asteroid dynamics. *The Annual Review of Earth and Planetary Science*, 34, 157-191.

Boyd, I. D., (2000). Computation of atmospheric entry flow about a Leonid meteoroid. *Earth, Moon, and Planets*, 82-83, 93-108.

Breiter, S., Vokrouhlický, D., Nesvorný, D., (2010). Analytical YORP torques model with an improved temperature distribution function. *Monthly Notices of the Royal Astronomical Society*, 401, 1933-1949.

Brown, P., Ceplecha, Z., Hawkes, R. L., Wetherill, G., Beech, M., Mossman, K., (1994). The orbit and atmospheric trajectory of the Peekskill meteorite from video records. *Nature*, 367, 624-626.

Campbell-Brown, M., Jones, J., (2003). Determining the initial radius of meteor trains: fragmentation. *Monthly Notices of the Royal Astronomical Society*, 343, 775-780.

Campbell-Brown, M. D., Koschny, D., (2004). Model of the ablation of faint meteors. *Astronomy & Astrophysics*, 418, 751-758.

Campbell-Brown, M. D., Borovička, J., Brown, P. G., Stokan, E., (2013). High-resolution modelling of meteoroid ablation. *Astronomy & Astrophysics*, 557, A41, 13pp.

Ceplecha, Z., (1987). Geometric, dynamic, orbital, and photometric data on meteoroids from photographic fireball networks. *Bulletin of the Astronomical Institutes of Czechoslovakia*, 38, 222-234.

Ceplecha, Z., Borovička, J., Elford, W. G., ReVelle D. O., Hawkes, R. L., Porubčan, V., Šimek, M., (1998). Meteor phenomena and bodies. *Space Science Reviews*, 84, 327-471.

DeForest, S. E., (1972). Spacecraft charging at synchronous orbit. *Journal of Geophysical Research*, 77 (4), 651-659.

Elford, W. G., Campbell, L., (2001). Effect of meteoroid fragmentation on radar observations of meteor trails. In: Proceedings of the Meteoroids 2001 Conference, edited by B. Warmbein. ESA SP-495, Noordwijk: ESA Publications Division. 419-423.

Fisher, A. A., Hawkes, R. L., Murray, I. S., Campbell, M. D., LeBlanc, A. G., (2000). Are meteoroids really dustballs? *Planetary and Space Science*, 48, 911-920.

Gural, P. S., Jenniskens, P. M., Varros, G., (2004). Results from the AIM-IT meteor tracking system. *Earth, Moon, and Planets*, 95, 541-552.

Hawkes, R. L., Jones, J., (1975). A quantitative model for the ablation of dustball meteors. *Monthly Notices of the Royal Astronomical Society*, 173, 339-356.

Hawkes, R. L., Jones, J., (1978). The effect of rotation on the initial radius of meteor trains. *Monthly Notices of the Royal Astronomical Society*, 185, 727-734.

Hedin, A. E., (1991). Extension of the MSIS thermospheric model into the middle and lower atmosphere. *Journal of Geophysical Research*, 96, 1159-1172.

Hill, J. R., Mendis, D. A., (1979). Charged dust in the outer planetary magnetospheres. *The Moon and the Planets*, 21, 3-16.

Jacchia, L. G., (1955). The physical theory of meteors. VIII. Fragmentation as a cause of the faint-meteor anomaly. *The Astrophysical Journal*, 121, 521-527.

Kramer, E. N., (1968). On the structure and chemical composition of meteor bodies of cometary origin. In: *Physics and Dynamics of Meteors*, edited by L. Kresak, P. M. Millman. Dordrecht, D. Reidel, 236-238.

Madiedo, J. M., Trigo-Rodríguez, J. M., Konovalova, N., Williams, I. P., Castro-Tirado, A. J., Ortiz, J. L., Cabrera-Caño, J., (2013). The 2011 October Draconids outburst – II. Meteoroid chemical abundances from fireball spectroscopy. *Monthly Notices of the Royal Astronomical Society*, 433, 571-580.

Mendis, D. A., Maravilla, D. (2009). A note on the altitude profiles of the electron production in the atmosphere by micrometeoroids entering it at different speeds. *Geophysical Research Letters*, 36, L22804, 6pp.

Mendis, D. A., Wong, W.-H., Rosenberg, M., Sorasio, G., (2005). Micrometeoroid flight in the upper atmosphere: electron emission and charging. *Journal of Atmospheric and Solar-Terrestrial Physics*, 67, 1178-1189.

Musci, R., Weryk, R. J., Brown, P., Campbell-Brown, M. D., Wiegert, P. A., (2012). An optical survey for millimeter-sized interstellar meteoroids. *The Astrophysical Journal*, 745:161, 6pp.

Paddack, S. J., Rhee, J. W., (1975). Rotational bursting of interplanetary dust particles. *Geophysical Research Letters*, 2 (9), 365-367.

Passey, Q. R., Melosh, H. J., (1980). Effects of atmospheric breakup on crater field formation. *Icarus*, 42, 211-233.

Popova, O., Borovička, J., Hartmann, W. K., Spurný, P., Gnos, E., Nemtchinov, I., Trigo-Rodríguez, J. M., (2011). Very low strengths of interplanetary meteoroids and small asteroids. *Meteoritics & Planetary Science*, 46 (10), 1525-1550.

Rubincam, D. P., (2000). Radiative spin-up and spin-down of small asteroids. *Icarus*, 148, 2-11.

Sorasio, G., Mendis, D. A., Rosenberg, M., (2001). The role of thermionic emission in meteor physics. *Planetary and Space Science*, 49, 1257-1264.

Spurný, P., Ceplecha, Z., (2008). Is electric charge separation the main process for kinetic energy transformation into the meteor phenomenon? *Astronomy & Astrophysics*, 489, 449-454.

Stoch, L., (1991). Explosive thermal dehydration of solids. *Journal of Thermal Analysis*, 37, 1415-1429.

Stokan, E., Campbell-Brown, M. D., Brown, P. G., Hawkes, R. L., Doubova, M., Weryk, R. J., (2013). Optical trail widths of faint meteors observed with the Canadian Automated Meteor Observatory. *Monthly Notices of the Royal Astronomical Society*, 433 (2), 962-975.

Trigo-Rodríguez, J. M., Blum, J., (2009). Tensile strength as an indicator of the degree of primitiveness of undifferentiated bodies. *Planetary and Space Science*, 57, 243-249.

Trigo-Rodríguez, J. M., Llorca, J., (2006). The strength of cometary meteoroids: clues to the structure and evolution of comets. *Monthly Notices of the Royal Astronomical Society*, 372, 655-660.

Trigo-Rodríguez, J. M., Llorca, J., (2007). Erratum: the strength of cometary meteoroids: clues to the structure and evolution of comets. *Monthly Notices of the Royal Astronomical Society*, 375, 415.

Weryk, R. J., Brown, P. G., (2012). Simultaneous radar and video meteors—I: Metric comparisons. *Planetary and Space Science*, 62, 132-152.

Weryk, R. J., Brown, P. G., (2013). Simultaneous radar and video meteors—II: Photometry and ionisation. *Planetary and Space Science*, 81, 32-47.

Weryk, R. J., Campbell-Brown, M. D., Wiegert, P. A., Brown, P. G., Krzeminski, Z., Musci, R., (2013). The Canadian Automated Meteor Observatory (CAMO): System overview. *Icarus*, 225, 614-622.

Chapter 5

High-resolution ablation modelling for small meteoroids

A version of this chapter has been accepted for publication as:

- Stokan, E., Campbell-Brown, M. D., (2014). *A particle-based model for ablation and wake formation in faint meteors*. Monthly Notices of the Royal Astronomical Society, accepted November 29, 2014.

5.1 Introduction

As meteoroids collide with the atmosphere, they ablate, emit light, and form a luminous trail called the wake. The formation of the wake and its composition (particularly, the relative contributions from excited atoms and molecules that emit photons versus small, luminous meteoroid fragments that disperse) are poorly understood and may provide insight into physical properties of the meteoroid, such as the atomic masses of the species comprising the body, or the mass and density of fragments released from the meteoroid. Characterising the width of the wake is important for minimising bias in radar observations of meteors, while the length

allows for calculation of the size distribution of grains comprising a dustball meteoroid. Previous investigations of meteor wake have revealed a large variance in observed sizes and there have been few attempts to verify models of wake formation with observations. These studies will now be reviewed briefly.

The earliest observations of faint meteor wakes were presented by Hawkins & Whipple (1958) and Cook et al. (1962), making use of a 48-inch Schmidt camera with limiting magnitude +4. Meteor trail widths up to 6 m were observed, though the heights of the meteoroids were ambiguous since only a single station was available to record data. Subsequent dual-frequency backscatter radar investigations revealed similarly sized (ion) trail widths at heights above 90 km. In particular, Greenhow & Hall (1960) observed trail widths between 1 m at 97 km and 3 m at 103 km, while Baggaley (1970, 1980) determined widths of 0.48 m at 90 km and 2.90 m at 115 km. Jones & Campbell-Brown (2005) found slightly narrower ion trails with their radar study, ranging from 0.5 m at 80 km and 1.3 m at 100 km. A study of 34 faint meteors with intensified video by Kaiser et al. (2004) yielded a maximum luminous trail width of 1.4 m after correction for image bloom. These meteors had a mean height of 83 km, and the system had a limiting magnitude of +9.

Unprecedentedly large meteor wakes were reported by other intensified video studies, however. Murray et al. (1999) captured a Leonid with a 900 m wide trail at an estimated height of 138 km during the 1998 Leonid multi-instrument aircraft campaign (MAC). At 138 km the meteor had a magnitude of +1.6, though it later reached a peak of -4 . Similarly, Spurný et al. (2000) observed eight bright (brighter than -7 peak magnitude) Leonids with exceptional beginning heights, above 150 km, with trail widths up to 4 km. Another Leonid was presented by Stenbaek-Nielsen & Jenniskens (2004) with a width of nearly 100 m at a relatively low height of 105 km and a peak magnitude of -3 .

Disagreement between the narrow wakes observed initially with Schmidt cameras and radar versus the wide wakes observed with intensified video may be explained by considering the differences in instrumentation and the populations of meteoroids studied. The earlier

studies examined Geminids and sporadics that were typically slower and luminous at lower heights than the wide Leonids. As atmospheric density increases approximately exponentially with decreasing height, it is expected that the excited particles and fragments comprising the wake will be increasingly constrained by the atmosphere, resulting in narrower wakes at lower heights. Similarly, the difference in sensitivity and spectral response between the Schmidt cameras (limiting magnitude +4) and the intensified systems (limiting magnitude typically around +9, red sensitive) may explain differences in meteor appearance. Finally, radar detects trails of ionised particles and electrons, while optical detects trails of excited particles. As ions tend to have smaller collisional mean free paths compared to the corresponding atomic species (Phelps 1991), it is likely that ion trails are narrower than the luminous wakes.

Koten et al. (2006) suggested that sputtering was responsible for diffuse, wide meteors with beginning heights above 130 km, such as the Leonids observed by Spurný et al. (2000). Stenbaek-Nielsen & Jenniskens (2004) alternately suggested that atmospheric scattering of ultraviolet radiation emitted from a meteoroid may be responsible for large meteor wakes. Quantitative models of ion trail formation and diffusion were presented by Manning (1958) and Kascheyev & Lebedinets (1963), where ion trail widths up to 14 mean collision free path lengths were calculated by determining the radial distance that an excited ion would travel before being thermalised. Both of these models suggested that the trail width should vary with height as the atmospheric collisional mean free path, but a weaker dependence was observed in the previous radar surveys. Converting radar observations (amplitudes) to ion trail widths requires an assumption of the ion trail radial density profile, which most studies assumed is Gaussian. Jones (1995) determined that the radial profile of the ion trail is actually non-Gaussian by tracking the collisions of 10 000 evaporated meteoric ions in a detailed simulation, explaining the discrepancy between modelled and observed ion trail widths.

An alternative explanation for the weak height dependence of observed meteor trail widths was formulated by Hawkes & Jones (1978), who suggested that the wake could be widened by small fragments that were flung perpendicularly to the meteoroid's direction of travel, by

rotation. Campbell-Brown & Jones (2003) were able to explain differences in the observed height distribution of Geminids at three radar frequencies using a model where non-Gaussian radial ion trail distributions could be created through fragmentation of the meteoroid and lateral dispersion of the fragments.

In several studies, the length of meteor wakes has been assumed to represent the longitudinal (along the travel direction of the meteoroid) separation of meteoroid fragments. Fisher et al. (2000) measured lengths up to 1.9 km for the wakes of nine faint meteors observed with an image-intensified system and suggested that fragments with masses in the range 10^{-6} – 10^{-11} kg, decelerating at different rates, could separate and account for the observations, depending on the height of fragmentation. These mechanisms for meteoroid fragmentation to contribute to the width and length of the meteor wake complemented the previous models based on the thermalisation of evaporated meteoric particles.

Spectral observations of meteors (Borovička 1993, 1994) provided the motivation for two detailed models of the environment around a 1 cm Leonid at a height of 95 km. Popova et al. (2000) treated air molecules impinging on a meteoroid analogously to a high-energy ion beam ablating a surface and found that the meteor wake extended up to approximately 0.1 m around the meteoroid. Evaporation was found to screen the meteoroid from direct interaction with the atmosphere, attenuating the beam of atmospheric particles. Boyd (2000) applied the direct simulation Monte Carlo (DSMC) method, which solves for the position- and time-dependent state (temperature, density, velocity) of a flow. This is done by numerically simulating collisions between particles comprising the flow and then taking local averages (Bird 1994, Shen 2005). DSMC is particularly applicable to the rarefied conditions for a 1 cm object at 95 km, called the free molecular flow regime, where the diameter of the object is smaller than the mean collision free path length of ambient particles. The meteor wake was found to be of order 10 m wide, corresponding to the observations of Kaiser et al. (2004) for sporadic meteors at lower heights and speeds. Interestingly, both of these models found that the wake was in thermal equilibrium at temperature of order 1000 K, which was not expected from spectral models of

Borovička (1994). Only a single snapshot of the meteor was output by Boyd's model, due to the intensity of computations and the lack of high-resolution data for quantitative comparison.

More recently, Vinković (2007) employed DSMC to model light production due to sputtering for meteors above 130 km, proposed to be the case for the eight Leonids observed by Spurný et al. (2000). Collisions between sputtered and atmospheric particles were assumed to produce all of the meteor's light. Synthetic, high-resolution snapshots of the meteor were produced at heights up to 200 km, showing a diffuse conical shape that narrowed as the meteoroid height decreased, qualitatively matching the observations of Spurný et al. (2000) and Koten et al. (2006). Simulated light curves were also produced, but not compared with any observations.

Several observations of meteor wake have been presented and a few models proposed, but comprehensive, quantitative evaluation of the models using observations have been scarce. The most recent image-intensified video survey of faint meteor trail widths was presented in our previous paper (Stokan et al. 2013), revealing widths up to 100 m for small meteoroids ($< 10^{-4}$ kg) at heights above 105 km. In this work, we present a model for meteoroid ablation and wake formation based on the simulation of collisions between atmospheric particles, meteoric particles, and the meteoroid. Investigations by Boyd (2000) and Vinković (2007) have revealed particle-based techniques are promising for description of the luminous region around the meteoroid. Nine meteors from the first paper have been selected to evaluate the model, and the goal is to quantitatively compare simulated wake widths, lengths, as well as light curves, and deceleration profiles to observations. Section 5.2 introduces the model, while Section 5.3 reviews how the meteor observations were gathered and processed. Section 5.4 compares the model results with observations, Section 5.5 discusses assumptions in the model and suggests possible improvements, while Section 5.6 summarises the findings.

5.2 Ablation model

5.2.1 Review of faint meteor ablation models

The goal of a meteoroid ablation model is to fit observations by solving coupled differential equations describing object height, speed, mass, and luminosity as a function of time. Values such as the initial speed, mass, and density of the meteoroid are calculated as a result. The first ablation models (cf. Bronshten 1983, Ceplecha et al. 1998) conceptualised the meteoroid as a non-fragmenting spherical body and considered conservation of momentum and energy to derive the *canonical* equations of motion,

$$\frac{dv}{dt} = -\frac{\Gamma S \rho_{\text{atm}} v^2}{m}, \quad (5.1)$$

and mass loss,

$$\frac{dm}{dt} = -\frac{\Lambda S \rho_{\text{atm}} v^3}{2Q_{\text{abl}}}, \quad (5.2)$$

where m is the mass, v is the speed, and S is the cross-sectional area of the meteoroid. Γ is the drag coefficient, which ranges between 0 and 2, describing how efficiently momentum is transferred from the atmospheric flow field to the meteoroid. Λ is the heat transfer coefficient, related to the fraction of imparted energy that goes into ablating the meteoroid, while the heat of ablation, Q_{abl} , describes the specific energy required to ablate mass from the meteoroid. Finally, ρ_{atm} is the mass density of the atmosphere at the height of the meteoroid. The radiated luminous power of the meteoroid, I , is described by

$$I = -\frac{\tau}{2} \frac{dm}{dt} v^2, \quad (5.3)$$

where τ is the luminous efficiency of the meteoroid, the proportionality coefficient between the kinetic energy lost and the energy radiated by the meteoroid.

Principal applications of single-body meteoroid ablation theory showed good agreement

with photographic observations of bright meteors (McKinley 1961). Conversely, short luminous trajectories (smaller than expected intervals between the meteor beginning and ending heights), early peaks in brightness, and larger than expected meteoroid decelerations observed in faint meteors showed poor agreement with the classical model (Jacchia 1955, Hawkins & Southworth 1958). In response, Hawkes & Jones (1975) proposed the two-component dustball model, suggesting that a meteoroid may be comprised of grains held together in a volatile matrix or glue. Energy from atmospheric interactions is consumed in ablating the non-radiating glue, releasing grains that ablate individually as single-body meteoroids. The total meteor light is the sum of the light production for each of the grains.

The dustball model was able to explain the anomalies associated with faint meteors and has been applied to investigate meteoroid physical characteristics, such as heat of ablation and mass density. Observations of the length of meteor wakes have allowed for the calculation of grain sizes comprising a meteoroid, as noted in the Introduction section. Two modern iterations of the dustball model, the thermal fragmentation model by Campbell-Brown & Koschny (2004) and the erosion model by Borovička et al. (2007), were evaluated using high-resolution observations of ten meteors (Campbell-Brown et al. 2013). The goal was to simultaneously match light curves, deceleration profiles, and meteor wake lengths computed by each model with observations. It was assumed that the length of the wake was entirely due to the dispersion of fragments, proportional to the difference in minimum and maximum masses considered in the grain size distribution, since smaller grains experience more drag than larger grains by Eq. (5.1). Contributions to the length of the wake from collisions of excited and ionised particles were neglected.

Both models produced wake lengths that disagreed with observations. In some cases, simulated wakes were almost an order of magnitude longer than observed, such as for event 20101016_075031, where a length of 450 m was computed by one model versus an observed length of under 40 m. For other meteors, simulated wakes were shorter than observations. Both models were able to match the observed light curves and meteoroid decelerations, but

meteoroid densities computed with the two models showed some disagreement. These results suggest that modifications to dustball theory are required to accommodate the new constraints from high-resolution observations, and also that the effect of chemical wake (resulting from particle collisions) should be considered.

For this model, the opposite approach is being taken: it is assumed that all of the meteor wake originates from particle collisions and that the meteoroid does not fragment in flight. This allows for study of the simplest case of meteoroid ablation, no fragmentation, and limits the number of free parameters. Simulated light curves that persistently start higher or end lower than observations, as well as insufficient meteoroid deceleration will indicate that fragmentation is significant and must be considered.

5.2.2 Model overview

This particle-based model for meteoroid ablation consists of three main steps, summarised as follows:

1. Undisturbed atmospheric molecules undergo collisions with the meteoroid. Momentum and energy are transferred from the atmospheric particles to the meteoroid, causing deceleration and mass loss by evaporation, respectively. This process is described in Section 5.2.4. Effectively, the canonical equations for deceleration, Eq. (5.1), and mass loss, Eq. (5.2), are solved.
2. Collisions between undisturbed atmospheric particles and the set of reflected and evaporated particles, collectively called *excited particles*, are simulated. Section 5.2.5 describes this in more detail. The location and energy of each collision with respect to the meteoroid are recorded for conversion to a simulated narrow-field (high-resolution) image in the next step.
3. The location of each collision is binned in two dimensions to produce a narrow-field image using the pixel scale and angle of perspective (angle between the image plane and

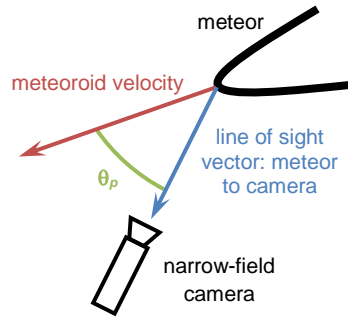


Figure 5.1: Illustration of the perspective angle, θ_p .

the meteor’s trajectory, illustrated in Fig. 5.1) for the observed meteor. The brightness of each pixel is assumed to be proportional to either the number, or total energy, of collisions in each pixel. The first assumption implicitly states that each collision has an equal likelihood of emitting light, while the second implies that collisions of higher energy are more likely to emit light. Images based on both assumptions are produced (and will be compared with observations in Section 5.4). The simulated images are processed with image smear and broadening with a Gaussian point spread function (PSF) appropriate for comparison with the observed video frame, as will be described in Sections 5.2.6 and 5.3. A simulated light curve is obtained by taking the natural logarithm of the sum of pixel brightness in each simulated meteor image (the same process applied to the observed meteor). The meteor trail width and length are also measured and plotted as a function of height.

These three steps are repeated for each time step of the simulation until the meteoroid’s mass is 10^{-5} of the initial mass, or its speed is below 5 km s^{-1} .

There are three principal free parameters in this model: the meteoroid’s initial mass, density, and composition. The composition, either stony or cometary, affects the meteoroid’s heat of ablation, Q_{abl} , and mean molecular mass, μ . The respective values are $6.3 \times 10^6 \text{ J kg}^{-1}$ and 23.6 g mol^{-1} for stony objects, and $3.8 \times 10^6 \text{ J kg}^{-1}$ and 8.26 g mol^{-1} for cometary objects (Campbell-Brown & Koschny 2004). The coefficient of elasticity for collisions between atmospheric particles and the meteoroid, c_{elas} , was set to 0, resulting in totally inelastic collisions

with the meteoroid. This is analogous to setting the drag coefficient, Γ , to the commonly used value of unity in the canonical equation of motion, Eq. (5.1).

The meteoroid's initial speed and zenith distance were obtained from the observed meteoroid's trajectory. The beginning height of the simulation was set to be near the beginning height of the recorded light curve. This saved computation time, and was allowed since the meteoroid temperature was assumed to stay constant at its boiling point. The time step in the simulation was set to 10^{-3} s, and 2000 particles were selected to represent each of the reflected and evaporated particle populations. Setting the number of particles between 100 and 10 000 was tested, and 2000 was found to be a good balance between simulation precision and speed. The MSIS-E-90 model (Hedin 1991) is referenced for the atmospheric density and temperature for the height of the meteoroid at each time step of the simulation.

5.2.3 Assumption of negligible shielding and excited particle interactions

In simulating interactions between the atmosphere and meteoroid, we assume that there is negligible shielding by evaporated meteoroid particles. Similarly, we assume that evaporated particles will only collide with atmospheric particles, and not with other evaporated particles or the meteoroid. Previous studies disagree regarding the validity of these assumptions. Campbell-Brown & Koschny (2004) postulate that there is an approximate 10^{-6} probability of an incoming atmospheric particle being deflected by an evaporate, while Popova et al. (2000) suggest that energy and momentum transfer between the atmosphere and meteoroid must be considered hydrodynamically. Both of these models consider similar meteoroid sizes ($r_{\text{met}} < 0.4$ cm if the largest meteoroid mass is 10^{-4} kg, and the density is at least 600 kg m^{-3}) and height ranges ($h > 90$ km, typically) as for this model. Boyd (2000) noted an approximately 10^4 increase in density in front of an ablating meteoroid, but the meteoroid was a bit larger (1 cm) than those being studied here. Vinković (2007) neglected vapour screening and interactions between meteoric particles, but only examined sputtering, not intensive evaporation. We will now briefly investigate the validity of these assumptions for this model.

Consider a particle evaporated from the meteoroid at time 0. At time τ_c , the particle will have travelled, on average, for the mean collision free time given by

$$\tau_c \approx \frac{\lambda}{v}, \quad (5.4)$$

where λ is the mean collision free path length, and v is the speed of the meteoroid, which is the majority of the evaporated particle's speed. The distance travelled by the particle, ℓ , is given by

$$\ell = v_{\text{evap}} \tau_c, \quad (5.5)$$

where the particle has been released with speed v_{evap} with respect to the meteoroid. It should be noted that λ is measured in the frame where the atmospheric particles are at rest, while ℓ is measured in the frame where the meteoroid is at rest. In time interval τ_c ,

$$N_{\text{atm}} = S v \tau_c \delta_{\text{atm}} \quad (5.6)$$

atmospheric particles have impacted the meteoroid, releasing kN_{atm} evaporated particles throughout the sphere centred around the meteoroid with radius ℓ , where δ_{atm} is the number density of atmospheric particles and k is the approximate number of evaporated meteoric atoms per impinging particle. The number density of evaporated particles around the meteoroid is then

$$\delta_{\text{evap}} = \frac{kS v \tau_c \delta_{\text{atm}}}{\frac{4}{3}\pi(v_{\text{evap}} \tau_c)^3}. \quad (5.7)$$

This expression can be simplified to

$$\frac{\delta_{\text{evap}}}{\delta_{\text{atm}}} = \frac{3k}{4} \left(\frac{r_{\text{met}}}{\lambda} \right)^2 \left(\frac{v}{v_{\text{evap}}} \right)^3. \quad (5.8)$$

Equation (5.8) gives the ratio of the evaporated to atmospheric particle number density. If this ratio is significantly smaller than 1, the assumption that shielding is negligible (and that

evaporated particles generally interact with atmospheric particles only) is valid. We can consider a representative meteoroid travelling at 40 km s^{-1} , with a radius of 10^{-3} m (corresponding to an approximate mass of 10^{-5} kg with a density of 1000 kg m^{-3}) at heights between 80 and 110 km. 100 particles evaporated for each incoming particle is an appropriate value for k , assuming N_2 collides with the meteoroid at 40 km s^{-1} , and the heat of ablation and mean meteoric molecular mass are $6.3 \times 10^6 \text{ J kg}^{-1}$ and 23.6 g mol^{-1} as stated earlier. The speed of the evaporated particle with respect to the meteoroid is a particularly important parameter, and we consider the lower bound to be the mean thermal speed of a meteoric particle at 3000 K, and the upper bound to be equivalent to the speed of the meteoroid in the atmosphere. The upper bound is unrealistic, especially given Eq. (5.4), but effectively eliminates the speed ratio term of Eq. (5.8).

Ratios for various heights and both assumptions for the speed of evaporated particles are given in Table 5.1. If it is assumed that the particles are released with thermal velocities, then the ratio of evaporated to atmospheric particles is significant ($\sim 1/10$) below about 105 km, and evaporative screening along with interactions between evaporated particles cannot be neglected. Conversely, if the upper bound for particle release speed is considered, the ratio of is insignificant at even 80 km, making our assumptions valid at all heights. The actual situation is more complicated, since the evaporated particles quickly fall behind the meteoroid after the first collision, gaining a significant velocity in the frame of reference where the meteoroid is at rest. To definitively answer the question of how important evaporated particles are in moderating the interaction between the atmosphere and meteoroid, we would ideally track the entire flow field in a true DSMC simulation, as did Boyd (2000). For now, we hold our assumptions valid, but with caution that results for heights below 105 km may be unrealistic.

Table 5.1: Ratio of evaporated particle density to atmospheric density at the first collision, as calculated with Eq. (5.8). Ratio 1 assumes that the evaporated particle has the mean speed of a 3000 K distribution with respect to the meteoroid, while ratio 2 assumes that the particle is released at a speed equivalent to the meteoroid's speed through the atmosphere.

h (km)	Ratio 1	Ratio 2
80	3.1×10^2	2.2×10^{-2}
85	6.9×10^1	4.8×10^{-3}
90	1.5×10^1	1.0×10^{-3}
95	3.0×10^0	2.1×10^{-4}
100	5.2×10^{-1}	3.6×10^{-5}
105	8.2×10^{-2}	5.6×10^{-6}
110	1.3×10^{-2}	9.0×10^{-7}

5.2.4 Collisions with the meteoroid

At the beginning of each time step, the radius of the assumed spherical meteoroid,

$$r_{\text{met}} = \left(\frac{3m}{4\pi\rho_{\text{met}}} \right)^{1/3}, \quad (5.9)$$

is determined using the instantaneous mass m . The actual number of atmospheric particles encountered, on average, by the meteoroid over this time step with interval Δt is then given by

$$N_{\text{refl,act}} = \pi r_{\text{met}}^2 v \Delta t \delta_{\text{atm}}. \quad (5.10)$$

This is called $N_{\text{refl,act}}$ for clarity (the other pertinent population is the evaporated particles) since each impinging atmospheric particle is also reflected. $N_{\text{refl,sim}}$ particles are generated to represent those particles by randomly generating their identity (O, O₂, or N₂) based on the local abundances at the height of the meteoroid, and then generating an initial velocity for each based on the Maxwell-Boltzmann distribution at the local atmospheric temperature. We consider the frame of reference where the meteoroid is stationary, so the velocity generated for each atmospheric particle has the meteoroid velocity subtracted. This is convenient for calculations, as it is effectively the centre-of-mass frame for the meteoroid-atmospheric particle system.

The velocity vectors for the impinging particles are then used to determine where they col-

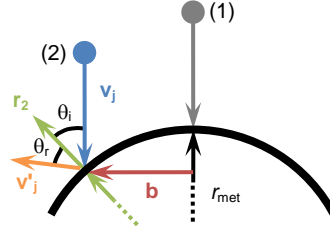


Figure 5.2: A schematic of an atmospheric particle colliding with the meteoroid. Position (1) is for a hypothetical head-on collision before impact parameter \mathbf{b} is generated. Position (2) indicates where the particle actually is before the collision. \mathbf{r}_2 leads from the centre of the meteoroid to the collision site, while \mathbf{v}_j and \mathbf{v}'_j are the pre- and post-collision velocities for the particle, respectively. Since the collision is specular, the angle of incidence, θ_i , and reflection, θ_r , are equal.

lide with the meteoroid. First, a head-on collision is generated, and a random impact factor is chosen from a uniform distribution between 0 (a head-on collision) and r_{met} (a grazing collision). Each collision is assumed to be specular, and the post-collision velocity, \mathbf{v}'_j , is given by

$$\mathbf{v}'_j = c_{\text{elas}}(\mathbf{v}_j - 2[\mathbf{v}_j \cdot \hat{\mathbf{r}}_2]\hat{\mathbf{r}}_2), \quad (5.11)$$

where \mathbf{v}_j is the pre-collision velocity for the particle, and \mathbf{r}_2 is the vector leading from the centre of the meteoroid to the location of the collision. For convenience of notation, any variable with subscript j will pertain to the simulated particles. The particle-meteoroid collision is illustrated in Figure 5.2.

The momentum imparted to the meteoroid by the collisions is given by

$$\Delta \mathbf{p} = - \left(\frac{N_{\text{refl,act}}}{N_{\text{refl,sim}}} \right) \sum_j [m_j(\mathbf{v}'_j - \mathbf{v}_j)], \quad (5.12)$$

where the sum over j encompasses all simulated particles. Consequently, the change in meteoroid velocity over the time step is $\Delta \mathbf{v} = \Delta \mathbf{p}/m$. The imparted energy is calculated similarly,

$$\Delta E = - \frac{1}{2} \left(\frac{N_{\text{refl,act}}}{N_{\text{refl,sim}}} \right) \sum_j [m_j(v_j'^2 - v_j^2)]. \quad (5.13)$$

All of the energy is assumed to go into immediately evaporating meteoric particles, making total ablated mass $\Delta m = \Delta E/Q_{\text{abl}}$ over this time step, distributed across $N_{\text{evap,act}} = \Delta m/\mu$ actual particles. $N_{\text{evap,sim}}$ simulated particles are created to represent the evaporated material, with velocities generated from a Maxwell-Boltzmann distribution at the meteoroid's assumed temperature of $T_{\text{met}} = 3000$ K.

5.2.5 Particle-particle interactions

Once the initial set of excited particles have been generated, they are tracked for up to 21 collisions each. The number of tracked collisions was set to 21 because most of the excited particles attain atmospheric thermal velocities by then. As mentioned previously, collisions are assumed to occur only with ambient, undisturbed atmospheric particles; collisions between excited particles, and between the excited particles and the meteoroid, are neglected. If the post-collision velocities of any of the undisturbed particles are significantly larger than the pre-collision velocities, they are counted as excited particles and also tracked. The goal of this step is to store the location and energy of each collision for later plotting.

First, an undisturbed atmospheric particle is randomly generated for each excited particle. This procedure is the same as generating particles to collide with the meteoroid: the particle type is chosen by local abundances and the velocity is generated from the appropriate Maxwell-Boltzmann distribution. The relative velocity and the velocity in the frame where the centre of mass is stationary for each particle pair are also calculated. The collisional cross section, σ_j , is then calculated for each particle pair using

$$\sigma_j = \sigma_{\text{ref}} \left(\frac{v_{\text{ref}}}{v_{j,\text{rel}}} \right)^s, \quad (5.14)$$

where $\sigma_{\text{ref}} = 5 \times 10^{-19} \text{ m}^2$, $v_{\text{ref}} = (5 \times 10^3 / \bar{\mu}_{\text{atm}})^{1/2} \text{ m s}^{-1}$ ($\bar{\mu}_{\text{atm}}$ is the mean atmospheric molecular mass in kg mol^{-1}), and $s = 0.5$ are reference values appropriate for atmospheric molecules from Bird (1994), Boyd (2000), Shen (2005), and Vinković (2007). The collision free time interval

for each particle,

$$\tau_j = -\frac{1}{v_{j,\text{rel}}} \frac{\ln R_j}{\rho_{\text{atm}} \sigma_j}, \quad (5.15)$$

is then generated using a random number, R_j , selected from a uniform distribution between 0 and 1, and the displacement travelled (in the frame where the meteoroid is at rest) by the excited particle between collisions is

$$\Delta \mathbf{r}_j = \mathbf{v}_j \tau_j. \quad (5.16)$$

The three-dimensional position of the collision with respect to the meteoroid is recorded, as well as the energy of the collision. The time of the collision, given by the total amount of time since the original particle collided with or was evaporated from the meteoroid, is also recorded.

Post-collision velocities for each particle are then found. All collisions are assumed to be elastic. A similar simplification was employed by Vinković (2007), allowing for a first-approximation to whether or not the width of observed wakes can be described by collisional interactions. This may be improved in a future iteration of the model, and effects of this assumption will be discussed in Sections 5.4 and 5.5. First, the value of the impact parameter for the collision, b_j , is randomly selected (uniform distribution) between zero and the molecular diameter, d_j , and the angle through which the initial relative velocity vector is deflected is calculated with

$$\chi_j = 2 \cos^{-1} \left(\frac{b_j}{d_j} \right). \quad (5.17)$$

This is the variable hard sphere (VHS) model described in detail by Bird (1994) and Shen (2005), where a head-on collision with $b_j = 0$ results in the energetic atom reflecting backwards ($\chi_j = \pi$), while a glancing collision with $b_j/d_j = 1$ results in the energetic atom not scattering ($\chi_j = 0$) from its original velocity. Calculating angle χ_j allows for computation of the post-collision relative velocity of the particles, which is then converted to the post-collision velocities of each individual particle in the frame where the meteoroid is at rest.

To ensure that all collisions that can potentially produce light are tracked, the pre- and post-collision velocities of the ambient particle are compared. If a hypothetical impact between

the pre- and post-collision particles exceeds the energy of a 700 nm photon (approaching the longest wavelengths of light that would be observed effectively with our intensified video system), the ambient particle is tracked as a new excited particle; otherwise, it is discarded. A separate lower energy threshold (10 eV) is used later when calculating the light emitted from each collision for generation of the simulated high-resolution meteor images, and will be discussed in Section 5.4.

5.2.6 Generating narrow-field images and light curves

After all of the particle collisions have been simulated, their recorded positions are used to make a two-dimensional histogram of the number of particle collisions in the region around the meteoroid. A second two-dimensional histogram applies a collision energy weighting to each collision, effectively making the value of each bin representative of the total energy of collisions that occurred inside. The size of each of the histogram's bins is set equal to the pixel scale of the narrow-field video for the meteor, and the axes are rotated to match the observed perspective angle (illustrated in Fig. 5.1). These are the unprocessed simulated images of the meteor before any image broadening or smearing is applied.

It is implicitly assumed that the excited gas around the meteoroid is optically thin (i.e. that collisions throughout the column defined by each bin contribute equally to the pixel brightness) in preparing these images. This assumption seems reasonable given the low atmospheric densities at the heights being considered. The observed Gaussian PSF and motion smear are applied to the unprocessed image to create the synthetic narrow-field image for comparison with observations. Determination of the observed smear and PSF will be discussed in Section 5.3.

Once the simulated image has been created, the relative magnitude of the meteor is determined for the simulated light curve by taking the logarithm of the sum of the pixel intensity,

$$M_{\text{rel}} = -\frac{5}{2} \log_{10} \sum_{x,y} p(x,y), \quad (5.18)$$

where $p(x, y)$ is the brightness of pixel at location (x, y) . The magnitude of the observed meteor is calculated in the same way. To get the absolute magnitude of the meteor (for comparison with the observed light curve), an offset is calculated by computing the power radiated by the meteoroid, I , using the simulated meteor's mass loss rate and the classical luminosity equation, Eq. (5.3). The luminous efficiency expression by Weryk & Brown (2013),

$$\log_{10} \tau = -0.09v^{1/2} - 3.00 \log_{10} v - \frac{9.56}{\log_{10} v} + 10.11, \quad (5.19)$$

where v is the meteoroid speed in km s^{-1} , is used as well as the relationship

$$\frac{M_1}{M_2} = -\frac{5}{2} \log_{10} \left(\frac{I_1}{I_2} \right), \quad (5.20)$$

to determine the peak absolute magnitude of the meteor, knowing that a zero magnitude meteor has a bolometric power output of 820 W (Weryk & Brown 2013). The magnitude offset is then the difference between the peak absolute magnitude just calculated and the corresponding peak relative magnitude, and is added to all of the relative magnitudes to obtain absolute magnitudes for direct comparison with observed data.

In addition to comparing simulated and observed meteor light curves, meteoroid deceleration, trail width and length are also measured and compared. Meteoroid deceleration is quantified as the meteoroid's lag compared to a theoretical object moving at a constant speed (equal to the meteoroid's speed on the first half of its trajectory) on an equivalent heading. Measurements for trail widths and lengths are done identically for simulated and observed data and will be described in Section 5.3.

5.3 Observations

5.3.1 The Canadian Automated Meteor Observatory (CAMO)

CAMO is an automated, two-station, image-intensified video observatory for faint meteors. Details of observations and wake measurements with CAMO are presented in the previous paper (Stokan et al. 2013), but will be reviewed here. The two CAMO stations are separated by a baseline of approximately 45 km and are each comprised of a wide-field camera, with a fixed 28° field of view, and high-resolution, narrow-field camera, with a 1.5° degree field of view, that automatically tracks the meteor in flight. Video from the wide-field cameras is used to determine the meteoroid trajectory, deceleration, and the meteor light curve, while video from the narrow-field cameras is used to analyse meteor morphology. Each camera is lens-coupled to a third-generation ITT NiteCam 380i image intensifier, with peak sensitivity between 500 and 800 nm, and limiting magnitude of approximately +5, corresponding to a minimum meteoroid mass of about 10^{-6} kg. All video is recorded at a resolution of 640×480 at 12-bits per pixel to minimise saturation, and between 60 and 110 frames per second to capture transient meteor morphology. Additional information on CAMO is given in Weryk et al. (2013).

One of the nine meteors studied was recorded with the CAMO influx system. This is similar to the wide-field camera, with a narrower field of view (20°), larger frame resolution (1600×1200 , 14-bits per pixel), and decreased frame rate (20 frames per second). The same image intensifiers are used for the influx, wide-, and narrow-field systems, ensuring the consistency in spectral response. Since data was not available from the wide-field system for this meteor, influx camera video was substituted, allowing for determination of the trajectory and meteor light curve.

5.3.2 Wide-field reductions

Two-station wide-field video was processed with the software package METAL to produce the trajectory and light curve of each meteor (Weryk & Brown 2012). First, the user generates

an astrometric plate by picking stars in the video and mapping their pixel positions to their catalogue celestial coordinates. Next, a photometric plate is generated by converting the observed brightness of stars in the video to an instrumental magnitude using Eq. (5.18) introduced earlier, and comparing that to the catalogue R-band magnitude.

After the astro- and photometric plates are generated, the position of the meteor is selected in each frame of the wide-field video. Similarly, the meteor is masked in each frame, giving the location of pixels to sum for the instrumental magnitude. The iterative trajectory solver MILIG (Borovička 1990) is then used to calculate the meteoroid's path through the atmosphere, giving the height, range to each station, and velocity as a function of time. The instrumental magnitude of the meteor is converted to an apparent magnitude using the photometric plate, and then to an absolute magnitude (magnitude normalised to a range of 100 km) using the calculated range to the meteoroid.

5.3.3 Narrow-field reductions

To make it easier to compare narrow-field meteor frames with the simulation output, the frames were rotated such that the meteor appeared to travel from the top of the frame to the bottom. The rotation angle (the angle of the meteor's trail in the video) was determined using a linear Hough transform (Duda & Hart 1972). The meteor was then centred in each image by finding the location of peak pixel brightness and cropping the image to encompass 40 pixels in each direction around that location. Although the narrow-field system endeavoured to track the meteor continuously, it could slowly shift in position throughout the video. This caused motion smear, artificially widening or lengthening the meteor trail. Instantaneous image smear for each frame was quantified by examining the drift (in pixels) in the meteor's position in consecutive frames, decomposing the displacement into components perpendicular and parallel to the trail.

In addition to motion smear, the image of the meteor was widened by the PSF of the narrow-field system, which was analysed by examining stationary stars (point sources) in narrow-field videos recorded on the same night as the meteor observations. Stars were found to have

nearly Gaussian profiles, representing the system's PSF, and were fitted with two-dimensional isotropic Gaussian curves,

$$p_{\text{star}}(x, y) = a + (b - a) \exp \left[-\frac{(x - c_x)^2 + (y - c_y)^2}{2d^2} \right], \quad (5.21)$$

where $p_{\text{star}}(x, y)$ is the brightness of the pixel at (x, y) , a is the fitting parameter related to the mean background brightness in the frame, b is the peak brightness of the star, (c_x, c_y) is the pixel location of the centre of the star, and d is related to the width of the PSF. Rather than attempting to remove smear and broadening from the recorded images, simulated images were motion smeared by the observed amount and broadened with the observed Gaussian PSF.

The pixel scale for each frame,

$$s_{\text{pixel}} = R\psi, \quad (5.22)$$

was determined using the instantaneous range to the meteoroid, R , and the known angle (in radians) subtended by each pixel, ψ . The orientation of the meteor with respect to the narrow-field camera's image plane was determined by calculating the perspective angle, θ_p (depicted in Fig. 5.1), between the range vector leading from the meteoroid to the camera, \mathbf{R} , and the meteor velocity vector \mathbf{v} ,

$$\cos \theta_p = \frac{\mathbf{R} \cdot \mathbf{v}}{|\mathbf{R}| |\mathbf{v}|}. \quad (5.23)$$

The perspective angle has a significant effect on the appearance of the meteor in the narrow-field video, as observed by Vinković (2007). As with the image smear and PSF, the pixel scale and perspective angle were used to modify the simulated meteor images, rather than attempt to correct the narrow-field observations.

To provide a quantitative comparison between the simulation and high-resolution observations, meteor trail width and length were measured in each frame of the simulated and observed videos. The trail width was measured as a function of distance along the trail by selecting a row of pixels in the rotated image (corresponding to a certain distance along the meteor) and finding the points in the pixel brightness profile immediately to the left and right of the central

peak brightness that crossed a threshold value set at two standard deviations above the mean background brightness. The distance between the points defined the trail width at the selected distance along the meteor. Since noise was not modelled for the simulated images, the simulated and observed images were normalised to the same peak brightness and the threshold calculated in the observed image was applied for measurements in the simulated image. The peak of the trail width measured in each frame was then plotted as a function of frame height to see how the morphology of the meteor varied.

The trail length was measured similarly to the width. The brightness profile along the centreline of the meteor was inspected to find the points where the profile crossed threshold brightnesses of five, ten, and twenty standard deviations above the background brightness. Again, identical brightness thresholds, determined from the observed frames, were applied to both the observed and simulated data. Since the end of the trail is poorly defined, faint, and patchy in many narrow-field images, threshold values for length measurements were set higher than for width measurements. The distance between the points was taken to be the trail length for the selected frame. As with peak trail width, trail length was also plotted as a function of frame height.

5.3.4 Selected meteors

Nine meteors were selected from the observations of Stokan et al. (2013) for initial testing of this model. Parameters derived from observations are given in Table 5.2. These meteors were chosen for analysis as each tended to have high-quality narrow-field observations with little image smear. Also, the light curve for each meteor showed the peak magnitude towards the end height. Late-peaked light curves are typically associated with meteoroids that do not fragment, giving the best chance for a single-body model that neglects fragmentation to match observations.

It should be noted that one of the meteors, 20101020_100214, had a particularly low convergence angle of $Q^* = 4.2^\circ$. The convergence angle is the angle formed by the vectors leading

Table 5.2: Observation parameters for the nine meteoroids, including the right ascension and declination of the radiant, α and δ , initial speed, v_i , beginning and ending heights from the wide-field camera, h_B and h_E , peak absolute magnitude M_{peak} , and convergence angle between the two stations and the meteor, Q^* .

	α ($^\circ$)	δ ($^\circ$)	v_i (km s^{-1})	h_B (km)	h_E (km)	M_{peak}	Q^* ($^\circ$)
20101020_100214	175.6 ± 5.1	49.4 ± 3.3	41.1 ± 2.4	106.5 ± 1.3	95.3 ± 1.0	1.6 ± 0.1	4.2
20101020_101727	94.7 ± 0.8	15.8 ± 0.8	70.1 ± 0.5	115.2 ± 0.3	94.4 ± 0.2	-0.9 ± 0.1	20.2
20101102_233359	268.1 ± 1.0	32.8 ± 0.8	18.9 ± 0.3	88.9 ± 0.2	78.0 ± 0.2	1.6 ± 0.2	17.6
20101103_031542	90.2 ± 9.6	26.1 ± 8.6	61.2 ± 3.4	111.4 ± 6.2	95.0 ± 5.2	-1.2 ± 0.1	5.4
20101103_033400	35.1 ± 8.6	-24.4 ± 7.8	58.5 ± 2.7	111.7 ± 5.1	104.6 ± 4.7	2.5 ± 0.2	6.0
20101103_061127	48.2 ± 1.0	21.5 ± 0.9	30.4 ± 0.2	98.2 ± 0.2	85.1 ± 0.2	2.3 ± 0.2	21.3
20101103_061856	51.2 ± 0.7	21.6 ± 0.7	31.4 ± 0.3	101.9 ± 0.3	85.5 ± 0.2	1.6 ± 0.1	23.8
20101103_062801	105.2 ± 3.8	15.5 ± 3.7	67.0 ± 0.5	115.9 ± 0.6	104.0 ± 0.6	0.2 ± 0.2	10.2
20101103_063032	130.6 ± 4.6	27.2 ± 4.1	71.4 ± 1.4	113.8 ± 1.0	105.7 ± 0.8	2.2 ± 0.2	6.4

from each station to the meteoroid. Small convergence angles increase the uncertainty in the trajectory solution. This is apparent in the relatively large uncertainties in the beginning and ending heights of this meteor. Three other meteors, 20101103_031542, 20101103_033400, and 20101103_063032, had convergence angles below 10° , also increasing the uncertainty in their trajectory solutions. Future studies will look to choose meteors with better geometries (ideally, $Q^* \sim 20^\circ$), but the priority for this study was high-quality narrow-field observations for initial comparisons with the simulation. Additionally, one of the meteors, 20101102_233359, occurs at low heights, between 78 and 89 km, which may violate the assumption that there is negligible evaporated particle shielding of the meteoroid.

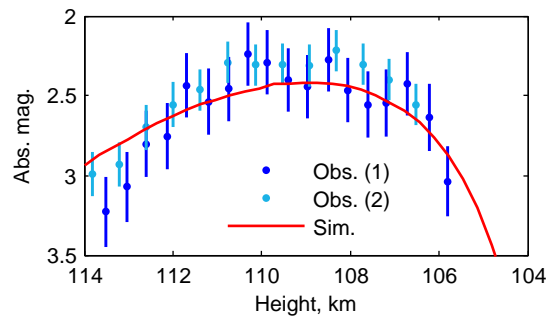
5.4 Model results and analysis

Analysis of a single meteor will be presented first to show intermediate steps in the derivation of the meteor trail lengths and widths, as well as the light curve and deceleration profile. Afterwards, results from modelling the remaining eight meteors will be presented and discussed. Finally, the major assumptions for the model will be reviewed and improvements suggested.

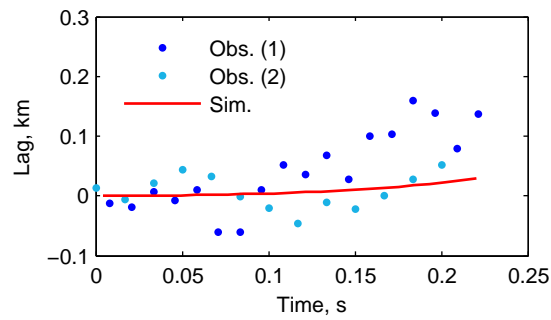
5.4.1 Sample meteor analysis: 20101103_063032

Event 20101103_063032 had the largest initial speed, 71.4 km s^{-1} , of the meteors selected for this study. The meteor began at a height of 113.8 km and was relatively faint, reaching a peak absolute magnitude of +2.2. Figure 5.3 (a) shows the observed and modelled light curve, while the deceleration profile is given in Figure 5.3 (b). The best fit to the meteor light curve was with an initial meteoroid mass of $(1.8 \pm 0.2) \times 10^{-7} \text{ kg}$ and a density of $900 \pm 200 \text{ kg m}^{-3}$. It was not possible to simultaneously match the light curve and the deceleration profile since the latter required a density of 200 kg m^{-3} .

To fit the meteor light curve, the peak magnitude was matched by varying the initial mass of the meteoroid, while the beginning and ending heights were matched by varying the meteoroid



(a) Light curve



(b) Deceleration profile

Figure 5.3: Observed and simulated light curve and deceleration profile for meteor 20101103_063032. Blue points are observations (the two stations are marked separately), while the red curve is the model result.

density. The beginning and ending heights are simultaneously modified by changing the meteoroid density, and it is not possible to change one independently from the other. As a result, the simulated meteor begins a bit higher and ends a bit lower than was observed. The other free parameter is the meteoroid composition, giving the heat of ablation and mean meteoric particle mass, which influences the height of the light curve. A stony composition matched the observed light curve best, while a cometary composition resulted in a light curve that was translated upward in height by about 10 km. The deceleration curve is mostly influenced by the meteoroid density, with smaller densities giving larger decelerations.

Simulated beginning heights and meteoroid decelerations that are, respectively, too high and low compared to observations suggest that continuous fragmentation occurred during the ablation of this meteoroid. High-resolution observations of fragmentation should yield a meteor with longer wake than single-body ablation simulations predict, since fragments of different sizes spread along the meteoroid's trajectory as they decelerate at different rates. If fragmentation is not apparent, any modification to the model meteoroid parameters that either increases energy transfer to the meteoroid from the atmosphere (such as decreasing meteoroid density, which increases the cross-sectional area), or decreases the meteoroid heat of ablation may help to explain shorter light curves, though these typically also translate the light curve higher in the atmosphere.

Figure 5.4 compares high-resolution narrow-field observations with output from the model. The two left columns of images show the simulated meteor using different methods to derive pixel brightness, while the right column shows three snapshots of the meteor recorded at heights of 108.4, 107.1, and 105.8 km. For the left column, it is assumed that brightness is proportional to the *number* of particle collisions in each pixel, while in the middle column, it is assumed that brightness is proportional to the total *energy* of all collisions in each pixel. The shape of the wake differs depending on which assumption is taken: assuming that the brightness is proportional to the number of collisions gives a meteor with a conical shape that widens with distance back from the meteoroid, while taking the other assumption gives a droplet-

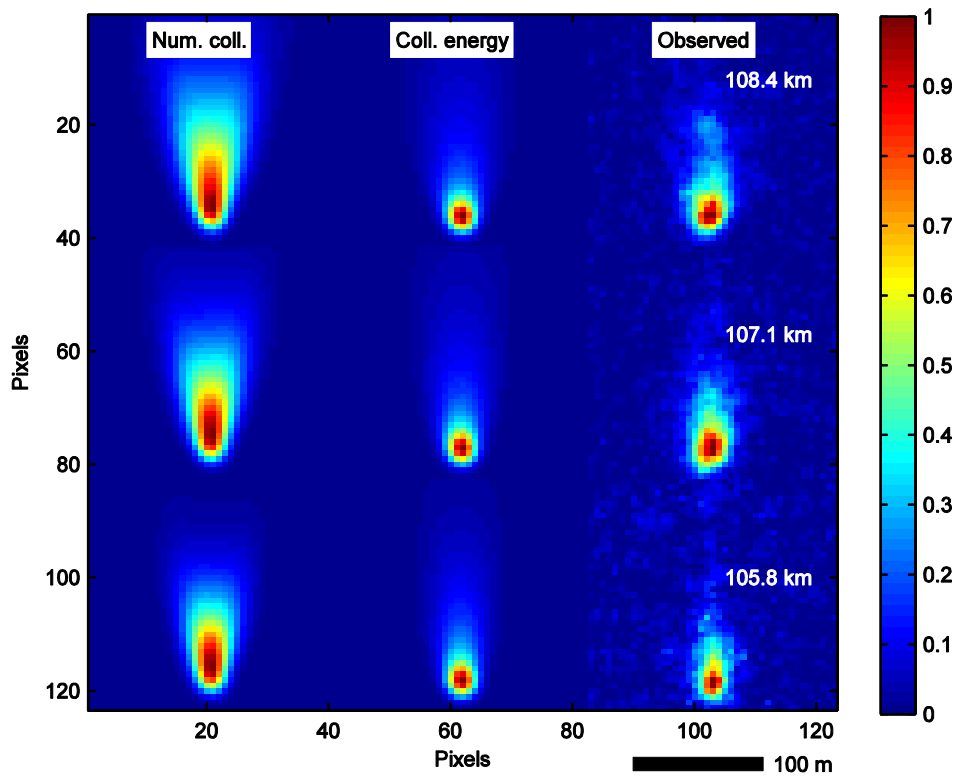
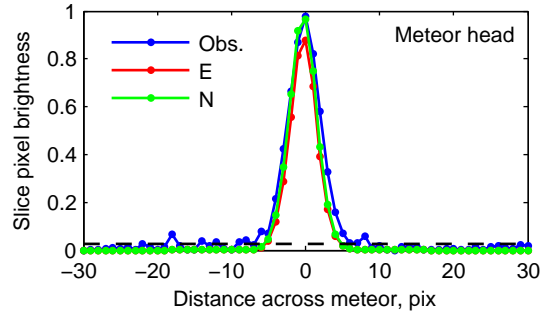


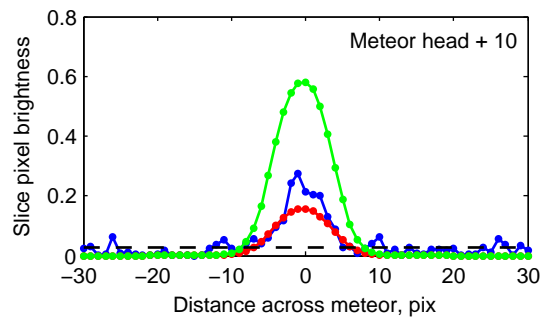
Figure 5.4: A comparison of a simulated and observed meteor (20101103_063032) at three heights. The meteors on the left and centre are simulated, with brightness based on the *number of collisions* (left) or the *total collision energy* (centre) in each pixel. Images on the right were observed with the narrow-field camera. All of the images have been normalised to the same peak brightness, and a high-contrast colour scale has been applied. An approximate scale bar is given in the bottom.

shaped meteor that is widest near the meteoroid, providing a better match to the observed meteor.

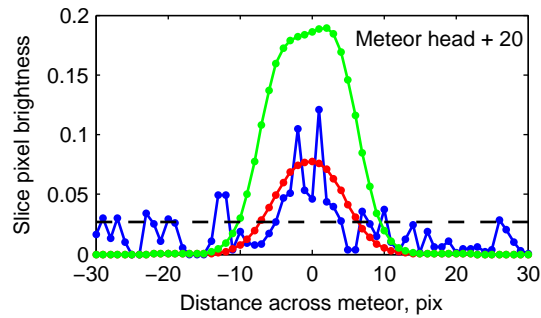
Measurements of the brightness profile across the meteor (simulated and observed) at three locations are given in Figure 5.5. These measurements apply to the snapshot at 107.1 km, corresponding to the middle row of frames in Figure 5.4. The width of the observed and both simulated meteors agree at the meteor head (the front of the meteor, near the position of the meteoroid) in Fig. 5.5 (a). Farther back along the meteor, however, the meteor simulated with brightness proportional to number of collisions widens considerably, Figs. 5.5 (b) and (c), while the observed and other simulated meteor show much less variance in width.



(a) Profile at the meteoroid (meteor head)



(b) Profile 10 pixels (~ 47 m) behind the meteoroid



(c) Profile 20 pixels (~ 93 m) behind the meteoroid

Figure 5.5: Three brightness profiles across the meteor trail at different locations along the meteor for the snapshot at 107.1 km in Figure 5.4. Measurements for the observed meteor are in blue, for the simulated meteor with brightness proportional to the collision energy per pixel (E) in red, and for the simulated meteor with brightness proportional to the number of collisions per pixel (N) in green. The threshold brightness for measuring width is plotted as a black dashed line.

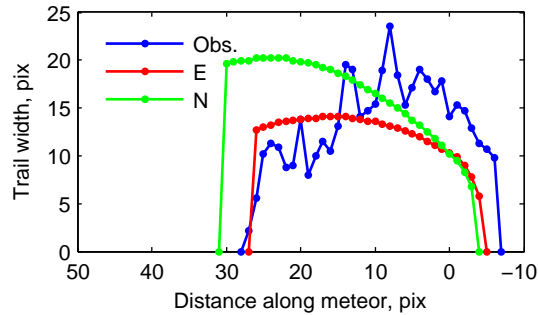


Figure 5.6: Observed and simulated meteor trail width as a function of distance along the trail for the snapshot at 107.1 km in Figure 5.4. The meteoroid is located at zero on the horizontal axis.

Width measurements for all distances along the meteor at a height of 107.1 km are compiled in Figure 5.6. This is another way of showing that the morphology of the meteor simulated with brightness proportional to number of collisions is a poor match to the observed meteor: while the peak width of the observed wake (23.6 pixels) is represented better by this assumption for brightness (giving a peak width of 20.2 pixels), the location at which this peak occurs is mismatched, occurring just behind the head in the observations, compared to near the back of the meteor in the simulation. Conversely, assuming that the brightness is proportional to the total collision energy produces a wake that is narrower than observations (14.1 pixels peak width), but better emulates how the width varies as a function of distance back from the head, as well as the wake length. Interestingly, matching the observed length of the wake with a single-body ablation model suggests negligible fragmentation at the time of this snapshot.

A better agreement between observations and the output that assumes pixel brightness is proportional to sum of the collision energy in each pixel suggests that the probability that a collision will emit detectable light is proportional to the energy of the collision. This is opposed to the assumption that each collision is equally likely to emit light, which occurs when the number of collisions in each pixel is counted to calculate the brightness. Vinković (2007) took the second assumption and simulated meteors with a similar conical shape to the images on the left of Figure 5.4.

When counting the number of collisions to give the brightness of each pixel, only colli-

sions with an energy of at least 10 eV are counted. Varying this lower energy threshold has a significant effect on the appearance of the simulated meteor wake, as illustrated in Figure 5.7, where the conical shape becomes longer and more apparent as collisions of decreasing energy are considered. This lengthening can be explained by considering Figure 5.8, plotting the mean collision energy, root mean squared collision radial distance, and mean collision distance behind the meteoroid as a function of collision number. About seven collisions are required before the mean energy is 10 eV, but twelve are required to reach the energy of a 700 nm photon. The RMS radial distance has a weak dependence on collision number, explaining why the width of the wake does not vary significantly as the energy threshold is decreased, but the distance behind the meteor head where the collisions occur increases rapidly with collision number, accounting for the dramatic increase in the length of the wake.

A threshold energy of 10 eV for collisions to be counted for light production was selected based on spectral observations that suggest much of the light from the wake is related to O, N, and N₂ excitations around 10 eV (Borovička, pers. comm.). Since most of the meteor light consists of emission lines rather than a continuum (Borovička 1993), the appearance of the wake should not vary significantly with the collision energy cut-off. This emphasises the need for a physically realistic model of light production, where inelastic collisions, excitation states, and photo de-excitations are considered explicitly. For now, brightness simulated as being proportional to the total collision energy is the more suitable assumption for light production since the meteor appearance does not change significantly with the collision energy threshold.

The width and length of the wake are plotted as a function of height in Figure 5.9. There is good agreement in meteor widths, and their variance as a function of height, between observations and model output (using both assumptions for pixel brightness). This implies the width of the wake may be described by collisions of particles evaporated from a non-fragmenting object. Similarly, simulated images based on both assumptions yield trail lengths that mostly agree with observations. It is likely that this meteoroid did not fragment, contrary to what is inferred from fitting the light curve and deceleration profile, or that meteoroid fragments did not

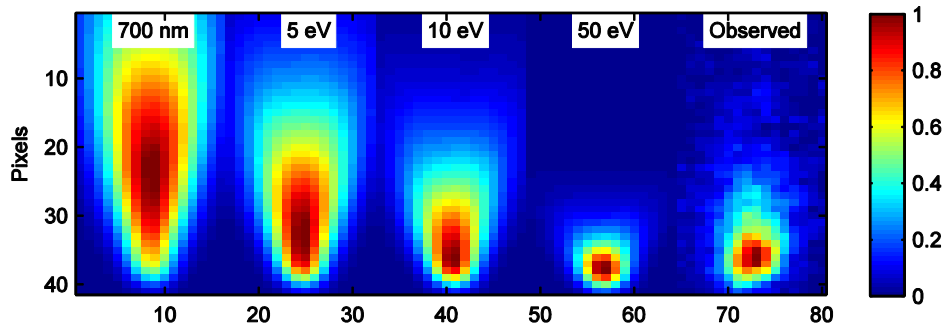


Figure 5.7: The simulated meteor at 107.1 km with pixel brightness based on the number of collisions per pixel. The minimum collision energy threshold used for calculating the brightness of pixels is given at the top of each image.

contribute to the length of the wake. For some of the other eight meteors studied, fragmentation appeared to occur, and those observations will be presented next.

5.4.2 General results from all of the meteors

Snapshots from the eight remaining meteors are given in Figures 5.10, 5.11, and 5.12, showing simulated meteors with pixel brightness proportional to the number of collisions (N), the total energy of collisions (E), and the observed meteors (Obs.). The nine meteors examined in this study can be broken into three groups based on how well the model fit observations, which will now be discussed.

The first group of meteors, 20101020_101727, 20101102_233359, and 20101103_062801, illustrated in Fig. 5.10 are fit poorly by the model, likely due to apparent gross fragmentation of the meteoroid, as evidenced by long and patchy trails. The simulated wakes are narrower and shorter than observed, as shown in Figs. 5.13 and 5.14 (b), (c), and (h). Only the simulated trail widths and lengths obtained by assuming pixel brightness is proportional to the total energy of collisions are plotted in these figures as they represent the shape of each meteor better. Gross fragmentation may increase the width of the wake if the fragments have a transverse speed component, perpendicular to the velocity of the meteoroid. Previous studies have observed meteoroids in this size range showing fragments with significant transverse

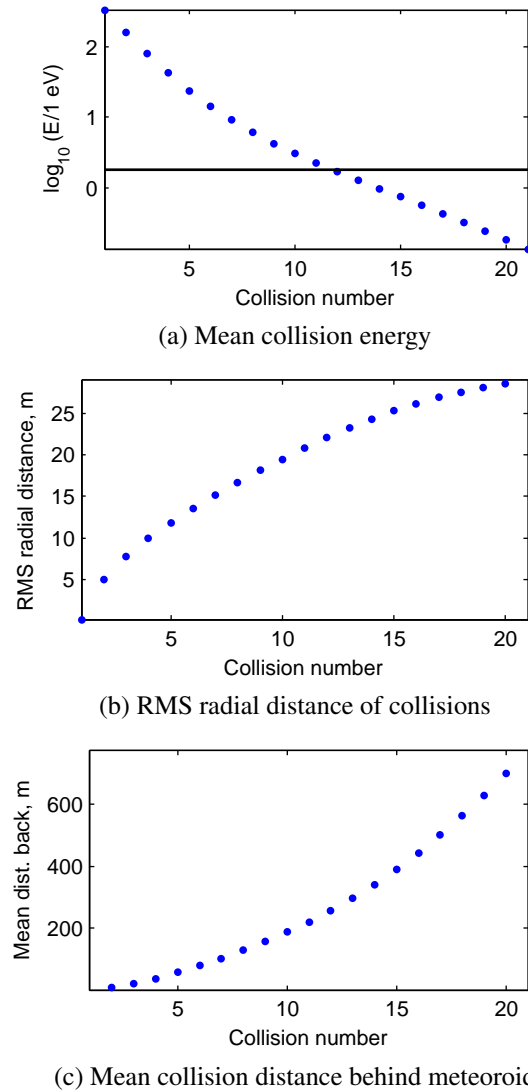
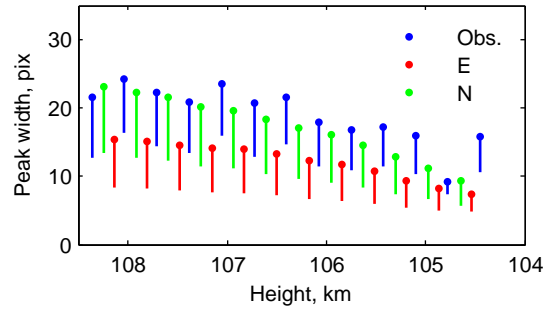
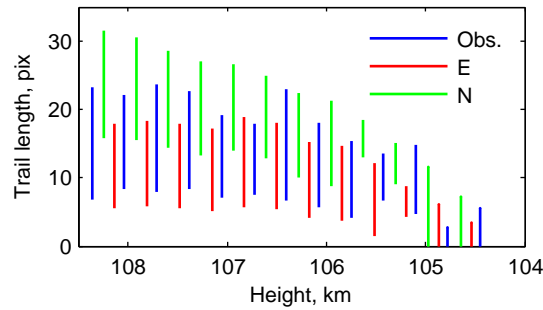


Figure 5.8: Collision properties (mean energy, RMS radial distance, mean distance behind the meteoroid) as a function of collision number for the simulated meteor at a height of 107.1 km. The energy of the 700 nm photon is given for reference in the energy graph.



(a) Peak trail width over all frames



(b) Trail length over all frames

Figure 5.9: Peak trail width and length measurements for all frames of the observation (blue points) and simulation (red and green points) of meteor 20101103_063032. Variance bars in the trail width graph are from the standard deviation in trail width in a single frame. For the trail length, the interval connects length measurements with thresholds of 5, 10, and 20 standard deviations above the image background. A horizontal offset has been added to both graphs to allow data plotted at the same height to be visible.

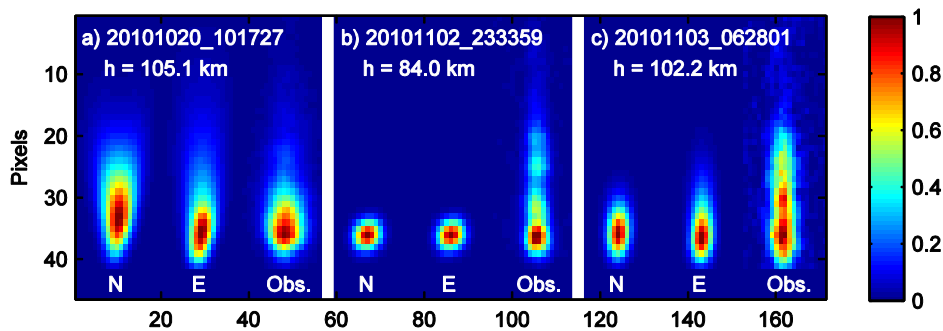


Figure 5.10: Meteors that were difficult to model, showing significant disagreement between observed and simulated trail widths, lengths, light curves, or deceleration profiles. Events 20101102_233359 and 20101103_062801 appeared to show gross fragmentation.

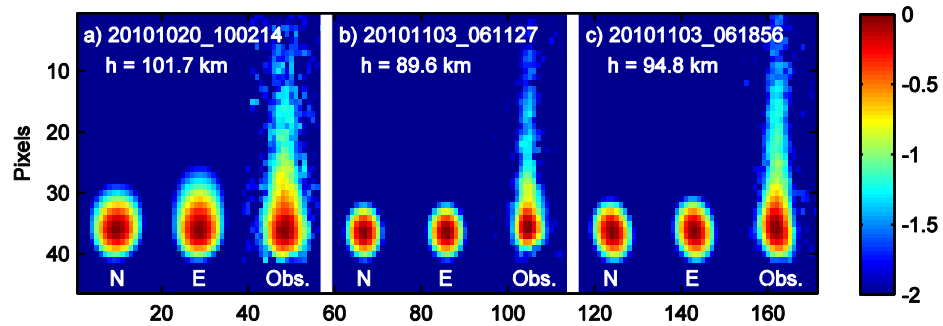


Figure 5.11: Meteors that showed agreement between observations and model output, except for significant disagreements in trail length. Snapshots are plotted in a logarithmic scale to highlight the faint trails that are present in observed meteors, but not the simulations.

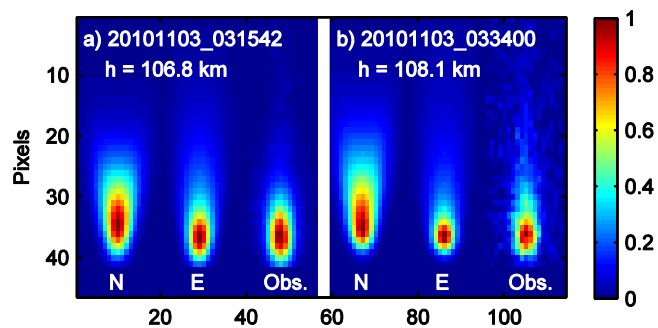


Figure 5.12: Meteors that showed agreement between observations and model output.

speeds, up to 100 m s^{-1} , likely due to meteoroid rotation, electrostatic charging, or explosive devolatilisation (Stokan & Campbell-Brown 2014).

A small fragment, with a transverse speed of 100 m s^{-1} , which remains luminous for three frames (approximately 0.03 s, at a frame rate of 110 frames per second), would travel nearly 3 m laterally from the main body, about the distance spanned by a pixel in the narrow-field system at the range of the meteoroid. Figure 5.13 shows that the disagreement between observed and simulated trail widths is much larger for these events, around 10 pixels at all heights, suggesting that there is another physical process that broadens the meteor wakes, or there is additional instrumental bloom in the observations that is unaccounted for. Alternately, a fragment with significant transverse speed could stay luminous for longer than three frames. This seems unlikely, as the trail width should then increase with decreasing height as the fragment disperses from the main body, a trend that is not observed the three meteors in this group. Alternatively, the narrow-field images should show meteors that are widest towards the back of the trail, since those fragments have had the longest time to move away from the main body, which is also not the case in Fig. 5.10. Figure 5.14 shows that the observed trail is longer than predicted by simulations of a non-fragmenting object, and the trail length of each of these meteors slowly increases as a function of time, suggesting that the fragments were luminous for longer than three frames, but possessed negligible transverse speeds.

Interestingly, the light curves for these three events exhibiting apparent gross fragmentation do not appear to show flares, which are generally associated with the onset of fragmentation. The simulated light curve for 20101020_101727, Fig. 5.15 (b), matches the observed peak magnitude and end height, but yields a begin height that is slightly above the observed equivalent. Similarly, simulations are able to reproduce the peak magnitude and ending height for the other two events, but with a significant discrepancy in beginning heights. The simulated meteoroid deceleration profile for 20101020_101727 shown in Figure 5.16 (b) is a poor match to observations, but there is better agreement for 20101102_233359 and 20101103_062801. Again, these discrepancies may be each explained by continuous fragmentation that may have

complemented the apparent gross fragmentation.

The model was able to fit observations of the next group of meteors, 20101020_100214, 20101103_061127, and 20101103_061856, more closely. A comparison of light curves, Figs. 5.15 (a), (f), and (g), reveals better agreement in beginning heights between the simulation and observations, particularly for 20101103_061127 and 20101103_061856, than for the previous group of meteors. Similarly, the modelled deceleration profiles provide good matches to observations for 20101103_061127 and 20101103_061856, though the simulated lag is underestimated for 20101020_100214, as shown in Figure 5.16. As for high-resolution results, the observed wake widths are largely reproduced by the model, but the simulated wakes are too short, from Figures 5.13 and 5.14. Each of these meteors show a bright core with a very faint and continuous trail that becomes visible when a logarithmic scale is applied to the narrow-field images, Fig. 5.11. This trail is conspicuously absent from the modelled meteors, possibly indicating that they are related to small-scale continuous fragmentation, such as the shedding of grains from a dustball, in contrast to the discrete fragmentation inferred for the previous group of meteors.

The third group of meteors, 20101103_031542, 20101103_033400, and the meteor examined in detail in the previous section, 20101103_063032, showed wakes that were relatively well-matched by the model, both in terms of widths and lengths. Specifically, the simulated widths of 20101103_033400 and 20101103_063032 were a bit narrow but still in agreement with observations as depicted in Figs. 5.9 (a) and 5.14 (e), but simulations matched the observed width of 20101103_031542 almost perfectly, shown in Fig. 5.14 (d). It is a possibility that fragmentation was negligible for these meteors, explaining the good agreement between simulated and observed trail lengths, in Figs. 5.9 (b), and 5.14 (d) and (e). Surprisingly, there is a significant difference in modelled and observed beginning heights in the light curves for 20101103_031542 and 20101103_033400, Figs. 5.15 (d) and (e), and the simulated deceleration is underestimated compared to observations for all three meteoroids. Also, there is an offset in the meteoroid deceleration curve from each station for observations of 20101103_031542, likely related to the poor geometry of the observations ($Q^* = 5.4^\circ$), reiterating the requirement

Table 5.3: Initial meteoroid mass, m_i , density, ρ_{met} , and composition (giving heat of ablation and mean meteoric particle mass), for model fits to the meteors of this study. A bracketed number in the density column indicates the ideal value to fit the deceleration curve.

	m_i (10^{-6} kg)	ρ_{met} (kg m^{-3})	Comp.
20101020_100214	1.2 ± 0.1	600 ± 100 (200)	stony
20101020_101727	3.0 ± 0.5	1400 ± 100 (400)	stony
20101102_233359	35 ± 5	700 ± 100	stony
20101103_031542	10 ± 2	1100 ± 100 (400)	stony
20101103_033400	0.27 ± 0.02	900 ± 100 (400)	stony
20101103_061127	1.4 ± 0.2	2400 ± 300 (1200)	stony
20101103_061856	2.8 ± 0.2	1800 ± 300	stony
20101103_062801	1.5 ± 0.1	600 ± 100	cometary
20101103_063032	0.18 ± 0.02	900 ± 100 (200)	stony

for better observations for any follow-up studies.

Finally, the parameters used to fit the observations of each meteor are given in Table 5.3. Masses ranged from 1.8×10^{-7} to 3.5×10^{-5} kg, while densities varied between 600 and 2400 kg m^{-3} . These densities correspond to objects with cometary origins according to a recent image-intensified study employing the dustball model (Kikwaya et al. 2011), but only one of the events, 20101103_062801, was well-matched with a cometary composition. As noted earlier, composition defines the heat of ablation and the mean meteoric particle mass. Cometary meteoroids are assumed to have a smaller heat of ablation, translating their light curves higher, while smaller mean particle masses make the wake narrower and longer, as the particles are more rapidly thermalised in collisions with atmospheric particles compared to meteoric particles with higher mass.

5.5 Discussion of model assumptions and improvements

The four principal assumptions of the model are that

1. the meteoroid is monolithic and does not fragment;
2. the meteoroid temperature is constant, the heat of ablation is constant, and all of the

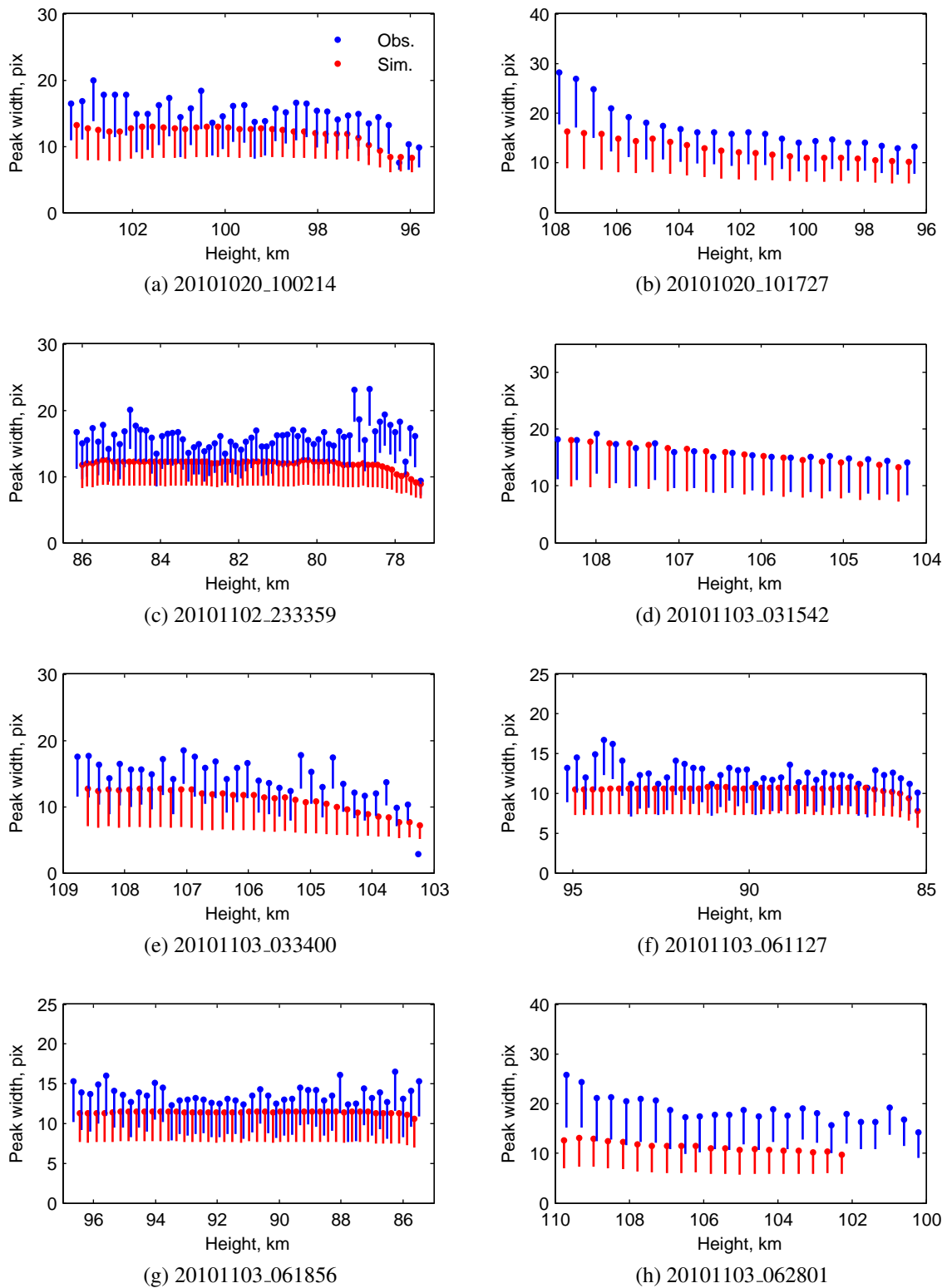


Figure 5.13: Trail width measurements for observed and simulated meteors.

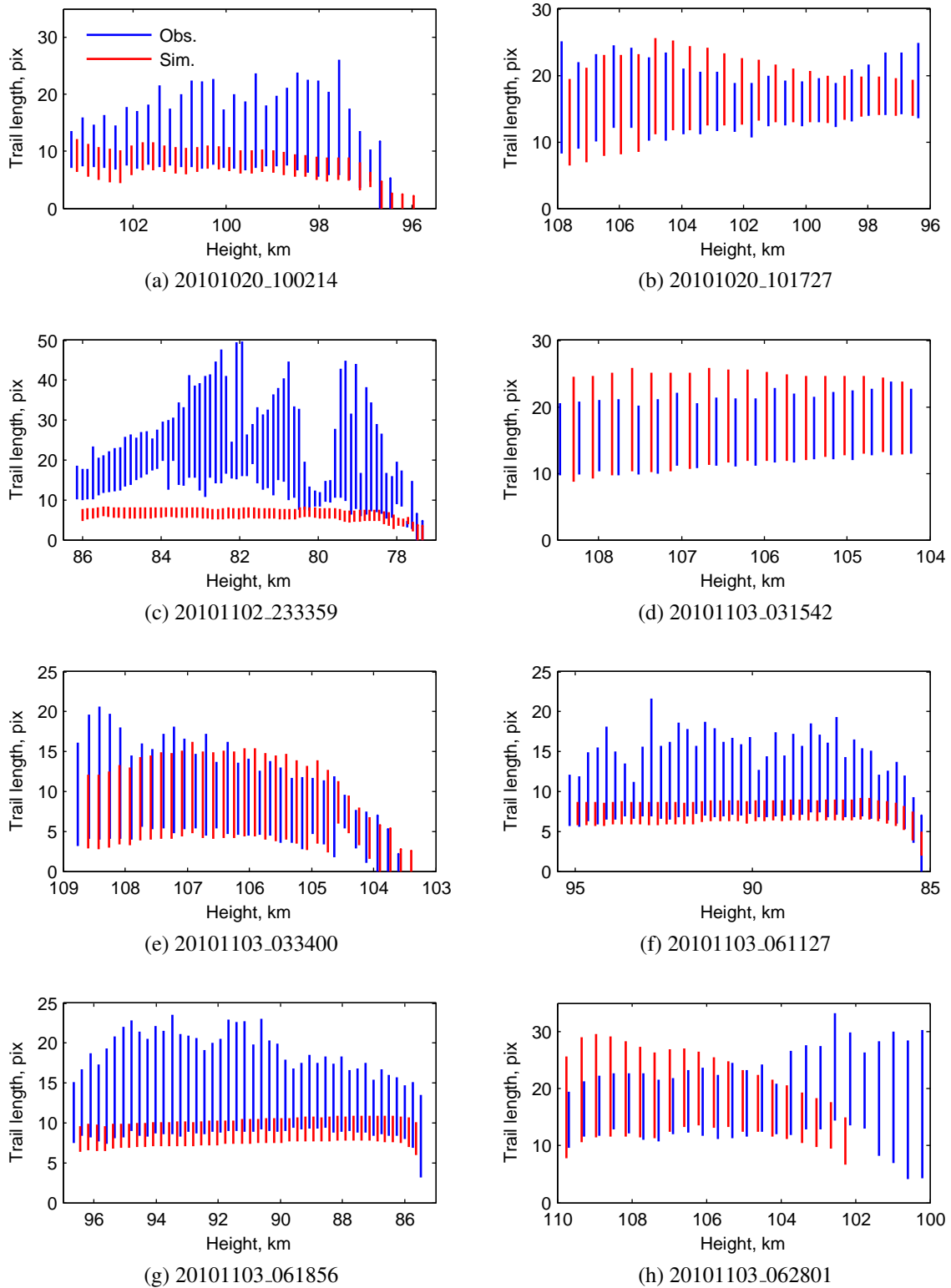
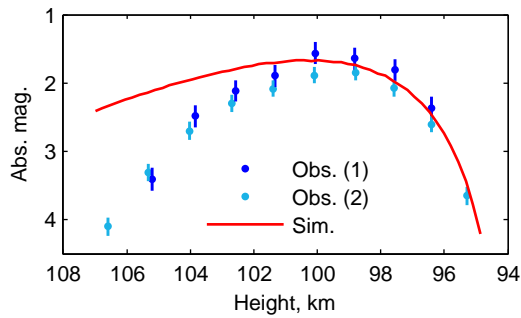
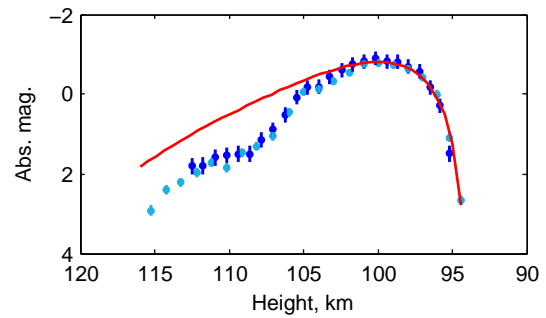


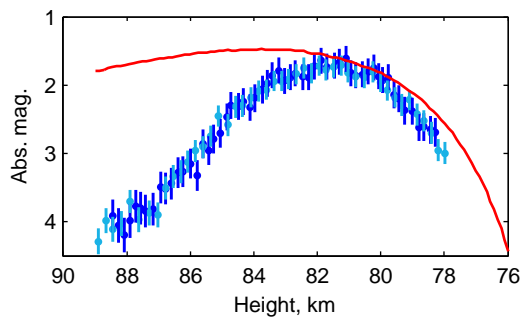
Figure 5.14: Trail length measurements for observed and simulated meteors.



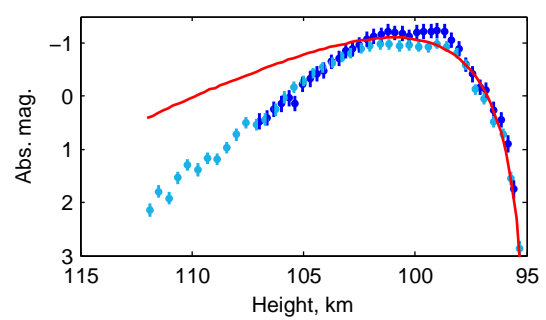
(a) 20101020_100214



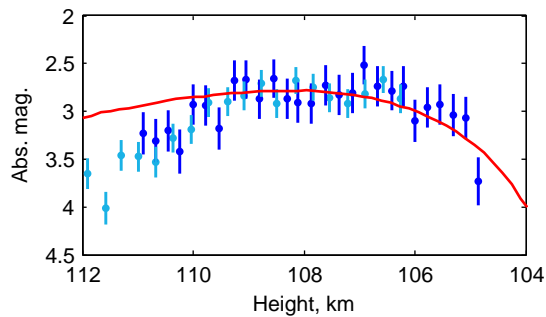
(b) 20101020_101727



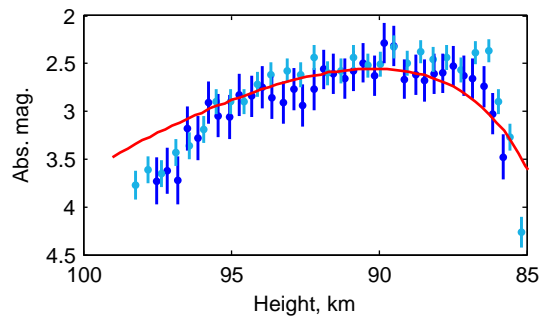
(c) 20101102_233359



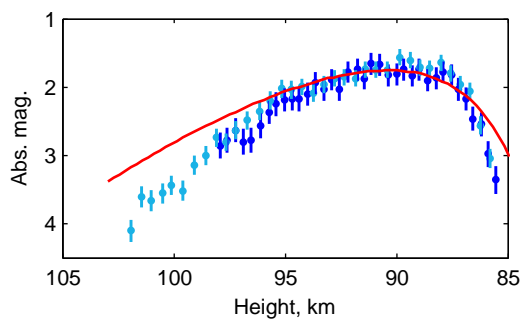
(d) 20101103_031542



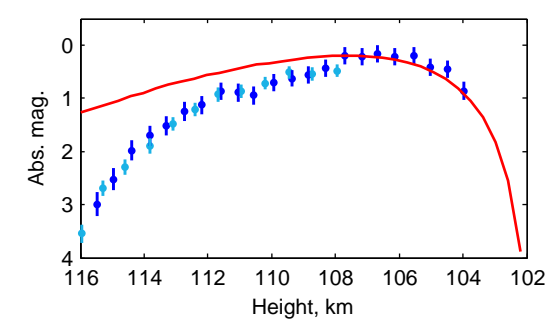
(e) 20101103_033400



(f) 20101103_061127



(g) 20101103_061856



(h) 20101103_062801

Figure 5.15: Observed and simulated meteor light curves.

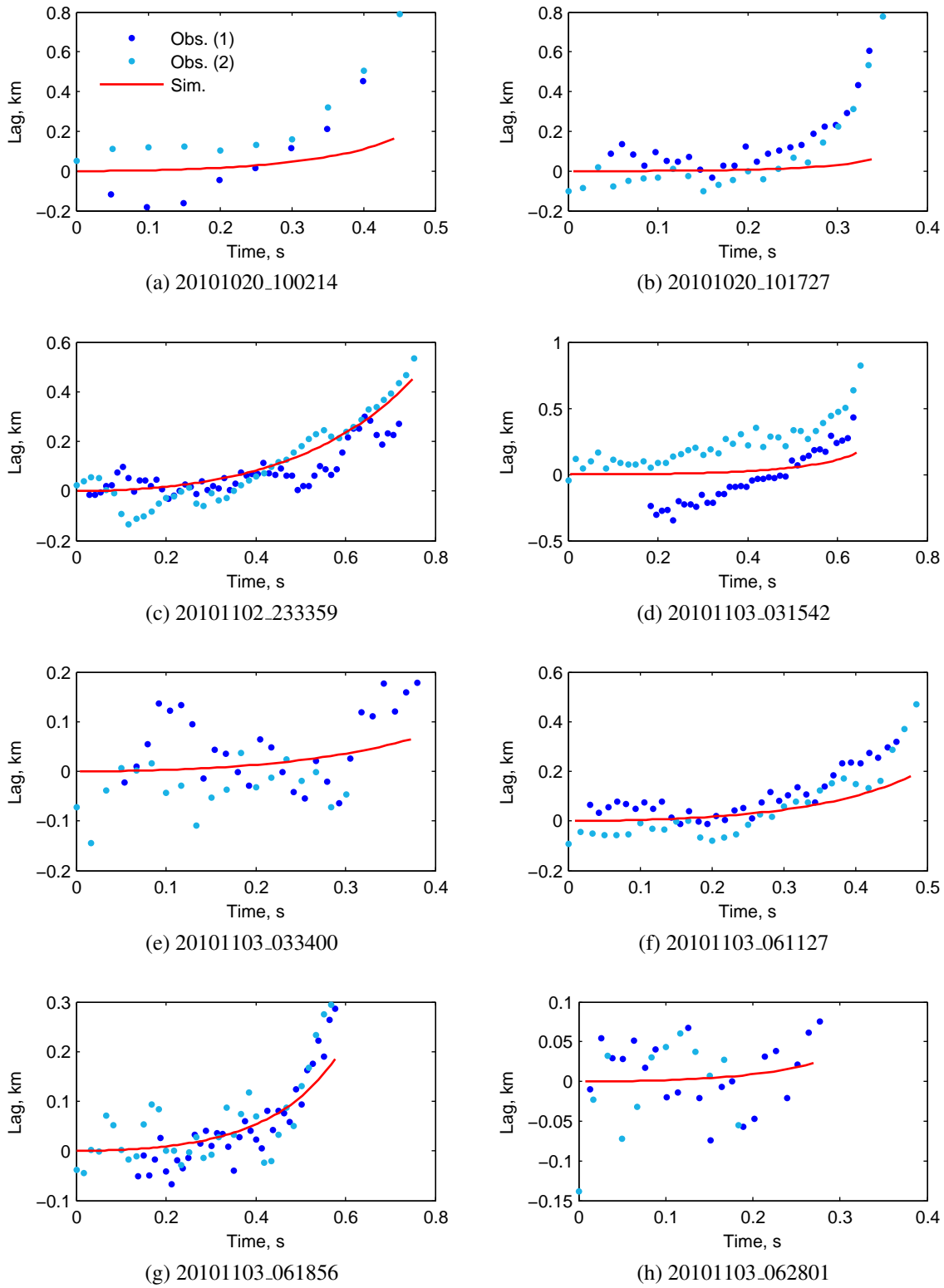


Figure 5.16: Observed and simulated meteoroid deceleration profiles.

- incoming particle energy is used, instantaneously, to evaporate the meteoroid;
3. collisions between particles are elastic and are assumed to produce detectable light with either uniform probability, or probability that is proportional to the energy of the collisions; and
 4. atmospheric particles are not screened by evaporated particles, and evaporated particles only interact with atmospheric particles, and not with each other.

Explicitly modelling fragmentation would help to account for the discrepancy between simulated and observed light curves and deceleration profiles. The meteor wake length would increase, while wake width would likely not be affected significantly compared to a non-fragmenting meteoroid, assuming the fragments have negligible transverse speed components. The disadvantage of including fragmentation is the potential addition of some new parameters that are poorly defined, such as the melting temperature and heat of sublimation of the volatile matrix binding the meteoroid grains. Careful consideration of the grain size distribution would also be required to ensure that simulated wakes do not become significantly longer than observed (Campbell-Brown et al. 2013). Additionally, a few of the meteoroids (20101103_031542, 20101103_033400, and 20101103_063032) did not appear to fragment, yet were not fitted (light curve, deceleration profile) by a single-body ablation model, suggesting other processes may have to be considered.

To make the light curve shorter, or decrease the interval between the beginning and ending heights, the rate of ablation, Eq. (5.2), must be increased since the luminous power output of the meteoroid is proportional to the rate of mass loss, as given by Eq. (5.3). As noted earlier, increasing the rate of ablation by setting the initial density or heat of ablation lower also translates the beginning height upwards. Fragmentation is a convenient way of introducing time-varying parameters, namely the effective cross-section of the meteoroid, to attain large rates of ablation at relatively low heights in the atmosphere. The heat transfer coefficient describes the proportion of incident energy from atmosphere collisions that is consumed in ablating the meteoroid.

For this simulation, it was assumed that all of the energy was used to evaporate particles, but it is possible that some of energy was consumed in heating the meteoroid initially, producing a time-varying heat transfer coefficient that started off relatively small as energy was used to heat the meteoroid, but converged towards unity as the meteoroid heated to the temperature of intensive evaporation. More detailed modelling of the meteoroid temperature, especially when considering a non-isothermal body, is a promising prospect to improve how well the model reflects observations, but also introduces new parameters, such as the meteoroid heat capacity and thermal conductivity, which are not well-defined.

A significant improvement to the model would be a more detailed model for light production resulting from particle collisions. In the current iteration of this model, simulated meteor images are generated by assuming that pixel brightness is either proportional to the number of collisions, or the total energy of collisions in the area of the pixel. These assumptions implicitly state that each collision has an equal probability of producing light, or that the probability of producing light is proportional to the collision energy, respectively. Neither assumption for light production is satisfactory, as was shown in Section 5.4.1. All collisions are also assumed to be elastic, which can artificially widen (or lengthen) the meteor wake. Ideally, an inelastic collision model for excitation and ionization of particles should be implemented. A mechanism for the subsequent de-excitation of those particles would also have to be considered. This would improve the realism of the simulated high-resolution output, allow for comparison with observed meteor spectra, as well as possibly improve the agreement between simulated and observed light curves. This may also provide insight into the value of the luminous efficiency, τ in Eq. (5.3), as a function of meteoroid height and speed.

Perhaps the most important (and complex) area of improvement would be to simulate the state of the flow around the meteoroid. Right now, it is assumed that the atmospheric atoms and molecules dominate the addition of any energetic evaporated particles in the area around the meteoroid. In practical terms, it is assumed that there is negligible screening between atmospheric particles and the meteoroid, and that evaporated meteoric particles interact only

with atmospheric particles. If there was a co-moving concentration of dense gas around the meteoroid, this could reduce the width (and possibly increase the length) of the meteor wake, as excited particles would be stopped and thermalise more rapidly. Interestingly, many of the simulated meteor wakes were narrower than observed, suggesting that screening may actually be insignificant at the heights of the meteors examined in this study, but this should be examined in more detail.

5.6 Conclusions

A new, particle-based model for faint meteor ablation has been presented. The model is able to reproduce the widths for nine selected meteors by assuming that light is emitted from collisions between atmospheric and evaporated meteoric particles. The assumption that the probability that a collision produces light is proportional to the collision energy yields better agreement with observed meteor morphology than simply assuming that all collisions above a certain energy threshold produce light with equal efficiency. In any case, this suggests that the observed width of faint meteors can be explained by chemical (collisional), rather than physical (lateral dispersion of fragments), processes. Alternately, since many of the simulated wakes resulting from this single-body model were shorter than observations, it seems that fragmentation makes a significant contribution to the wake length.

Light curves and deceleration profiles were also produced for the nine events, yielding values for initial meteoroid mass and density, as well as a coarse segregation into either stony or cometary material. Eight of the observed light curves were mostly matched by this single-body model, but the deceleration profiles proved difficult to simultaneously reproduce, suggesting that fragmentation or other effects must be considered.

In addition to considering fragmentation and detailed monitoring of the conditions of the flow around the meteoroid in the next iteration of this model, a more detailed model of energy deposition into the meteoroid, as well as a model for light production involving inelastic

collisions and subsequent de-excitation of atoms should be considered. Implementing these changes should allow the simulation to match observations more closely, and ultimately provide better information about meteoroid structure and ablation processes.

Bibliography

Baggaley, W. J., (1970). The determination of the initial radii of meteor trains. *Monthly Notices of the Royal Astronomical Society*, 147, 231-243.

Baggaley, W. J., (1980). Measurements of the velocity dependence of the initial radii of meteor trails. *Bulletin of the Astronomical Institute of Czechoslovakia*, 31 (5), 308-311.

Bird, G. A., *Molecular Gas Dynamics and the Direct Simulation of Gas Flows*. Oxford University Press, 1994.

Borovička, J., (1990). The comparison of two methods of determining meteor trajectories from photographs. *Bulletin of the Astronomical Institutes of Czechoslovakia*, 41, 391-396.

Borovička, J., (1993). A fireball spectrum analysis. *Astronomy & Astrophysics*, 279, 627-645.

Borovička, J., (1994). Two components in meteor spectra. *Planetary and Space Science*, 42 (2), 145-150.

Borovička, J., Spurný, P., Koten, P., (2007). Atmospheric deceleration and light curves of Draconid meteors and implications for the structure of cometary dust. *Astronomy & Astrophysics*, 473, 661-672.

Boyd, I. D., (2000). Computation of atmospheric entry flow about a Leonid meteoroid. *Earth, Moon, and Planets*, 82-83, 93-108.

Bronshten, V. A., *Physics of Meteoric Phenomena*. D. Reidel Publishing Co., 1983.

Campbell-Brown, M. D., Borovička, J., Brown, P. G., Stokan, E., (2013). High-resolution modelling of meteoroid ablation. *Astronomy & Astrophysics*, 557, A41, 13pp.

Campbell-Brown, M., Jones, J., (2003). Determining the initial radius of meteor trains: fragmentation. *Monthly Notices of the Royal Astronomical Society*, 343, 775-780.

Campbell-Brown, M. D., Koschny, D., (2004). Model of the ablation of faint meteors. *Astronomy & Astrophysics*, 418, 751-758.

Cepelcha, Z., Borovička, J., Elford, W. G., ReVelle D. O., Hawkes, R. L., Porubčan, V., Šimek, M., (1998). Meteor phenomena and bodies. *Space Science Reviews*, 84, 327-471.

Cook, A. F., Hawkins, G. S., Stienon, F. M., (1962). Meteor trail widths. *The Astronomical Journal*, 67 (3), 158-162.

Duda, R. O., Hart, P. E., (1972). Use of the Hough transformation to detect lines and curves in pictures. *Communications of the ACM*, 15 (1), 11-15.

Fisher, A. A., Hawkes, R. L., Murray, I. S., Campbell, M. D., LeBlanc, A. G., (2000). Are meteoroids really dustballs? *Planetary and Space Science*, 48, 911-920.

Greenhow, J. S, Hall, J. E., (1960). The importance of initial trail radius on the apparent height and number distributions of meteor echoes. *Monthly Notices of the Royal Astronomical Society*, 121 (2), 183-197.

Hawkes, R. L., Jones, J., (1975). A quantitative model for the ablation of dustball meteors. *Monthly Notices of the Royal Astronomical Society*, 173, 339-356.

Hawkes, R. L., Jones, J., (1978). The effect of rotation on the initial radius of meteor trains. *Monthly Notices of the Royal Astronomical Society*, 185, 727-734.

Hawkins, G. S., Southworth, R. B., (1958). The statistics of meteors in the Earth's atmosphere. *Smithsonian Contribution to Astrophysics*, 2 (11), 349-364.

Hawkins, G. S., Whipple, F. L., (1958). The width of meteor trails. *The Astronomical Journal*, 63 (1261), 283-291.

Hedin, A. E., (1991). Extension of the MSIS thermospheric model into the middle and lower atmosphere. *Journal of Geophysical Research*, 96, 1159-1172.

Jacchia, L. G., (1955). The physical theory of meteors. VIII. Fragmentation as a cause of the faint-meteor anomaly. *The Astrophysical Journal*, 121, 521-527.

Jones, J., Campbell-Brown, M., (2005). The initial train radius of sporadic meteors. *Monthly Notices of the Royal Astronomical Society*, 359, 1131-1136.

Jones, W., (1995). Theory of the initial radius of meteor trains. *Monthly Notices of the Royal Astronomical Society*, 275, 812-818.

Kaiser, N., Brown, P., Hawkes, R. L., (2004). Optical trail width measurements of faint meteors. *Earth, Moon, and Planets*, 95, 579-586.

Kascheyev, B. L., Lebedinets, V. N., (1963). The initial radius of ionized meteor trails. *Smithsonian Contribution to Astrophysics*, 7, 19-22.

Kikwaya, J.-B., Campbell-Brown, M. D., Brown, P. G., (2011). Bulk density of small meteoroids. *Astronomy & Astrophysics*, 530, A113, 17pp.

Koten, P., Spurný, P., Borovička, J., Evans, S., Elliott, A., Betlem, H., Štork, R., Jobse, K., (2006). The beginning heights and light curves of high-altitude meteors. *Meteoritics & Planetary Science*, 41 (9), 1305-1320.

Manning, L. A., (1958). The initial radius of meteoric ionization trails. *Journal of Geophysical Research*, 63 (1), 181-196.

McKinley, D. W. R., *Meteor Science and Engineering*. McGraw-Hill, 1961.

Murray, I. S., Hawkes, R. L., Jenniskens, P., (1999). Airborne intensified charge-coupled device observations of the 1998 Leonid shower. *Meteoritics & Planetary Science*, 34, 949-958.

Popova, O. P., Sidneva, S. N., Shuvalov, V. V., Strelkov, A. S., (2000). Screening of meteoroids by ablation vapor in high-velocity meteors. *Earth, Moon, and Planets*, 82-83, 109-128.

Phelps, A. V., (1991). Cross sections and swarm coefficients for nitrogen ions and neutrals in N₂ and argon ions and neutrals in Ar for energies from 0.1 eV to 10 keV. *Journal of Physical and Chemical Reference Data*, 20 (3), 557-573.

Shen, C., *Rarefied Gas Dynamics: Fundamentals, Simulations and Micro Flows*. Springer, 2005.

Spurný, P., Betlem, H., Jobse, K., Koten, P., van't Leven, J., (2000). New type of radiation of bright Leonid meteors above 130 km. *Meteoritics & Planetary Science*, 35, 1109-1115.

Stenbaek-Nielsen, H. C., Jenniskens, P., (2004). A “shocking” Leonid meteor at 1000 fps. *Advances in Space Research*, 33, 1459-1465.

Stokan, E., Campbell-Brown, M. D., (2014). Transverse motion of fragmenting faint meteors observed with the Canadian Automated Meteor Observatory. *Icarus*, 232, 1 - 12.

Stokan, E., Campbell-Brown, M. D., Brown, P. G., Hawkes, R. L., Doubova, M., Weryk, R. J., (2013). Optical trail widths of faint meteors observed with the Canadian Automated Meteor Observatory. *Monthly Notices of the Royal Astronomical Society*, 433 (2), 962-975.

Vinković, D., (2007). Thermalization of sputtered particles as the source of diffuse radiation from high altitude meteors. *Advances in Space Research*, 39, 574-582.

Weryk, R. J., Brown, P. G., (2012). Simultaneous radar and video meteors—I: Metric comparisons. *Planetary and Space Science*, 62, 132-152.

Weryk, R. J., Brown, P. G., (2013). Simultaneous radar and video meteors—II: Photometry and ionisation. *Planetary and Space Science*, 81, 32-47.

Weryk, R. J., Campbell-Brown, M. D., Wiegert, P. A., Brown, P. G., Krzeminski, Z., Musci, R., (2013). The Canadian Automated Meteor Observatory (CAMO): System overview. *Icarus*, 225, 614-622.

Chapter 6

Conclusions

6.1 Summary of work

The goal of this thesis was to improve understanding of the processes of fragmentation and wake formation in faint meteors. As discussed in Chapter 1, these processes are poorly understood, and have implications for models of meteoroid structure and composition, the accuracy of specular radar observations of meteors, and estimates of meteor height distributions and flux. High-resolution observations were analysed to quantify meteor trail widths as a function of height and provide estimates of the strength of meteoric material. The formation of the meteor wake was also investigated through a new small meteoroid ablation model based on these observations.

In Chapter 3, the trail widths of thirty faint meteors were measured. The trails were captured with the narrow-field cameras of the Canadian Automated Meteor Observatory (CAMO) and measured with the image analysis software ImageJ. To correct for instrumental bloom, the widths of stars (assumed to be point sources broadened by the system point spread function) with equivalent brightness to the meteor trails were subtracted from the measured trail widths. Meteor wake widths up to 110 m at heights above 110 km were measured after bloom correction. These widths were between the values measured for sporadic meteors by Kaiser et al.

(2004) and those of high-altitude Leonids observed by Spurný et al. (2000). Since the trail widths varied roughly as the inverse of the atmospheric density, collisional processes involving evaporated meteoric atoms were suggested to be responsible for wake formation. Chapter 5 would investigate the wake formation process in more detail.

Nine faint meteors showing gross fragmentation were observed and analysed in Chapter 4. In particular, the transverse speeds (perpendicular to the meteoroid velocity) of the fragments were measured to suggest possible causes for meteoroid fragmentation. To determine the transverse speeds, the location of each fragment was marked on each frame of the narrow-field videos of a meteor. Image enhancements, such as 3×3 median and wavelet filtering were employed to help make dim fragments distinguishable from the background noise. The fragments' positions were converted to displacements from a reference fragment throughout the entire video, the displacements were then decomposed into components parallel and perpendicular to the meteor trail, and the perpendicular displacement components were fit by first- and second-order polynomials as a function of time to determine the fragments' transverse speeds.

Eight of the nine meteors were found show fragments having transverse speeds up to 100 m s^{-1} , while transverse acceleration of the fragments was found to be negligible. These speeds were not explained by aerodynamic loading theory, typically applied to brighter meteors that fragment at lower heights where the atmosphere is more dense. Instead, breakup due to rotation and due to electrostatic charge accumulation were examined in separate cases, with simple models yielding rotation speeds up to $2 \times 10^4 \text{ Hz}$ and meteoroid potentials up to $4 \times 10^6 \text{ V}$, respectively. Meteoroid rotational speeds up to $1.3 \times 10^4 \text{ Hz}$ were previously speculated by Hawkes & Jones (1978), while Sorasio et al. (2001) estimated that a $40 \mu\text{m}$ meteoroid could acquire a peak surface potential of 4 V , suggesting that rotational fragmentation was more plausible. In either case, strengths of up to 1 MPa were derived for the meteoroids, matching strengths observed in bolide meteoroids and meteorites (Borovička 2006).

In Chapter 5, the process of meteor wake formation was revisited. A single-body meteoroid ablation model, based on simulating the interactions between atmospheric molecules,

the meteoroid, and evaporated meteoric atoms, was devised and tested with observations of nine meteors from Chapter 3. Atmospheric molecules undergo collisions with the meteoroid, imparting energy and momentum, which respectively ablate and decelerate the meteoroid. Evaporated meteoric molecules are then tracked in twenty-one elastic collisions with atmospheric molecules. The energy and position of each collision is recorded to produce a simulated narrow-field image for comparison with observations. Meteor light is assumed to result from collisions either by assuming that each collisions has equal likelihood of emitting a photon, or by assuming that collisions with higher energy have greater probability of emitting a photon.

Observed meteor trail widths were mostly reproduced by the model when it was assumed that light production was proportional to the energy of collisions. Simulated meteor trail lengths tended to be too short compared to observations, suggesting that the effect of continuous meteoroid fragmentation should be considered. Light curves were mostly reproduced by the model for the nine selected meteors, but the lengths of simulated light curves were too long. Conversely, simulated meteoroids consistently showed insufficient deceleration compared to observations. Modelled light curves that are too long, as well as decelerations that are inadequate, suggest that continuous fragmentation should be considered in the next version of the ablation model. In the end, the model suggests that the width of meteor wakes is due to collisional de-excitation of energetic evaporated meteoric particles, rather than transverse motion of small meteoroid fragments, at least for the nine meteors examined.

6.2 Next steps

Observations and modelling in this thesis suggest that the width of the meteor wake can be explained by atomic collisional processes, but the length of the wake is ambiguous. Dustball ablation theory suggests that meteoroid grains of different mass should spread out along the meteoroid's direction of travel as a result of deceleration that is dependent on cross-sectional area. Curiously, previous image-intensified video observations (Fisher et al. 2000) have mea-

sured negligible wake lengths in the majority of meteors studied, while a more recent study was able to match meteor light curves and deceleration profiles with contemporary dustball ablation models, but also simulated trail lengths that were much longer than observed (Campbell-Brown et al. 2013).

A detailed study of meteor wake lengths, similar to Chapter 3 of this thesis, should be undertaken, combining trail length measurements with observed light curves and deceleration profiles. A simple model may be devised to determine the smallest grain size that would account for the measured trail lengths. Observations of the relative deceleration of grains resulting from gross fragmentation would also allow for calculation of grain sizes. Both of the studies would yield information on the grain size distribution of meteoroids, which would be particularly instructive in a comparison between meteoroids of different streams, informing about structural differences amongst parent bodies.

Similarly, a survey of the width of meteor wakes across different showers may serve to inform about relative differences in composition. Our current study focused on meteors occurring over three nights (20 October, 3 November, and 6 November 2010) but selected sporadic meteors with the best observations, limiting what could be learned about the relationship between meteoroid composition and trail widths. Chapter 5 noted that meteoric atoms with smaller mass appear to form thinner, longer trails. Producing a figure of trail width as a function of height for several different showers could indicate relative compositions. At the very least, the effect of meteoroid speed on trail widths could be investigated, as meteoroids from a certain stream all have similar velocities.

Much future work lies in improving the ablation model discussed in Chapter 5, where the four main assumptions were outlined in Section 5.5. Including continuous fragmentation of the meteoroid would likely have the largest effect on the model output, allowing for shorter light curves without a late peak in brightness, more meteoroid deceleration, and longer trails. Unfortunately, including fragmentation would render the assumption that there is no screening by evaporated meteoric atoms, and that meteoric atoms only interact with atmospheric atoms

less valid. Perhaps a more detailed model for the flow around the meteoroid, as in Boyd (2000), should be considered first for improvement of the model since this would allow for interactions between meteoroid grains to be modelled explicitly. Both of these improvements would provide information about the mass distribution of grains comprising the meteoroid, as with other dustball models (Campbell-Brown et al. 2013), but would consider meteor wake lengths in more detail as an additional constraint.

A better model for light production, involving inelastic collisions, electronic, rotational, and vibrational modes is also important. This would provide verification of the meteor wake morphologies produced with the current model's assumptions, and would allow the luminous efficiency coefficient (giving the fraction kinetic energy dissipated as meteor light), and its relationship to meteoroid composition, to be investigated. Studying plasma interactions in the meteor wake may reveal alternate methods of wake formation and widening, though perhaps over different time scales than what is observed optically (Dyrud et al. 2001, Oppenheim et al. 2003). Additionally, considering the uncertainty in the atmospheric density (Stober et al. 2012), different values of the drag coefficient, and different distributions for the velocities of reflected and evaporated particles would illustrate how the wake morphology varies with uncertainty in model parameters not directly related to the meteoroid.

Finally, differential ablation as a method of producing non late-peaked light curves without fragmentation may be investigated by considering meteoroids with an inhomogeneous composition. Meteor light production is proportional to the rate of ablation, which is related to the heat of ablation. An example might be a meteoroid comprised of a shell of volatile material around a core of more refractory material, resulting in a quick rise in brightness as the volatile shell is ablated away, then a more gradual rise during the ablation of the remainder. This would provide more information about relative abundances in the meteoroid, but would likely require spectral observations to constrain fully.

Bibliography

Borovička, J., (2006). Physical and chemical properties of meteoroids as deduced from observations. In: Asteroids, Comets, Meteors, Proceedings of the 229th Symposium of the International Astronomical Union, edited by D. Lazzaro, S. Ferraz-Mello, J. A. Fernández. Cambridge: Cambridge University Press. 249-271.

Boyd, I. D., (2000). Computation of atmospheric entry flow about a Leonid meteoroid. *Earth, Moon, and Planets*, 82-83, 93-108.

Campbell-Brown, M. D., Borovička, J., Brown, P. G., Stokan, E., (2013). High-resolution modelling of meteoroid ablation. *Astronomy & Astrophysics*, 557, A41, 13pp.

Dyrud, L. P., Oppenheim, M. M., vom Endt, A. F., (2001). The anomalous diffusion of meteor trails. *Geophysical Research Letters*, 28 (14), 2775-2778.

Fisher, A. A., Hawkes, R. L., Murray, I. S., Campbell, M. D., LeBlanc, A. G., (2000). Are meteoroids really dustballs? *Planetary and Space Science*, 48, 911-920.

Hawkes, R. L., Jones, J., (1978). The effect of rotation on the initial radius of meteor trains. *Monthly Notices of the Royal Astronomical Society*, 185, 727-734.

Kaiser, N., Brown, P., Hawkes, R. L., (2004). Optical trail width measurements of faint meteors. *Earth, Moon, and Planets*, 95, 579-586.

Oppenheim, M. M., Dyrud, L. P., Ray, L., (2003). Plasma instabilities in meteor trails: Linear theory. *Journal of Geophysical Research*, 108 (A2), SIA 7, 8pp.

Sorasio, G., Mendis, D. A., Rosenberg, M., (2001). The role of thermionic emission in meteor physics. *Planetary and Space Science*, 49, 1257-1264.

Spurný, P., Betlem, H., Jobse, K., Koten, P., van't Leven, J., (2000). New type of radiation of bright Leonid meteors above 130 km. *Meteoritics & Planetary Science*, 35, 1109-1115.

Stober, G., Jacobi, C., Matthias, V., Hoffman, P., Gerding, M., (2012). Neutral air density variations during strong planetary wave activity in the mesopause region derived from meteor radar observations. *Journal of Atmospheric and Solar-Terrestrial Physics*, 74, 55-63.

Appendix A

Copyright Permissions

Journal: Monthly Notices of the Royal Astronomical Society

DOI: 10.1093/mnras/stt779

Title: Optical trail widths of faint meteors observed with the Canadian Automated Meteor Observatory

Standard Licence

You hereby grant to Oxford University Press an exclusive licence for the full period of copyright throughout the world:

- to publish the final version of the Article in the above Journal, and to distribute it and/or to communicate it to the public, either within the Journal, on its own, or with other related material throughout the world, in printed, electronic or any other format or medium whether now known or hereafter devised;
- to make translations and abstracts of the Article and to distribute them to the public;
- to authorize or grant licences to third parties to do any of the above;
- to deposit copies of the Article in online archives maintained by OUP or by third parties authorized by OUP.

You authorize us to act on your behalf to defend the copyright in the Article if anyone should infringe it and to register the copyright of the Article in the US and other countries, if necessary.

In the case of a multi authored article, you confirm that you are authorized by your co-authors to enter the licence on their behalf.

You confirm to OUP that the Article

- is your original work;
- has not previously been published (in print or electronic format) is not currently under consideration by another journal or if it has already been submitted to other journals, it will be immediately withdrawn;
- will not be submitted for publication to any other journal following acceptance in the above Journal; and
- OUP will be the first publisher of the Article.

You warrant to OUP that

- no part of the Article is copied from any other work,
- you have obtained ALL the permissions required (for print and electronic use) for any material you have used from other copyrighted publications in the Article; and
- you have exercised reasonable care to ensure that the Article is accurate and does not contain anything which is libellous, or obscene, or infringes on anyone's copyright, right of privacy, or other rights.

Further Information

(Full details of OUP's publication rights policies, including author rights can be found at http://www.oxfordjournals.org/access_purchase/publication_rights.html)

Author Self-Archiving Policy

You may post the FINAL PUBLISHED version of the Article onto your own website, your institution's website and in institutional or subject-based repositories, PROVIDED THAT: (1) you include a link (url) to the published version of the Article on the Journal's website; (2) the Journal is attributed as the original place of publication with the correct citation details given.

On publication of your Article in the Journal you are not required to remove any previously posted PRE-PRINT versions from your own personal website or that of your employer or free public servers of pre-prints and/or articles in your subject area, provided (1) you include a link (url) to the published version of the Article on the Journal's website; AND (2) the Journal is attributed as the original place of publication with the correct citation details given.

Free Link to Published Article

On publication of your article, you will receive a URL, giving you access to the published article on the Journal website, and information on use of this link.

Educational Use

You may use the Article within your employer's institution or company for educational or research purposes only, including use in course-packs, as long as: (1) you do not use it for commercial purposes or re-distribution outside of the institution/company; (2) you acknowledge the Journal as the original place of publication with the correct citation details given.

Edward Stokan signed this licence on 2013-05-05 12:28:03 GMT.

**ELSEVIER LICENSE
TERMS AND CONDITIONS**

Nov 02, 2014

This is a License Agreement between Edward Stokan ("You") and Elsevier ("Elsevier") provided by Copyright Clearance Center ("CCC"). The license consists of your order details, the terms and conditions provided by Elsevier, and the payment terms and conditions.

All payments must be made in full to CCC. For payment instructions, please see information listed at the bottom of this form.

Supplier	Elsevier Limited The Boulevard, Langford Lane Kidlington, Oxford, OX5 1GB, UK
Registered Company Number	1982084
Customer name	Edward Stokan
Customer address	Department of Physics and Astronomy London, ON N6A3M1
License number	3501051321300
License date	Nov 02, 2014
Licensed content publisher	Elsevier
Licensed content publication	Icarus
Licensed content title	Transverse motion of fragmenting faint meteors observed with the Canadian Automated Meteor Observatory
Licensed content author	E. Stokan, M.D. Campbell-Brown
Licensed content date	April 2014
Licensed content volume number	232
Licensed content issue number	n/a
Number of pages	12
Start Page	1
End Page	12
Type of Use	reuse in a thesis/dissertation
Portion	full article
Format	both print and electronic
Are you the author of this Elsevier article?	Yes
Will you be translating?	No
Title of your thesis/dissertation	Fragmentation and wake formation in faint meteors: implications for the structure and ablation of small meteoroids
Expected completion date	Nov 2014

Estimated size (number of pages)	240
Elsevier VAT number	GB 494 6272 12
Permissions price	0.00 CAD
VAT/Local Sales Tax	0.00 CAD / 0.00 GBP
Total	0.00 CAD
Terms and Conditions	

INTRODUCTION

1. The publisher for this copyrighted material is Elsevier. By clicking "accept" in connection with completing this licensing transaction, you agree that the following terms and conditions apply to this transaction (along with the Billing and Payment terms and conditions established by Copyright Clearance Center, Inc. ("CCC"), at the time that you opened your Rightslink account and that are available at any time at <http://myaccount.copyright.com>).

GENERAL TERMS

2. Elsevier hereby grants you permission to reproduce the aforementioned material subject to the terms and conditions indicated.

3. Acknowledgement: If any part of the material to be used (for example, figures) has appeared in our publication with credit or acknowledgement to another source, permission must also be sought from that source. If such permission is not obtained then that material may not be included in your publication/copies. Suitable acknowledgement to the source must be made, either as a footnote or in a reference list at the end of your publication, as follows:

“Reprinted from Publication title, Vol /edition number, Author(s), Title of article / title of chapter, Pages No., Copyright (Year), with permission from Elsevier [OR APPLICABLE SOCIETY COPYRIGHT OWNER].” Also Lancet special credit - “Reprinted from The Lancet, Vol. number, Author(s), Title of article, Pages No., Copyright (Year), with permission from Elsevier.”

4. Reproduction of this material is confined to the purpose and/or media for which permission is hereby given.

5. Altering/Modifying Material: Not Permitted. However figures and illustrations may be altered/adapted minimally to serve your work. Any other abbreviations, additions, deletions and/or any other alterations shall be made only with prior written authorization of Elsevier Ltd. (Please contact Elsevier at permissions@elsevier.com)

6. If the permission fee for the requested use of our material is waived in this instance, please be advised that your future requests for Elsevier materials may attract a fee.

7. Reservation of Rights: Publisher reserves all rights not specifically granted in the combination of (i) the license details provided by you and accepted in the course of this

licensing transaction, (ii) these terms and conditions and (iii) CCC's Billing and Payment terms and conditions.

8. License Contingent Upon Payment: While you may exercise the rights licensed immediately upon issuance of the license at the end of the licensing process for the transaction, provided that you have disclosed complete and accurate details of your proposed use, no license is finally effective unless and until full payment is received from you (either by publisher or by CCC) as provided in CCC's Billing and Payment terms and conditions. If full payment is not received on a timely basis, then any license preliminarily granted shall be deemed automatically revoked and shall be void as if never granted. Further, in the event that you breach any of these terms and conditions or any of CCC's Billing and Payment terms and conditions, the license is automatically revoked and shall be void as if never granted. Use of materials as described in a revoked license, as well as any use of the materials beyond the scope of an unrevoked license, may constitute copyright infringement and publisher reserves the right to take any and all action to protect its copyright in the materials.

9. Warranties: Publisher makes no representations or warranties with respect to the licensed material.

10. Indemnity: You hereby indemnify and agree to hold harmless publisher and CCC, and their respective officers, directors, employees and agents, from and against any and all claims arising out of your use of the licensed material other than as specifically authorized pursuant to this license.

11. No Transfer of License: This license is personal to you and may not be sublicensed, assigned, or transferred by you to any other person without publisher's written permission.

12. No Amendment Except in Writing: This license may not be amended except in a writing signed by both parties (or, in the case of publisher, by CCC on publisher's behalf).

13. Objection to Contrary Terms: Publisher hereby objects to any terms contained in any purchase order, acknowledgment, check endorsement or other writing prepared by you, which terms are inconsistent with these terms and conditions or CCC's Billing and Payment terms and conditions. These terms and conditions, together with CCC's Billing and Payment terms and conditions (which are incorporated herein), comprise the entire agreement between you and publisher (and CCC) concerning this licensing transaction. In the event of any conflict between your obligations established by these terms and conditions and those established by CCC's Billing and Payment terms and conditions, these terms and conditions shall control.

14. Revocation: Elsevier or Copyright Clearance Center may deny the permissions described in this License at their sole discretion, for any reason or no reason, with a full refund payable to you. Notice of such denial will be made using the contact information provided by you. Failure to receive such notice will not alter or invalidate the denial. In no event will Elsevier or Copyright Clearance Center be responsible or liable for any costs, expenses or damage incurred by you as a result of a denial of your permission request, other than a refund of the amount(s) paid by you to Elsevier and/or Copyright Clearance Center for denied

permissions.

LIMITED LICENSE

The following terms and conditions apply only to specific license types:

15. Translation: This permission is granted for non-exclusive world **English** rights only unless your license was granted for translation rights. If you licensed translation rights you may only translate this content into the languages you requested. A professional translator must perform all translations and reproduce the content word for word preserving the integrity of the article. If this license is to re-use 1 or 2 figures then permission is granted for non-exclusive world rights in all languages.

16. Posting licensed content on any Website: The following terms and conditions apply as follows: Licensing material from an Elsevier journal: All content posted to the web site must maintain the copyright information line on the bottom of each image; A hyper-text must be included to the Homepage of the journal from which you are licensing at <http://www.sciencedirect.com/science/journal/xxxxx> or the Elsevier homepage for books at <http://www.elsevier.com>; Central Storage: This license does not include permission for a scanned version of the material to be stored in a central repository such as that provided by Heron/XanEdu.

Licensing material from an Elsevier book: A hyper-text link must be included to the Elsevier homepage at <http://www.elsevier.com> . All content posted to the web site must maintain the copyright information line on the bottom of each image.

Posting licensed content on Electronic reserve: In addition to the above the following clauses are applicable: The web site must be password-protected and made available only to bona fide students registered on a relevant course. This permission is granted for 1 year only. You may obtain a new license for future website posting.

For journal authors: the following clauses are applicable in addition to the above: Permission granted is limited to the author accepted manuscript version* of your paper.

***Accepted Author Manuscript (AAM) Definition:** An accepted author manuscript (AAM) is the author's version of the manuscript of an article that has been accepted for publication and which may include any author-incorporated changes suggested through the processes of submission processing, peer review, and editor-author communications. AAMs do not include other publisher value-added contributions such as copy-editing, formatting, technical enhancements and (if relevant) pagination.

You are not allowed to download and post the published journal article (whether PDF or HTML, proof or final version), nor may you scan the printed edition to create an electronic version. A hyper-text must be included to the Homepage of the journal from which you are licensing at <http://www.sciencedirect.com/science/journal/xxxxx>. As part of our normal production process, you will receive an e-mail notice when your article appears on Elsevier's online service ScienceDirect (www.sciencedirect.com). That e-mail will include the article's Digital Object Identifier (DOI). This number provides the electronic link to the published article and should be included in the posting of your personal version. We ask that

you wait until you receive this e-mail and have the DOI to do any posting.

Posting to a repository: Authors may post their AAM immediately to their employer's institutional repository for internal use only and may make their manuscript publically available after the journal-specific embargo period has ended.

Please also refer to [Elsevier's Article Posting Policy](#) for further information.

18. **For book authors** the following clauses are applicable in addition to the above: Authors are permitted to place a brief summary of their work online only.. You are not allowed to download and post the published electronic version of your chapter, nor may you scan the printed edition to create an electronic version. **Posting to a repository:** Authors are permitted to post a summary of their chapter only in their institution's repository.

20. **Thesis/Dissertation:** If your license is for use in a thesis/dissertation your thesis may be submitted to your institution in either print or electronic form. Should your thesis be published commercially, please reapply for permission. These requirements include permission for the Library and Archives of Canada to supply single copies, on demand, of the complete thesis and include permission for Proquest/UMI to supply single copies, on demand, of the complete thesis. Should your thesis be published commercially, please reapply for permission.

Elsevier Open Access Terms and Conditions

Elsevier publishes Open Access articles in both its Open Access journals and via its Open Access articles option in subscription journals.

Authors publishing in an Open Access journal or who choose to make their article Open Access in an Elsevier subscription journal select one of the following Creative Commons user licenses, which define how a reader may reuse their work: Creative Commons Attribution License (CC BY), Creative Commons Attribution – Non Commercial - ShareAlike (CC BY NC SA) and Creative Commons Attribution – Non Commercial – No Derivatives (CC BY NC ND)

Terms & Conditions applicable to all Elsevier Open Access articles:

Any reuse of the article must not represent the author as endorsing the adaptation of the article nor should the article be modified in such a way as to damage the author's honour or reputation.

The author(s) must be appropriately credited.

If any part of the material to be used (for example, figures) has appeared in our publication with credit or acknowledgement to another source it is the responsibility of the user to ensure their reuse complies with the terms and conditions determined by the rights holder.

Additional Terms & Conditions applicable to each Creative Commons user license:

CC BY: You may distribute and copy the article, create extracts, abstracts, and other revised versions, adaptations or derivative works of or from an article (such as a translation), to include in a collective work (such as an anthology), to text or data mine the article, including for commercial purposes without permission from Elsevier

CC BY NC SA: For non-commercial purposes you may distribute and copy the article, create extracts, abstracts and other revised versions, adaptations or derivative works of or from an article (such as a translation), to include in a collective work (such as an anthology), to text and data mine the article and license new adaptations or creations under identical terms without permission from Elsevier

CC BY NC ND: For non-commercial purposes you may distribute and copy the article and include it in a collective work (such as an anthology), provided you do not alter or modify the article, without permission from Elsevier

Any commercial reuse of Open Access articles published with a CC BY NC SA or CC BY NC ND license requires permission from Elsevier and will be subject to a fee.

Commercial reuse includes:

- Promotional purposes (advertising or marketing)
- Commercial exploitation (e.g. a product for sale or loan)
- Systematic distribution (for a fee or free of charge)

Please refer to [Elsevier's Open Access Policy](#) for further information.

21. Other Conditions:

v1.7

Questions? customer@copyright.com or +1-855-239-3415 (toll free in the US) or +1-978-646-2777.

Gratis licenses (referencing \$0 in the Total field) are free. Please retain this printable license for your reference. No payment is required.

Curriculum Vitae

Edward Stokan

Education

Ph. D. Physics & Planetary Science
The University of Western Ontario
London, Ontario, Canada
2008 - 2014

B. Sc. (Hon.) Physics
Trent University
Peterborough, Ontario, Canada
2004 - 2008

Related Work Experience

Teaching Assistant, Physics and Astronomy
The University of Western Ontario
2008 - 2013

Teaching Assistant, Physics
Trent University
2007

Awards

Faculty of Science Graduate Student Teaching Award
The University of Western Ontario
2013

Postgraduate Scholarship, PGS-D
Natural Sciences and Engineering Research Council
2010 - 2012

Department of Physics and Astronomy Teaching Assistant Award
The University of Western Ontario
2010

Canada Graduate Scholarship, CGS-M
Natural Sciences and Engineering Research Council
2008 - 2010

Governor General's Silver Academic Medal
2008

Publications

Stokan, E., Campbell-Brown, M. D., (2014). *A particle-based model for ablation and wake formation in faint meteors*. Monthly Notices of the Royal Astronomical Society, accepted November 29, 2014.

Stokan, E., Campbell-Brown, M. D., (2014). *Transverse motion of fragmenting faint meteors observed with the Canadian Automated Meteor Observatory*. Icarus, 232, 1-12.

Campbell-Brown, M. D., Borovička, J., Brown, P. G., Stokan, E., (2013). *High-resolution modelling of meteoroid ablation*. Astronomy & Astrophysics, 557, A41, 13pp.

Stokan, E., Campbell-Brown, M. D., Brown, P. G., Hawkes, R. L., Doubova, M., Weryk, R. J., (2013). *Optical trail widths of faint meteors observed with the Canadian Automated Meteor Observatory*. Monthly Notices of the Royal Astronomical Society, 433 (2), 962-975.

Stokan, E., Campbell-Brown, M. D., (2010). *An investigation of how a meteor light curve is modified by meteor shape and atmospheric density perturbations*. In: *Meteoroids: The Smallest Solar System Bodies, Proceedings of the Meteoroids 2010 Conference*, edited by W. J. Cooke, D. E. Moser, B. F. Hardin, and D. Janches. NASA/CP-2011-216469, 163-167.